



**THE AERODYNAMIC PERFORMANCE OF THE HOUCK CONFIGURATION
FLOW GUIDES**

THESIS

Dermot N. Killian II, Ensign, USN

AFIT/GAE/ENY/07-J09

**DEPARTMENT OF THE AIR FORCE
AIR UNIVERSITY**

AIR FORCE INSTITUTE OF TECHNOLOGY

Wright-Patterson Air Force Base, Ohio

APPROVED FOR PUBLIC RELEASE; DISTRIBUTION UNLIMITED

The views expressed in this thesis are those of the author and do not reflect the official policy or position of the United States Air Force, Department of Defense, or the U.S. Government.

AFIT/GAE/ENY/07-J09

**THE AERODYNAMIC PERFORMANCE OF THE HOUCK CONFIGURATION FLOW
GUIDES**

THESIS

Presented to the Faculty

Department of Aeronautical and Astronautical Engineering

Graduate School of Engineering and Management

Air Force Institute of Technology

Air University

Air Education and Training Command

In Partial Fulfillment of the Requirements for the
Degree of Master of Science in Aeronautical Engineering

Dermot N. Killian II, B.S.

Ensign, USN

June 2007

APPROVED FOR PUBLIC RELEASE; DISTRIBUTION UNLIMITED

Abstract

In an effort to explore efficient wing designs for UAV's, the Air Force is investigating the patented Houck Aircraft Configuration, which is a joined-wing aircraft with curved flow guides of varying camber connecting the upper and lower wingtips. Models were drawn in three-dimensions using Solidworks® with upper and lower wings drawn as identical NACA 2412 airfoil sections for all models. A variety of airfoil sections between the upper and lower wingtips were drawn and rotated to achieve a combination of cant and angle of attack variation. Subsequently, a solid part was lofted through these sections and merged with the upper and lower wings. Each model was built by a rapid prototype machine. A six-component balance in the AFIT low-speed wind tunnel provided measurements yielding the aerodynamic data of each model. Comparisons are made to the same basic planform area without flow guides and to a case where the wingtips are joined with a flat plate. At a Reynolds number of 38K, the increase in skin friction drag outweighed any possible reduction of induced drag. However for Reynolds numbers in the 57K to 120K range, improvements in L/D_{\max} of about 2-5% over the no flow guide case were measured.

Acknowledgments

I would like to express my sincere appreciation to my faculty advisor, Dr. Mark Reeder, for his direction, help, and support throughout the course of this thesis effort. I would like to thank my sponsors, Captain Elaine Bryant and Cale Zeune, from the Air Force Research Laboratory, Air Vehicles Directorate for the support provided to me in this endeavor. Thanks to John Hixenbaugh for his expertise and coordination during the wind tunnel tests. I would also like to thank Chris Zickefoose, Jay Anderson, Captain Michael Walker, Tim Fry, Chris Gillum, Ron Houck, Colonel Raymond Maple, and Dr. Robert Canfield for their help along the way. Finally, a special thanks to my fiancé and family for their support and prayers throughout this process.

Dermot N. Killian II

Table of Contents

	Page
Abstract.....	iv
Acknowledgments.....	v
Table of Contents.....	vi
List of Figures.....	x
List of Tables.....	xvii
List of Symbols.....	xx
I. Introduction.....	1
1.1 Background.....	1
1.2 Problem Statement.....	4
1.3 Research Focus.....	4
II. Literature Review.....	7
2.1 Overview.....	7
2.2 Camber.....	7
2.3 Drag.....	8
2.4 Wing-Tip Vortices.....	13
2.5 Winglets.....	16
2.6 Biplanes.....	18
2.7 Joined Wings.....	22
2.8 Lift-to-Drag Ratio.....	23
2.9 Hot-Wire Anemometry.....	25
2.10 <i>SolidWorks</i> ®.....	26
III. Methodology.....	28

	Page
3.1 Chapter Overview	28
3.2 <i>SolidWorks</i> Construction.....	28
3.2.1 Patent Specification.....	28
3.2.2 Step 1: Airfoil.....	29
3.2.3 Step 2: Airfoil Section Extrusion	30
3.2.4 Step 3: Upper Wing Construction	30
3.2.5 Step 4: Mirroring the Extrusions.....	32
3.2.6 Step 5: Creating the Body that Joins the Wings.....	32
3.2.7 Step 6: Creating the Flow Guides that Join the Wings	33
3.2.8 Step 7: Scaling the Model	35
3.2.9 Step 8: Adding the Balance Attachment	36
3.2.10 Step 9: Final Review before 3-D Printing.....	40
3.2.11 Step 10: 3-D Printing.....	41
3.3 Models.....	43
3.3.1 Original Configuration Model.....	43
3.3.2 Original Configuration Model Flow Guides	44
3.3.3 Positive 5° Canted Flow Guide Model.....	47
3.3.4 Negative 5° Canted Flow Guide Model	49
3.3.5 Endplate Configuration	51
3.3.6 No Flow Guide Configuration.....	52
3.4 Experimental Equipment.....	53
3.4.1 AFIT Low-Speed Wind Tunnel	53

	Page
3.4.2 AFIT 10 lb Strain Gage Balance	57
3.5 Collecting and Processing Data.....	58
3.5.1 Correction of Balance Data using <i>MATLAB</i> ® 10 lb Balance Code.....	58
3.5.2 Uncertainty Analysis	61
3.5.3 Houck 24" Hot-Wire Analysis	63
3.6 Test Plan.....	64
3.6.1 Overview	64
3.6.2 Original Configuration	65
3.6.3 + 5° Configuration.....	66
3.6.4 - 5° Configuration	66
3.6.5 Endplate Configuration	66
3.6.6 No Flow Guide Configuration.....	67
IV. Results and Analysis.....	68
4.1 Chapter Overview	68
4.2 Wind Tunnel Balance Data – Alpha Sweeps: Individual Models.....	68
4.2.1 Original Configuration Model.....	68
4.2.2 + 5° Cant Configuration Model.....	80
4.2.3 - 5° Cant Configuration Model	85
4.2.4 Endplate Configuration Model.....	89
4.2.5 No Flow Guide Configuration Model	93
4.3 Wind Tunnel Data – Alpha Sweeps: Model Comparisons by Speed.....	97
4.3.1 $Re \approx 38K$ / 20 MPH.....	97

	Page
4.3.2 $Re \approx 57K / 30 \text{ MPH}$	102
4.3.3 $Re \approx 78K / 40 \text{ MPH}$	107
4.3.4 $Re \approx 120K / 60 \text{ MPH}$	112
4.3.5 Trends.....	117
4.4 Neutral Longitudinally Stable $C_{m\alpha}$	123
4.5.1 Calculation	123
4.5.2 Results	124
4.5 Vortex Centroid and Moment Calculations and Results	125
V. Conclusions and Recommendations	129
5.1 Conclusions of Research	129
5.2 Recommendations for Future Research	132
Appendix A: 10 lb Balance Dimensions.....	134
Appendix B: <i>MATLAB</i> 10 lb Balance Code	135
Appendix C: Aerodynamic Data of the Five Model Configurations.....	147
Appendix D: <i>MATLAB</i> Code for Vortex Centroid Calculations	155
Bibliography	157
Vita.....	160

List of Figures

	Page
Figure 1: Isometric View of the Houck Lifting Foil (reproduced from Reference 16).....	1
Figure 2: Flow Guide Structure and Pressure Distribution (reproduced from Reference 16)	2
Figure 3: Flow Guide Combining Wing-Tip Vortices.....	2
Figure 4: Resultant Force of Progressive Camber Opposing Resultant Force of Flow Guide Vortex	3
Figure 5: Original Configuration Model Utilizing the Flow Guides as prescribed by the Houck Lifting Foil Patent.....	5
Figure 6: Three-View Representation of 24" Houck Configuration (reproduced from Reference 31)	6
Figure 7: Airfoil geometrical elements (reproduced from Reference 17)	8
Figure 8: Effects of Zero and Positive Camber (reproduced from Reference 28).....	8
Figure 9: Effect of Induced Drag on Finite Wing (reproduced from Reference 11)	10
Figure 10: Drag vs Velocity for Turbofan/Turbojet Aircraft in Level Flight (reproduced from Reference 5)	11
Figure 11: Drag vs Velocity for Propeller-Driven Aircraft in Level Flight (reproduced from Reference 5)	12
Figure 12: Equalizing Pressure at the Wing-Tips (reproduced from Reference 28)	14
Figure 13: Formation of Wing-Tip Vortices (reproduced from Reference 28).....	15
Figure 14: Creation of Downwash (reproduced from Reference 28)	15

	Page
Figure 15: Biplane Parameters: Stagger and Gap (reproduced from Reference 19)	20
Figure 16: Isometric View of Gall’s Semi-span Model (reproduced from Reference 13)	21
Figure 17: Front View of a Joined-Wing Aircraft (reproduced from Reference 33).....	22
Figure 18: Historic Maximum Lift-to-Drag Ratios of Propeller-Driven Aircraft (reproduced from Reference 19)	25
Figure 19: Planes and Axes of an Empty <i>SolidWorks</i> Part Workspace	27
Figure 20: Progressive Camber of the Flow Guide (reproduced from Reference 16).....	29
Figure 21: NACA 2412 Coordinates Splined Together in <i>SolidWorks</i>	29
Figure 22: Sketch to Guide Airfoil Section in <i>SolidWorks</i>	30
Figure 23: Sketch to Guide Airfoil Section in <i>SolidWorks</i>	30
Figure 24: Gap Measurement for Upper Wing	31
Figure 25: Upper Wing Guide Sketch and Subsequent Extrusion.....	31
Figure 26: Mirroring over the Y-Z Plane.....	32
Figure 27: Body Airfoil and Guide Sketch	32
Figure 28: Extrusion of NACA 0010 Airfoil Body Section, Isometric and Side View...	33
Figure 29: Connecting Mid-Chord Points on Upper and Lower Wing-Tips	33
Figure 30: Guide Plane and Sketch for Flow Guide Loft	34
Figure 31: Lofting of the Flow Guide and the Comparison to the Guide Sketch	34
Figure 32: Mirroring the Flow Guide in the Y-Z Plane	35
Figure 33: Uniform Scaling of the Model.....	35
Figure 34: Sketch of the Mid-Point for the Balance	36

	Page
Figure 35: Sketch Plane and Geometry for the Sting Attachment Cylinder.....	37
Figure 36: Extrusion of the Balance Attachment.....	37
Figure 37: Cutout for the Balance.....	38
Figure 38: Flat Sides of the Balance Attachment	38
Figure 39: Hole Cutouts for the Balance Screws.....	39
Figure 40: Bottom Hole Cutouts for the Balance Screws.....	39
Figure 41: Counter-Bores for the Sting Attachment Holes	40
Figure 42: Final Review of the Original Configuration Model	40
Figure 43: Export Options of the Part to STL File Save.....	41
Figure 44: The Objet Eden 333 Printer and the Printer Head during the Build Process .	42
Figure 45: The Completed Original Configuration Model	42
Figure 46: Left, Front, Top, and Isometric Views of the Original Configuration Model with Dimensions (in).....	44
Figure 47: Maximum Camber of Flow Guide at Upper and Lower Wings.....	45
Figure 48: Gradually Diminishing Camber of the Airfoil on the Flow Guide	45
Figure 49: Symmetrical Airfoil at the Midpoint of the Flow Guide.....	46
Figure 50: Past Midpoint: Gradually Diminishing Camber of the Airfoil on the Flow Guide	46
Figure 51: Comparison of the Houck Patent Claim 17 and the Original Configuration Flow Guide (reproduced from Reference 16)	47
Figure 52: The 45° and 135° planes where the Canted Airfoils are Located	48
Figure 53: The Rotated Airfoils and Subsequent +5° Canted Airfoil.....	48

	Page
Figure 54: Left, Front, Top, and Isometric Views of the + 5° Canted Flow Guide Model	49
Figure 55: Front View of the + 5° Canted Flow Guide Model.....	49
Figure 56: The Rotated Airfoils and Subsequent -5° Canted Airfoil	50
Figure 57: Left, Front, Top, and Isometric Views of the -5° Canted Flow Guide Model	50
Figure 58: Front View of the - 5° Canted Flow Guide Model.....	51
Figure 59: Left, Front, Top, and Isometric Views of the End Plate Configuration Model	51
Figure 60: Front View of the End Plate Configuration Model	52
Figure 61: Left, Front, Top, and Isometric Views of the No Flow Guide Configuration Model	52
Figure 62: Front View of the No Flow Guide Configuration Model.....	53
Figure 63: Schematic of the Low-Speed Wind Tunnel (reproduced from Reference 31:24)	53
Figure 64: Intake and Convergent Section of the Wind Tunnel (reproduced from Reference 31:25)	54
Figure 65: Test Section, Balance, Sting, and Moveable Table (reproduced from Reference 31:25)	55
Figure 66: Angle Control Device (reproduced from Reference 31:26).....	55
Figure 67: Computerized Data Acquisition System	56
Figure 68: 10 lb Balance Mounted in Test Section of the Wind Tunnel (reproduced from Reference 31:28)	57
Figure 69: Location of Aircraft Center of Gravity and Balance Moment Center.....	59

	Page
Figure 70: 24" Houck Configuration Three-View Representation (reproduced from Reference 31)	64
Figure 71: Drag Coefficient – Original Configuration Model.....	70
Figure 72: Lift Coefficient vs. Angle of Attack – Original Configuration Model	71
Figure 73: Pitch Moment Coefficient vs. Angle of Attack – Original Configuration Model (X _{cmb} = 1.0025").....	72
Figure 74: Lift-to-Drag – Original Configuration Model	73
Figure 75: Lift-to-Drag – Conservative Uncertainty Analysis – Original Configuration Model	74
Figure 76: Lift-to-Drag – Tested Uncertainty Analysis – Original Configuration Model	76
Figure 77: C _L ^{3/2} /C _D – Max Endurance – Original Configuration Model.....	79
Figure 78: Drag Coefficient – + 5° Cant Configuration Model.....	81
Figure 79: Lift Coefficient vs. Angle of Attack – + 5° Cant Configuration Model	82
Figure 80: Pitch Moment Coefficient vs. Angle of Attack – + 5° Cant Configuration Model (X _{cmb} = 1.0025").....	83
Figure 81: Lift-to-Drag – + 5° Cant Configuration Model	84
Figure 82: C _L ^{3/2} /C _D – Max Endurance – + 5° Cant Configuration Model.....	84
Figure 83: Drag Coefficient – - 5° Cant Configuration Model.....	86
Figure 84: Lift Coefficient vs. Angle of Attack – - 5° Cant Configuration Model	86
Figure 85: Pitch Moment Coefficient vs. Angle of Attack – - 5° Cant Configuration Model (X _{cmb} = 1.0025").....	87

	Page
Figure 86: Lift-to-Drag – - 5° Cant Configuration Model.....	88
Figure 87: $C_L^{3/2}/C_D$ – Max Endurance – - 5° Cant Configuration Model.....	88
Figure 88: Drag Coefficient – Endplate Configuration Model.....	90
Figure 89: Lift Coefficient vs. Angle of Attack – Endplate Configuration Model.....	90
Figure 90: Pitch Moment Coefficient vs. Angle of Attack – Endplate Configuration Model ($X_{cmb} = 1.0025''$).....	91
Figure 91: Lift-to-Drag – Endplate Configuration Model.....	92
Figure 92: $C_L^{3/2}/C_D$ – Max Endurance – Endplate Configuration Model.....	92
Figure 93: Drag Coefficient – No Flow Guide Configuration Model.....	94
Figure 94: Lift Coefficient vs. Angle of Attack – No Flow Guide Configuration Model	94
Figure 95: Pitch Moment Coefficient vs. Angle of Attack – No Flow Guide Configuration Model ($X_{cmb} = 1.0025''$).....	95
Figure 96: Lift-to-Drag – No Flow Guide Configuration Model.....	96
Figure 97: $C_L^{3/2}/C_D$ – Max Endurance – No Flow Guide Configuration Model.....	96
Figure 98: Drag Polar vs. Angle of Attack – $Re \sim 38K / 20MPH$	99
Figure 99: Lift-to-Drag vs. Angle of Attack – $Re \sim 38K / 20MPH$	100
Figure 100: $C_L^{3/2}/C_D$ – Max Endurance vs. Angle of Attack – $Re \sim 38K / 20MPH$	101
Figure 101: Drag Polar vs. Angle of Attack – $Re \sim 57K / 30MPH$	104
Figure 102: Lift-to-Drag vs. Angle of Attack – $Re \sim 57K / 30MPH$	105
Figure 103: $C_L^{3/2}/C_D$ – Max Endurance vs. Angle of Attack – $Re \sim 57K / 30MPH$	106
Figure 104: Drag Polar vs. Angle of Attack – $Re \sim 78K / 40MPH$	109
Figure 105: Lift-to-Drag vs. Angle of Attack – $Re \sim 78K / 40MPH$	110

	Page
Figure 106: $C_L^{3/2}/C_D$ – Max Endurance vs. Angle of Attack – $Re \sim 78K / 40MPH$	111
Figure 107: Drag Polar vs. Angle of Attack – $Re \sim 120K / 60MPH$	114
Figure 108: Lift-to-Drag vs. Angle of Attack – $Re \sim 120K / 60MPH$	115
Figure 109: $C_L^{3/2}/C_D$ – Max Endurance vs. Angle of Attack – $Re \sim 120K / 60MPH$	116
Figure 110: % Change of L/D_{max} vs. Reynolds Number – $Re \sim 38K, 57K, 78K, \& 120K$	118
Figure 111: % Change of $C_L^{3/2}/C_{Dmax}$ vs. Reynolds Number – $Re \sim 38K, 57K, 78K, \&$ 120K.....	119
Figure 112: % C_D/C_{Di} vs. Reynolds Number – $Re \sim 38K, 57K, 78K, \& 120K$	121
Figure 113: Variation of Aircraft Center of Gravity and Balance Moment Center.....	123
Figure 114: Coefficient of Pitch Moment vs. Alpha to determine the Neutral Longitudinally Stable $C_{m\alpha}$	125
Figure 115: Hot-Wire Vorticity Analysis – $Re \sim 125K \& \alpha = 4.13^\circ$ (reproduced from Reference 30)	126
Figure 116: Y-coordinate Centroid on Hot-Wire Vorticity Analysis – $Re \sim 125K \& \alpha =$ 4.13° (reproduced from Reference 31)	127

List of Tables

	Page
Table 1: Lift-to-Drag Ratios of Historical Aircraft (reproduced from Reference 12).....	24
Table 2: Max Allowable Forces and Moments for the 10 lb Balance	57
Table 3: Summary of Tests Performed	65
Table 4: Original Configuration Test Dates, Temperature, and Pressure.....	66
Table 5: + 5° Canted Flow Guide Configuration Test Dates, Temperature, and Pressure	66
Table 6: - 5° Canted Flow Guide Configuration Test Dates, Temperature, and Pressure	66
Table 7: Endplate Configuration Test Dates, Temperature, and Pressure	66
Table 8: No Flow Guide Configuration Test Dates, Temperature, and Pressure	67
Table 9: Aerodynamic Performance of the Original Configuration Model.....	69
Table 10: Conservative Uncertainty Analysis in L/D for the Original Configuration Model	75
Table 11: Tested Uncertainty Analysis in L/D for the Original Configuration Model	77
Table 12: Aerodynamic Performance of the + 5° Cant Configuration Model.....	80
Table 13: Aerodynamic Performance of the – -5° Cant Configuration Model.....	85
Table 14: Aerodynamic Performance of the – Endplate Configuration Model.....	89
Table 15: Aerodynamic Performance of the – No Flow Guide Configuration Model	93
Table 16: Summary of the Aerodynamic Performance Comparison of the Five Models – Re ~ 38K	98
Table 17: Comparison of Induced and Parasite Drag of the Five Models – Re ~ 38K	99
Table 18: Comparison of L/D_{\max} and $C_L^{3/2}/C_{D\max}$ of the Five Models – Re ~ 38K.....	100

	Page
Table 19: Comparison of Aspect Ratio for the Five Models – Re ~ 38K	101
Table 20: Summary of the Aerodynamic Performance Comparison of the Five Models – Re ~ 57K	103
Table 21: Comparison of Induced and Parasite Drag of the Five Models – Re ~ 57K ..	104
Table 22: Comparison of L/D_{\max} and $C_L^{3/2}/C_{D\max}$ of the Five Models – Re ~ 57K.....	105
Table 23: Comparison of Aspect Ratio for the Five Models – Re ~ 57K	106
Table 24: Summary of the Aerodynamic Performance Comparison of the Five Models – Re ~ 78K	108
Table 25: Comparison of Induced and Parasite Drag of the Five Models – Re ~ 78K ..	109
Table 26: Comparison of L/D_{\max} and $C_L^{3/2}/C_{D\max}$ of the Five Models – Re ~ 78K.....	110
Table 27: Comparison of Aspect Ratio for the Five Models – Re ~ 78K	111
Table 28: Summary of the Aerodynamic Performance Comparison of the Five Models – Re ~ 120K	113
Table 29: Comparison of Induced and Parasite Drag of the Five Models – Re ~ 120K	114
Table 30: Comparison of L/D_{\max} and $C_L^{3/2}/C_{D\max}$ of the Five Models – Re ~ 120K.....	115
Table 31: Comparison of Aspect Ratio for the Five Models – Re ~ 120K	116
Table 32: Aerodynamic Performance Comparison for the Models – Re ~ 38K, 57K, 78K, & 120K.....	117
Table 33: Span Efficiency Comparison for the Models – Re ~ 38K, 57K, 78K, & 120K	122
Table 34: Varying $C_{m\alpha}$ for the Models – Re ~ 120K	124
Table 35: Vortex Centroid Calculations – Re ~ 120K.....	127

	Page
Table 36: Original Configuration at 20 mph: Alpha Sweep	147
Table 37: Original Configuration at 30 mph: Alpha Sweep	147
Table 38: Original Configuration at 40 mph: Alpha Sweep	148
Table 39: Original Configuration at 60 mph: Alpha Sweep	148
Table 40: +5° Cant Configuration at 20 mph: Alpha Sweep	148
Table 41: +5° Cant Configuration at 30 mph: Alpha Sweep	149
Table 42: +5° Cant Configuration at 40 mph: Alpha Sweep	149
Table 43: +5° Cant Configuration at 60 mph: Alpha Sweep	150
Table 44: -5° Cant Configuration at 20 mph: Alpha Sweep	150
Table 45: -5° Cant Configuration at 30 mph: Alpha Sweep	150
Table 46: -5° Cant Configuration at 40 mph: Alpha Sweep	151
Table 47: -5° Cant Configuration at 60 mph: Alpha Sweep	151
Table 48: Endplate Configuration at 20 mph: Alpha Sweep	151
Table 49: Endplate Configuration at 30 mph: Alpha Sweep	152
Table 50: Endplate Configuration at 40 mph: Alpha Sweep	152
Table 51: Endplate Configuration at 60 mph: Alpha Sweep	153
Table 52: No Flow Guide Configuration at 20 mph: Alpha Sweep	153
Table 53: No Flow Guide Configuration at 30 mph: Alpha Sweep	153
Table 54: No Flow Guide Configuration at 40 mph: Alpha Sweep	154
Table 55: No Flow Guide Configuration at 60 mph: Alpha Sweep	154

List of Symbols

A	axial load force	(lb _f)
AR	aspect ratio	(-)
α	angle of attack	(°)
b	wing span	(in)
\bar{c}	average chord	(in)
C_D	total drag coefficient	(-)
C_{Di}	induced drag coefficient	(-)
C_{D0}	minimum coefficient of drag	(-)
C_L	lift coefficient	(-)
C_{Lmax}	maximum coefficient of lift	(-)
C_m	pitch moment coefficient	(-)
D	drag	(lbs)
D_{form}	form drag	(lbs)
$D_{induced}$	induced drag	(lbs)
$D_{interference}$	interference drag	(lbs)
$D_{parasite}$	parasite drag	(lbs)
$D_{skin\ friction}$	skin friction drag	(lbs)
D_{total}	total drag	(lbs)
δ_b	blockage correction factor	(-)
e	span efficiency factor	(-)

$e AR$	effective aspect ratio	(-)
Γ	circulation	(in ² /s)
k	ratio of span to tunnel height	(-)
Ke	normalized turbulent kinetic energy	(-)
L/D	lift-to-drag ratio	(-)
L/D_{\max}	maximum lift-to-drag ratio	(-)
λ	wind tunnel aspect ratio	(-)
N	normal load force	(lb _f)
P_{baro}	barometric pressure in test room	(psi)
q	dynamic pressure	(in Hg)
ρ	air density	(slug/ft ³)
Re	Reynolds number	(-)
S	planform area of wing	(in ²)
T_{room}	temperature in test room	(°F)
u	u-component of velocity in wind axis	(mph, m/s)
u_{rms}	root mean squared of u measurements	(mph, m/s)
v	v-component of velocity in wind axis	(mph, m/s)
v_{rms}	root mean squared of v measurements	(mph, m/s)
V	average wind tunnel velocity	(mph, m/s)
w	w-component of velocity in wind axis	(mph, m/s)
w_{rms}	root mean squared of w measurements	(mph, m/s)
W	aircraft weight	(lbs)

x	x-component of velocity in hot-wire axis	(mph, m/s)
X_{cg}	x location of center of gravity from aircraft nose	(in)
X_{cmb}	x distance from balance moment center to $\frac{1}{4}$ chord	(in)
y	y-component of velocity in hot-wire axis	(mph, m/s)
z	z-component of velocity in hot-wire axis	(mph, m/s)
Z_{cmb}	z distance from balance moment center to $\frac{1}{4}$ chord	(in)
ω_x	curl or vorticity about x axis	(rad/s)

THE AERODYNAMIC PERFORMANCE OF THE HOUCK CONFIGURATION FLOW GUIDES

I. Introduction

1.1 Background

As previously summarized by Michael Walker's Thesis (31), The Air Force Research Lab (AFRL) has been investigating the claims of a patent for a new aircraft wing design known as the Houck Lifting Foil (see Figure 1). The purpose of the Houck Lifting Foil is to provide an aerodynamically efficient design for a joined-wing aircraft. A description of the Houck Lifting Foil, as described by the patent's abstract, is as follows:

A lifting foil for an aircraft, a hydrofoil or the like having a pair of courses or wings. Vortex losses due to spanwise fluid flow are substantially reduced by joining the tips of the courses with flow guides configured for jointly terminating the undesired flows. Termination is effected by providing the flow guides with crosssections cambered for reducing the dynamic pressure of fluid flowing in a spanwise direction across the flow guide surfaces (16).

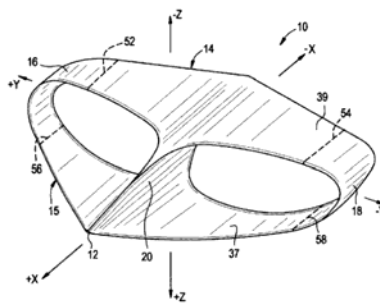
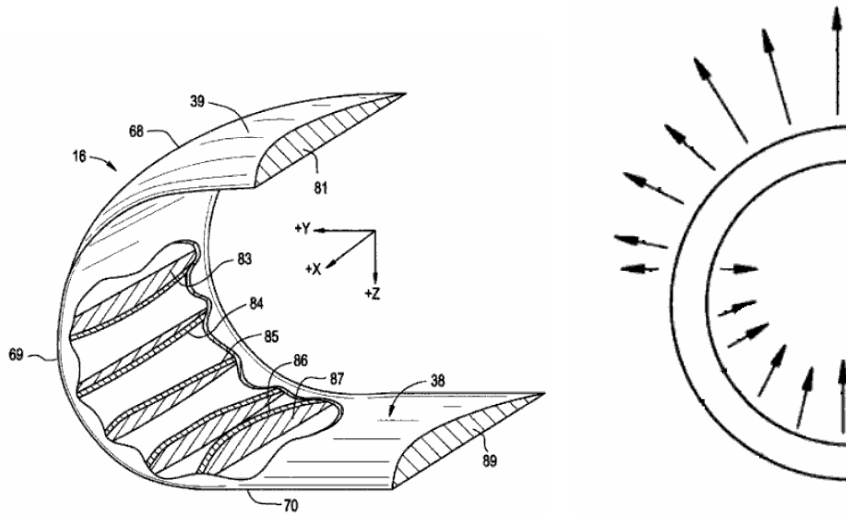


Figure 1: Isometric View of the Houck Lifting Foil (reproduced from Reference 16)

The upper and lower wings of the Houck Lifting Foil are connected by flow guides that are specially cambered and curved to direct airflow along a specified path (see

Figure 2). The cambered airfoil sections are placed at precise locations to control the pressure distribution along the surface of the curved flow guide.

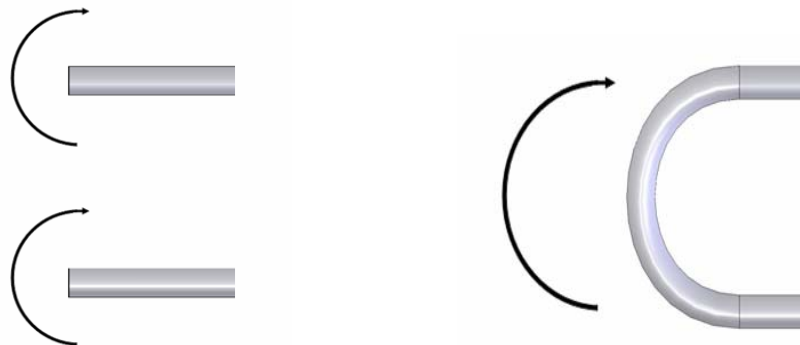


Varying Camber throughout Flow Guide

Pressure Distribution along Surface

Figure 2: Flow Guide Structure and Pressure Distribution (reproduced from Reference 16)

The purpose of the curved flow guide connection between the upper and lower wings is to combine the individual wing-tip vortices (without the flow guide) into a single vortex that is more spread out (see Figure 3), thus reducing induced drag.

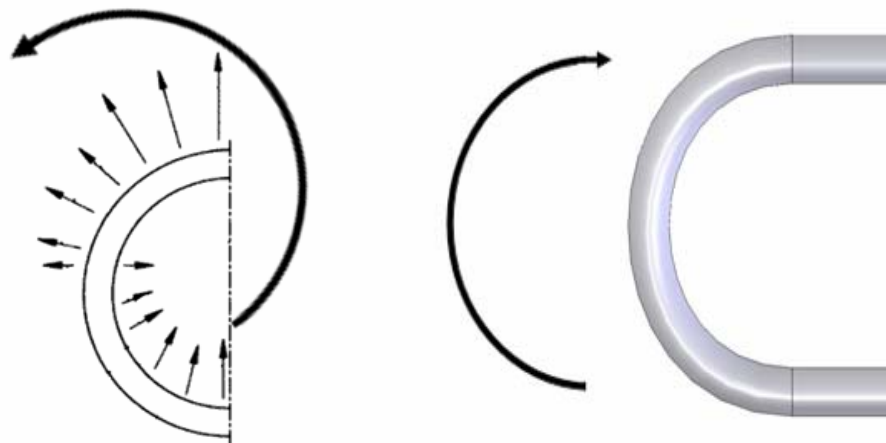


Individual Wing-Tip Vortices on Upper and Lower Wing

Combined Wing-Tip Vortex due to Flow Guide

Figure 3: Flow Guide Combining Wing-Tip Vortices

The flow guides are also progressively cambered along the curve in order to manipulate the flow near the wing-tips. From the lower wing the airfoil sections become progressively less cambered until the mid-point of the flow guide. At this point the airfoil is symmetric and does not provide any pressure difference (hence vortex). The process of progressive camber continues in the opposite direction until the camber of the flow guide matches the camber of the upper wing. The purpose of this variable camber flow guide design is to produce an aerodynamic force that opposes the aerodynamic force created by the wing-tip vortex of the flow guide (see Figure 4).



Resultant Force from the Progressive Camber Changes Resultant Force from Flow Guide Vortex
Figure 4: Resultant Force of Progressive Camber Opposing Resultant Force of Flow Guide Vortex

The designer of the Houck Lifting Foil claims that the use of the flow guides increases the aerodynamic efficiency by reducing the span-wise fluid flow over the wings, the cause of wing-tip vortices (16). The reduction of the wing-tip vortices strength would result in a reduction of induced drag (drag due to lift). If the reduction of induced drag is greater than the increase in parasite drag (profile drag, skin friction drag, and

interference drag) then the total drag will be reduced. Profile or form drag is related to the size of the aircraft whereby the flow guides would increase size. Skin friction is related to the friction of the fluid flow over the surface area of the aircraft whereby flow guides would increase surface area. Interference drag is caused the interference of boundary layers caused by other portions of the aircraft whereby the flow guides would increase interference. Hence, if this design is able to produce the aforementioned results, then it can be applied to various applications where aerodynamic efficiency is desired. These applications include, but are not limited to: fixed wing aircraft, rotary wing aircraft, submarines, and hydrofoils (16).

1.2 Problem Statement

The root question that is to be answered at the conclusion of this report is to determine whether or not the flow guides are able to perform as designed and stated in the patent. Does the progressive and variable camber along the flow guide create a resultant force that opposes the wing-tip vortex of the flow guide? Further more does this reduction in wing-tip vortices lower the induced drag as to the opposed increase in parasite drag due to the extra flow guide surface area? These questions will be attempted to be answered at the conclusion of this report.

1.3 Research Focus

The purpose of this report is to further investigate the aerodynamic performance of the Houck Lifting Foil. The primary investigative focus is on the aerodynamic properties associated with the variable camber flow guides. As prescribed by Patent

Number 7,100,867's 14th and 17th claims, models were constructed using *SolidWorks* that employ the variable camber flow guides (16). Figure 5 shows the Original Configuration Model that was constructed for testing.

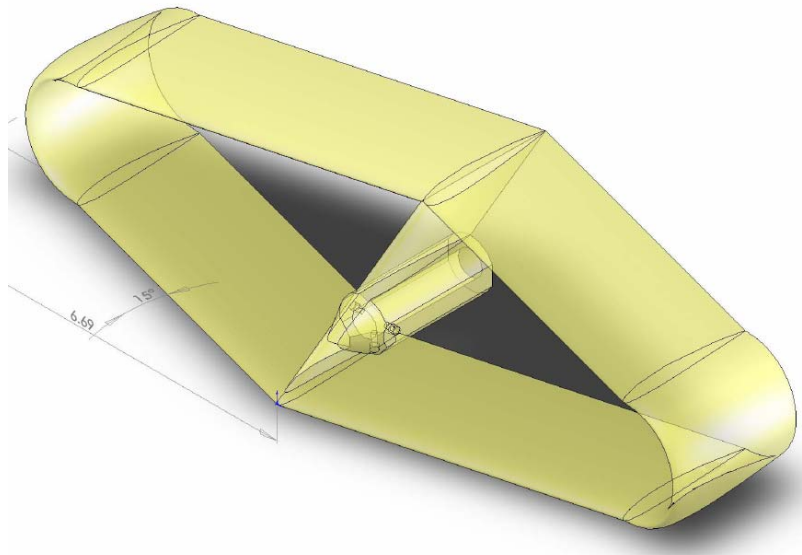


Figure 5: Original Configuration Model Utilizing the Flow Guides as prescribed by the Houck Lifting Foil Patent

The model has an average chord (\bar{c}) of 2.55", a wingspan (b) of 13.808", and a length of 5.59". The wing is based on a NACA 2412 airfoil section. It has a planform area (S) of 72.58 in². Further discussion of parameters is located in Section 3.3.

The models were built using the AFIT Objet 3D printer. In order to achieve aerodynamic analyses of the models, numerous tests were run in the AFIT low-speed wind tunnel. In addition to the aerodynamic analyses of the models, there was further examination of the Hot-Wire Anemometry data from the previous thesis investigation by Michael Walker (31). The model used for Hot-Wire Anemometry data is located in Figure 6.

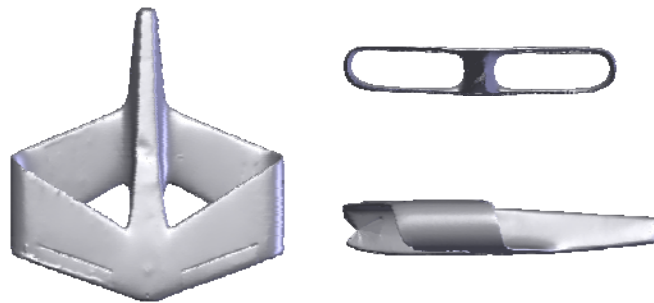


Figure 6: Three-View Representation of 24" Houck Configuration (reproduced from Reference 31)

The combination of these results in this report will be used in conjunction with other studies carried out by the Air Force Research Lab, Air Vehicles Directorate, Wright Patterson AFB, Ohio to determine the viability of the Houck Lifting Foil for the United States Air Force (6).

II. Literature Review

2.1 Overview

Since the dawn of manned flight there has been a constant effort to improve and refine aircraft aerodynamics. Before improvements can be made, the fundamentals of flight must first be understood. Therefore the beginning of this chapter begins with a few of the fundamentals of flight that will be the basis of discussion throughout the paper. This includes camber, drag, and wing-tip vortices. Next the chapter will progress into a discussion of devices and aircraft configurations that are the primary designs associated with the Houck configuration. This includes winglets, biplanes, and joined-wing aircraft. After that the chapter will discuss the evolution of aircraft efficiency which is primarily measured by lift-to-drag ratio. Finally the chapter will end with a discussion of measurement and building methods that were used to find the data for this paper.

2.2 Camber

Typical airfoil shape is determined by six elements: the leading edge, the trailing edge, the chord line, the camber line, the upper surface, and the lower surface. Camber is defined as the curvature of the mean camber line. The mean camber line is the line midway between upper and lower surfaces, extending from leading to the trailing edge (9). Figure 7 shows a positively cambered airfoil with the placement of the elements aforementioned.

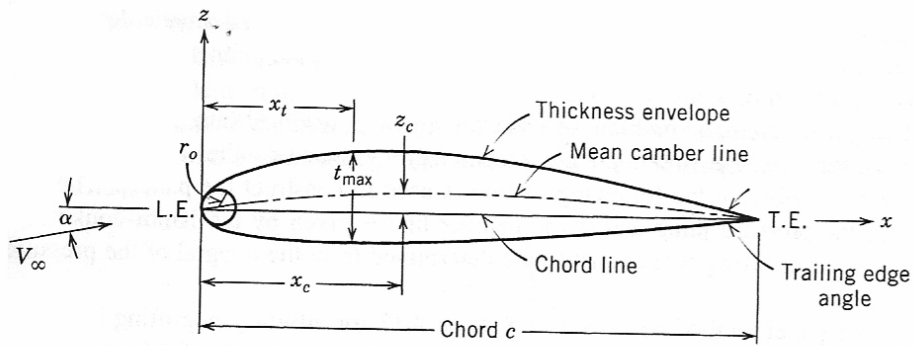


Figure 7: Airfoil geometrical elements (reproduced from Reference 17)

Camber contributes to the lift produced by the airfoil. At an angle of attack of zero, an airfoil with zero camber produces zero lift, an airfoil with positive camber produces positive lift, and an airfoil with negative camber produces negative lift. Figure 8 demonstrates how camber can affect lift.

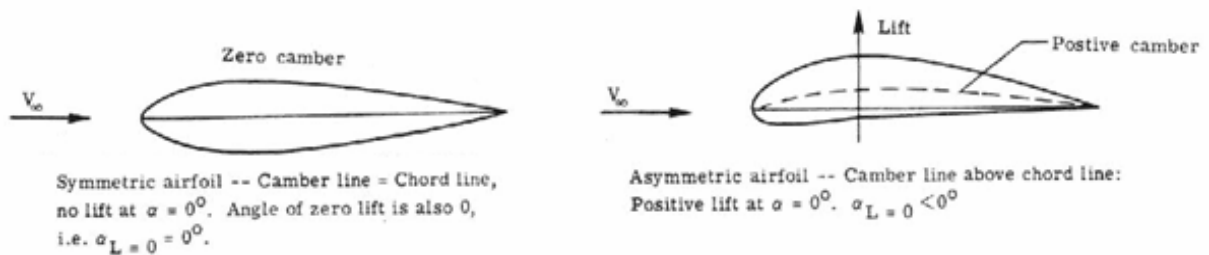


Figure 8: Effects of Zero and Positive Camber (reproduced from Reference 28)

2.3 Drag

“Drag is the component of the aerodynamic force that is parallel to the relative wind and retards the forward motion of the aircraft. At subsonic speeds, there are two kinds of drag: parasite drag and induced drag” (11). There is a third type of drag, compressibility drag; however this occurs at speeds higher than those considered in this study. The basic drag equation follows:

$$D = C_D q S \quad (1)$$

Where D (lbs) is drag, C_D is coefficient of drag, q is dynamic pressure (in Hg), and S is planform area of the wing (in²). The coefficient of drag, C_D , is the ratio of drag pressure to the dynamic pressure and is shown in the following equation:

$$C_D = \frac{D/S}{q} \quad (2)$$

These values of C_D are usually obtained experimentally.

Parasite drag, $D_{parasite}$, is made up of three different components: skin friction drag ($D_{skinfriction}$), form drag (D_{form}), and interference drag ($D_{interference}$). Skin friction drag is caused by the viscous friction within the boundary layer. The total area of the aircraft skin that is exposed to the airstream and its smoothness affects this type of drag. The major way to reduce the skin friction drag is to maintain the laminar airflow over the skin surface by maintaining a smooth surface by waxing and polishing the surfaces. Another method is to use laminar flow airfoils to delay boundary layer transition. Form drag, also known as pressure drag, is caused by the form of the aircraft. This drag occurs due to the turbulent wake behind the aircraft created by the pressure differences of flight.

Streamlining the fuselage and various other aircraft extremities reduces form drag.

Interference drag is caused by the interference of boundary layers from different parts of the aircraft (e.g. wing and fuselage). The total drag of the assembled components is

higher than the sum of the individual drag of the components unassembled. Smooth fairings at surface junctions reduce interference drag by creating fillets where sharp angles would otherwise occur. The breakdown of parasite drag in equation form is as follows:

$$D_{\text{parasite}} = D_{\text{skinfriction}} + D_{\text{form}} + D_{\text{interference}} \quad (3)$$

Where D_{parasite} is parasite drag (lbs), $D_{\text{skinfriction}}$ is skin friction drag (lbs), D_{form} is form drag (lbs), and $D_{\text{interference}}$ is interference drag (lbs).

Induced drag, D_{induced} , is the “least understood type of drag, but it is the most important, especially in the low-speed region of flight” (11). Induced drag, also known as drag to lift, is primarily caused by wing-tip vortices that form as the aircraft produces lift. Induced drag also includes the incremental change in pressure drag due to lift (due to the change in the angle of attack). Figure 9 shows the effect of induced drag on a finite wing.

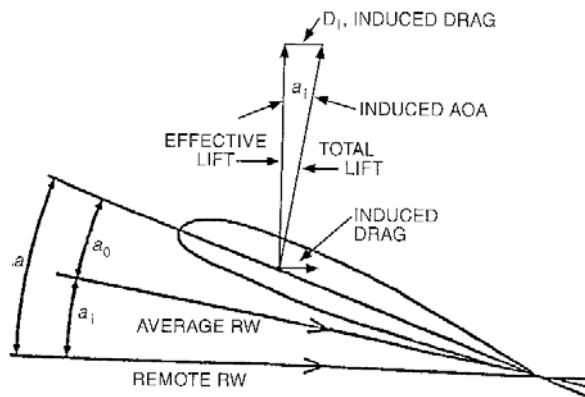


Figure 9: Effect of Induced Drag on Finite Wing (reproduced from Reference 11)

Total Drag, D_{total} (lbs), is the drag that is sum of induced drag, $D_{induced}$ (lbs), and parasite drag, $D_{parasite}$ (lbs). The total drag equation follows:

$$D_{total} = D_{induced} + D_{parasite} \quad (4)$$

For an aircraft in steady unaccelerated level flight with constant weight, the drag vs. velocity curve helps to approximate the speeds necessary for maximizing range and endurance. Additionally, the maximum endurance and range are factors determined by engine type for an aircraft. A turbojet/turbofan aircraft has a different method of measurement than a propeller-driven aircraft. Figure 10 shows the drag vs velocity curve for a turbofan/turbojet aircraft in steady unaccelerated flight with constant weight.

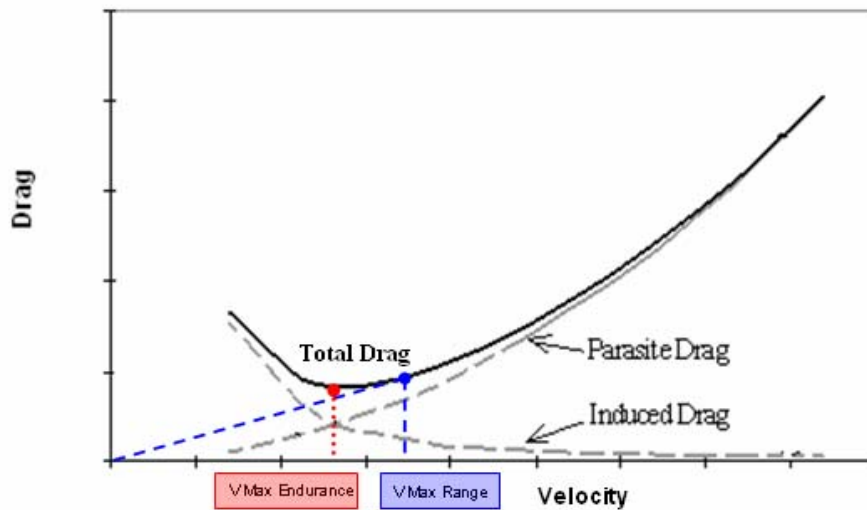


Figure 10: Drag vs Velocity for Turbofan/Turbojet Aircraft in Level Flight (reproduced from Reference 5)

The velocity that will allow the aircraft to maximize its endurance is the velocity where the total drag is minimized. At this velocity, the lift-to-drag ratio, L/D , is maximized and $D_{induced}$ is equal to $D_{parasite}$ (5). The velocity for maximum range is found by finding the values of drag, D , and velocity, V , which minimizes the ratio of D/V . This is achieved by drawing a line tangent to the Total Drag curve from the origin. At maximum range velocity, the ratio of $C_L^{1/2}/C_D$ is maximized (5). According to Brandt (5), usually the ratio $C_L^{1/2}/C_D$ is not used in a biplane analysis due the atypical use of turbofan/turbojet engines in the airframe. Figure 11 shows the drag vs. velocity curve for a propeller-driven aircraft in steady unaccelerated flight with constant weight.

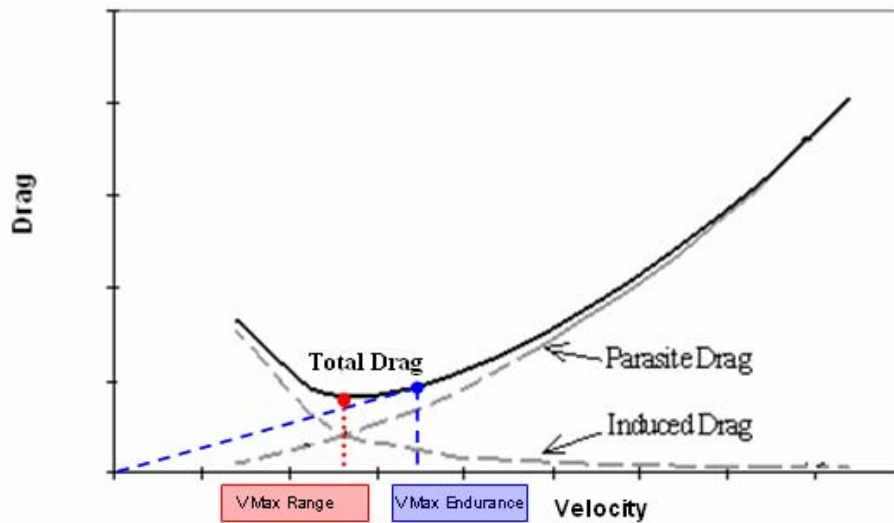


Figure 11: Drag vs Velocity for Propeller-Driven Aircraft in Level Flight (reproduced from Reference 5)

Unlike the Turbojet/Turbofan aircraft example, the velocity that will allow the propeller-driven aircraft to maximize its range is the velocity where the total drag is minimized. At this velocity, the lift-to-drag ratio, L/D , is maximized and $D_{induced}$ is equal to $D_{parasite}$ (5).

The velocity for maximum endurance is found by finding the values of drag, D , and velocity, V , which minimizes the ratio of D/V . This is achieved by drawing a line tangent to the Total Drag curve from the origin. At maximum-endurance velocity, the ratio of $C_L^{3/2}/C_D$ is maximized and the induced drag is equal to three times the parasite drag (34). The following equations summarize the relationship of parasite drag, C_{D_o} , to induced drag, C_{D_i} :

$$C_{D_o} = C_{D_i} \text{ at } \frac{L}{D_{\max}} \quad (5)$$

$$3C_{D_o} = C_{D_i} \text{ at } \frac{C_L^{\frac{3}{2}}}{C_{D_{\max}}} \quad (6)$$

Where C_{D_o} and C_{D_i} are dimensionless.

2.4 Wing-Tip Vortices

The flow phenomena at the wingtips of finite wings, known as wing-tip vortices, account for the major difference between a two-dimensional (infinite span) and three-dimensional (finite span) representation of wings. This difference between finite and infinite spans results from the formation of span-wise fluid flow that occurs in the three-dimensional case (5) and the assumption that in the two-dimensional case “the upflow in front of the wing exactly balances the downflow at the rear of the wing, so that there exists no net downward movement of air past wing caused by the circulation, Γ (in^2/s)” (28).

The primary cause for the formation of wing-tip vortices is lift. Lift, generated by a wing, results when there is a net pressure difference between the upper and lower surfaces of the wing. When the higher pressure exists on the lower surface of the wing, then positive lift is created. Due to the fact that wings are finite in length, the flow over the wing acts in a three-dimensional manner and has the tendency to equilibrate at the wing-tip (28). This phenomenon is seen in Figure 12.

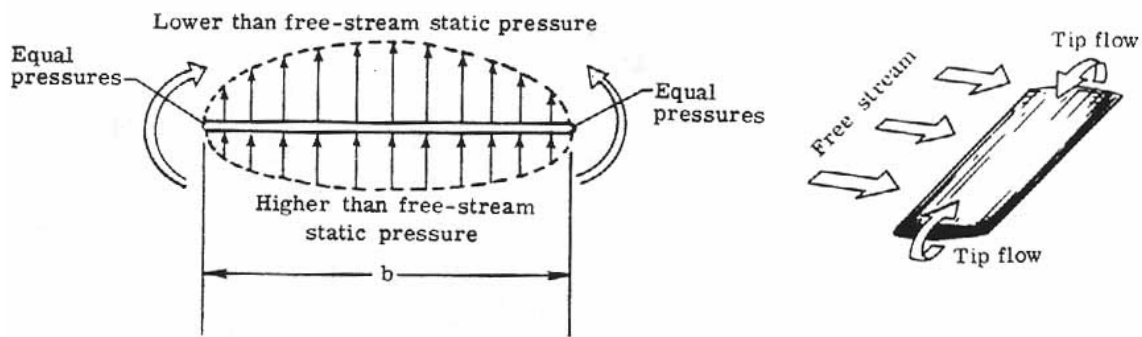


Figure 12: Equalizing Pressure at the Wing-Tips (reproduced from Reference 28)

Vortices form when the high pressure below the wing induces a circular velocity from below the wing that continues around the wing-tip to the lower pressure area on the upper surface of the wing. This movement in combination with the free stream flow of air, creates “very strong tornado-like swirling flows” also known as wing-tip vortices or trailing vortices that flow downstream (5). Wing-tip vortices are located above the wing-tips and have the tendency to sink and roll towards each other downstream of the wing (28). The tangential velocity at the core of the vortices can approach 70% of the aircraft’s forward velocity (18:304). Figure 13 demonstrates the formation of wing-tip vortices.

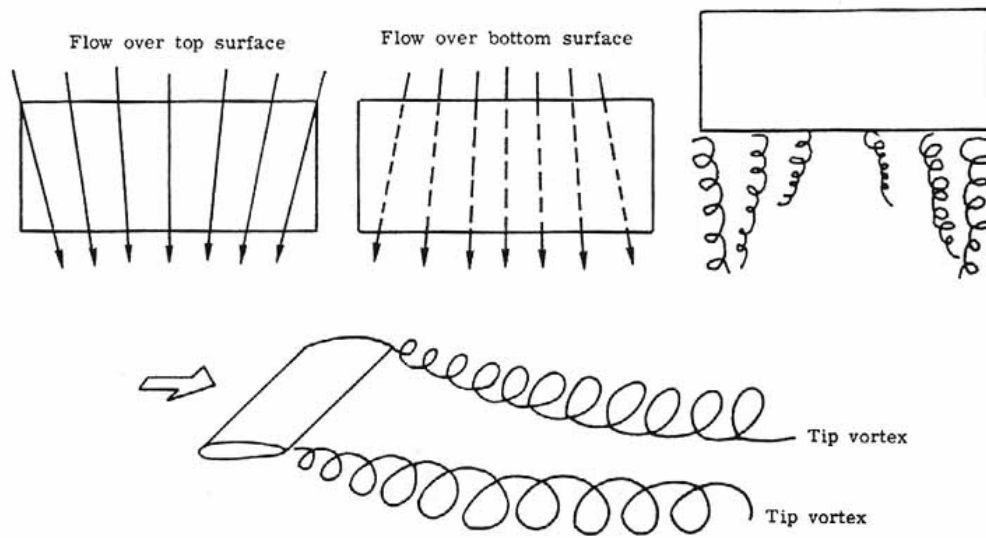


Figure 13: Formation of Wing-Tip Vortices (reproduced from Reference 28)

The circular flow pattern of the wing-tip vortices results in a downward component of the flow over the wing. This downward flow component is called downwash (see Figure 14). Downwash acts most strongly at the wingtips and loses strength toward the mid-span where its value is the least.

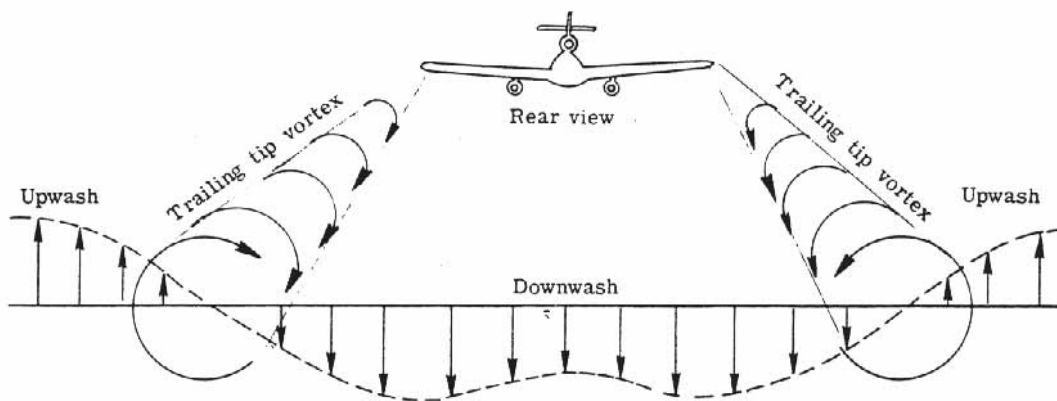


Figure 14: Creation of Downwash (reproduced from Reference 28)

Downwash produces two negative effects on the performance of a finite wing. First, it reduces the angle of attack that each section effectively sees, effective angle of attack.

Second, it creates a component of drag. This component of drag is known as induced drag and results from the kinetic energy associated with the rotation of the wing-tip vortices (2:355).

Wing-tip vortices “can significantly diminish the aerodynamic performance of a finite wing as opposed to an airfoil” (18:304). For a two-dimensional case (infinite span wing), the induced drag is equal to zero (13:2; 31). For a three-dimensional case (finite span wing) induced drag is a factor and contributes to total drag. Induced drag portion of total drag varies for various portions of flight. Induced drag becomes more prevalent at lower airspeeds for aircraft. At slow speeds, such as landing or takeoff, “wing-tip vortices may contribute about 75% of the total drag” of an aircraft. At higher speeds, such as cruise speed, wing-tip vortices contribute “about 25% of total drag” (18:304; 31).

To reduce induced drag, an aircraft can increase its aspect ratio, AR . The aspect ratio effect on induced drag is shown in Equation 7.

$$AR = \frac{C_L^2}{\pi \cdot e \cdot C_{D_i}} \quad (7)$$

where AR is the aspect ratio (-), C_{D_i} is the induced drag coefficient (-), C_L is the lift coefficient (-), and e is the span efficiency factor ($e = 1$ for elliptical wing).

2.5 Winglets

A winglet is best described by Jean Chattot’s quote: “Winglets are aerodynamic components placed at the tip of a wing to improve its efficiency in cruise” (7:386; 31:10). For over a century it has been known that an endplate at the tip of a finite wing reduces the spanwise flow and thereby can reduce the induced drag. However, for the endplate to

be effective, it must be “so large that the increase in wetted area drag far outweighs any drag reduction” (22:3). Unlike an endplate, a winglet does not just act as a fence against spanwise flow. “The winglet diffuses or spreads out the influence of the tip vortex such that the downwash and, in turn, the induced drag, are reduced” (22:3). A properly designed winglet can also “reduce total drag, increase lift, provide added stability, increase safety, and improve roll performance” (31:10). “Concepts for reducing wing-tip vortices have been developed and demonstrated throughout the history of aviation by individuals and companies and by the government agencies including NASA and the Air Force” (18:305; 31:11). The addition of winglets and their reduction in induced drag has been researched since the mid-1970’s when Dr. Richard Whitcomb, working at NASA Langley, first proposed them (20; 31:11). The use of winglets is widely used on many different aircraft platforms both commercially and militarily. The use of winglets has significantly reduced the amount of fuel needed for flight. “Data available for the Boeing 747-400 indicate that without winglets the aircraft suffers about 2.5 % drag losses, which corresponds to +9.5 tons at take-off” (12; 31:11).

With this reduction of induced drag there is a small cost in weight, viscous drag, and compressibility drag (17:201). These small costs are associated with the design of the winglet. The disadvantages to the use of the winglet are caused by the increase in wetted and cross-sectional area, which both cause an increase in profile drag. “The effect of the increased area is felt primarily at higher speeds, as the profile coefficient remains relatively constant while the drag increases with the square of velocity” (22:3). Optimizing winglet geometry becomes complicated due to requirement that the winglet

must maximize efficiency during the entire flight envelope (22:3). Usually when an improvement in one area of performance is made, there is a lack of consideration for its effects on other areas of aerodynamics. “An evaluation of effectiveness of various devices for the attenuation of trailing vortices was performed by Kirkman et al. It was found that while many devices show reduction of the maximum swirling velocity in the wake effects are typically accompanied by high drag penalties. Obviously, continued evolutionary advances in methods and processes are still needed in order to provide continued improvement of the aerodynamic design technologies” (18:305). In spite of all the disadvantages, many aviation manufacturers have accepted winglets as a proven fuel-saving aerodynamic device (4).

A study conducted by Smith and Campbell in 1996 showed the effect of winglets on aerodynamic efficiency of a low-aspect-ratio model with respect to lift-to-drag. The experiment has shown an approximate increase of about 6.96% for L/D at L/D_{max} as compared to no winglet case for delta wing configuration at a $Re = 1,900K$ (27:38). This value serves as a baseline for the aerodynamic efficiency of winglets for this study.

2.6 Biplanes

“Humankind’s dream of powered flight became a reality when, in 1903, the Wright brothers demonstrated that high lift and structural rigidity of the biplane was essential to lifting man and engine into the air” (1:398). Biplanes were used in the early days of aviation primarily because the structural materials could not support a monoplane design. Wing structures, as compared to modern technology, were thin and therefore; were weak and inadequate. The biplane used struts and wires to support the upper and

lower wing which gave the aircraft a box-shaped configuration. The bracing of the wings against each other strengthened the wings and allowed for shorter wingspans. This compact layout allows for greater maneuverability as compared to monoplanes. The dual wing configuration does produce more lift than a monoplane with similar wingspan. However, there is additional drag associated with the struts, wires, extra wing surface area, and the aerodynamic interference between the wings. “It is known that in a biplane the load is not distributed equally between the wings. The presence of one wing will affect the lift characteristics of the other wing” (23:1). “For a constrained wing span, however, biplanes do possess aerodynamic efficiency advantages as compared to monoplanes...the vortex drag of a biplane tends to half that of a monoplane” (29:536). However, for a constrained wing area, the monoplane holds the aerodynamic advantage (31:12). “A biplane has many advantages, such as...good load carry capability, good lift-to-drag ratio combined with a low wing loading...high lift at low speeds...(and) excellent low-speed maneuverability” (1:399).

A biplane is uniquely defined by the following important parameters: angle of decalage, gap, and stagger. “The angle of decalage is the acute angle between the chords of the wings of a biplane. The decalage shall be called positive when the lower wing has a smaller angle of attack than the upper wing” (23:2). Gap is the distance between the planes of the chords of the upper and lower wings. It is measured along a line perpendicular to the chord of the upper wing at its leading edge. Stagger is “the amount of advance of the leading edge of the upper wing...over that of a lower wing” (23:2). Stagger is measured parallel to the chord of the upper wing. Stagger is considered

positive when the upper wing is fore of the lower wing (23:3). Figure 15 shows a biplane with a few of the listed parameters.

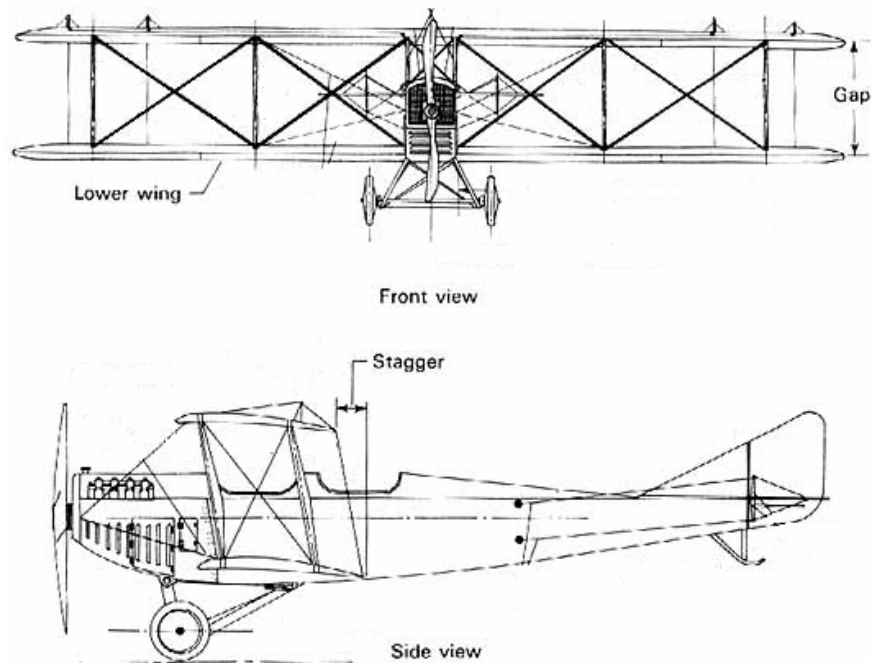


Figure 15: Biplane Parameters: Stagger and Gap (reproduced from Reference 19)

An investigation into the optimum configuration for these parameters has been conducted by two aerodynamicists, Nenadovitch and Olson (24: 6; 31:13). They concluded that a certain combination of gap, stagger, and the angle of decalage for an untwisted biplane wing design may produce lower C_D , increased C_L/C_D , and increased $C_L^{3/2}/C_D$. The optimum values are a gap of 1 chord, a stagger of 0.875 chord, and a decalage angle of -5° (24:6). “Numerical two-dimensional analysis by Rokhsaz confirmed that the combinations of gap, stagger, and decalage determined by Nenadovitch do approach optimum arrangements” (13:2).

Multiple studies have investigated the optimization of the biplane wing configuration with the use of winglets. One joint study, which consisted of efforts by Pennsylvania State University and NASA Langley Research Center, investigated the use of winglets on a box-like biplane semi-span (see Figure 16).

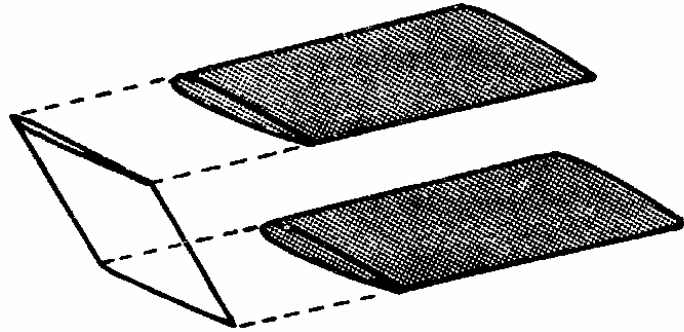


Figure 16: Isometric View of Gall's Semi-span Model (reproduced from Reference 13)

The model's wings consisted of NACA 0012 sections with constant chords of 8 inches and semi-spans of 20 inches. The airfoil that connected the two wings consisted of a constant chord, NACA 0003 section. The model was constructed to have a fixed gap and stagger that were both equal to one chord in length. The decalage angle could be varied between 0 and -5° . The results of the test revealed that there was a 5% increase in $C_{L\alpha}$ and a 4% increase in C_{Lmax} with the addition of winglets. The advantages of the winglet cannot be realized at zero lift. This is due to the induced drag being unable to overcome the increase in profile drag. It is only at lift coefficients (C_L) greater than 0.4 that winglets produce less total drag (13:3).

2.7 Joined Wings

The joined wing concept was first introduced as Patent 4,365,773 by Julian Wolkovitch in 1980. He states in his AIAA article, “The joined-wing airplane may be defined as an airplane that incorporates tandem wings arranged to form diamond shapes in both plan and front views” (33:161). Often joined wing airplanes have the rear wing attached at its root to the top of the vertical tail or the rear of the aircraft. The rear wing then sweeps forward to join the trailing edge of the swept back main forward wing (32). The rear wing acts as a unique tail and is used for pitch control, longitudinal stability, and as a structural support for the forward wing (15:215). An example of a joined-wing aircraft can be seen in Figure 17.

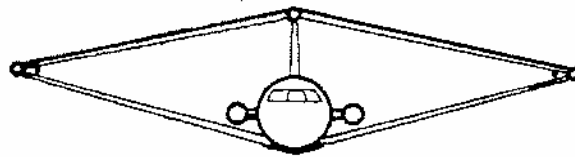


Figure 17: Front View of a Joined-Wing Aircraft (reproduced from Reference 33)

“The main concern of the early biplanes was the large profile drag due to the structural wires that connected the wings. Today, the joined-wing configurations have eliminated the connecting wires” (8:2; 31:15). Initially the use of biplanes was necessary due to the inferior strength of the structural materials in airframes. However, as material strength increased over time, the monoplane became a more efficient design as compared to a biplane. A monoplane can be designed with high aspect ratios, AR , which allows for more efficient flight (31:15). But there are limits to how high the aspect ratio can go.

Performance wise, the aircraft loses maneuverability. Structurally, the material is unable to support airframe (i.e. wingspan). The joined-wing aircraft allows for more of an increase in aspect ratio as compared to a monoplane.

As compared to an aircraft with the same wing-span, an optimally configured joined-wing aircraft has many advantages. These advantages include: lighter weight, higher stiffness, good stability and control for normal flight and stall, higher possible aspect ratios, lower induced drag, reduced wetted areas, lower total drag, suitability for thin airfoils, and higher efficiency factors (8:2; 15:215; 31:15; 33:161).

The benefits that the joined-wing can provide depend on its design goals and application. Some applications may require light weight; others may require reducing induced and parasite drag; furthermore some applications require thinner airfoils for reducing wave drag during supersonic flight (31:15; 33:175). “Joined wings are not always lighter than single wings. Weight will be saved only if the geometric parameters of the joined wing are properly chosen and if the internal wing structure is optimized” (8:2; 31:16). Although certain configurations of joined-winged aircraft will reduce drag, thus increasing aerodynamic efficiency, all flight conditions of a mission must be considered. “Performance constraints such as takeoff field length, landing field length, and climb gradient could increase the wing area required for a joined-wing configuration, thereby eliminating potential drag reduction” (14:898).

2.8 Lift-to-Drag Ratio

The lift-to-drag ratio, L/D , is a measure of aerodynamic cruise efficiency of an aircraft. As discussed in section 2.3, a propeller-driven aircraft can optimize its range by

flying at the velocity of maximum lift-to-drag, L/D_{\max} . “ L/D is usually optimized for given flight conditions (altitude) and desired lift (or aircraft weight for straight and level flight)” (31:16). At each flight condition there is a specific combination of velocity and angle of attack that maximizes the ratio of lift-to-drag. For maximum aerodynamic cruise efficiency, these values for velocity and angle of attack should be flown for the given flight condition. Table 1 lists historic values of lift-to-drag for common aircraft. Notice that L/D_{\max} is generally bounded from 8 to 20.

Table 1: Lift-to-Drag Ratios of Historical Aircraft (reproduced from Reference 12)

Type of Aircraft	L/D Ratio
Supersonic Jet Transport (Concorde)	8
Tilt-rotor aircraft	9 to 10
New Supersonic Transport*	15
Oblique Flying Wing*	16 to 17
Subsonic Jet Transport	16 to 18
Bomber B-52	20
* Estimated data	

Subsonic Aircraft	L/D_{\max}
Boeing B707-320	19.4
Douglas DC-8	17.9
Airbus A320	17
Boeing 767-200	19
Boeing 747-100	17.7
Douglas DC-10	17.7
Lockeed Tristar L1011	17
Douglas DC-9 (1966)	16.5
Boeing B727-200	16.4
Fokker 50 (1966)	16
Douglas DC-3 (1935)	14.7
Ford Trimotor (1927)	12
Wright Flyer I (1903)	8.3

Figure 18 shows the historical trend of maximum lift-to-drag ratio for propeller-driven aircraft. During the years from 1920 to the early 1930’s there is a sharp increase in the L/D_{\max} upper bound curve. This increase in L/D_{\max} is a result of the reduction in parasitic drag, the advancement of structural materials, and the switch from the biplane to the monoplane (with its higher aspect ratio). The reduction in parasite drag is due to the advancement in aerodynamic design (i.e. a strut-and-wire-braced biplane to the streamlined, internally braced monoplane) (19; 31:17).

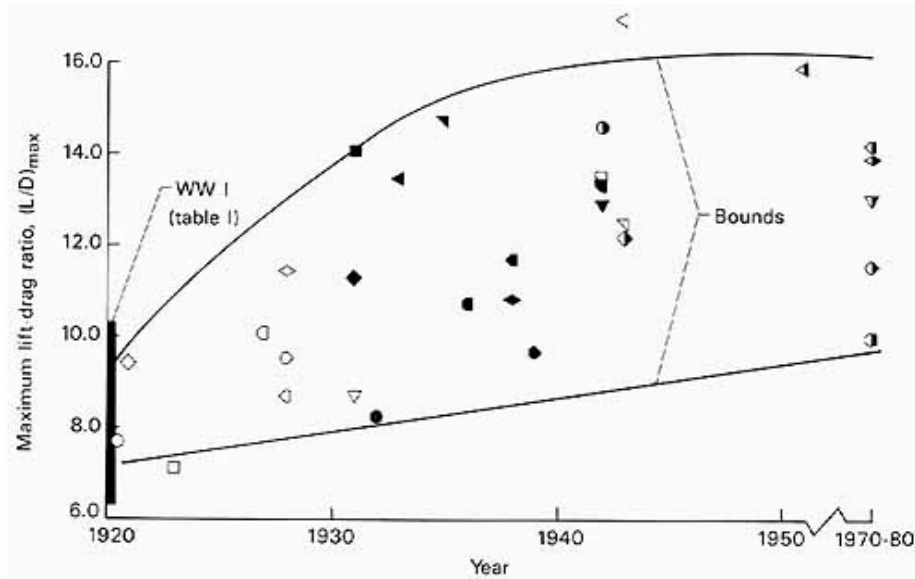


Figure 18: Historic Maximum Lift-to-Drag Ratios of Propeller-Driven Aircraft (reproduced from Reference 19)

Another measure of aerodynamic efficiency is the effective aspect ratio, eAR . The effective aspect ratio of an aircraft can be solved with Equation (8) and with additional information concerning lift and induced drag.

$$C_{D_i} = \frac{C_L^2}{\pi \cdot e \cdot AR} \quad (8)$$

where C_{D_i} is the induced drag coefficient, C_L is the lift coefficient, e is the span efficiency factor, AR is the aspect ratio, and the combination of $e AR$ is the effective aspect ratio (17:186; 31:18).

2.9 Hot-Wire Anemometry

A constant temperature anemometer (CTA) is used as one method for fluid flow data acquisition. A CTA maintains a constant wire temperature through the use of a control algorithm. A CTA also has constant resistance. As electric current is supplied to

the wire to maintain the temperature, the rate of current is measured. The air velocity is directly related to the amount of current needed to maintain the temperature in the wire. Therefore, as the velocity of the fluid changes, the controller must increase or decrease the supplied current to the constant wire resistance (thereby keeping temperature constant). The change in current is measured and calibrated, and further processing of the data converts it into a fluid velocity. “Two advantageous reasons for using a CTA are accuracy and high time-dependent resolution. The latter reason lends itself to use in collecting and analyzing turbulent flow data” (31:18).

2.10 SolidWorks®

SolidWorks is a three-dimensional computer-aided-design program, CAD. The program currently only runs on Windows-based personal computer (PC) systems. *SolidWorks* was developed in 1993 and is produced by Solid Works Corporation located in Concord, Massachusetts. *SolidWorks* utilizes a parametric, feature-based approach to the construction of models. Parameters refer to the constraints that determine size, shape, behavior, and characteristics that make up a model. Parameters can be numerical (length, width, etc) or geometric (tangent, concentric, parallel, etc). Features are the building blocks of the part. They are the shapes and operations of the part. Shapes are the functions that either add or subtract material from the part (holes, bosses, etc). Shapes usually require the use of sketches before the operation is carried out. Operations are the functions that do not require sketches but still affect the part (fillets, shelling, etc) (26).

To construct a part in *SolidWorks*, the first step usually is creating a two or three-dimensional sketch. The sketch consists of geometry (lines, arcs, etc) and then

dimensions are assigned to define the location and size of the geometry. The geometry can also have relational constraints (parallel, concentric, etc) that further define the part. A complicated design involves the use of multiple parts and is constructed in the assembly. The assembly works in the same manner as the part construction by assigning numerical and geometric parameters between parts. Finally, the model can be drafted using the drawing module of *SolidWorks*. See Figure 19 for an empty *SolidWorks* part workspace.

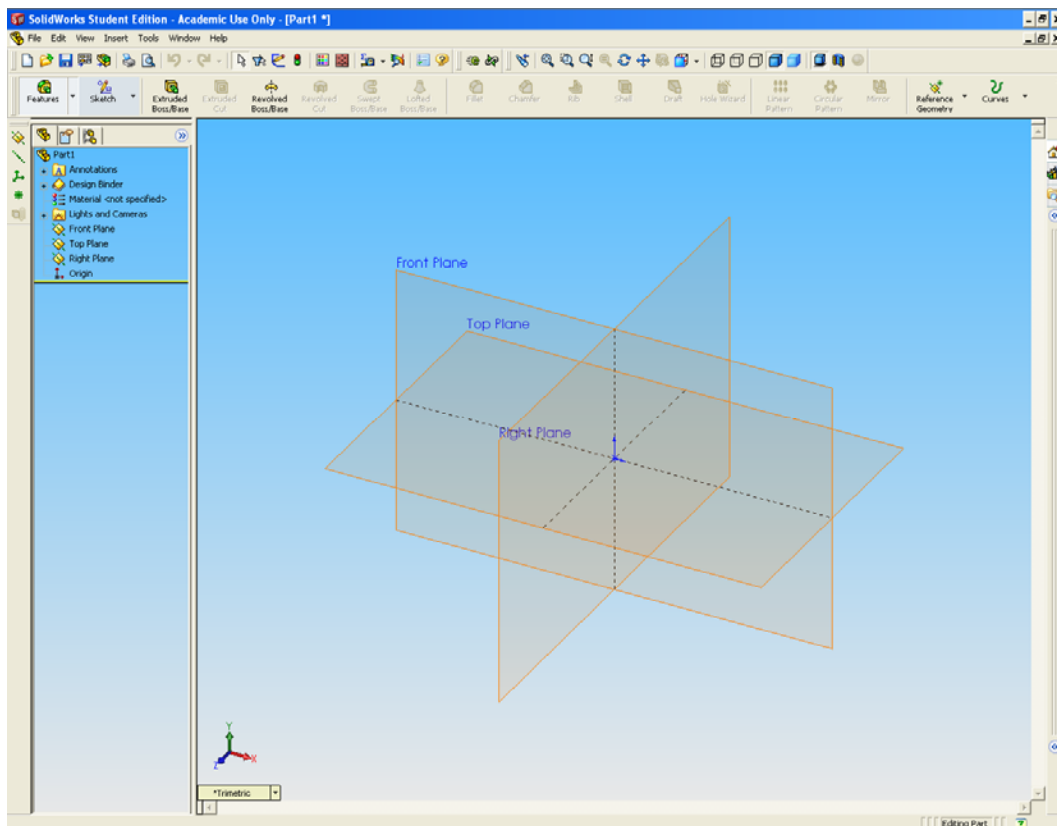


Figure 19: Planes and Axes of an Empty *SolidWorks* Part Workspace

SolidWorks in tandem with a rapid prototype machine, such as an Objet Eden series printer described in Section 3.2.11, allows for a relatively quick design to build process for any type of model.

III. Methodology

3.1 Chapter Overview

The beginning of this chapter outlines the instructions for the construction of the Original Configuration Model in SolidWorks. After that, all the model configurations that were constructed using the previously outlined method are presented in detail. Next, the chapter covers the AFIT low-speed wind tunnel and the subsequent test data that was retrieved from the tunnel α sweeps. The methods for reducing the data from these tests are also covered in this chapter. Furthermore, this chapter covers the 24" Houck Configuration data that will be used for comparison to this study. Finally, the test plan that was used to collect data is outlined.

3.2 *SolidWorks* Construction

3.2.1 Patent Specification

The models used for this study were designed using the CAD program *SolidWorks*. The model construction followed the claims specified in Ronald G. Houck II's Lifting Foil patent. More specifically, the flow guide in the model followed Claim 14 and 17, whereby the camber of the flow guide has maximum camber at the upper and lower wing-tips and has minimum camber at the mid-point of the flow guide (Figure 20) (16).

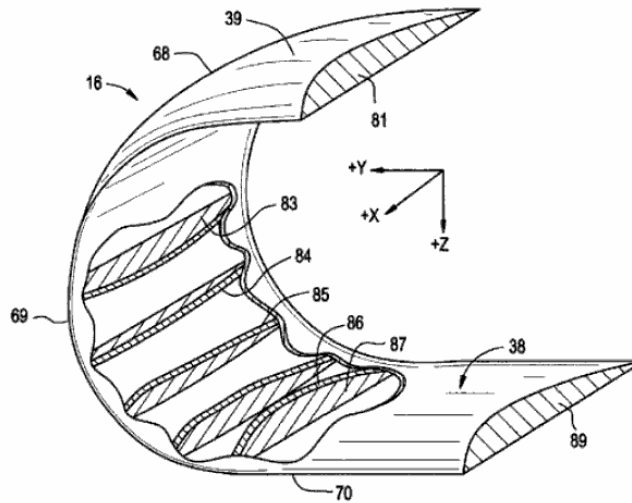


Figure 20: Progressive Camber of the Flow Guide (reproduced from Reference 16)

3.2.2 Step 1: Airfoil

The initial construction of the base model, or original configuration, began with the selection of a NACA 2412 airfoil for the biplane wings from the UIUC Airfoil Coordinate Database (30). The airfoil coordinates provided were of unit length but were resized to be three times larger (chord length of 3"). The airfoil coordinates were entered on the Y-Z sketch plane and then were splined together (Figure 21).

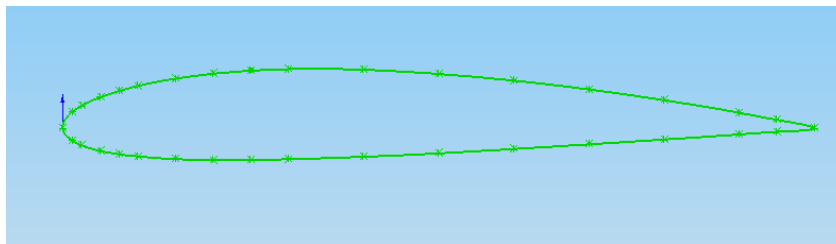


Figure 21: NACA 2412 Coordinates Splined Together in *SolidWorks*

3.2.3 Step 2: Airfoil Section Extrusion

The next step in the construction was to extrude the airfoil section with a 15° sweep and a 6.69" half-span. For this to be done, another sketch was added to guide the airfoil section extrusion (Figure 22 and Figure 23).

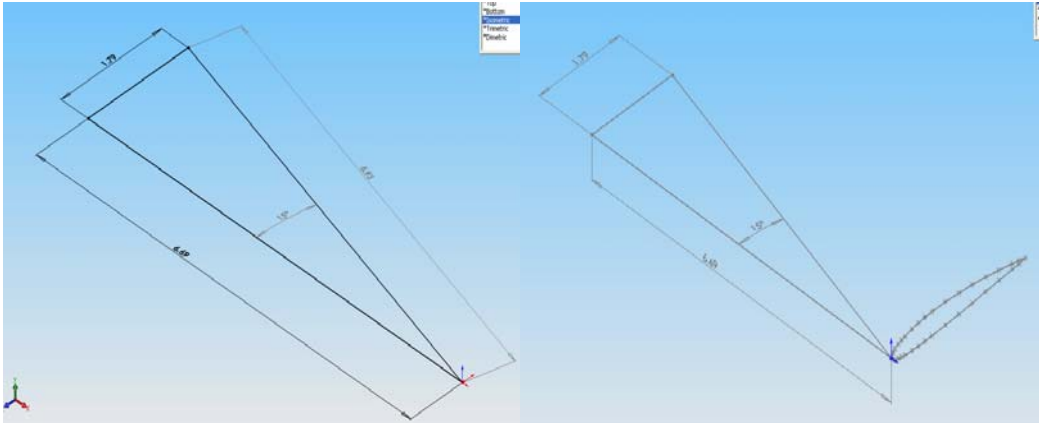


Figure 22: Sketch to Guide Airfoil Section in *SolidWorks*

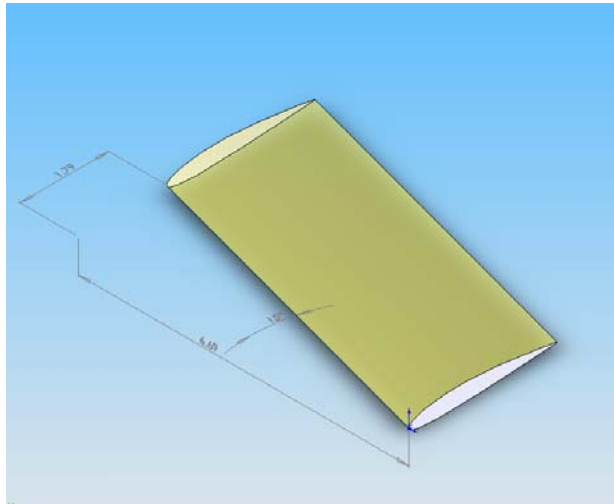


Figure 23: Sketch to Guide Airfoil Section in *SolidWorks*

3.2.4 Step 3: Upper Wing Construction

To add the upper wing, a gap of 2.5" ($0.84 \bar{c}$) was measured from the leading edge of the wing-tip. The airfoil coordinates for the upper wing were entered using a

similar method outlined in Step 1 (Figure 24). The sketch plane was the wing-tip surface plane.

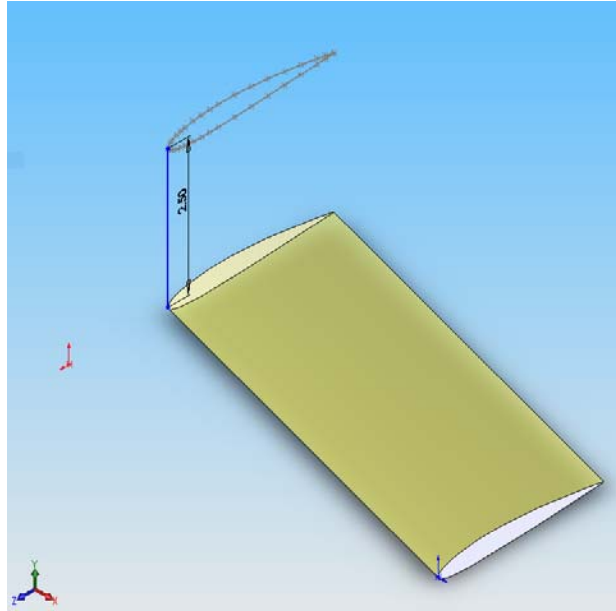


Figure 24: Gap Measurement for Upper Wing

To extrude the airfoil section with a 15° sweep and a 6.69" half-span, in the opposite direction to the lower wing, another guide sketch was added (Figure 25).

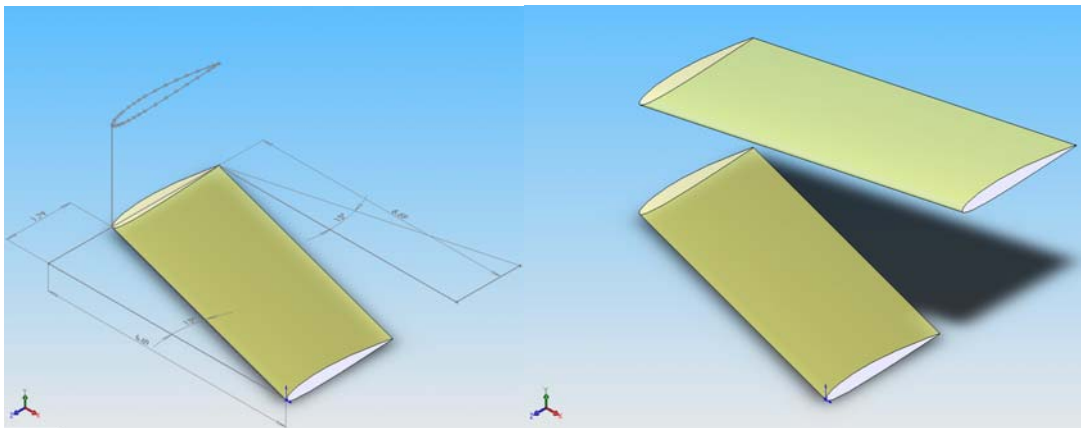


Figure 25: Upper Wing Guide Sketch and Subsequent Extrusion

3.2.5 Step 4: Mirroring the Extrusions

In order to make the model symmetric, the upper and lower wings were mirrored in the Y-Z plane (see Figure 26).

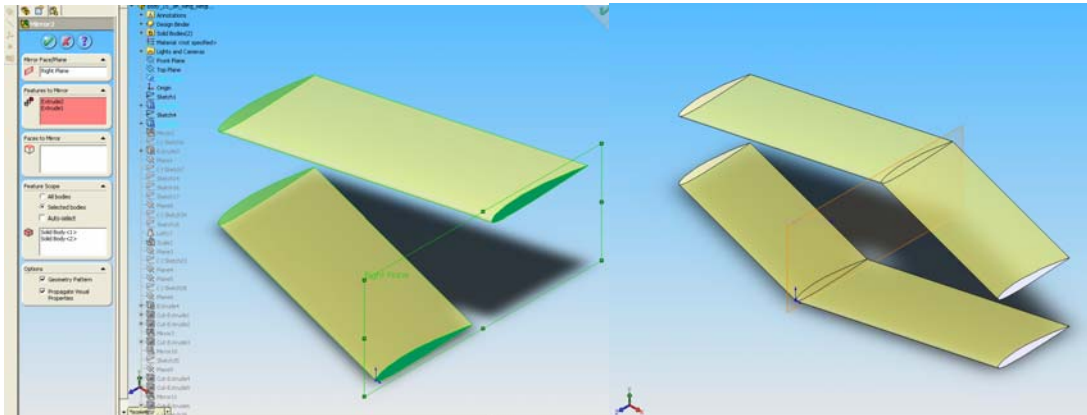


Figure 26: Mirroring over the Y-Z Plane

3.2.6 Step 5: Creating the Body that Joins the Wings

The center body that joins the wings is a NACA 0010 airfoil section that was extruded from the lower wing to the upper wing along the mid-span. The initial step was to enter the airfoil coordinates (from UIUC Airfoil Coordinate Database) in the X-Z sketch plane on the lower wing (3" chord length). Another sketch was added to guide the extrusion from lower wing leading edge to the upper wing leading edge (Figure 27).

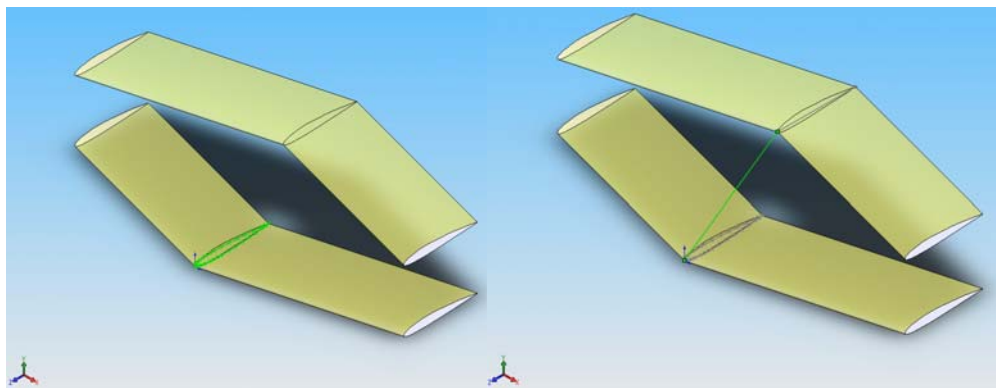


Figure 27: Body Airfoil and Guide Sketch

The extrusion of the NACA 0010 airfoil section is shown in Figure 28.

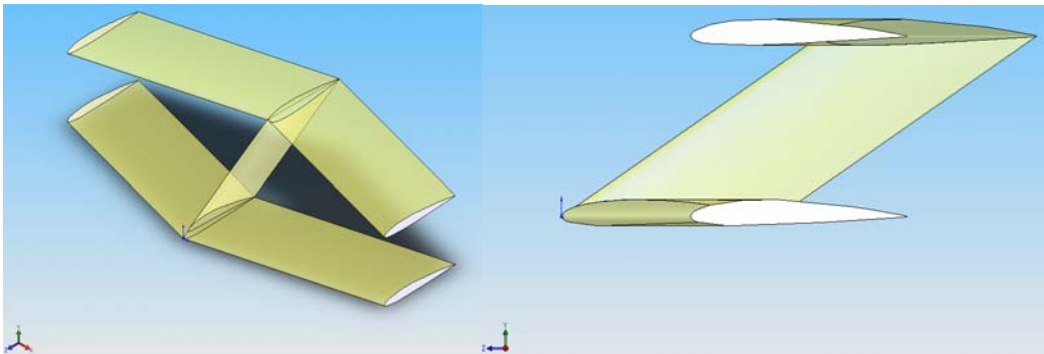


Figure 28: Extrusion of NACA 0010 Airfoil Body Section, Isometric and Side View

3.2.7 Step 6: Creating the Flow Guides that Join the Wings

The initial step for the construction of the Flow Guides was to create the sketch that would guide the lofting between the wings. The guide begins by sketching on the wing-tips of the upper and lower wings (parallel to the Y-Z plane). The points mid-chord on both wing-tips are joined by a guide line (Figure 29).

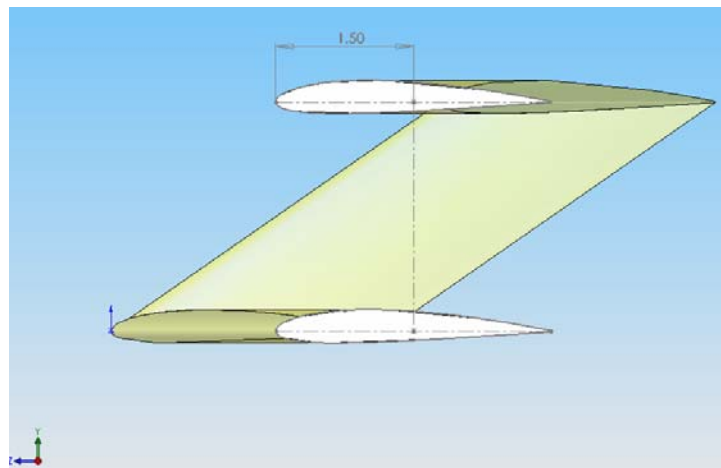


Figure 29: Connecting Mid-Chord Points on Upper and Lower Wing-Tips

Once the guide line has been drawn, the next step is to create a plane on the line that is parallel to the X-Y axis. After the plane is created, the guide sketch for loft is drawn. It is

a semi-circle with a radius of 1.25" and has guide lines drawn from 0° to 180° every 45° that originate from the center (Figure 30).

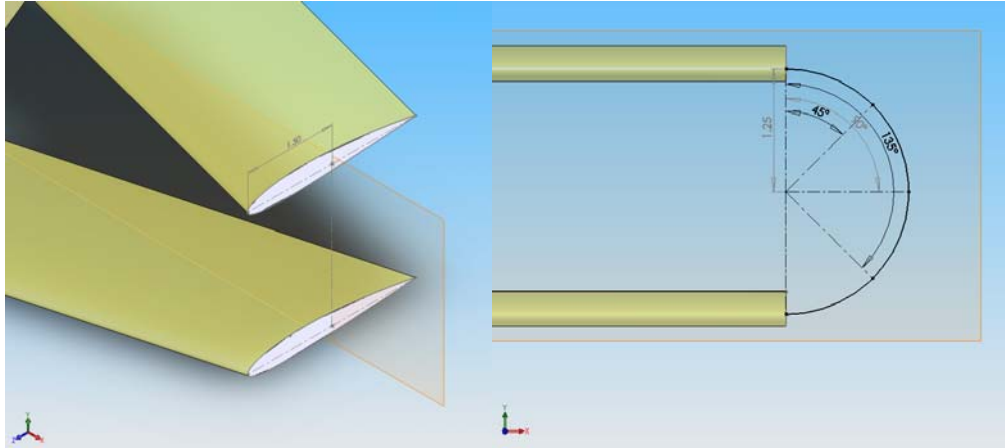


Figure 30: Guide Plane and Sketch for Flow Guide Loft

The next step is to loft the Flow Guide. Using the Loft command, select the upper and lower wing-tips' faces. Set the tangent length to 2 and complete the lofting (Figure 31).

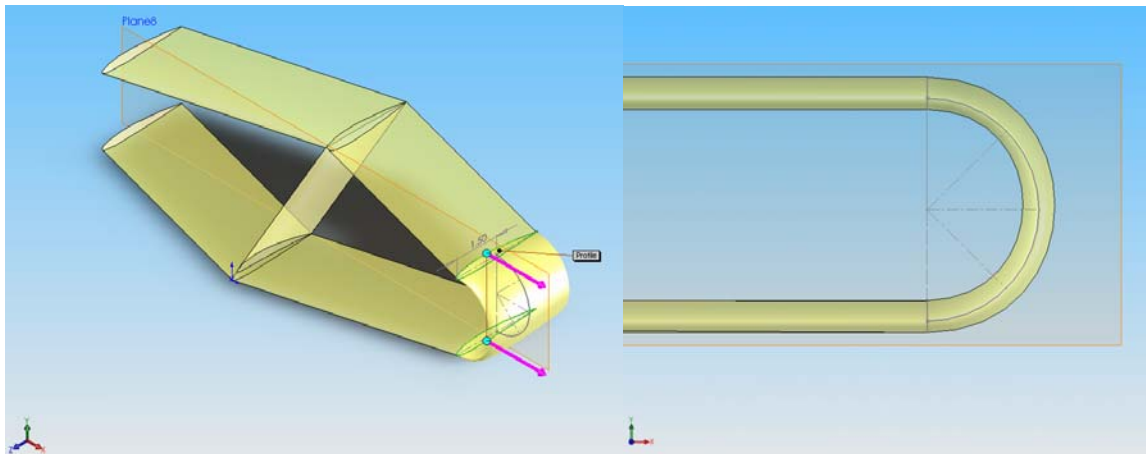


Figure 31: Lofting of the Flow Guide and the Comparison to the Guide Sketch

To finalize the lofting, the Flow Guide was mirrored in the Y-Z plane so the opposite wing would have symmetry (Figure 32).

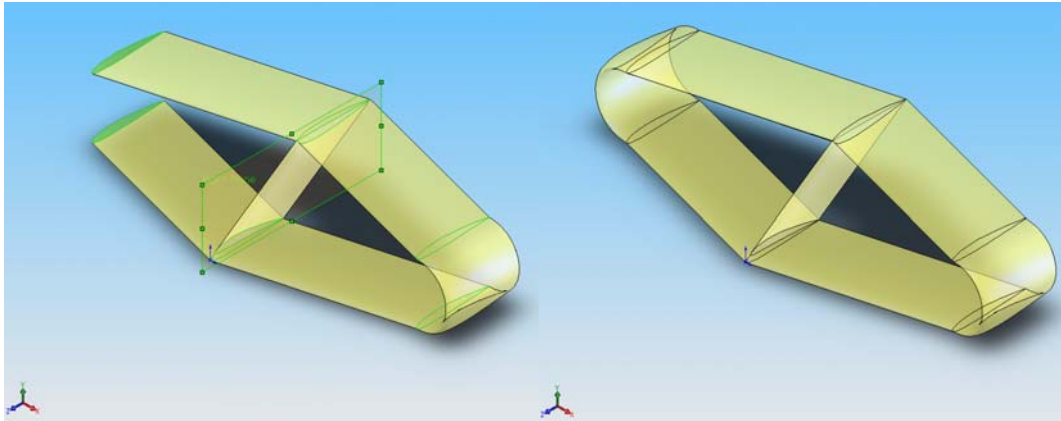


Figure 32: Mirroring the Flow Guide in the Y-Z Plane

3.2.8 Step 7: Scaling the Model

The model was resized so that the scale would be compatible with the wind tunnel. The scale of the model was set to 0.85 and it was uniformly scaled (Figure 33).

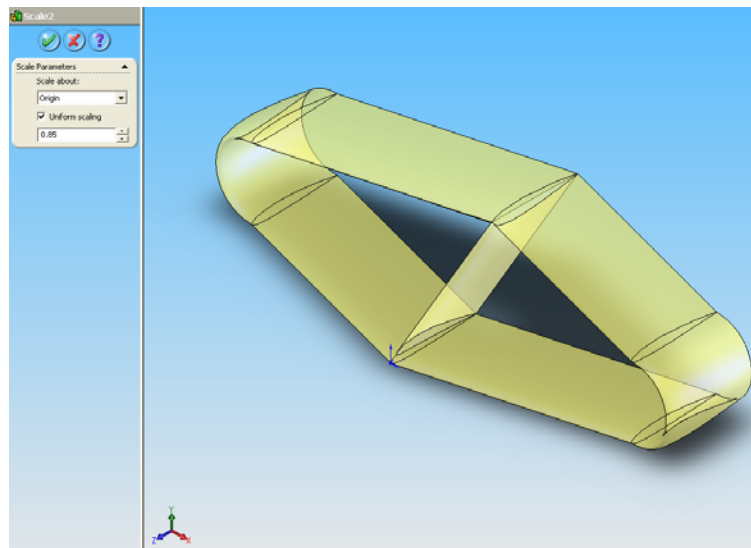


Figure 33: Uniform Scaling of the Model

3.2.9 Step 8: Adding the Balance Attachment

The initial step for the balance attachment is to sketch the mid-point for the sting in the model. It is located +0.53" in the Y-axis from the lower wing leading edge (Figure 34).

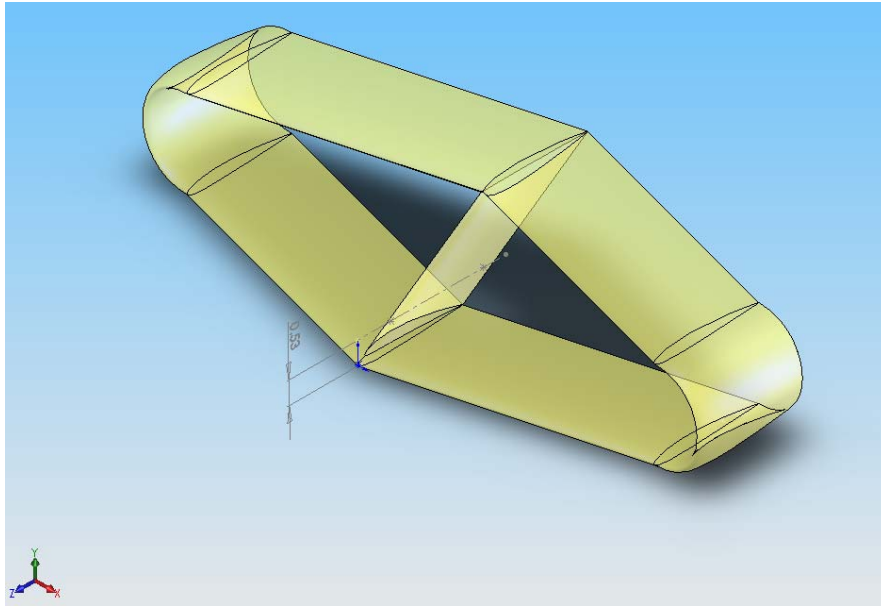


Figure 34: Sketch of the Mid-Point for the Balance

Once the mid-point is located, the guide-line for the center of the balance cylinder is drawn along the body parallel to the Z-axis. The following dimensions are needed to construct the balance attachment on the model. The plane for sketching the balance attachment's geometry is located 1.05" from the leading edge of the body that intersects the guide-line and is parallel to the X-Y plane. On this sketch plane, the diameter of the circle for the balance attachment is 1" and the center is located on the guide-line (Figure 35).

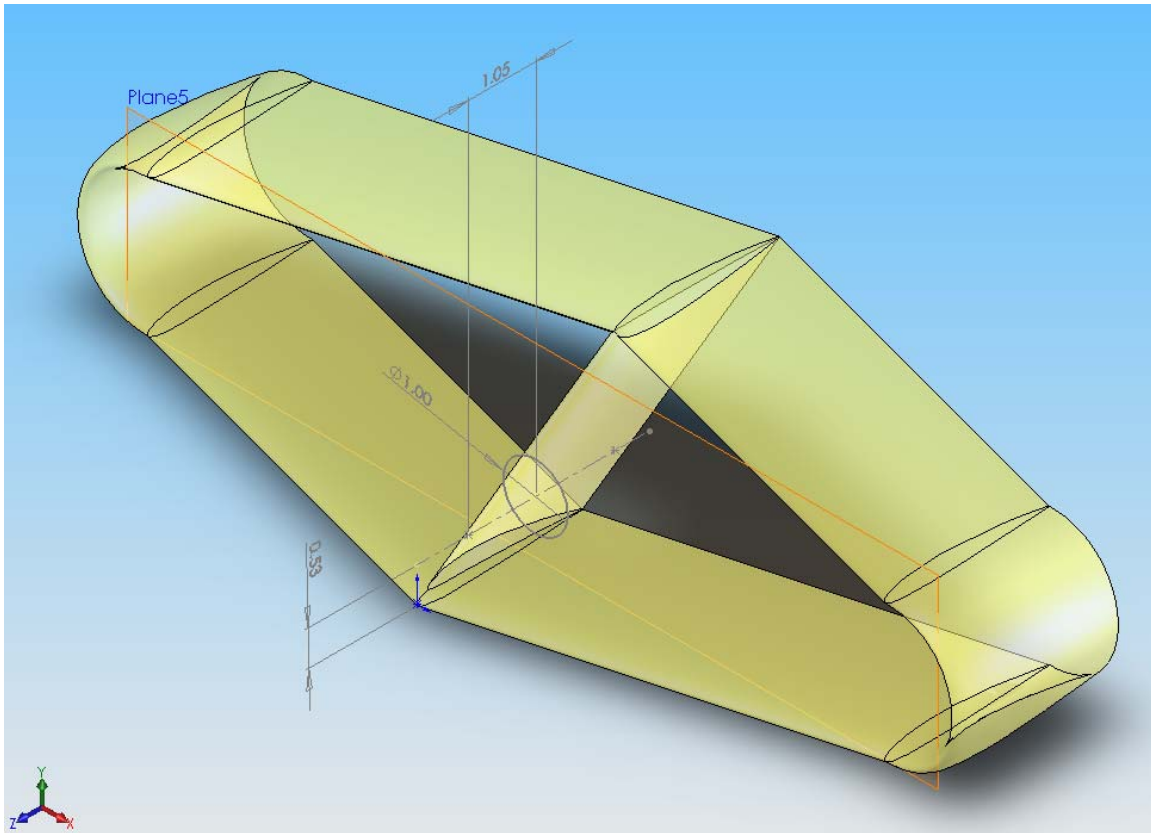


Figure 35: Sketch Plane and Geometry for the Sting Attachment Cylinder

The circle for the balance attachment is extruded out to 2.2" to the trailing edge of the body and tapered to a point 1" towards the leading edge of the body (Figure 36).

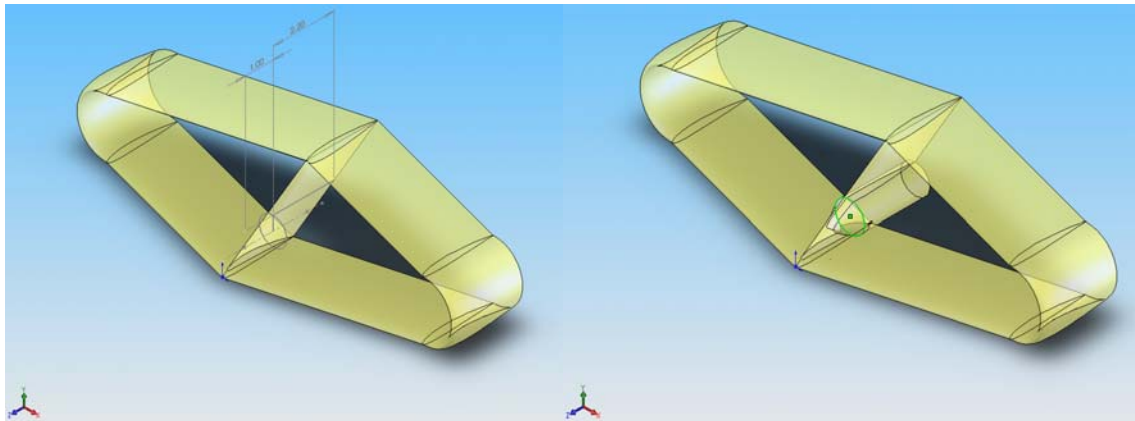


Figure 36: Extrusion of the Balance Attachment

The next step for the balance attachment is to cut out a cylinder so the balance can slide into the balance attachment. The sketch for the balance cutout is at the back of the model where the balance attachment juts out. The center of the circle is on the guide-line and the diameter is 0.5". The depth of the cutout is 2.2" (Figure 37).

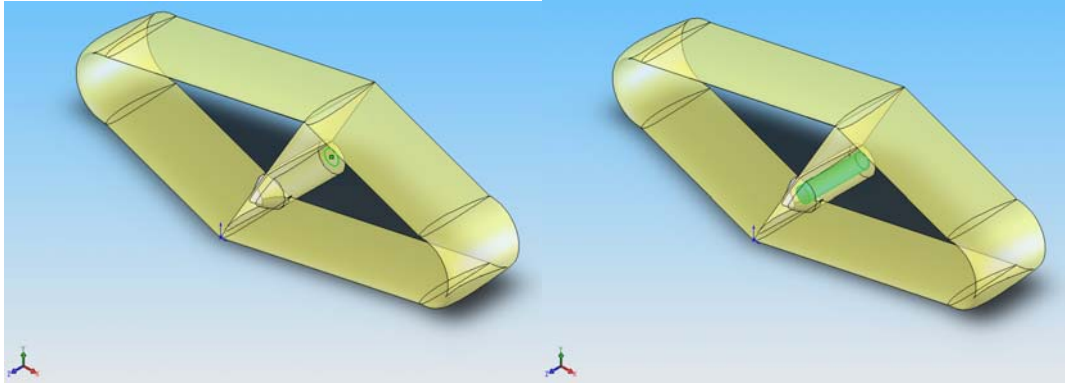


Figure 37: Cutout for the Balance

The final step for the balance attachment is to create the screw holes in the model so it can be affixed to the balance. The sides of the balance are cut, with a square drawing offset 0.46", so that they can be flat and then it is mirrored about the Y-Z plane for symmetry (Figure 38).

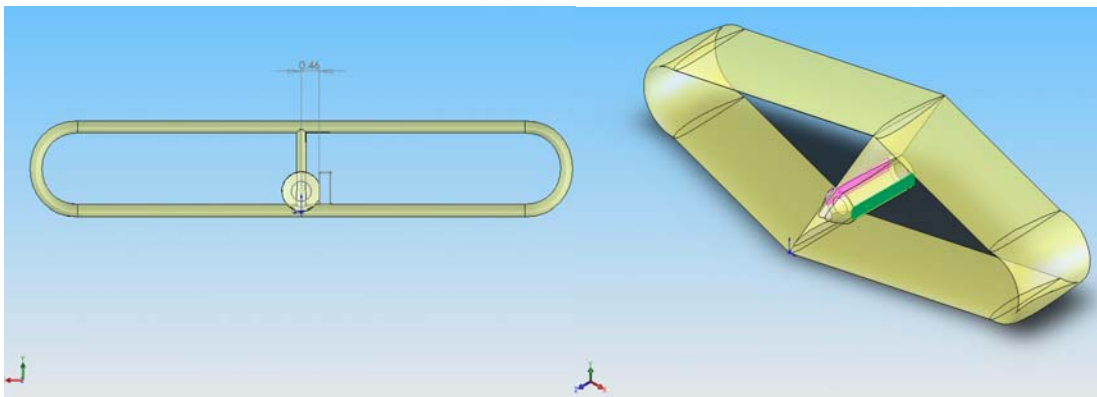


Figure 38: Flat Sides of the Balance Attachment

The screw hole is sketched on the origin's Y-Z plane. The center of the circle is located on the guide-line used for the balance attachment and is 1.25" from the leading edge of the body. The diameter of the circle is 0.09" (Figure 39).

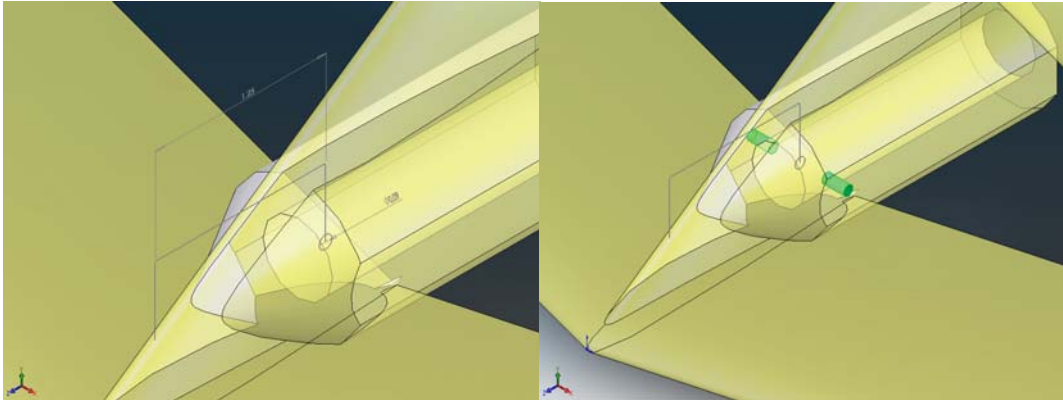


Figure 39: Hole Cutouts for the Balance Screws

The final screw hole for attachment is located on the underside of the model. It is cut in a similar method through the bottom of the model (Figure 40).

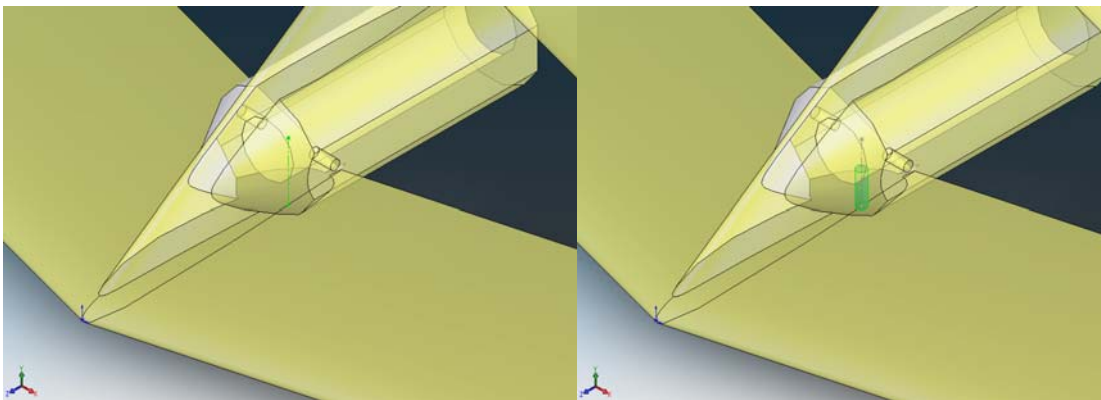


Figure 40: Bottom Hole Cutouts for the Balance Screws

Each of the holes has a counter-bore diameter of 0.14" and a depth of 0.095" (Figure 41).

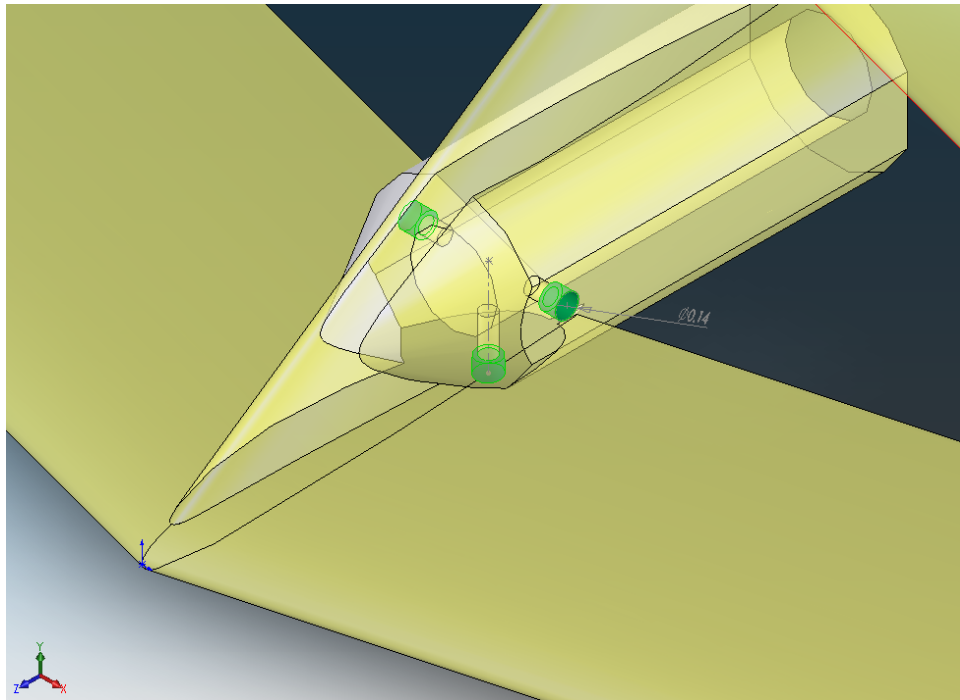


Figure 41: Counter-Bores for the Sting Attachment Holes

3.2.10 Step 9: Final Review before 3-D Printing

The final step before the build is to review the Original Configuration Model (Figure 42).

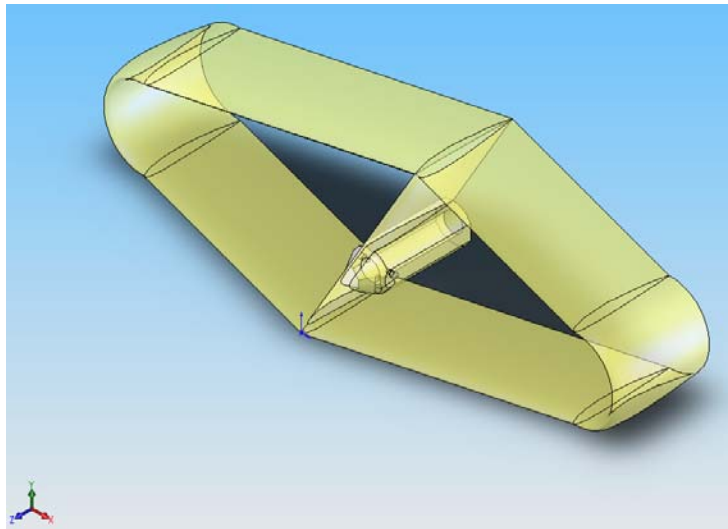


Figure 42: Final Review of the Original Configuration Model

3.2.11 Step 10: 3-D Printing

The initial step of the building process is to save the *SolidWorks* part file as a STL file. The file export options should be set as follows: output as ASCII and resolution as fine (Figure 43).

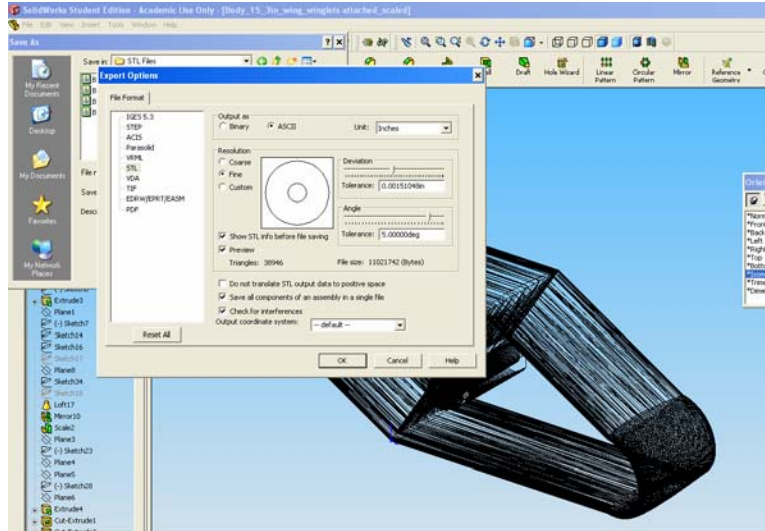


Figure 43: Export Options of the Part to STL File Save

Once the file has been converted to an STL file, it now can be built by the Objet Eden 333 series printer. The printer builds the model by layering acrylic with a print-head on a tray that drops along the z-axis. The acrylic is cured by the UV lamps that are built into the printer head (Figure 46).



Figure 44: The Objet Eden 333 Printer and the Printer Head during the Build Process

The build process for one model is approximately 26 hours. Each model requires approximately 1300 grams of support material and 500 grams of build material. Once the model is built, the support material is pressure washed away and the Original Configuration Model is complete (Figure 45).



Figure 45: The Completed Original Configuration Model

3.3 Models

3.3.1 Original Configuration Model

The Original Configuration Model was constructed according to the construction method outlined in Chapter 3.2. The aircraft parameters can be seen in Figure 46. The length of the Original Configuration Model is 5.59". The wingspan (b) is 13.808". The chord of the upper and lower wing is 2.55" and is uniform throughout each wing ($\bar{c} = 2.55$ "). The planform area (S) is 72.58 in² which included the planform areas of the upper and lower wing, and the areas of the Flow Guides. The aspect ratio, AR , was calculated for a monoplane and biplane and is as follows: $AR_{\text{mono}} = 2.63$ and $AR_{\text{bi}} = 5.26$. The aspect ratios for the rest of the models are calculated in Section 4.3.5. The volume of the aircraft is 17.78 in³. The lower wing has a leading edge sweep angle of 15°. The upper wing has a leading edge sweep angle of -15°. The distance between the leading edge of the upper and lower wing is 2.13". If biplane parameters were applied to the Original Configuration Model, it would have a gap of $0.84\bar{c}$, a stagger of $-1.2\bar{c}$, and a decalage angle of 0°. The aspect ratio of this model and each subsequent model was not calculated due to the numerous definitions available for different wing configurations (e.g., monoplane, biplane, and joined-wing). However in Section 4.3 the effective aspect ratio for each model is calculated.

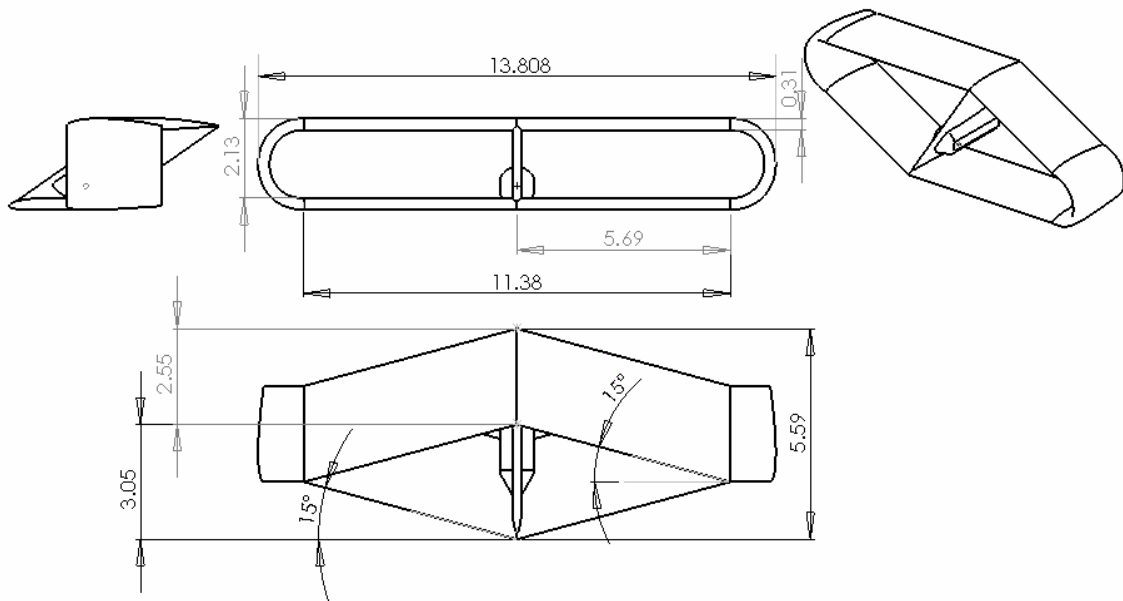


Figure 46: Left, Front, Top, and Isometric Views of the Original Configuration Model with Dimensions (in)

3.3.2 Original Configuration Model Flow Guides

The Flow Guides of the Original Configuration Model have been built to the description in Claim 17 of the Lifting Foil patent. The camber of the flow guide has maximum camber at the upper and lower wing-tips and has minimum camber at the mid-point of the flow guide. The Original Configuration Flow Guide has maximum camber at the upper and lower wing-tips (Figure 47).

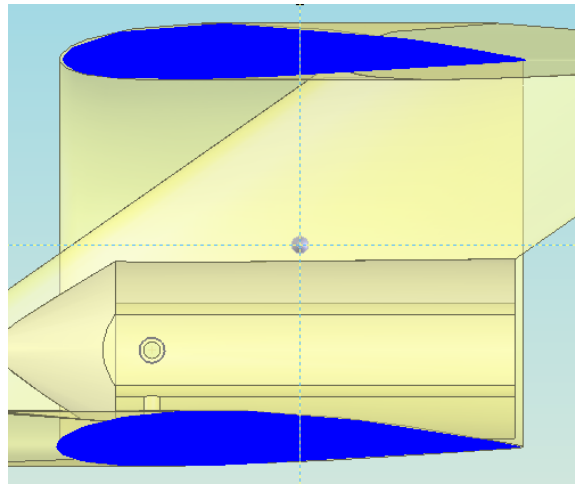


Figure 47: Maximum Camber of Flow Guide at Upper and Lower Wings

From the upper wing, the camber gradually (linearly with arc length) diminishes until it reaches the mid-point of the flow guide (Figure 48).

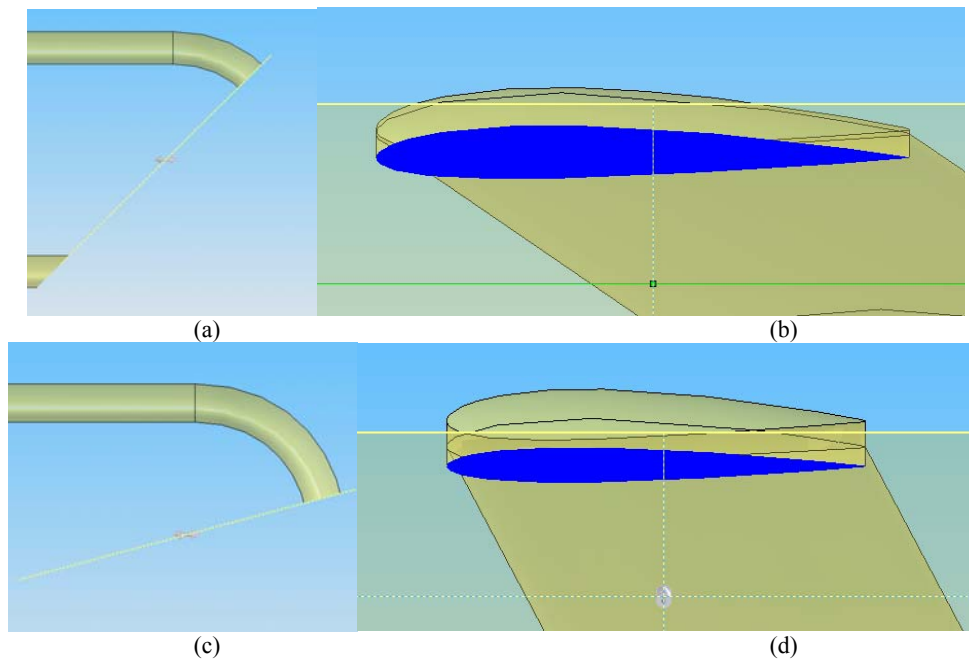


Figure 48: Gradually Diminishing Camber of the Airfoil on the Flow Guide
 (a) Front view of 45° Cut of Flow Guide, (b) Airfoil of 45° Cut,
 (c) Front view of 75° Cut of Flow Guide, (d) Airfoil of 75° Cut

Once at the midpoint of the flow guide, the flow guide has zero camber (symmetrical airfoil) (Figure 49).

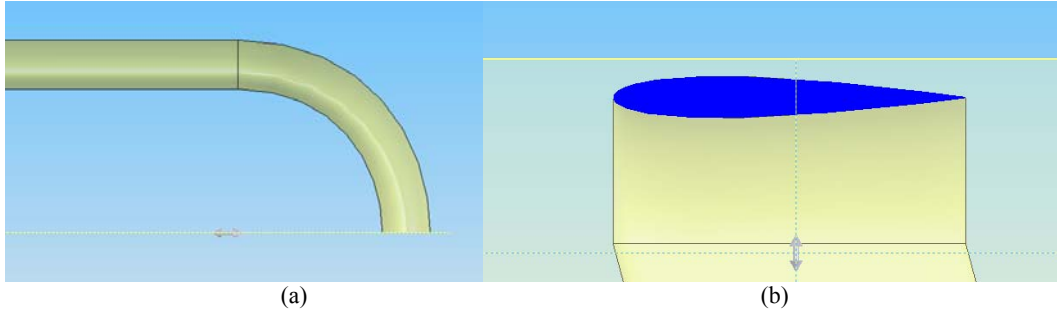


Figure 49: Symmetrical Airfoil at the Midpoint of the Flow Guide
 (a) Front view of 90° Cut of Flow Guide, (b) Airfoil of 90° Cut

Past the midpoint of the flow guide, the camber continues to diminish negatively; however, from the lower wing perspective the camber is increasing (Figure 50).

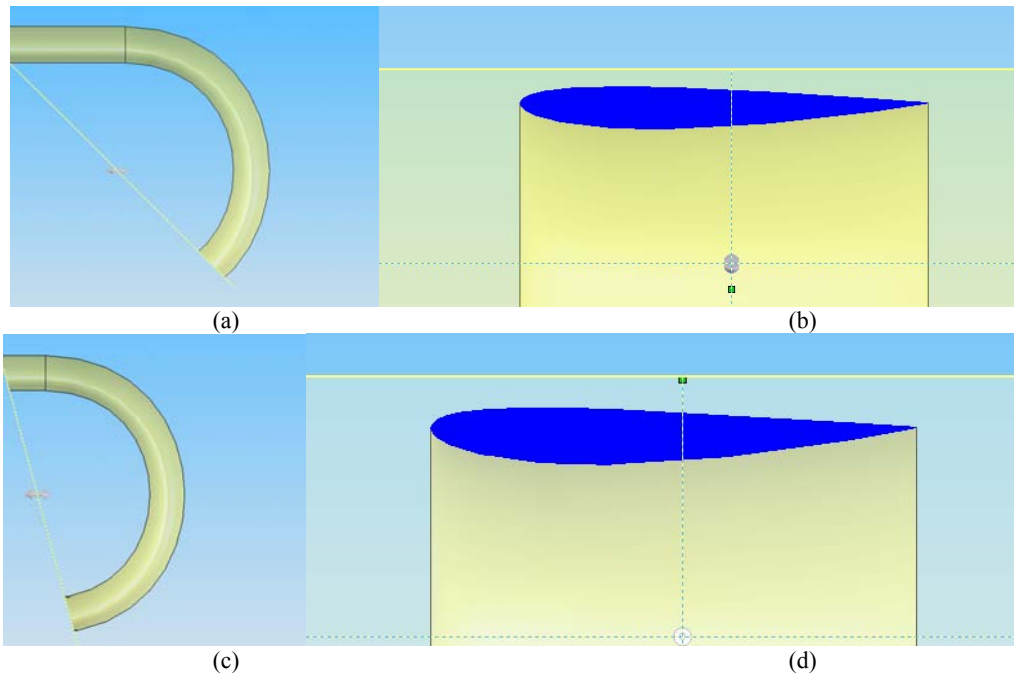


Figure 50: Past Midpoint: Gradually Diminishing Camber of the Airfoil on the Flow Guide
 (a) Front view of 135° Cut of Flow Guide, (b) Airfoil of 135° Cut,
 (c) Front view of 165° Cut of Flow Guide, (d) Airfoil of 165° Cut

Once the flow guide attaches to the lower wing, it is at maximum camber and is identical to the lower wing airfoil (Figure 47: Lower Wing). The comparison of the patent claim and the constructed flow guide is shown in Figure 51 (16)

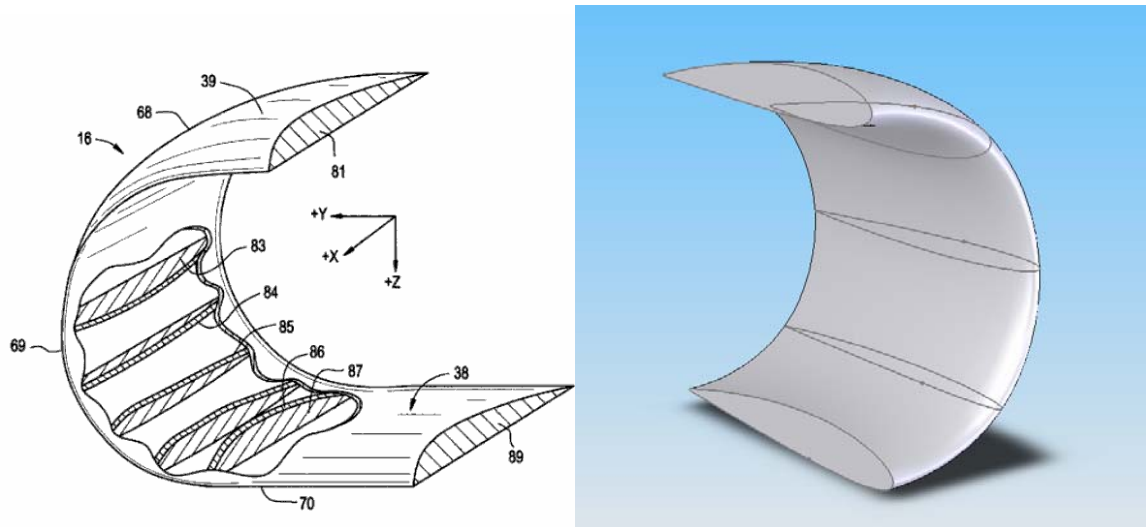


Figure 51: Comparison of the Houck Patent Claim 17 and the Original Configuration Flow Guide (reproduced from Reference 16)

3.3.3 Positive 5° Canted Flow Guide Model

The Positive 5° Canted Flow Guide Model (+ 5° Model) was built according to the same method for the Original Model except that the Flow Guides were altered with a + 5° cant in the airfoils located at the 45° and 135° planes (Figure 52).

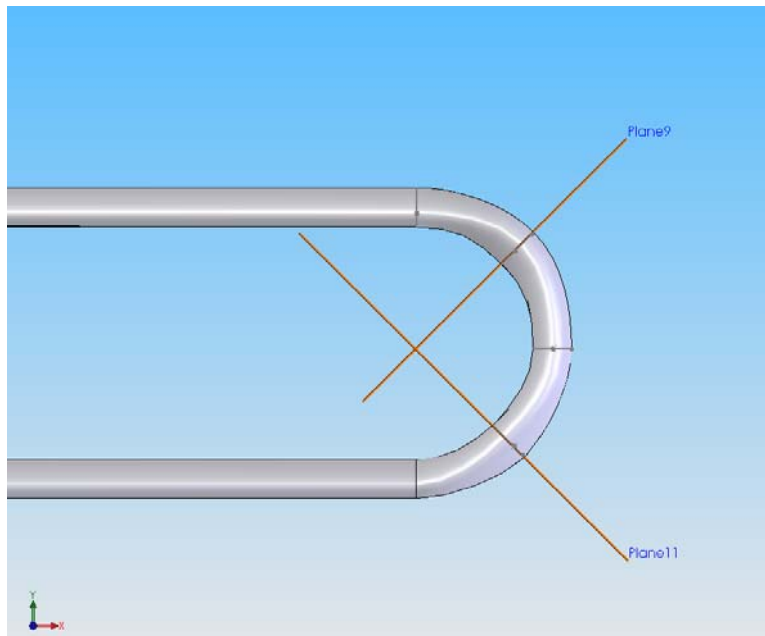


Figure 52: The 45° and 135° planes where the Canted Airfoils are Located

The + 5° cant was accomplished in *SolidWorks* by rotating the airfoils 5° in the clockwise direction about the mid-chord (Figure 53).

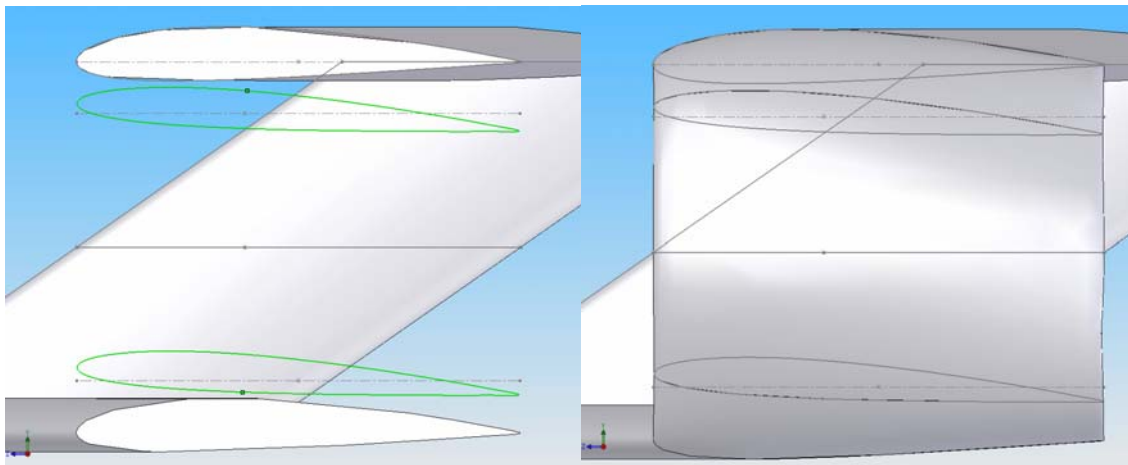


Figure 53: The Rotated Airfoils and Subsequent +5° Canted Airfoil

The aircraft views for the + 5° Model can be seen in Figure 54 and Figure 55. The + 5° Model differs from the Original Configuration Model with the following parameters. The

wingspan (b) is 13.806". The planform area (S) is 72.56in² and is calculated the same way as the Original Configuration Model. The volume of the model is 17.74 in³.

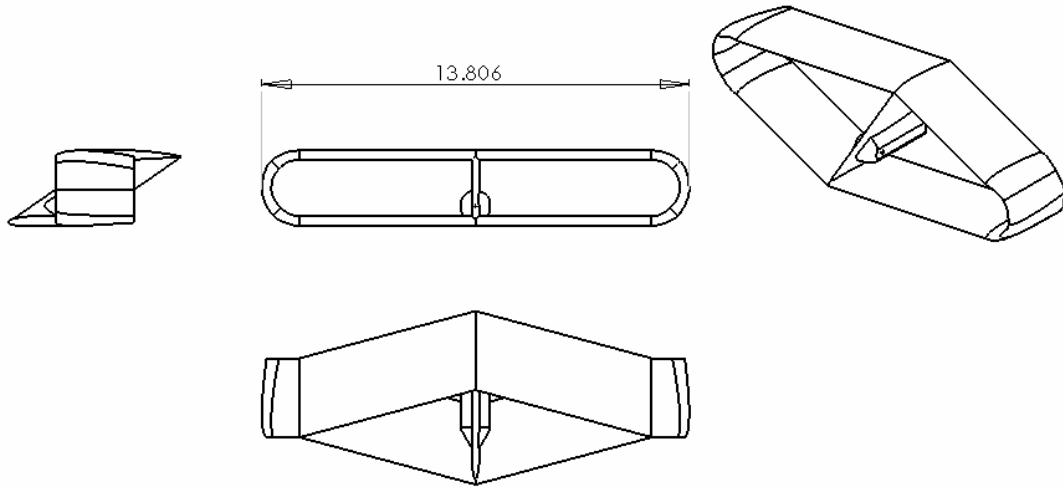


Figure 54: Left, Front, Top, and Isometric Views of the + 5° Canted Flow Guide Model

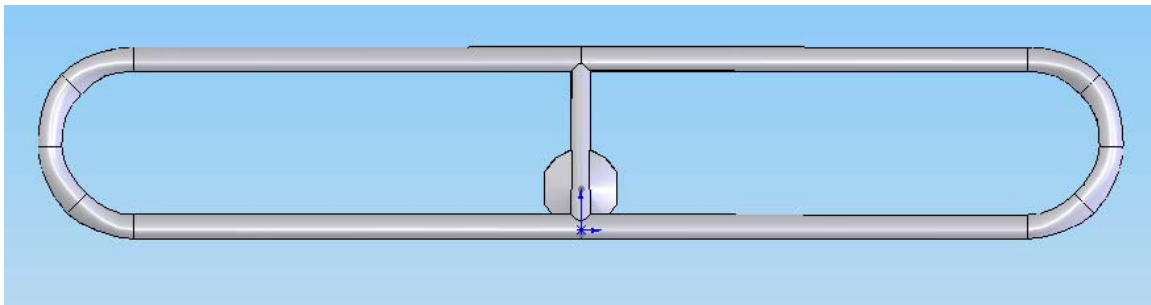


Figure 55: Front View of the + 5° Canted Flow Guide Model

3.3.4 Negative 5° Canted Flow Guide Model

The Negative 5° Canted Flow Guide Model (-5° Model) was built according to the same method for the Original Model except that the Flow Guides were altered with a -5° cant in the airfoils located at the 45° and 135° planes (Figure 52). The -5° cant was accomplished in *SolidWorks* by rotating the airfoils 5° in the counter-clockwise direction

about the mid-chord (Figure 56). The aircraft views for the -5° Model can be seen in Figure 57 and Figure 58. The parameters for the -5° model are identical to the $+5^\circ$ Model parameters.

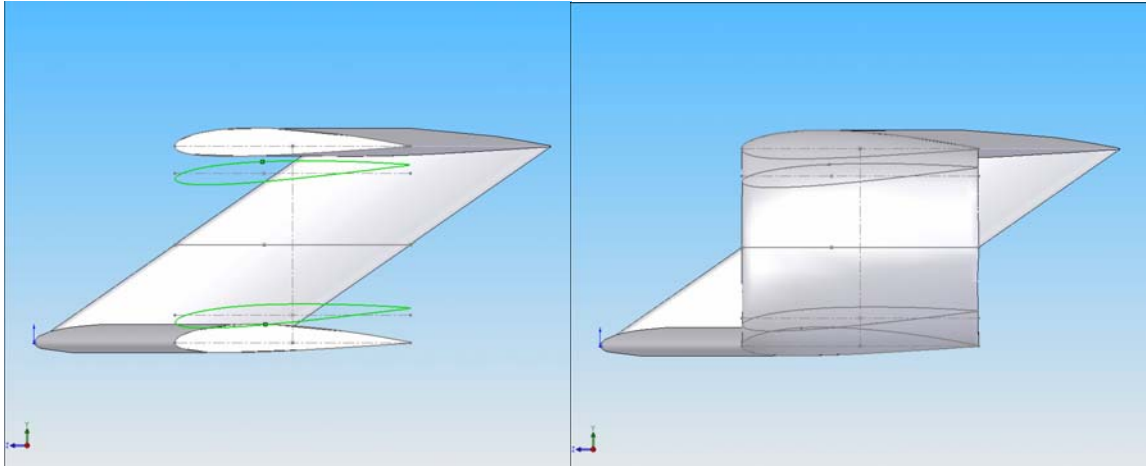


Figure 56: The Rotated Airfoils and Subsequent -5° Canted Airfoil

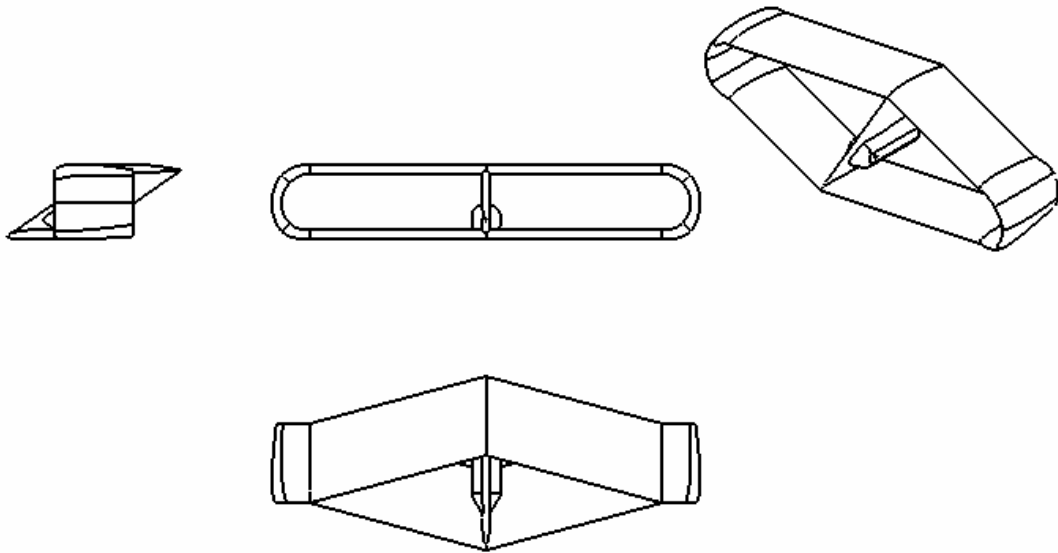


Figure 57: Left, Front, Top, and Isometric Views of the -5° Canted Flow Guide Model

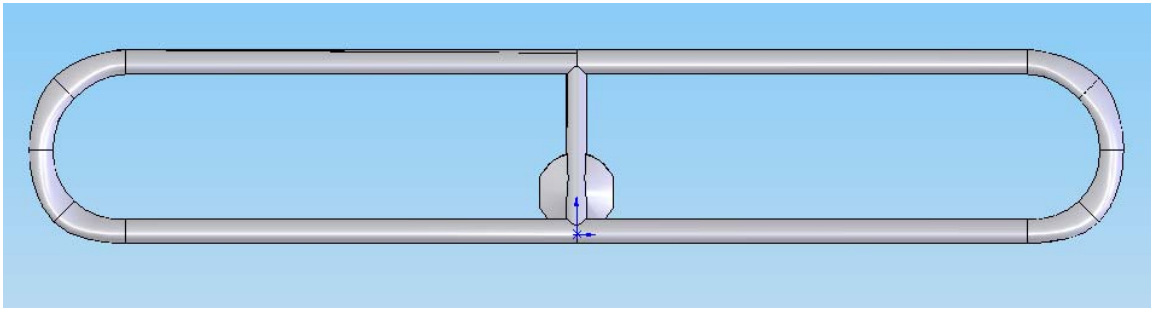


Figure 58: Front View of the - 5° Canted Flow Guide Model

3.3.5 Endplate Configuration

The Endplate Configuration Model was built according to the same method for the Original Configuration Model except that aluminum flat plates were substituted for the Flow Guides. The aluminum plates were cut to cover the upper and lower wingtips and to cover the gap. The plates are 0.0625" in depth. The aircraft views for the Endplate Configuration Model can be seen in Figure 59 and Figure 60. The Endplate Model differs from the Original Configuration Model with the following parameters. The wingspan (b) is 11.439". The planform area (S) is 58.326 in² and is calculated the same way as the Original Configuration Model minus the Flow Guides' area but including the End Plates' area. The volume of the model is 14.85 in³.

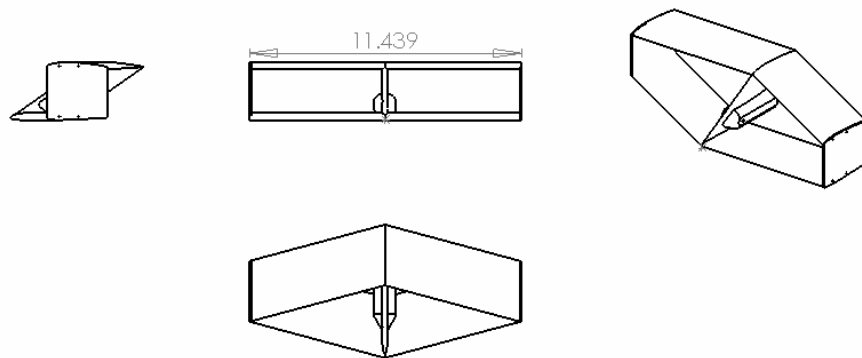


Figure 59: Left, Front, Top, and Isometric Views of the End Plate Configuration Model

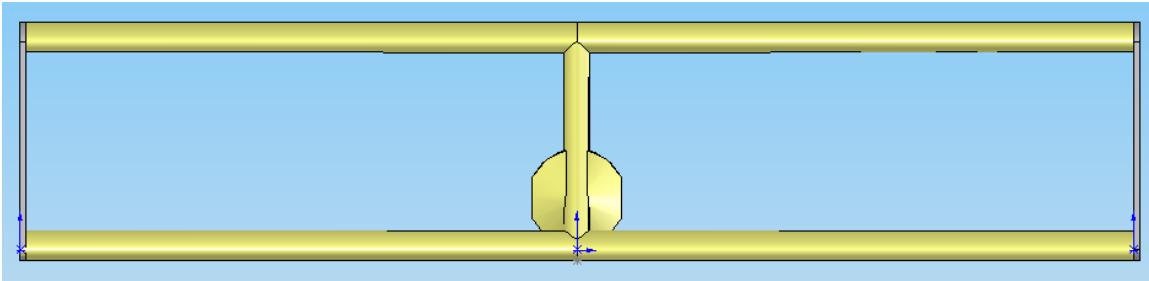


Figure 60: Front View of the End Plate Configuration Model

3.3.6 No Flow Guide Configuration

The No Flow Guide Configuration Model was built according to the same method for the Original Configuration Model except that the Flow Guides were not added. The aircraft views for the No Flow Guide Configuration Model can be seen in Figure 61 and Figure 62. The No Flow Guide Model differs from the Original Configuration Model with the following parameters. The wingspan (b) is 11.377". The planform area (S) is 58.02 in² and is calculated the same way as the Original Configuration Model minus the Flow Guides' area. The volume of the model is 14.10 in³.

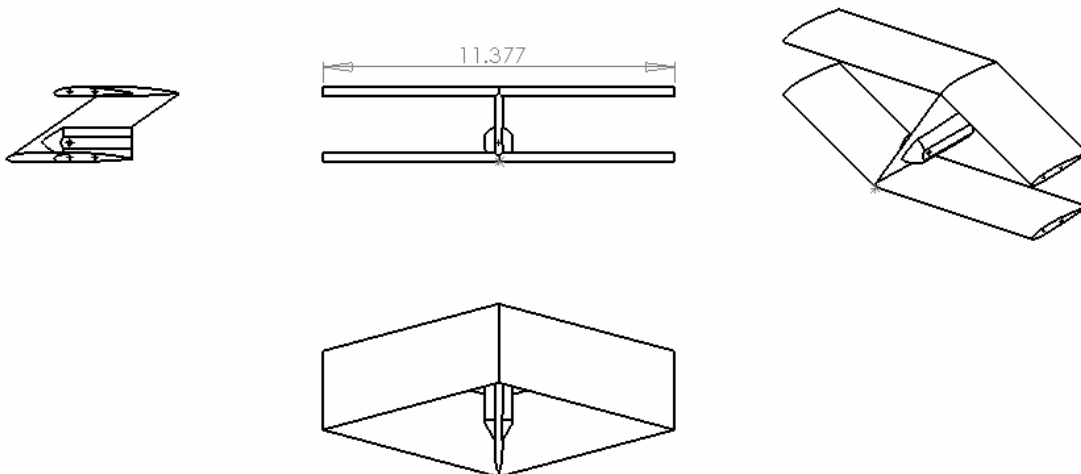


Figure 61: Left, Front, Top, and Isometric Views of the No Flow Guide Configuration Model

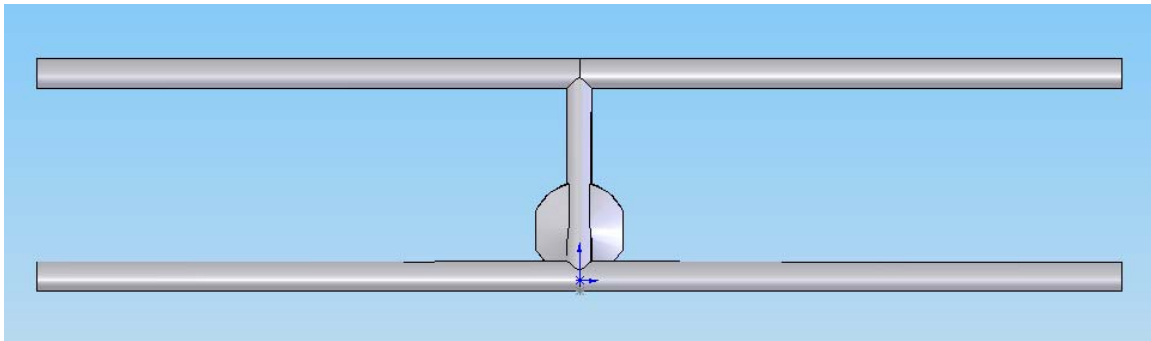


Figure 62: Front View of the No Flow Guide Configuration Model

3.4 Experimental Equipment

3.4.1 AFIT Low-Speed Wind Tunnel

The tests completed in this study utilized the Air Force Institute of Technology's low-speed, open-circuit wind tunnel. The schematic for the low-speed wind tunnel can be seen in Figure 63.

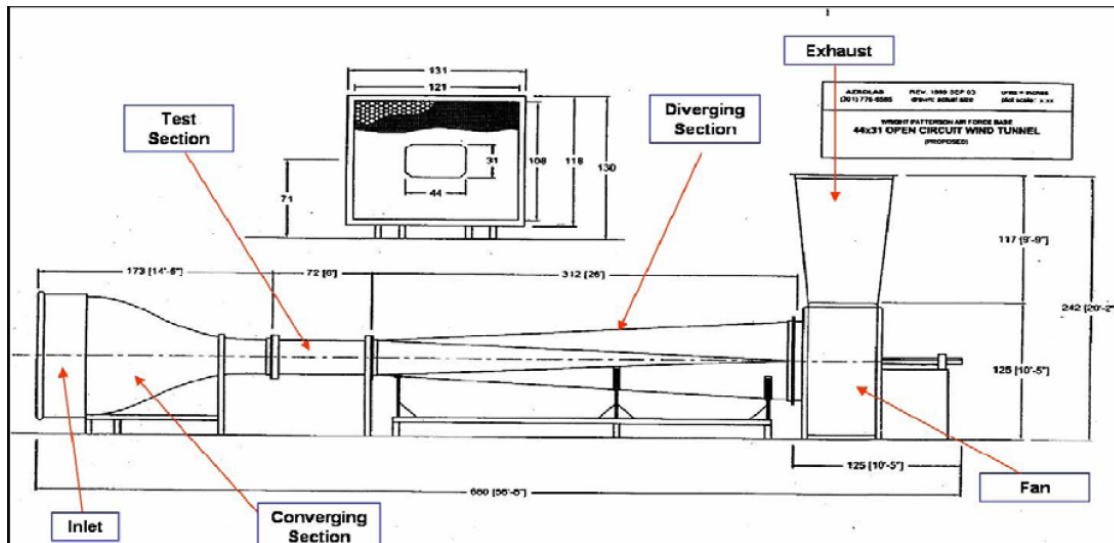


Figure 63: Schematic of the Low-Speed Wind Tunnel (reproduced from Reference 31:24)

Initially, ambient air is drawn through the intake plenum of the wind tunnel by the fan. Next, the air passes through an aluminum honeycomb flow-straightener and then through

steel mesh anti-turbulence screens. Once the flow passes through the last anti-turbulence screen it enters the convergent section of the tunnel. The intake and convergent section of the tunnel are shown in Figure 64.



Figure 64: Intake and Convergent Section of the Wind Tunnel (reproduced from Reference 31:25)

The convergent section of the wind tunnel accelerates the airflow into the octagon-shaped test section. The test section has a width of 44" and height of 31". Upon exiting the test section, the airflow enters the diffuser section of the wind tunnel. The diffuser decelerates the airflow and it is then exhausted vertically back into the room. The test models are mounted to an internal balance that is attached to a movable sting in the test section of the tunnel. The sting is manipulated by a movable control table and a pitch control device. The wind tunnel test section, balance, sting mechanism, and moveable table for β measurements are shown in Figure 65.

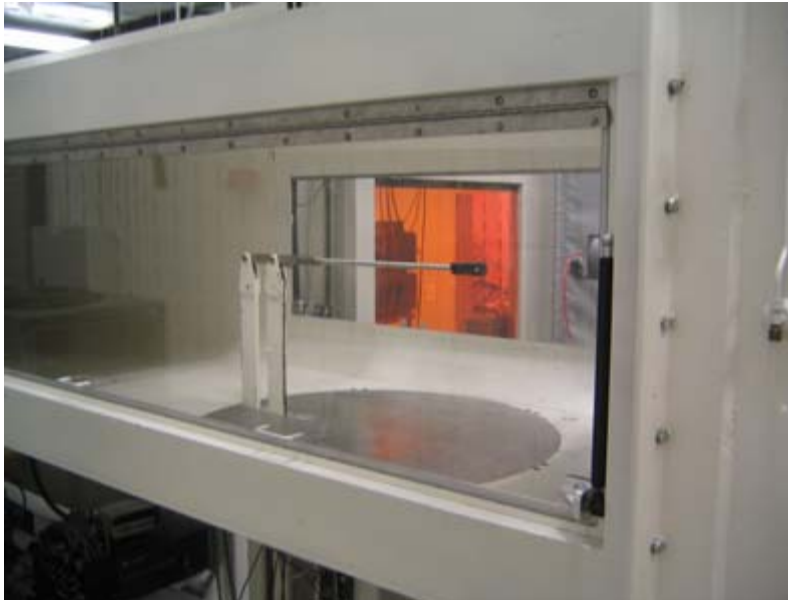


Figure 65: Test Section, Balance, Sting, and Moveable Table (reproduced from Reference 31:25)

Measurements can be taken by the balance once the wind tunnel reaches a desired velocity. Angle of attack sweeps (α sweeps) can be accomplished by pitching the balance and subsequent model using the angle control device. This device is a system of bars and cables that is controlled by motors underneath the tunnel (Figure 66).



Figure 66: Angle Control Device (reproduced from Reference 31:26)

The data acquisition was accomplished using a computerized data acquisition system (Figure 67) operated by AFIT lab technician John Hixenbaugh, who has been trained and is proficient with the system.



Figure 67: Computerized Data Acquisition System

All data files for each test run were stored on the hard drive of the acquisition system and were later retrieved for data reduction. The acquisition recorded the following values: α , β , tunnel speed, unresolved normal force, unresolved axial force, side force, pitch moment, yaw moment, and roll moment. All forces and moments were measured about the balance center. The balance records the force data by comparing voltage measurements to the calibrated voltage measurements. This comparison allows the forces that act on the balance to be determined.

Before testing each model, a tare run was completed for an identical α sweep that would be used for the actual test at speed. The tare was necessary to subtract the weight of the model from the data at all angles of attack. Between each change of airspeed during testing, the wind tunnel velocity was brought back to zero to ensure that the balance was still calibrated correctly.

3.4.2 AFIT 10 lb Strain Gage Balance

A 10 lb strain gage balance was used in the AFIT low-speed wind tunnel to record the force measurements on all the models. The balance is manufactured by Modern Machine and Tool Company. Figure shows the balance mounted in the sting of the test section of the wind tunnel.

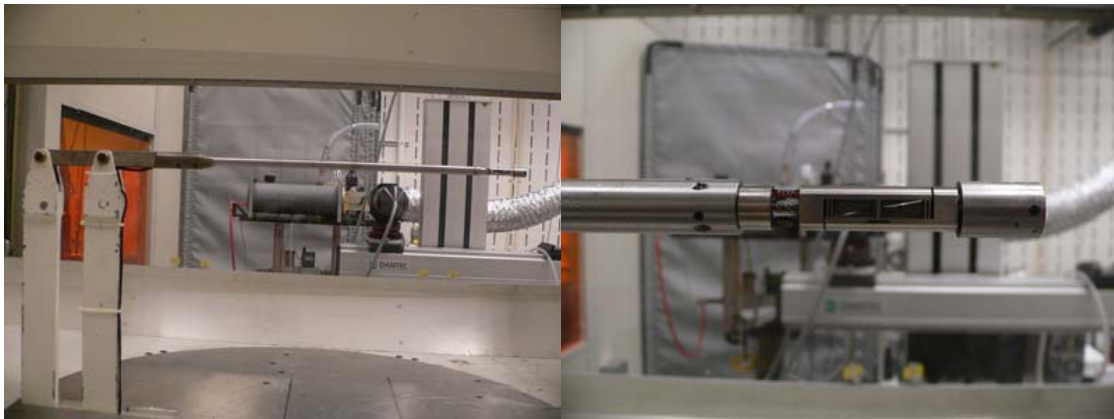


Figure 68: 10 lb Balance Mounted in Test Section of the Wind Tunnel (reproduced from Reference 31:28)

A list of the maximum allowable forces and moments is listed in Table 2. If forces or moments exceed the allowable range then the balance could be damaged and thus invalidate the calibration.

Table 2: Max Allowable Forces and Moments for the 10 lb Balance

Component	Max Load
Normal	10 lbs
Axial	5 lbs
Pitch	10 in-lbs
Roll	4 in-lbs
Yaw	5 in-lbs
Side	5 lbs

The balance's moment center is located 1.3350" aft of the screws. The screws are where the balance is attached to the model. The other dimensions of the balance can be seen in Appendix A.

3.5 Collecting and Processing Data

3.5.1 Correction of Balance Data using *MATLAB*® 10 lb Balance Code

Once the wind tunnel tests have been completed, the data has to be processed and reduced in order to receive useable results. This process is done using a *MATLAB* m-file to perform a series of operations and calculations on the tunnel output data. The *MATLAB* 10 lb Balance Code was adapted from previous research conducted by former AFIT students Rivera Parga, Deluca, and Walker (10; 25; 31). The modified *MATLAB* 10 lb Balance Code can be seen in Appendix B. The m-file requires multiple inputs about the model and ambient conditions at the time of testing (e.g., room temperature, barometric pressure) plus the tare and wind tunnel data for each model. The temperature and pressure in the wind tunnel room varied between each test run. These values were recorded for each test and were input into each model's corresponding code.

When the aircraft is mounted on the balance, it is at the reference zero angle of attack. When the balance is at the 0° position, the model is at 0° aircraft angle of attack, AoA.

In order to obtain the moment data from the wind tunnel results, a reference center of gravity for the aircraft must be determined. For the data reduction in this study, the center of gravity was placed at the mean of the quarter chord locations of the upper and lower wings (Equation 9).

$$c_{\frac{1}{4}} = \frac{0.25\bar{c}_{upper} + 0.25\bar{c}_{lower}}{2} \quad (9)$$

The resulting center of gravity is 2.1625" from the nose of the model in the x-direction, 0.53" above the lower wing's chord line in the z-direction, and is centered in the y - directions (aircraft body coordinate system located at nose of model) (Figure 69).

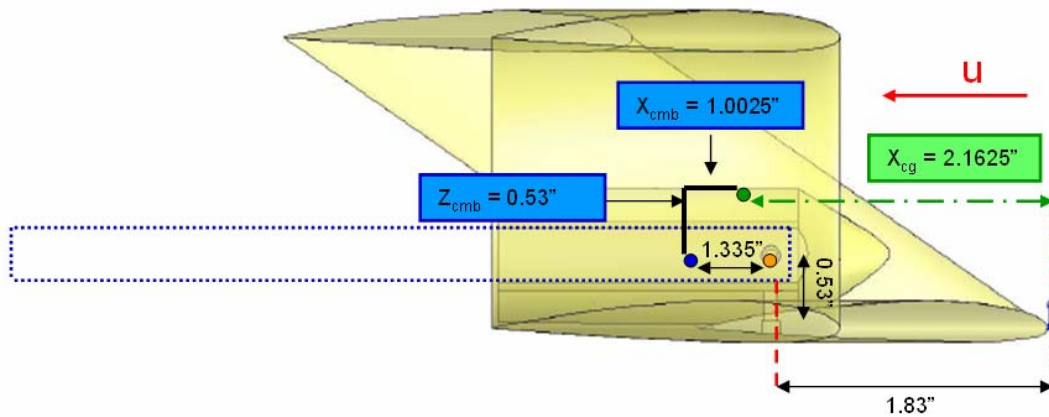


Figure 69: Location of Aircraft Center of Gravity and Balance Moment Center

The aircraft center of gravity (green dot) is located 1.0025" in front of the balance moment center (blue dot) and 0.53" above the balance moment center (in the wind axis coordinate system). These values were input into the *MATLAB* 10 lb Balance Code for data reduction.

Data reduction, using the *MATLAB* 10 lb Balance Code, begins by subtracting the tare data from the test data. Next, there are a few corrections to the data that must be added. The first correction to the data is to account for the blockage of flow in the wind tunnel by the model. This adjustment is done by determining the blockage correction factor. The blockage correction factor accounts for the change in speed of the airflow due

to the reduction in the available cross-sectional area of the tunnel near the model. The delta term (δ_b), blockage correction factor, is approximated for all the model configurations. This is due to their effective spans of 13.808" (Original Configuration), 13.806" (+ 5° and - 5° configurations), 11.5" (Endplate Configuration), and 11.38" (No Flow Guide Configuration) making little difference in the estimation of the parameter. The δ_b term was found to be 0.1177 using the chart found in Barlow, Rae, and Pope (3:387). The δ_b was found by first calculating the wind tunnel aspect ratio:

$$\lambda = \frac{height_{tunnel}}{width_{tunnel}} \quad (10)$$

where λ is the wind tunnel aspect ratio, $height_{tunnel}$ (ft) is the height of the wind tunnel cross-section, and $width_{tunnel}$ (ft) is the width of the wind tunnel cross-section. The AFIT low-speed wind tunnel has $\lambda = 0.705$. The next calculation that was needed was the ratio of the model's wingspan to the width of the wind tunnel:

$$k = \frac{b}{width_{tunnel}} \quad (11)$$

Where k (-) is the ratio of span to the wind tunnel test section width, and b (ft, m) is the wingspan of the model. For these tests, k ranged from 0.259 to 0.313 for the models tested. The values for λ and k are then used to find the blockage correction factor, δ_b .

The second correction to the data involves transferring the normal and axial balance data into the proper frame of reference with respect to the flow. This correction is necessary to translate the lift and force data so it is with respect to the free stream velocity and not the angle of attack of the balance or model. The calculations of the lift and drag coefficients from the normal and axial force acting on the balance is as follows:

$$C_L = \frac{N \cdot \cos \alpha - A \cdot \sin \alpha}{\frac{1}{2} \rho \cdot V^2 \cdot S} \quad (12)$$

$$C_D = \frac{N \cdot \sin \alpha + A \cdot \cos \alpha}{\frac{1}{2} \rho \cdot V^2 \cdot S} \quad (13)$$

Where C_L (-) is the lift coefficient, C_D (-) is the drag coefficient, N (lb) is the normal force acting on the balance, A (lb) is the axial force acting on the balance, α ($^\circ$) is the angle of attack of the balance, ρ (mmHg) is the air density, V (mph, m/s) is the tunnel wind velocity, and S (in²) is the planform area (wing area) of the aircraft model.

3.5.2 Uncertainty Analysis

The Uncertainty Analysis methodology followed Michael Walker's Thesis (31:37). Uncertainty analysis was performed on the lift-to-drag ratio for the Original Configuration Model in Section 4.2.1. The analysis was done by taking the equation for lift-to-drag and breaking it into a form consisting only of measurements from the wind tunnel results:

$$\frac{L}{D} = \frac{C_L}{C_D} = \frac{N \cdot \cos \alpha - A \cdot \sin \alpha}{N \cdot \sin \alpha + A \cdot \cos \alpha} \quad (14)$$

where L/D (-) is the lift-to-drag ratio, C_L (-) is the lift coefficient, C_D (-) is the drag coefficient, N (lb) is the normal force measurements on the balance, A (lb) is the axial force measurement on the balance, and α ($^\circ$) is the angle of the balance to the free stream velocity.

Then the partial of Equation (14) is taken with respect to both N and A :

$$\frac{\partial(L/D)}{\partial N} = \frac{A}{(N \cdot \sin \alpha + A \cdot \cos \alpha)^2} \quad (15)$$

$$\frac{\partial(L/D)}{\partial A} = \frac{-N}{(N \cdot \sin \alpha + A \cdot \cos \alpha)^2} \quad (16)$$

where $\frac{\partial(L/D)}{\partial N}$ is the partial of the lift-to-drag ratio with respect to the unresolved normal force, and $\frac{\partial(L/D)}{\partial A}$ is the partial of the lift-to-drag ratio with respect to the unresolved axial force.

Next, a worse case possible error and a realistic case possible error in lift-to-drag can be calculated:

$$\Delta(L/D)_{worst} = \left| \frac{\partial(L/D)}{\partial N} \cdot \Delta N \right| + \left| \frac{\partial(L/D)}{\partial A} \cdot \Delta A \right| \quad (17)$$

$$\Delta(L/D)_{realistic} = \sqrt{\left(\frac{\partial(L/D)}{\partial N} \cdot \Delta N \right)^2 + \left(\frac{\partial(L/D)}{\partial A} \cdot \Delta A \right)^2} \quad (18)$$

where $\Delta(L/D)_{worst}$ is a worst-case error value in lift-to-drag ratio, $\Delta(L/D)_{realistic}$ is a more realistic error value in lift-to-drag ratio, ΔN is the possible error in the normal force measurement, and ΔA is the possible error in the axial force measurement.

For the 10 lb balance, the uncertainty in the normal force measurement, ΔN , is specified by the manufacturer to be more than 0.025 lbs. The uncertainty in the axial force measurement, ΔA , is specified by the manufacturer to be more than 0.0125 lbs. These values are considered to be too conservative for actual data acquisition. The range for the possible lift-to-drag ratio can then be determined:

$$\frac{L}{D}_{range} = \frac{L}{D} \pm \Delta(\frac{L}{D}) \quad (19)$$

where L/D_{range} is the possible range of the lift-to-drag ratio given uncertainty in the measurements taken, L/D is the measured lift-to-drag ratio, and $\Delta(L/D)$ is the possible error in the L/D measurement (in one direction).

Another method, used to determine the uncertainty in the normal force measurement, ΔN , and in the axial force measurement, ΔA , was to determine the standard deviation of the force measurements at each given angle of attack (α) for a constant speed. Multiple data points are logged for each angle, therefore the actual sample variance and hence standard deviation can be computed. This method is explored in Section 4.2.1.6 and is labeled the tested uncertainty analysis. Uncertainty analysis by this method reflects a more realistic error value.

3.5.3 Houck 24" Hot-Wire Analysis

In the Fall of 2006 and Winter of 2007, a study on the Houck 24" Configuration was completed at the Air Force Institute of Technology by Masters thesis student 1st LT Michael Walker, USAF and his advisor Dr. Mark Reeder. The model, tested in the AFIT low-speed wind tunnel, was the 24" Houck Configuration. The 24" Houck Configuration can be seen in Figure 70. The Hot-Wire data from the study was analyzed to find the vortex moment (concentration of the vortex in the y-direction). The α sweep data of the Original 24" and No Flow Guide Houck 24" were used for comparison with the model configurations tested in this study.



Figure 70: 24" Houck Configuration Three-View Representation (reproduced from Reference 31)

3.6 Test Plan

3.6.1 Overview

A summary of tests performed on the various model configurations can be found in Table 3. Experimental information has primarily been collected through the use of balance data. The tests used for the 24" Houck comparison consisted of balance and the use of Hot-Wire data. Further detail of testing for each model configuration will be discussed in the remainder of this section.

Table 3: Summary of Tests Performed

Model Configuration	Re (-)	V (mph)	Balance Data	Hot Wire
			α sweep	$\alpha = 4^\circ$
Original	38K	20	√	
Original	57K	30	√	
Original	78K	40	√	
Original	120K	60	√	
+ 5° Cant	38K	20	√	
+ 5° Cant	57K	30	√	
+ 5° Cant	78K	40	√	
+ 5° Cant	120K	60	√	
- 5° Cant	38K	20	√	
- 5° Cant	57K	30	√	
- 5° Cant	78K	40	√	
- 5° Cant	120K	60	√	
Endplate	38K	20	√	
Endplate	57K	30	√	
Endplate	78K	40	√	
Endplate	120K	60	√	
No Flow Guide	38K	20	√	
No Flow Guide	57K	30	√	
No Flow Guide	78K	40	√	
No Flow Guide	120K	60	√	
Original 24" Houck	80K	20	√	
Original 24" Houck	125K	30	√	√
No Flow Guide 24" Houck	80K	20	√	
No Flow Guide 24" Houck	125K	30	√	√

3.6.2 Original Configuration

Testing began with the Original Configuration Model. The model was placed on the 10 lb balance in the AFIT low-speed wind tunnel. Data was taken for all configurations for four different α sweeps from -8° to 10° by 2° increments and then from 10° to 15° by 1° increments. Testing procedures were repeated for all models. The dates of the testing and the corresponding temperature and pressure can be seen in Tables 4-8.

Table 4: Original Configuration Test Dates, Temperature, and Pressure

Model Configuration: Original				
Re (-)	V (mph)	Date	Temperature (°F)	Barometric Pressure
38K	20	17-Apr-07	71	14.15 psi
57K	30	17-Apr-07	71	14.15 psi
78K	40	17-Apr-07	71	14.15 psi
120K	60	23-Apr-07	74.2	14.23 psi

3.6.3 + 5° Configuration

Table 5: + 5° Canted Flow Guide Configuration Test Dates, Temperature, and Pressure

Model Configuration: + 5°				
Re (-)	V (mph)	Date	Temperature (°F)	Barometric Pressure
38K	20	17-Apr-07	71	14.15 psi
57K	30	17-Apr-07	71	14.15 psi
78K	40	17-Apr-07	71	14.15 psi
120K	60	23-Apr-07	74.8	14.21 psi

3.6.4 - 5° Configuration

Table 6: - 5° Canted Flow Guide Configuration Test Dates, Temperature, and Pressure

Model Configuration: - 5°				
Re (-)	V (mph)	Date	Temperature (°F)	Barometric Pressure
38K	20	18-Apr-07	69.9	14.1 psi
57K	30	18-Apr-07	69.9	14.1 psi
78K	40	18-Apr-07	69.9	14.1 psi
120K	60	23-Apr-07	74.8	14.21 psi

3.6.5 Endplate Configuration

Table 7: Endplate Configuration Test Dates, Temperature, and Pressure

Model Configuration: Endplates				
Re (-)	V (mph)	Date	Temperature (°F)	Barometric Pressure
38K	20	20-Apr-07	72.6	14.32 psi
57K	30	20-Apr-07	72.6	14.32 psi
78K	40	20-Apr-07	72.6	14.32 psi
120K	60	20-Apr-07	72.6	14.32 psi

3.6.6 No Flow Guide Configuration

Table 8: No Flow Guide Configuration Test Dates, Temperature, and Pressure

Model Configuration: No Flow Guides		Date	Temperature (°F)	Barometric Pressure
Re (-)	V (mph)			
38K	20	18-Apr-07	71.2	14.09 psi
57K	30	18-Apr-07	71.2	14.09 psi
78K	40	18-Apr-07	71.2	14.09 psi
120K	60	20-Apr-07	71.9	14.33 psi

IV. Results and Analysis

4.1 Chapter Overview

In this chapter, results will be shown for wind tunnel tests conducted on the Original Configuration Model, +5° Cant Configuration Model, -5° Cant Configuration Model, Endplate Configuration Model, and the No Flow Guide Configuration Model. In addition to the wind-tunnel results, there will be analysis on the 24" Houck (with and without flow guides) Configuration's Hot-Wire results (31). The aerodynamic data for all five models can be seen in Appendix C.

The results will be divided into four main sections. The first section will present each model's results. This section includes analysis on the balance data from each model's α sweeps that were performed in the AFIT low-speed wind tunnel at various speeds (20 mph, 30 mph, 40 mph, and 60 mph). The second section will compare the results of each model at each speed. Only balance data using α sweeps performed in the AFIT low-speed wind tunnel will be described in this section. The third section will discuss the process and results of the Original Configuration Model's neutral longitudinally stable $C_{m\alpha}$. The fourth and final section will discuss the process and results of the vortex centroid analysis of the 24" Houck Configuration.

4.2 Wind Tunnel Balance Data – Alpha Sweeps: Individual Models

4.2.1 Original Configuration Model

4.2.1.1 Summary

In the AFIT low-speed wind tunnel, an α sweep from -8° to 10° in steps of 2° and then from 10° to 15° in steps of 1° was performed on the Original Configuration Model at

four different speeds: 20 mph (8.94 m/s), 30 mph (13.41 m/s), 40 mph (17.88 m/s), and 60 mph (26.82 m/s). A summary of the resulting aerodynamic performance of the Original Configuration Model at $Re \approx 38,000$ (20 mph), $Re \approx 57,000$ (30 mph), $Re \approx 78,000$ (40 mph), and $Re \approx 120,000$ (60 mph) can be seen in Table 9. The Reynolds numbers are based on the average root chord of the upper and lower wings ($\bar{c} = 2.55''$).

Table 9: Aerodynamic Performance of the Original Configuration Model

Model	Re (-)	Min Drag		Zero Lift	Slopes	
		C_{D0} (-)	α ($^\circ$)	$\alpha_{0 \text{ Lift}}$ ($^\circ$)	$C_{L\alpha}$ (l°)	$C_{m\alpha}$ (l°)
Original Configuration	38K	0.0327	-2.03	-0.52	0.0528	0.0106
Original Configuration	57K	0.0275	-2.02	-1.33	0.0555	0.0099
Original Configuration	78K	0.0251	0.03	-1.50	0.0538	0.0105
Original Configuration	120K	0.0204	0.12	-1.54	0.053	0.0114

Model	Re (-)	Max Range				Max Endurance			
		L/D (-)	α ($^\circ$)	C_L (-)	C_D (-)	$C_L^{(3/2)}/C_D$ (-)	α ($^\circ$)	C_L (-)	C_D (-)
Original Configuration	38K	6.2241	8.43	0.4631	0.0744	4.2385	10.55	0.5625	0.0995
Original Configuration	57K	9.4369	6.33	0.4252	0.0451	7.0672	10.57	0.6110	0.0676
Original Configuration	78K	10.5512	6.32	0.4154	0.0394	7.7068	10.56	0.5969	0.0598
Original Configuration	120K	11.8368	6.41	0.4240	0.0358	8.5435	10.56	0.6003	0.0544

4.2.1.2 Drag Coefficient

The drag coefficient, C_D , for the Original Configuration Model is shown in Figure 71 for four different Reynolds numbers (38K, 57K, 78K, and 120K). C_D has been plotted both versus C_L and α .

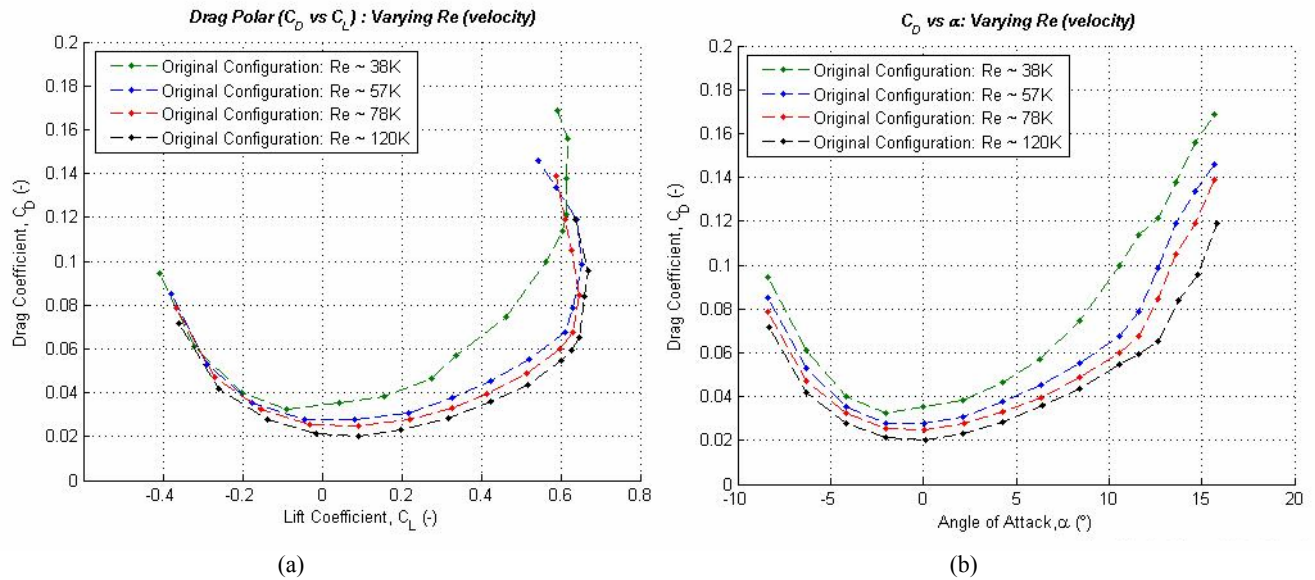


Figure 71: Drag Coefficient – Original Configuration Model
 (a) Drag Coefficient vs. Lift Coefficient (Drag Polar), (b) Drag Coefficient vs. Alpha

4.2.1.3 Lift Coefficient

Figure 72 plots the lift coefficient, C_L , vs. α for the Original Configuration Model at four different Reynolds numbers (38K, 57K, 78K, and 120K). From the lift curve, a number of important aerodynamic values can be attained. $C_{L_{max}}$ is the maximum lift coefficient of the aircraft. An aircraft flying at the α that corresponds to $C_{L_{max}}$ will produce the highest amount of lift at that speed. $C_{L_{max}}$ usually occurs right before stall. As seen in Figure 72, the Original Configuration Model exhibits the gradual stall characteristic of most aircraft past an $\alpha = 10^\circ$. $C_{L\alpha}$ is the lift curve slope, and gives a ratio of change of C_L with respect to α for the linear region (α from -8° to $+8^\circ$) of the lift curve, while $\alpha_{0_{Lift}}$ is the angle of attack where the aircraft produces zero lift.

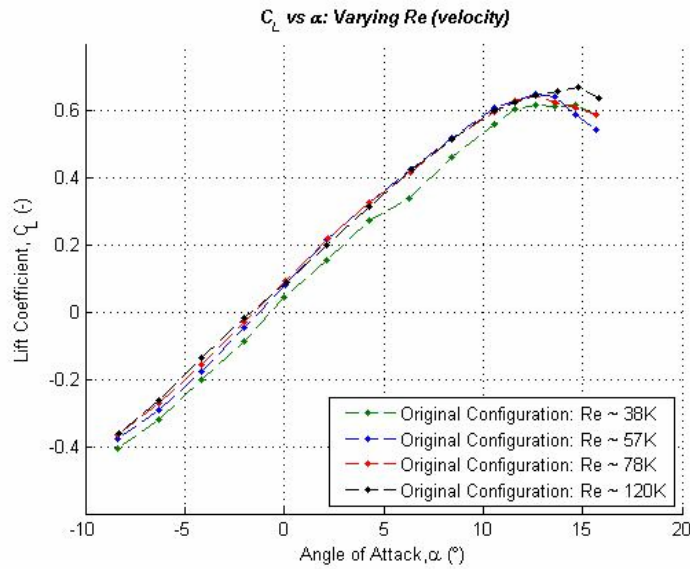


Figure 72: Lift Coefficient vs. Angle of Attack – Original Configuration Model

4.2.1.4 Pitching Moment Coefficient

Figure 73 plots the pitching moment coefficient, C_m , vs. α for the Original Configuration Model at four different Reynolds numbers (38K, 57K, 78K, and 120K). The longitudinal static stability derivative, $C_{m\alpha}$, can be attained from the linear portion of this plot (α from -8° to $+8^\circ$). It is desirable to have a negative value for $C_{m\alpha}$. A negative $C_{m\alpha}$ value will return the aircraft to trim state ($C_m = 0$) when it is perturbed. The Original Configuration Model is longitudinally unstable, due to a positive $C_{m\alpha}$ value, about the reference CG (2.1625" aft of nose), for all four Reynolds numbers tested.

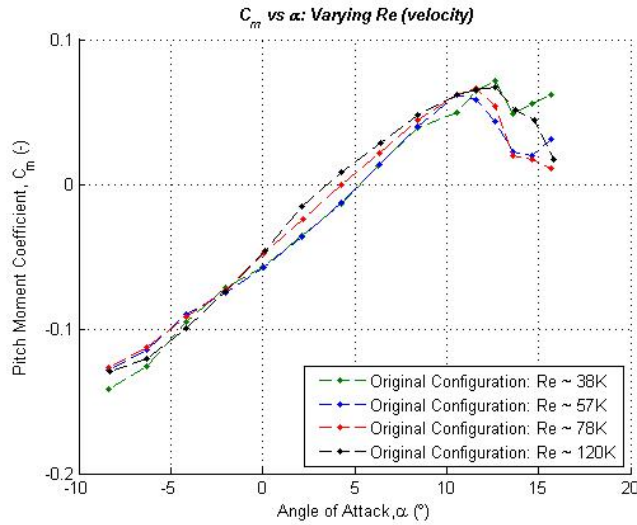


Figure 73: Pitch Moment Coefficient vs. Angle of Attack – Original Configuration Model ($X_{cmb} = 1.0025''$)

4.2.1.5 Lift-to-Drag Ratio

Figure 74 shows the lift-to-drag ratio for the Original Configuration Model at four different Reynolds numbers (38K, 57K, 78K, and 120K). L/D has been plotted versus α and C_L . Lift-to-drag is one measure of aircraft efficiency. An aircraft that flies at the angle of attack that corresponds to the maximum L/D , is maximizing its range (34). There is a strong correlation between an increase in Reynolds number and an increase in L/D values. The efficiency of the Original Configuration Model increases as the Reynolds number increases. L/D values for each Reynolds number increase over the range $\alpha \approx -4^\circ$ to 6° . Once L/D_{max} is reached for each Reynolds number, the L/D values start to decrease. This event occurs beyond $\alpha \approx 6^\circ$ and $C_L \approx 0.41$.

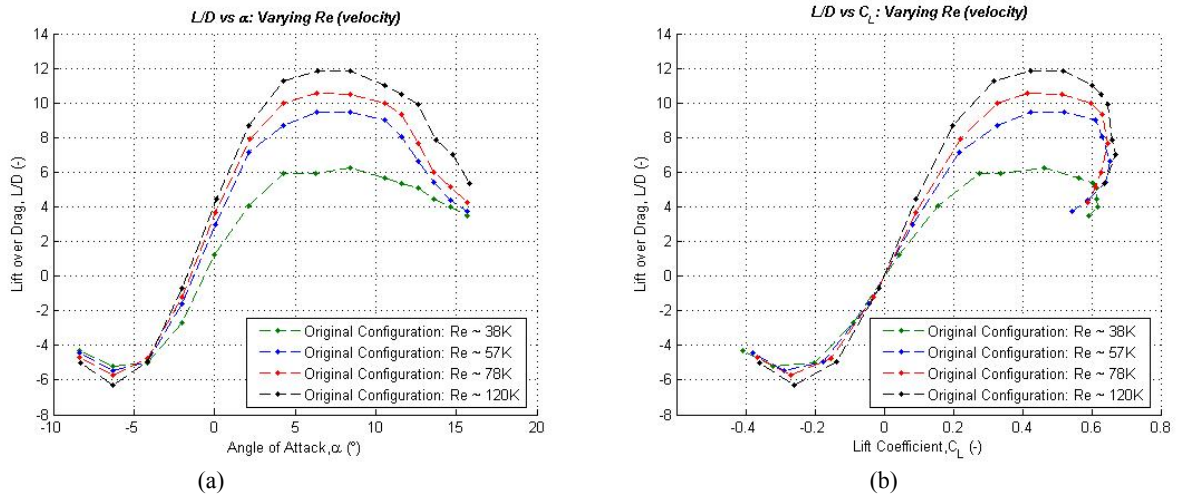


Figure 74: Lift-to-Drag – Original Configuration Model
 (a) Lift-to-Drag vs. Alpha, (b) Lift-to-Drag vs. Lift Coefficient

4.2.1.6 Lift-to-Drag Error Analysis

Figure 75 shows the lift-to-drag ratio plotted for all Reynolds numbers (38K, 57K, 78K, and 120K) with error bars. The error bars were calculated using the conservative method outlined in the beginning of Section 3.5.2. The results of lift-to-drag ratio at all Reynolds numbers for the Original Configuration Model can be seen in Table 10. The worst case scenario is the case where each possible case of error occurs in the same direction. The realistic case scenario is geometric mean of the possible errors and is a more probable occurrence.

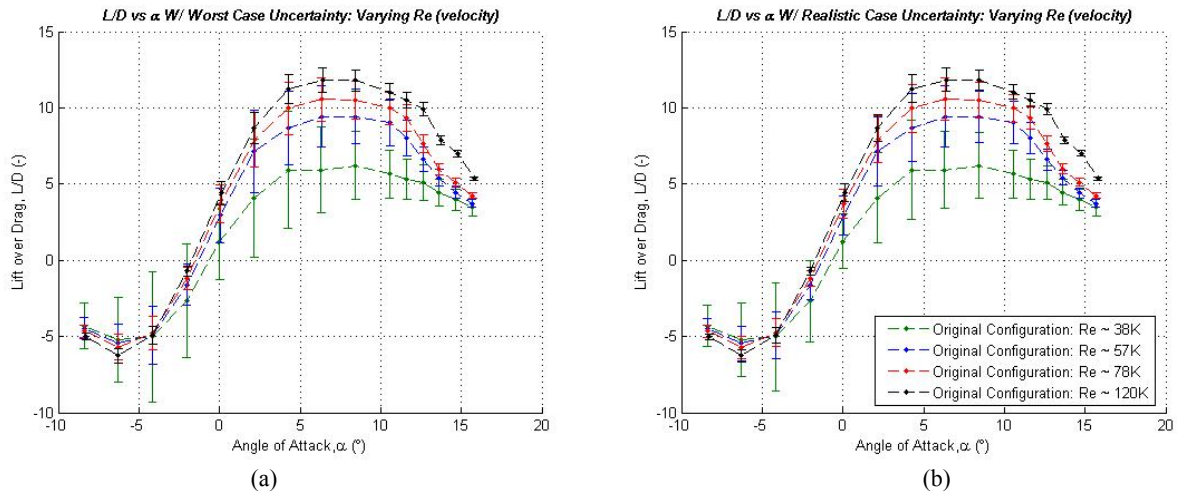


Figure 75: Lift-to-Drag – Conservative Uncertainty Analysis – Original Configuration Model
 (a) Worst Case Uncertainty Analysis, (b) Realistic Uncertainty Analysis

For a Reynolds number of approximately 38K, the worst case error ranges from 8.47% to 61.49% of L/D and the realistic case ranges from 8.54% to 61.38% of L/D. The possible error at L/D_{\max} is 40.98% for the worst case scenario and 36.69% for the realistic case scenario. For a Reynolds number of approximately 57K, the worst case error ranges from 3.93% to 38.84% of L/D and the realistic case ranges from 2.96% to 24.87% of L/D. The possible error at L/D_{\max} is 29.19% for the worst case scenario and 22.23% for the realistic case scenario. For a Reynolds number of approximately 78K, the worst case error ranges from 2.71% to 26.00% of L/D and the realistic case ranges from 1.76% to 16.12% of L/D. The possible error at L/D_{\max} is 20.61% for the worst case scenario and 14.05% for the realistic case scenario. For a Reynolds number of approximately 120K, the worst case error ranges from 1.89% to 14.68% of L/D and the realistic case ranges from 0.97% to 7.82% of L/D. The possible error at L/D_{\max} is 11.55% for the worst case scenario and 6.57% for the realistic case scenario.

Table 10: Conservative Uncertainty Analysis in L/D for the Original Configuration Model

Re = 38K (20 MPH)				Re = 57K (30 MPH)			
α (°)	L/D (-)	Error in % L/D		α (°)	L/D (-)	Error in % L/D	
		Worst	Realistic			Worst	Realistic
-8.39	-4.445	21.88%	19.14%	-8.38	-4.446	9.95%	6.71%
-6.27	-5.537	40.17%	35.18%	-6.26	-5.479	18.90%	12.78%
-4.15	-6.056	61.38%	50.72%	-4.14	-5.120	27.21%	17.05%
-2.03	-3.245	53.75%	38.71%	-2.02	-1.974	19.36%	10.48%
0.10	1.762	35.64%	25.93%	0.11	2.631	26.03%	14.26%
2.14	5.404	56.18%	42.80%	2.15	6.479	38.84%	24.87%
4.25	6.470	55.74%	47.39%	4.27	8.238	34.94%	24.51%
6.29	6.924	40.98%	36.69%	6.30	9.077	29.19%	22.23%
8.41	6.251	31.81%	30.76%	8.41	8.859	26.13%	18.62%
10.52	5.860	22.56%	22.39%	10.52	8.238	22.25%	15.04%
11.58	5.555	19.25%	18.80%	11.57	7.179	17.10%	11.48%
12.63	5.125	16.79%	16.10%	12.63	6.497	11.24%	7.64%
13.67	4.557	12.65%	12.35%	13.67	5.367	7.70%	5.38%
14.73	4.186	10.30%	10.22%	14.71	4.673	5.28%	3.82%
15.76	3.734	8.54%	8.39%	15.74	3.939	3.93%	2.96%

Re = 78K (40 MPH)				Re = 120K (60 MPH)			
α (°)	L/D (-)	Error in % L/D		α (°)	L/D (-)	Error in % L/D	
		Worst	Realistic			Worst	Realistic
-8.37	-4.606	5.96%	3.71%	-8.36	-5.042	2.99%	1.62%
-6.25	-5.596	11.76%	7.32%	-6.24	-6.322	6.49%	3.53%
-4.13	-4.790	15.99%	9.05%	-4.12	-5.031	8.51%	4.13%
-2.01	-1.602	10.17%	5.14%	-2.01	-0.928	4.50%	2.09%
0.11	3.614	18.26%	9.33%	0.11	4.241	10.93%	4.88%
2.15	7.769	26.00%	15.46%	2.14	8.770	14.68%	7.56%
4.27	9.475	24.59%	16.12%	4.27	11.204	13.70%	7.82%
6.29	9.956	20.61%	14.05%	6.29	11.676	11.55%	6.57%
8.40	9.718	18.11%	11.56%	8.41	11.308	10.05%	5.38%
10.52	9.201	15.08%	9.16%	10.52	10.403	8.06%	4.12%
11.58	8.782	12.82%	7.66%	11.58	9.889	7.10%	3.57%
12.63	7.249	8.40%	5.05%	12.63	9.358	6.21%	3.07%
13.67	5.844	5.16%	3.20%	13.68	8.682	3.87%	1.93%
14.72	5.179	3.91%	2.45%	14.73	6.640	3.11%	1.55%
15.75	4.615	2.71%	1.76%	15.77	5.206	1.89%	0.97%

The error values are decreasing as the Reynolds number is increased. This is due to higher velocities producing greater balance loading and therefore, increased sensitivity.

The lower loadings are closer to the balance’s minimum resolution which causes the error to increase. These uncertainty values are conservative, as the actual uncertainty values for the balance measurements are smaller than published.

The next method, the tested uncertainty analysis, produced results that had significantly less error percentages than the previous conservative error analysis. The average standard deviation of the normal force and axial force at each wind tunnel run speed for a given α were used as the ΔN and ΔA . The calculated average standard deviation values were $\Delta N = 0.0056$ and $\Delta A = 0.0011$. These standard deviation values provided a confidence interval of approximately 99.9% (3:453). Figure 76 shows the lift-to-drag ratio plotted for all Reynolds numbers (38K, 57K, 78K, and 120K) with error bars. The error bars were calculated using the tested method outlined at the end of Section 3.5.2. The tested error value results of lift-to-drag ratio at all Reynolds numbers for the Original Configuration Model can be seen in Table 11. The worst case scenario is the case where each possible case of error occurs in the same direction. The realistic case scenario is geometric mean of the possible errors and is a more probable occurrence.

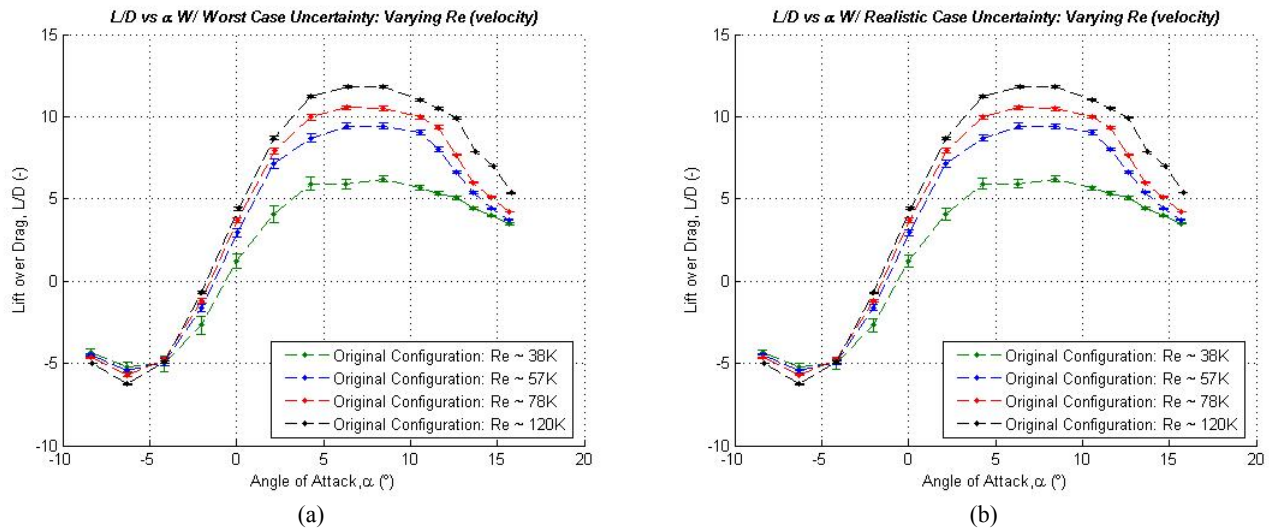


Figure 76: Lift-to-Drag – Tested Uncertainty Analysis – Original Configuration Model
 (a) Worst Case Uncertainty Analysis, (b) Realistic Uncertainty Analysis

Table 11: Tested Uncertainty Analysis in L/D for the Original Configuration Model

Re = 38K (20 MPH)			
α (°)	L/D (-)	Error in % L/D	
		Worst	Realistic
-8.39	-4.445	2.33%	1.79%
-6.27	-5.537	4.27%	3.29%
-4.15	-6.056	7.05%	5.12%
-2.03	-3.245	7.68%	5.62%
0.10	1.762	6.15%	5.10%
2.14	5.404	7.23%	5.12%
4.25	6.470	6.16%	4.59%
6.29	6.924	4.23%	3.36%
8.41	6.251	2.95%	2.72%
10.52	5.860	2.01%	1.97%
11.58	5.555	1.76%	1.66%
12.63	5.125	1.57%	1.42%
13.67	4.557	1.15%	1.09%
14.73	4.186	0.92%	0.90%
15.76	3.734	0.77%	0.74%

Re = 57K (30 MPH)			
α (°)	L/D (-)	Error in % L/D	
		Worst	Realistic
-8.38	-4.446	0.80%	0.62%
-6.26	-5.479	1.51%	1.18%
-4.14	-5.120	2.40%	1.74%
-2.02	-1.974	2.39%	1.89%
0.11	2.631	2.86%	2.10%
2.15	6.479	3.33%	2.45%
4.27	8.238	2.65%	2.21%
6.30	9.077	1.96%	1.96%
8.41	8.859	1.94%	1.66%
10.52	8.238	1.78%	1.39%
11.57	7.179	1.38%	1.07%
12.63	6.497	0.89%	0.70%
13.67	5.367	0.59%	0.49%
14.71	4.673	0.38%	0.34%
15.74	3.939	0.27%	0.26%

Re = 78K (40 MPH)			
α (°)	L/D (-)	Error in % L/D	
		Worst	Realistic
-8.37	-4.606	0.43%	0.34%
-6.25	-5.596	0.84%	0.67%
-4.13	-4.790	1.30%	0.94%
-2.01	-1.602	1.22%	1.01%
0.11	3.614	1.74%	1.25%
2.15	7.769	1.98%	1.49%
4.27	9.475	1.64%	1.43%
6.29	9.956	1.30%	1.24%
8.40	9.718	1.26%	1.04%
10.52	9.201	1.12%	0.86%
11.58	8.782	0.97%	0.73%
12.63	7.249	0.63%	0.48%
13.67	5.844	0.37%	0.29%
14.72	5.179	0.28%	0.22%
15.75	4.615	0.18%	0.16%

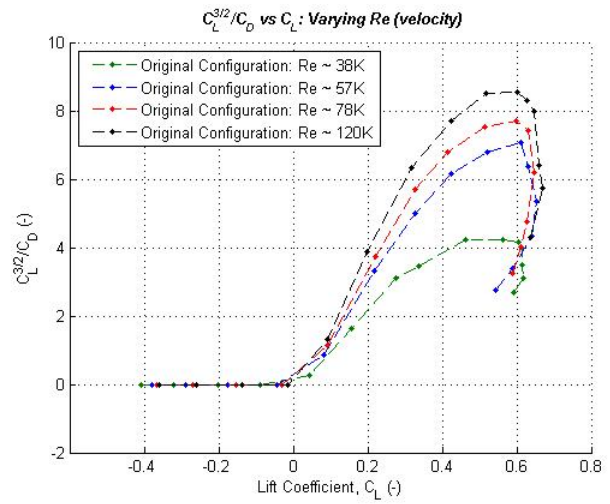
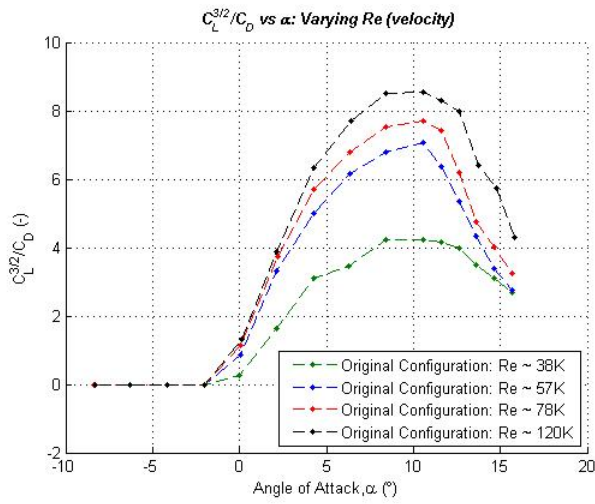
Re = 120K (60 MPH)			
α (°)	L/D (-)	Error in % L/D	
		Worst	Realistic
-8.36	-5.042	0.18%	0.15%
-6.24	-6.322	0.38%	0.32%
-4.12	-5.031	0.59%	0.42%
-2.01	-0.928	0.50%	0.45%
0.11	4.241	0.85%	0.60%
2.14	8.770	0.94%	0.71%
4.27	11.204	0.76%	0.69%
6.29	11.676	0.64%	0.58%
8.41	11.308	0.61%	0.49%
10.52	10.403	0.52%	0.39%
11.58	9.889	0.47%	0.35%
12.63	9.358	0.42%	0.31%
13.68	8.682	0.26%	0.19%
14.73	6.640	0.21%	0.15%
15.77	5.206	0.12%	0.09%

For a Reynolds number of approximately 38K, the worst case error ranges from 0.77% to 7.68% of L/D and the realistic case ranges from 0.74% to 5.62% of L/D. The possible error at L/D_{\max} is 4.23% for the worst case scenario and 3.36% for the realistic

case scenario. For a Reynolds number of approximately 57K, the worst case error ranges from 0.27% to 3.33% of L/D and the realistic case ranges from 0.26% to 2.45% of L/D. The possible error at L/D_{\max} is 1.96% for the worst case scenario and 1.96% for the realistic case scenario. For a Reynolds number of approximately 78K, the worst case error ranges from 0.18% to 1.98% of L/D and the realistic case ranges from 0.16% to 1.49% of L/D. The possible error at L/D_{\max} is 1.30% for the worst case scenario and 1.24% for the realistic case scenario. For a Reynolds number of approximately 120K, the worst case error ranges from 0.12% to 0.94% of L/D and the realistic case ranges from 0.09% to 0.71% of L/D. The possible error at L/D_{\max} is 0.64% for the worst case scenario and 0.58% for the realistic case scenario. As compared to the conservative error percentages, the tested error percentages are much smaller and thus reflect the actual precision of the 10lb balance for measurement.

4.2.1.7 Max Endurance

Figure 77 shows the ratio of $C_L^{3/2}/C_D$ plotted for the Original Configuration Model at four different Reynolds numbers (38K, 57K, 78K, and 120K). The $C_L^{3/2}/C_D$ has been plotted against α and C_L . $C_L^{3/2}/C_D$ is another measure of aircraft efficiency, more specifically the aircraft's maximum endurance. If an aircraft is flying at an α that corresponds to the maximum $C_L^{3/2}/C_D$, then it is maximizing its time in flight with a set amount of fuel (endurance).



(a) (b)
Figure 77: $C_L^{3/2}/C_D$ – Max Endurance – Original Configuration Model
 (a) $C_L^{3/2}/C_D$ vs. Alpha, (b) $C_L^{3/2}/C_D$ vs. Lift Coefficient

Similar to L/D , there is a strong correlation between an increase in Reynolds number and an increase in $C_L^{3/2}/C_D$ values. $C_L^{3/2}/C_D$ values increase for each Reynolds number case during the range $\alpha \approx -2^\circ$ to 10.5° . Once $C_L^{3/2}/C_{Dmax}$ is reached for each Reynolds number, the $C_L^{3/2}/C_D$ values start to decrease. This occurs beyond $\alpha \approx 11^\circ$ and $CL \approx 0.6$.

4.2.2 + 5° Cant Configuration Model

4.2.2.1 Summary

In the AFIT low-speed wind tunnel, an α sweep from -8° to 10° in steps of 2° and then from 10° to 15° in steps of 1° was performed on the + 5° Configuration Model at four different speeds: 20 mph (8.94 m/s), 30 mph (13.41 m/s), 40 mph (17.88 m/s), and 60 mph (26.82 m/s). A summary of the resulting aerodynamic performance of the + 5° Configuration Model at $Re \approx 38,000$ (20 mph), $Re \approx 57,000$ (30 mph), $Re \approx 78,000$ (40 mph), and $Re \approx 120,000$ (60 mph) can be seen in Table 12. The Reynolds numbers are based on the average root chord of the upper and lower wings ($\bar{c} = 2.55''$).

Table 12: Aerodynamic Performance of the + 5° Cant Configuration Model

Model	Re (-)	Min Drag		Zero Lift	Slopes	
		C_{D0} (-)	α (°)	$\alpha_{0 \text{ Lift}}$ (°)	$C_{L\alpha}$ (/°)	$C_{m\alpha}$ (/°)
+ 5° Configuration	38K	0.0278	-2.02	-0.99	0.0539	0.0107
+ 5° Configuration	57K	0.0277	-2.01	-1.60	0.0562	0.0098
+ 5° Configuration	78K	0.0250	-2.00	-1.78	0.0536	0.0103
+ 5° Configuration	120K	0.0218	0.13	-1.92	0.053	0.0113

Model	Re (-)	Max Range				Max Endurance			
		L/D (-)	α (°)	C_L (-)	C_D (-)	$C_L^{(3/2)}/C_D$ (-)	α (°)	C_L (-)	C_D (-)
+ 5° Configuration	38K	6.3652	8.44	0.5007	0.0787	4.5040	8.44	0.5007	0.0787
+ 5° Configuration	57K	9.3534	6.34	0.4503	0.0481	6.9491	10.58	0.6395	0.0736
+ 5° Configuration	78K	10.3334	6.33	0.4284	0.0415	7.3994	10.56	0.5971	0.0624
+ 5° Configuration	120K	11.7204	6.33	0.4387	0.0374	8.3031	8.45	0.5277	0.0462

4.2.2.2 Drag Coefficient

The drag coefficient, C_D , for the + 5° Cant Configuration Model is shown in Figure 78 for four different Reynolds numbers (38K, 57K, 78K, and 120K). C_D has been plotted both versus C_L and α .

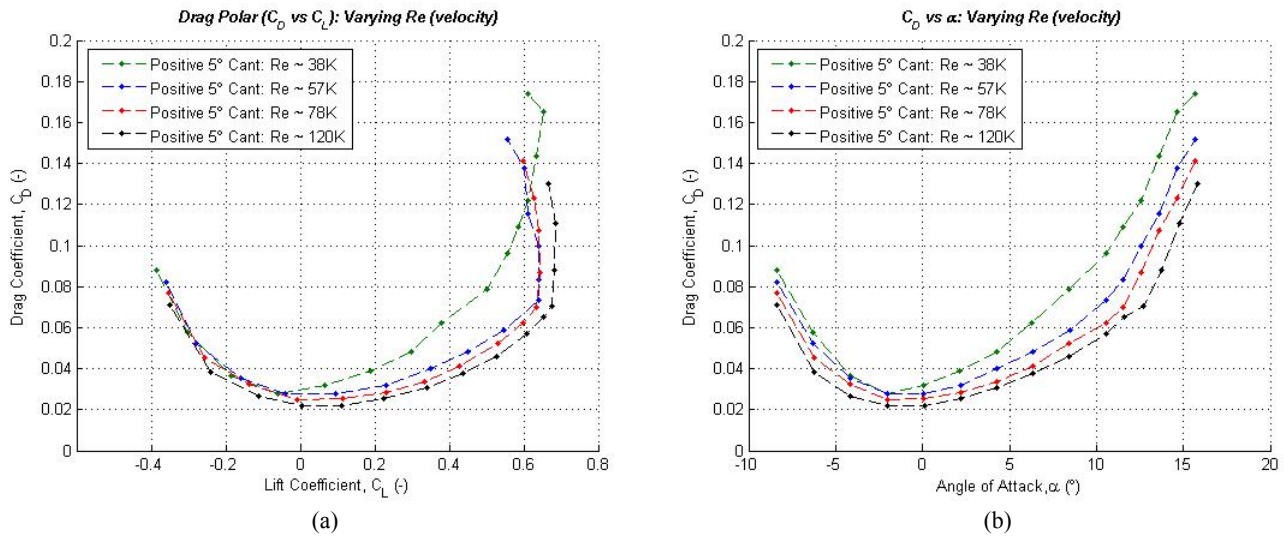


Figure 78: Drag Coefficient – + 5° Cant Configuration Model
 (a) Drag Coefficient vs. Lift Coefficient (Drag Polar), (b) Drag Coefficient vs. Alpha

4.2.2.3 Lift Coefficient

Figure 79 plots the lift coefficient, C_L , vs. α for the + 5° Cant Configuration Model at four different Reynolds numbers (38K, 57K, 78K, and 120K). As seen in Figure 79, the - 5° Cant Configuration Model exhibits the gradual stall characteristic of most aircraft past an $\alpha = 11^\circ$. $C_{L\alpha}$ is the lift curve slope, and gives a ratio of change of C_L with respect to α for the linear region (α from -8° to $+8^\circ$) of the lift curve, while $\alpha_{0\text{Lift}}$ is the angle of attack where the aircraft produces zero lift.

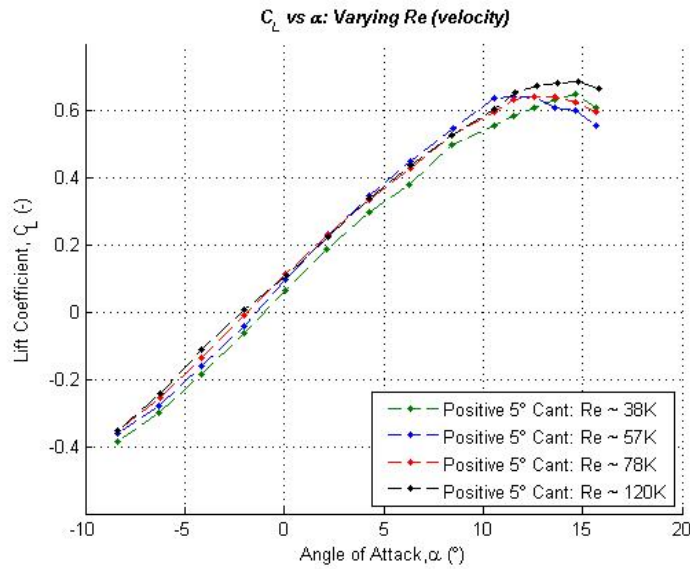


Figure 79: Lift Coefficient vs. Angle of Attack – + 5° Cant Configuration Model

4.2.2.4 Pitching Moment Coefficient

Figure 80 plots the pitching moment coefficient, C_m , vs. α for the + 5° Cant Configuration Model at four different Reynolds numbers (38K, 57K, 78K, and 120K). The longitudinal static stability derivative, $C_{m\alpha}$, can be attained from the linear portion of this plot (α from - 8° to + 8°). The + 5° Cant Configuration Model is longitudinally unstable, due to a positive $C_{m\alpha}$ value, about the reference CG (2.1625” aft of nose), for all four Reynolds numbers tested.

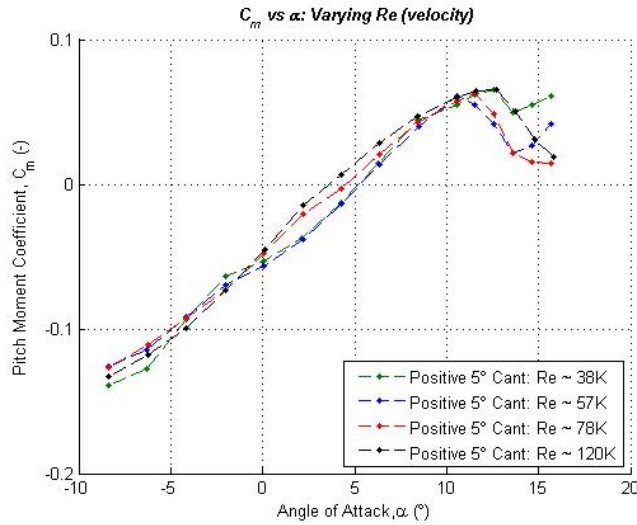
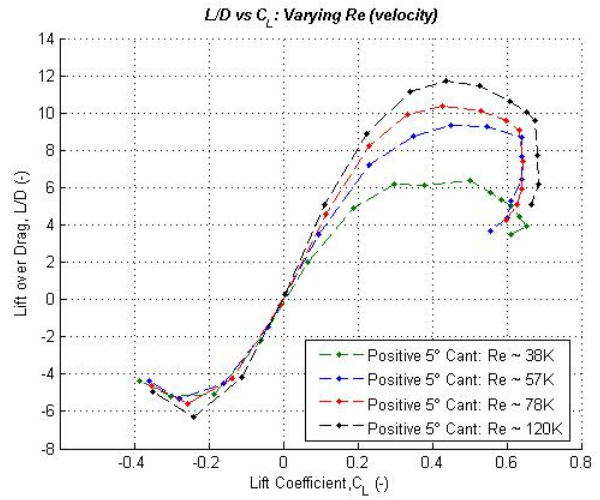
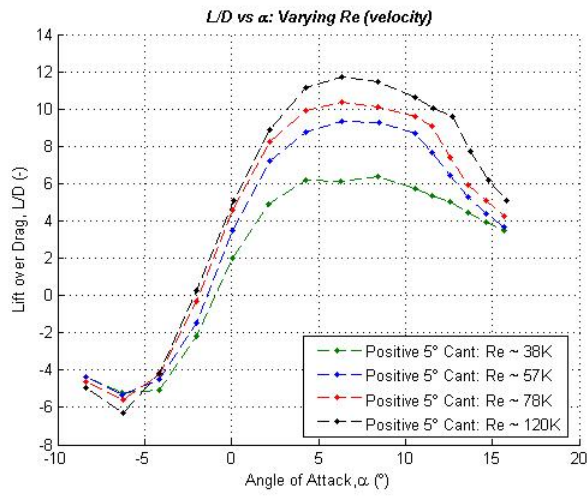


Figure 80: Pitch Moment Coefficient vs. Angle of Attack – + 5° Cant Configuration Model ($X_{cmb} = 1.0025''$)

4.2.2.5 Lift-to-Drag Ratio

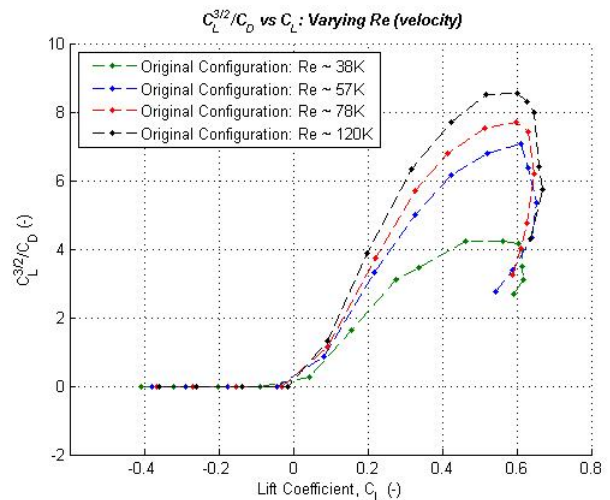
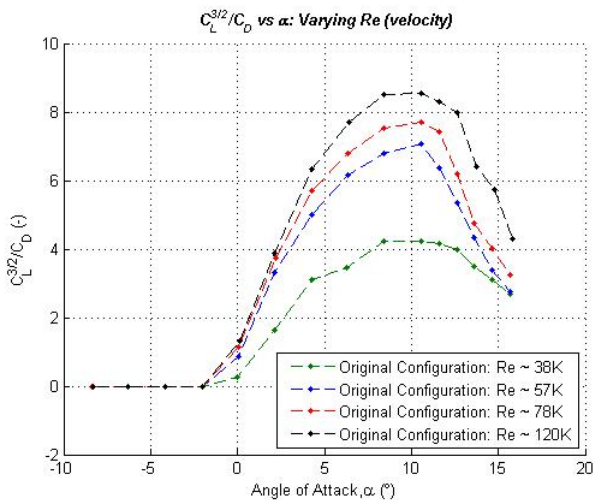
Figure 81 shows the lift-to-drag ratio for the + 5° Cant Configuration Model at four different Reynolds numbers (38K, 57K, 78K, and 120K). L/D has been plotted versus α and C_L . Lift-to-drag is one measure of aircraft efficiency. The efficiency of the + 5° Cant Configuration Model increases as the Reynolds number increases. L/D values for each Reynolds number increase over the range $\alpha \approx -4^\circ$ to 6° . Once L/D_{max} is reached for each Reynolds number, the L/D values start to decrease. This event occurs beyond $\alpha \approx 6^\circ$ and $C_L \approx 0.41$.



(a) (b)
Figure 81: Lift-to-Drag – + 5° Cant Configuration Model
 (a) Lift-to-Drag vs. Alpha, (b) Lift-to-Drag vs. Lift Coefficient

4.2.2.6 Max Endurance

Figure 82 shows the ratio of $C_L^{3/2}/C_D$ plotted for the + 5° Cant Configuration Model at four different Reynolds numbers (38K, 57K, 78K, and 120K). The $C_L^{3/2}/C_D$ has been plotted against α and C_L .



(a) (b)
Figure 82: $C_L^{3/2}/C_D$ – Max Endurance – + 5° Cant Configuration Model
 (a) $C_L^{3/2}/C_D$ vs. Alpha, (b) $C_L^{3/2}/C_D$ vs. Lift Coefficient

4.2.3 - 5° Cant Configuration Model

4.2.3.1 Summary

In the AFIT low-speed wind tunnel, an α sweep from -8° to 10° in steps of 2° and then from 10° to 15° in steps of 1° was performed on the -5° Configuration Model at four different speeds: 20 mph (8.94 m/s), 30 mph (13.41 m/s), 40 mph (17.88 m/s), and 60 mph (26.82 m/s). A summary of the resulting aerodynamic performance of the -5° Configuration Model at $Re \approx 38,000$ (20 mph), $Re \approx 57,000$ (30 mph), $Re \approx 78,000$ (40 mph), and $Re \approx 120,000$ (60 mph) can be seen in Table 13. The Reynolds numbers are based on the average root chord of the upper and lower wings ($\bar{c} = 2.55''$).

Table 13: Aerodynamic Performance of the -5° Cant Configuration Model

Model	Re (-)	Min Drag		Zero Lift	Slopes	
		C_{D0} (-)	α ($^\circ$)	$\alpha_{0 \text{ Lift}}$ ($^\circ$)	$C_{L\alpha}$ ($^\circ$)	$C_{m\alpha}$ ($^\circ$)
- 5° Configuration	38K	0.0324	0.00	-0.07	0.0529	0.0102
- 5° Configuration	57K	0.0273	0.01	-0.57	0.0569	0.0101
- 5° Configuration	78K	0.0241	0.10	-0.65	0.0541	0.0105
- 5° Configuration	120K	0.0201	0.11	-0.88	0.0536	0.0112

Model	Re (-)	Max Range				Max Endurance			
		L/D (-)	α ($^\circ$)	C_L (-)	C_D (-)	$C_L^{(3/2)}/C_D$ (-)	α ($^\circ$)	C_L (-)	C_D (-)
- 5° Configuration	38K	6.7311	8.42	0.4335	0.0644	4.5486	10.46	0.5422	0.0878
- 5° Configuration	57K	9.3586	8.44	0.5054	0.0540	6.6534	8.44	0.5054	0.0540
- 5° Configuration	78K	10.4259	8.43	0.4643	0.0445	7.2532	10.55	0.5486	0.0560
- 5° Configuration	120K	11.9833	6.40	0.3945	0.0329	8.3134	8.43	0.4842	0.0405

4.2.3.2 Drag Coefficient

The drag coefficient, C_D , for the -5° Cant Configuration Model is shown in Figure 83 for four different Reynolds numbers (38K, 57K, 78K, and 120K). C_D has been plotted both versus C_L and α .

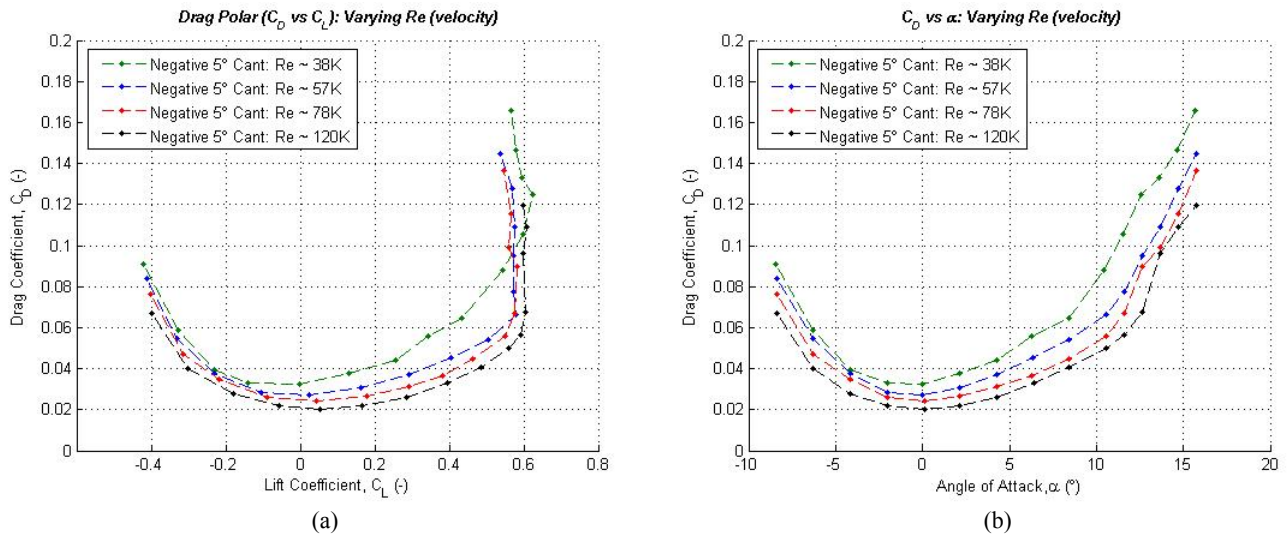


Figure 83: Drag Coefficient -- 5° Cant Configuration Model
 (a) Drag Coefficient vs. Lift Coefficient (Drag Polar), (b) Drag Coefficient vs. Alpha

4.2.3.3 Lift Coefficient

Figure 84 plots the lift coefficient, C_L , vs. α for the -5° Cant Configuration Model at four different Reynolds numbers (38K, 57K, 78K, and 120K). As seen in Figure 84, the -5° Cant Configuration Model exhibits the gradual stall characteristic of most aircraft past an $\alpha = 12^\circ$.

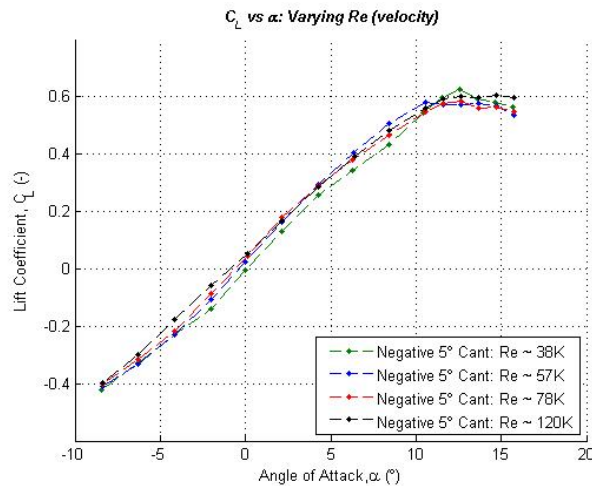


Figure 84: Lift Coefficient vs. Angle of Attack -- 5° Cant Configuration Model

4.2.3.4 Pitching Moment Coefficient

Figure 85 plots the pitching moment coefficient, C_m , vs. α for the - 5° Cant Configuration Model at four different Reynolds numbers (38K, 57K, 78K, and 120K). The - 5° Cant Configuration Model is longitudinally unstable, due to a positive $C_{m\alpha}$ value, about the reference CG (2.1625" aft of nose), for all four Reynolds numbers tested.

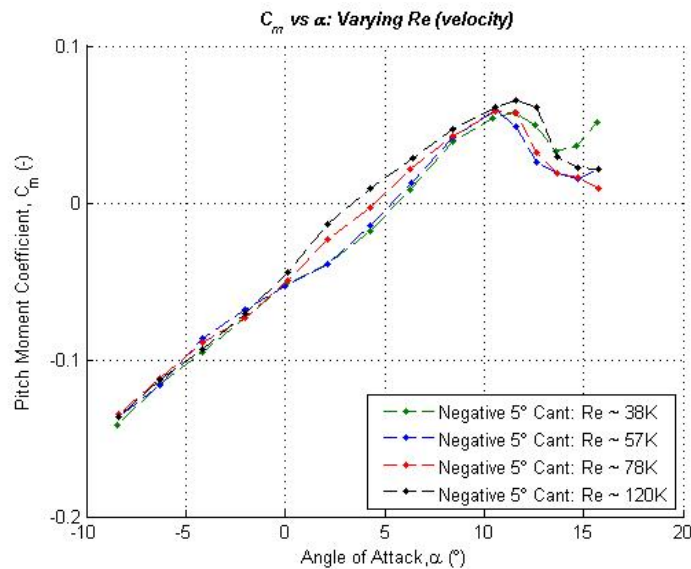
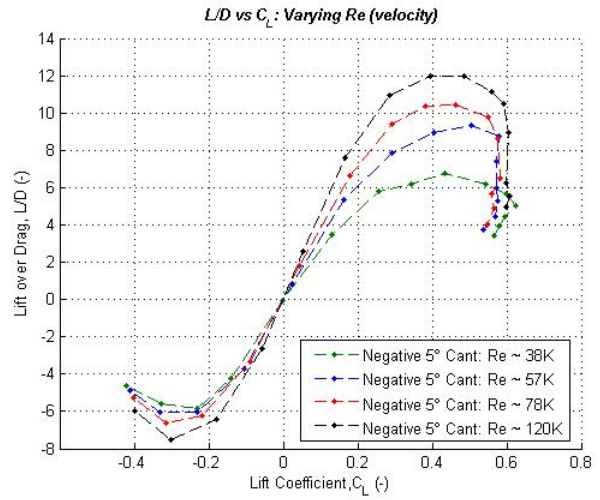
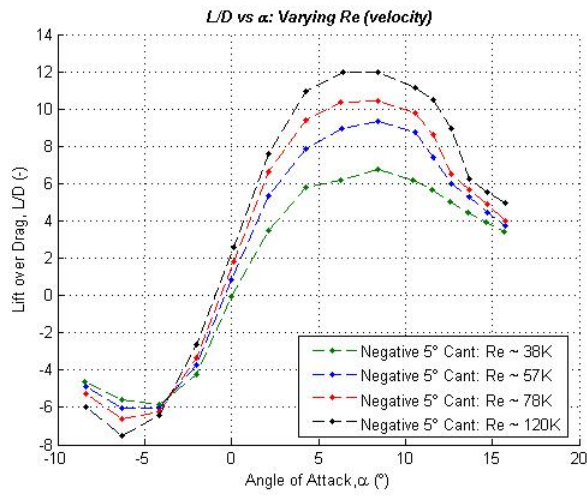


Figure 85: Pitch Moment Coefficient vs. Angle of Attack – - 5° Cant Configuration Model ($X_{cmb} = 1.0025''$)

4.2.3.5 Lift-to-Drag Ratio

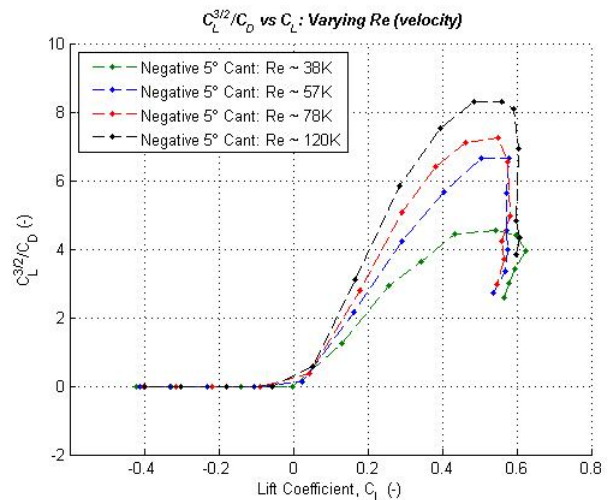
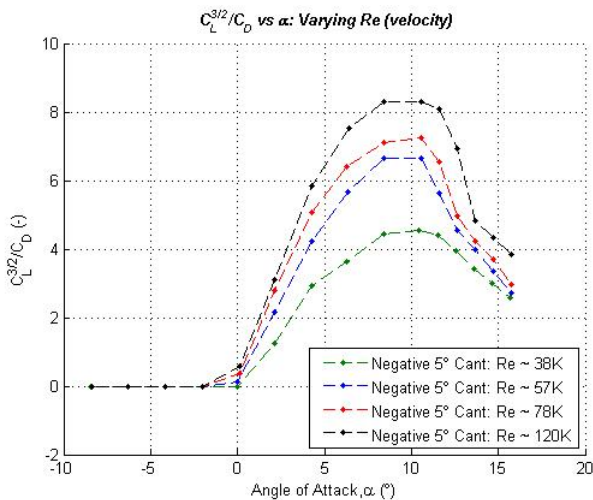
Figure 86 shows the lift-to-drag ratio for the - 5° Cant Configuration Model at four different Reynolds numbers (38K, 57K, 78K, and 120K). L/D has been plotted versus α and C_L . As the Reynolds number increases, the efficiency of the - 5° Cant Configuration Model increases as well. L/D values for each Reynolds number increase over the range $\alpha \approx -4^\circ$ to 7° . Once L/D_{max} is reached for each Reynolds number, the L/D values start to decrease. This event occurs beyond $\alpha \approx 7^\circ$ and $C_L \approx 0.43$.



(a) (b)
Figure 86: Lift-to-Drag -- 5° Cant Configuration Model
 (a) Lift-to-Drag vs. Alpha, (b) Lift-to-Drag vs. Lift Coefficient

4.2.3.6 Max Endurance

Figure 87 shows the ratio of $C_L^{3/2}/C_D$ plotted for the - 5° Cant Configuration Model at four different Reynolds numbers (38K, 57K, 78K, and 120K). The $C_L^{3/2}/C_D$ has been plotted against α and C_L .



(a) (b)
Figure 87: $C_L^{3/2}/C_D$ – Max Endurance -- 5° Cant Configuration Model
 (a) $C_L^{3/2}/C_D$ vs. Alpha, (b) $C_L^{3/2}/C_D$ vs. Lift Coefficient

4.2.4 Endplate Configuration Model

4.2.4.1 Summary

In the AFIT low-speed wind tunnel, an α sweep from -8° to 10° in steps of 2° and then from 10° to 15° in steps of 1° was performed on the Endplate Configuration Model at four different speeds: 20 mph (8.94 m/s), 30 mph (13.41 m/s), 40 mph (17.88 m/s), and 60 mph (26.82 m/s). A summary of the resulting aerodynamic performance of the Endplate Configuration Model at $Re \approx 38,000$ (20 mph), $Re \approx 57,000$ (30 mph), $Re \approx 78,000$ (40 mph), and $Re \approx 120,000$ (60 mph) can be seen in Table 14. The Reynolds numbers are based on the average root chord of the upper and lower wings ($\bar{c} = 2.55''$).

Table 14: Aerodynamic Performance of the – Endplate Configuration Model

Model	Re (-)	Min Drag		Zero Lift	Slopes	
		C_{D0} (-)	α ($^\circ$)	$\alpha_{0 \text{ Lift}}$ ($^\circ$)	$C_{L\alpha}$ ($^\circ$)	$C_{m\alpha}$ ($^\circ$)
Endplate Configuration	38K	0.0344	0.10	-0.72	0.0578	0.0114
Endplate Configuration	57K	0.0296	0.11	-1.25	0.0575	0.0106
Endplate Configuration	78K	0.0278	0.11	-1.37	0.0559	0.0112
Endplate Configuration	120K	0.0251	0.11	-1.40	0.0546	0.0125

Model	Re (-)	Max Range				Max Endurance			
		L/D (-)	α ($^\circ$)	C_L (-)	C_D (-)	$C_L^{(3/2)}/C_D$ (-)	α ($^\circ$)	C_L (-)	C_D (-)
Endplate Configuration	38K	6.3733	6.38	0.4194	0.0658	4.6633	10.53	0.6246	0.1059
Endplate Configuration	57K	8.6825	6.39	0.4453	0.0513	6.4561	10.52	0.6051	0.0729
Endplate Configuration	78K	9.2024	8.41	0.5198	0.0565	6.9288	10.52	0.6064	0.0682
Endplate Configuration	120K	10.3918	8.41	0.5281	0.0508	7.6841	10.53	0.6157	0.0629

4.2.4.2 Drag Coefficient

The drag coefficient, C_D , for the Endplate Configuration Model is shown in Figure 88 for four different Reynolds numbers (38K, 57K, 78K, and 120K). C_D has been plotted both versus C_L and α .

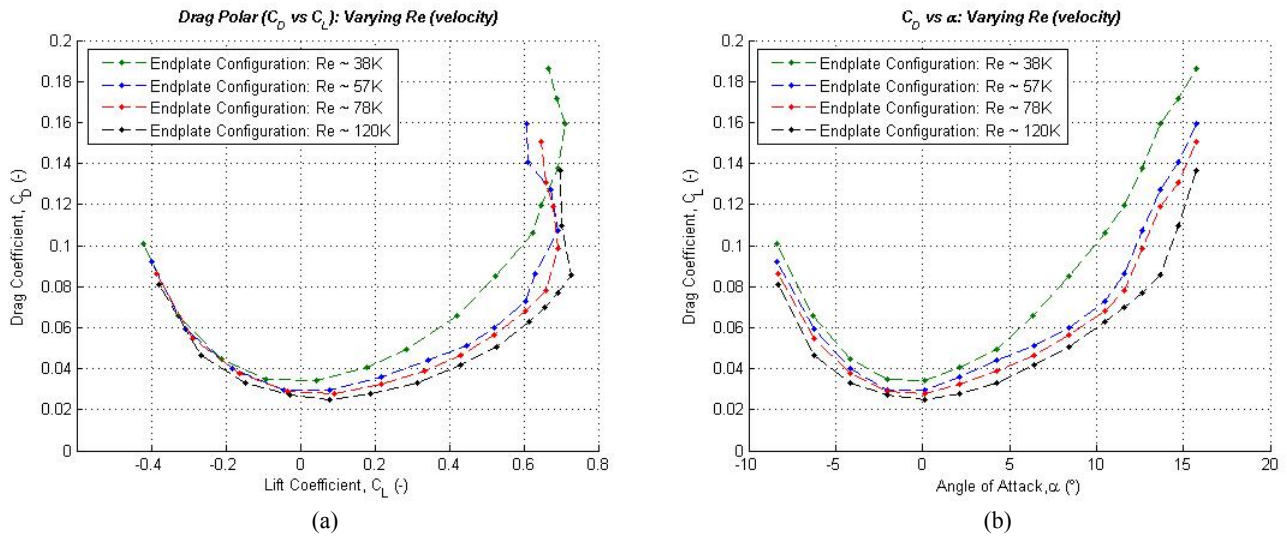


Figure 88: Drag Coefficient – Endplate Configuration Model
 (a) Drag Coefficient vs. Lift Coefficient (Drag Polar), (b) Drag Coefficient vs. Alpha

4.2.4.3 Lift Coefficient

Figure 89 plots the lift coefficient, C_L , vs. α for the Endplate Configuration Model at four different Reynolds numbers (38K, 57K, 78K, and 120K). As seen in Figure 89, the Endplate Configuration Model exhibits the gradual stall characteristic of most aircraft past an $\alpha = 13^\circ$.

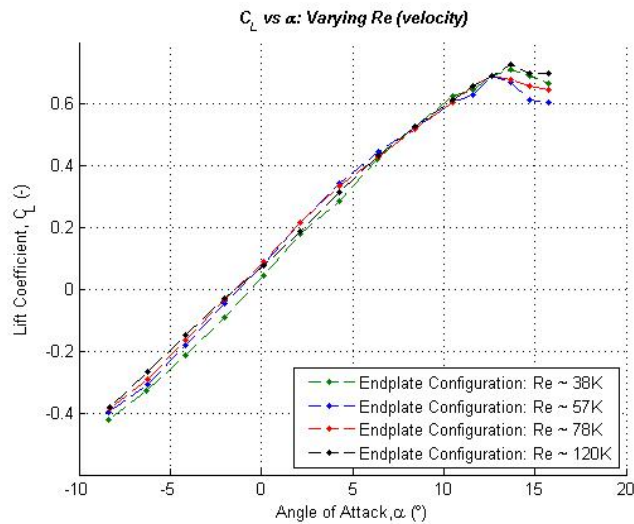


Figure 89: Lift Coefficient vs. Angle of Attack – Endplate Configuration Model

4.2.4.4 Pitching Moment Coefficient

Figure 90 plots the pitching moment coefficient, C_m , vs. α for the Endplate Configuration Model at four different Reynolds numbers (38K, 57K, 78K, and 120K). The longitudinal static stability derivative, $C_{m\alpha}$, can be attained from the linear portion of this plot (α from -8° to $+8^\circ$). The Endplate Configuration Model is longitudinally unstable for all four Reynolds numbers tested.

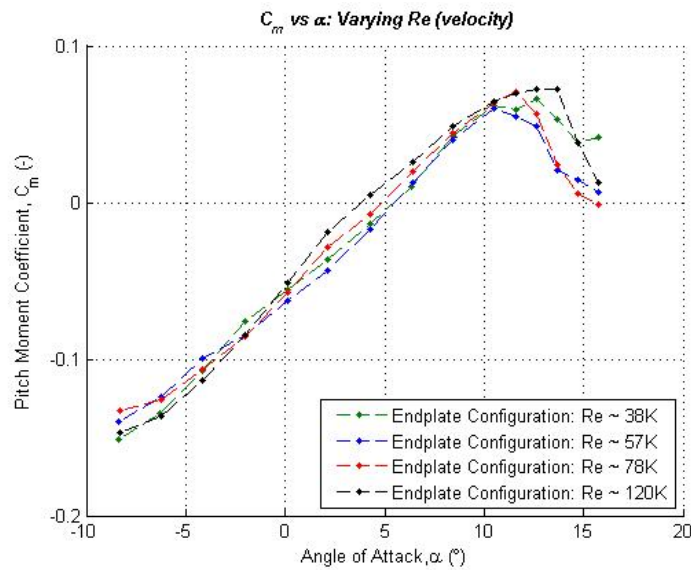
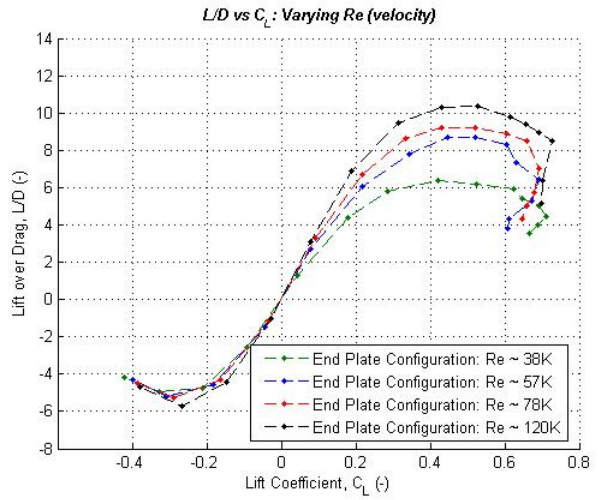
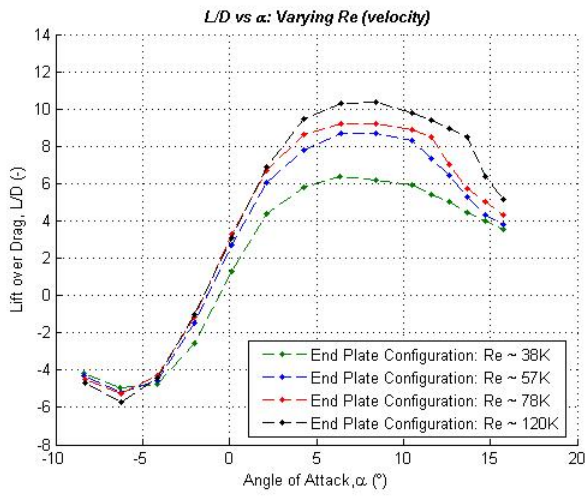


Figure 90: Pitch Moment Coefficient vs. Angle of Attack – Endplate Configuration Model ($X_{cmb} = 1.0025''$)

4.2.4.5 Lift-to-Drag Ratio

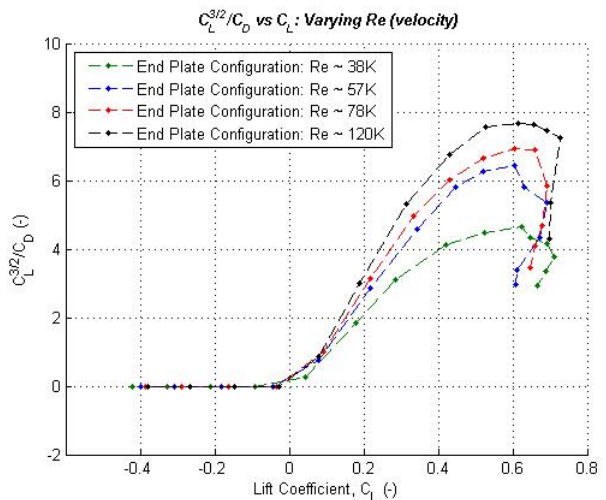
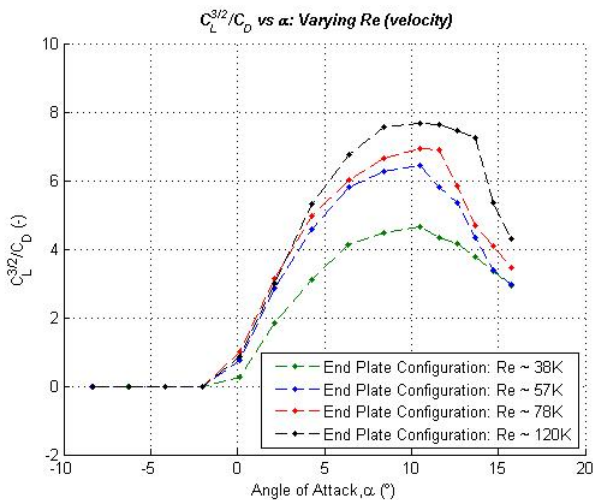
Figure 91 shows the lift-to-drag ratio for the Endplate Configuration Model at four different Reynolds numbers (38K, 57K, 78K, and 120K). L/D has been plotted versus α and C_L .



(a) (b)
Figure 91: Lift-to-Drag – Endplate Configuration Model
 (a) Lift-to-Drag vs. Alpha, (b) Lift-to-Drag vs. Lift Coefficient

4.2.4.6 Max Endurance

Figure 92 shows the ratio of $C_L^{3/2}/C_D$ plotted for the Endplate Configuration Model at four different Reynolds numbers (38K, 57K, 78K, and 120K). The $C_L^{3/2}/C_D$ has been plotted against α and C_L .



(a) (b)
Figure 92: $C_L^{3/2}/C_D$ – Max Endurance – Endplate Configuration Model
 (a) $C_L^{3/2}/C_D$ vs. Alpha, (b) $C_L^{3/2}/C_D$ vs. Lift Coefficient

4.2.5 No Flow Guide Configuration Model

4.2.5.1 Summary

In the AFIT low-speed wind tunnel, an α sweep from -8° to 10° in steps of 2° and then from 10° to 15° in steps of 1° was performed on the No Flow Guide Configuration Model at four different speeds: 20 mph (8.94 m/s), 30 mph (13.41 m/s), 40 mph (17.88 m/s), and 60 mph (26.82 m/s). A summary of the resulting aerodynamic performance of the No Flow Guide Configuration Model at $Re \approx 38,000$ (20 mph), $Re \approx 57,000$ (30 mph), $Re \approx 78,000$ (40 mph), and $Re \approx 120,000$ (60 mph) can be seen in Table 15. The Reynolds numbers are based on the average root chord of the upper and lower wings ($\bar{c} = 2.55''$).

Table 15: Aerodynamic Performance of the – No Flow Guide Configuration Model

Model	Re (-)	Min Drag		Zero Lift	Slopes	
		C_{D0} (-)	α ($^\circ$)	α_{0Lift} ($^\circ$)	$C_{L\alpha}$ ($1/^\circ$)	$C_{m\alpha}$ ($1/^\circ$)
No Flow Guide Configuration	38K	0.0260	0.10	-0.63	0.0576	0.0111
No Flow Guide Configuration	57K	0.0268	0.11	-1.09	0.0565	0.0100
No Flow Guide Configuration	78K	0.0233	0.11	-1.31	0.0539	0.0104
No Flow Guide Configuration	120K	0.0195	0.11	-1.58	0.0523	0.0115

Model	Re (-)	Max Range				Max Endurance			
		L/D (-)	α ($^\circ$)	C_L (-)	C_D (-)	$C_L^{(3/2)}/C_D$ (-)	α ($^\circ$)	C_L (-)	C_D (-)
No Flow Guide Configuration	38K	6.9259	6.29	0.4085	0.0590	4.5238	10.52	0.5960	0.1017
No Flow Guide Configuration	57K	9.0696	6.30	0.4248	0.0468	6.3719	10.52	0.5981	0.0726
No Flow Guide Configuration	78K	9.9634	6.29	0.4052	0.0407	7.1055	10.52	0.5962	0.0648
No Flow Guide Configuration	120K	11.6871	6.29	0.4145	0.0355	8.1126	10.52	0.6086	0.0585

4.2.5.2 Drag Coefficient

The drag coefficient, C_D , for the No Flow Guide Configuration Model is shown in Figure 93 for four different Reynolds numbers (38K, 57K, 78K, and 120K). C_D has been plotted both versus C_L and α .

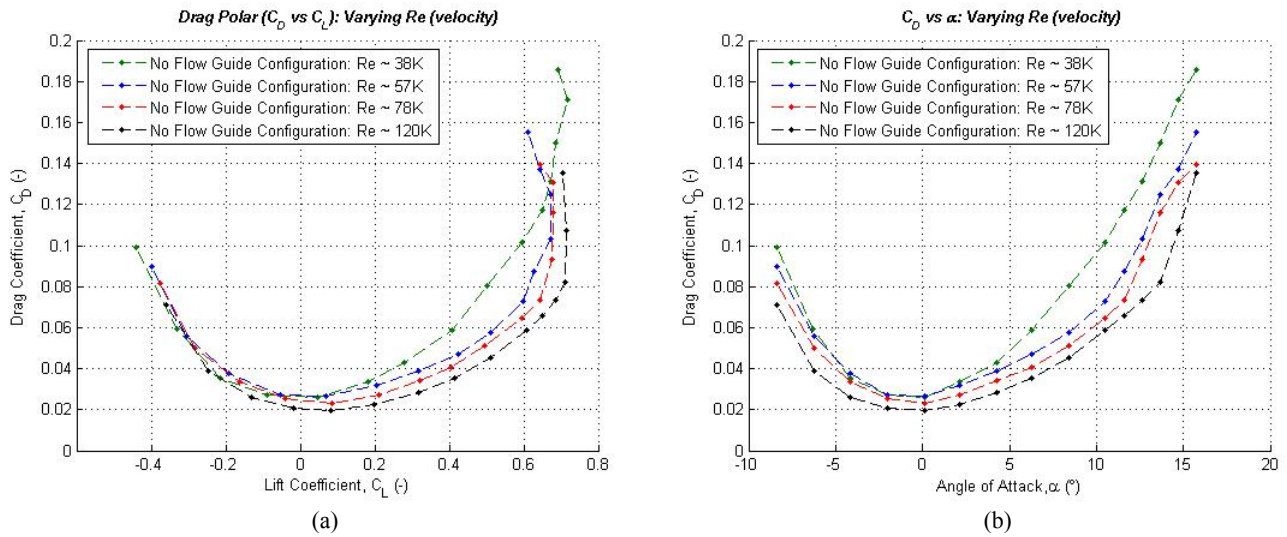


Figure 93: Drag Coefficient – No Flow Guide Configuration Model
 (a) Drag Coefficient vs. Lift Coefficient (Drag Polar), (b) Drag Coefficient vs. Alpha

4.2.5.3 Lift Coefficient

Figure 94 plots the lift coefficient, C_L , vs. α for the No Flow Guide Configuration Model at four different Reynolds numbers (38K, 57K, 78K, and 120K). As seen in Figure 94, the No Flow Guide Configuration Model exhibits the gradual stall characteristic of most aircraft past an $\alpha = 13^\circ$.

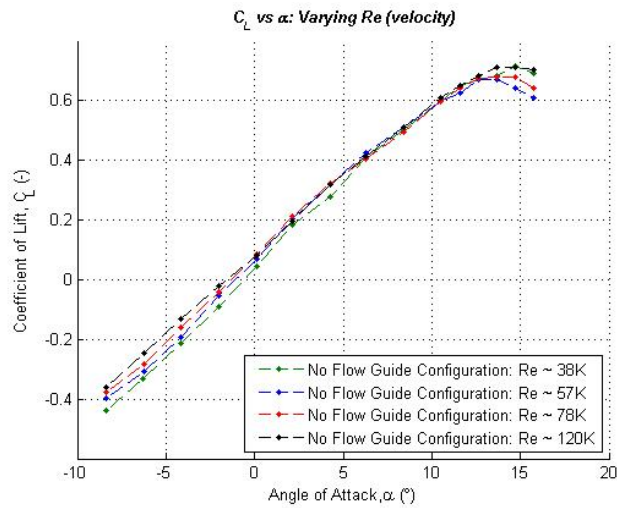


Figure 94: Lift Coefficient vs. Angle of Attack – No Flow Guide Configuration Model

4.2.5.4 Pitching Moment Coefficient

Figure 95 plots the pitching moment coefficient, C_m , vs. α for the No Flow Guide Configuration Model at four different Reynolds numbers (38K, 57K, 78K, and 120K). The Endplate Configuration Model is longitudinally unstable, due to a positive $C_{m\alpha}$ value, about the reference CG (2.1625" aft of nose), for all four Reynolds numbers tested.

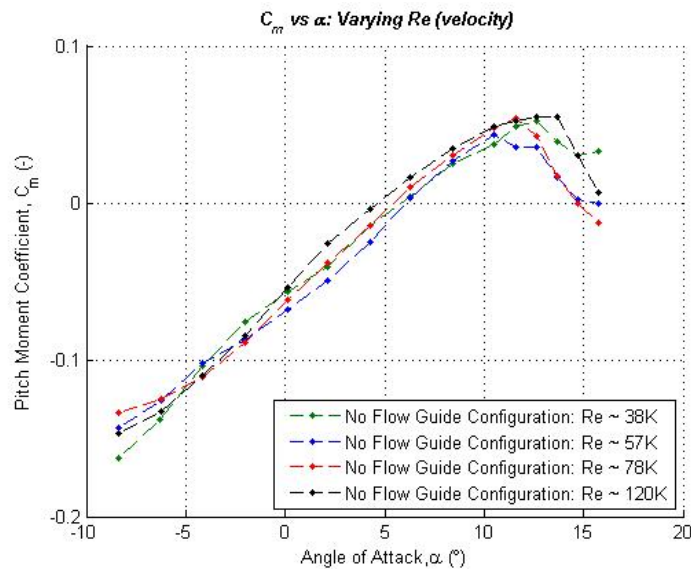
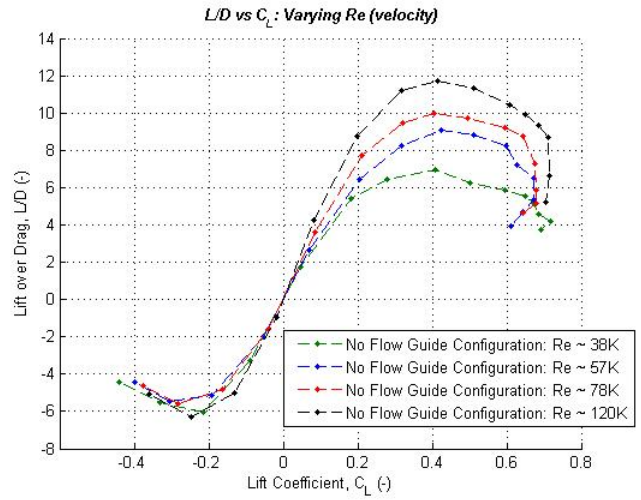
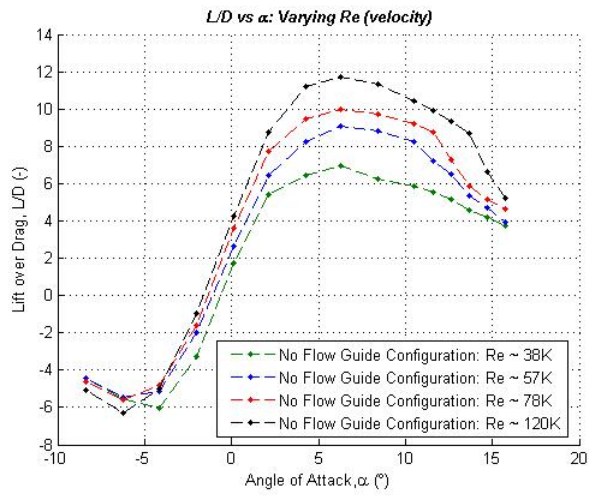


Figure 95: Pitch Moment Coefficient vs. Angle of Attack – No Flow Guide Configuration Model ($X_{cmb} = 1.0025''$)

4.2.5.5 Lift-to-Drag Ratio

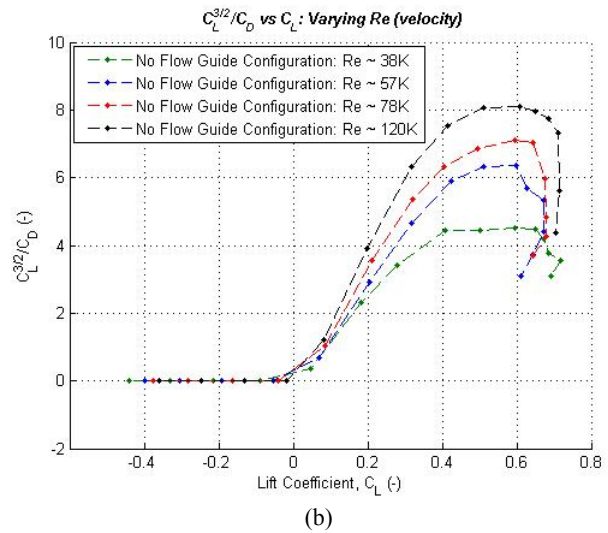
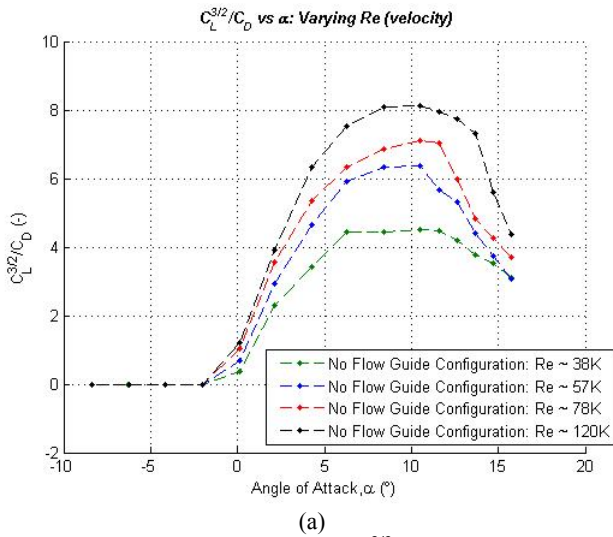
Figure 96 shows the lift-to-drag ratio for the No Flow Guide Configuration Model at four different Reynolds numbers (38K, 57K, 78K, and 120K). L/D has been plotted versus α and C_L .



(a) (b)
Figure 96: Lift-to-Drag – No Flow Guide Configuration Model
 (a) Lift-to-Drag vs. Alpha, (b) Lift-to-Drag vs. Lift Coefficient

4.2.5.6 Max Endurance

Figure 97 shows the ratio of $C_L^{3/2}/C_D$ plotted for the No Flow Guide Configuration Model at four different Reynolds numbers (38K, 57K, 78K, and 120K).



(a) (b)
Figure 97: $C_L^{3/2}/C_D$ – Max Endurance – No Flow Guide Configuration Model
 (a) $C_L^{3/2}/C_D$ vs. Alpha, (b) $C_L^{3/2}/C_D$ vs. Lift Coefficient

4.3 Wind Tunnel Data – Alpha Sweeps: Model Comparisons by Speed

4.3.1 $Re \approx 38K$ / 20 MPH

4.3.1.1 Summary

The data results of the five model configurations, which were presented in Section 4.2 at a Reynolds number of 38K (20 mph or 8.94 m/s), are compared to gauge the differences in aerodynamic performance of the models. The models that were included in the test were: the Original Configuration Model, the + 5° Cant Configuration Model, the – 5° Cant Configuration Model, the Endplate Configuration Model, and the No Flow Guide Configuration Model. The No Flow Guide Configuration Model served as the reference to base all the performance parameters.

A summary of aerodynamic performance comparisons between the five model configurations can be seen in Table 15. A discussion of the performance factors: drag, maximum range, maximum endurance, and effective aspect ratio will be discussed in this section with corresponding figures.

Table 16: Summary of the Aerodynamic Performance Comparison of the Five Models – Re ~ 38K

Model Configuration	Re (-)	S (in ²)	b (in)	Minimum Drag			Zero Lift	Slopes	
				C _{D0} (-)	α (°)	D (lb)	α _{0 Lift} (°)	C _{Lα} (1/°)	C _{mα} (1/°)
Original	38K	72.58	13.81	0.0327	-2.03	0.015	-0.52	0.053	0.011
+5° Cant	38K	72.56	13.81	0.0278	-2.02	0.014	-0.99	0.054	0.011
-5° Cant	38K	72.56	13.81	0.0324	0.00	0.016	-0.07	0.053	0.010
Endplate	38K	58.33	11.50	0.0344	0.10	0.012	-0.72	0.058	0.011
No Flow Guide	38K	58.02	11.38	0.0260	0.10	0.009	-0.63	0.058	0.011

Model Configuration	Re (-)	S (in ²)	b (in)	Maximum Range					
				L/D _{max} (-)	α (°)	C _L (-)	C _D (-)	L (lb)	D (lb)
Original	38K	72.58	13.81	6.2241	8.43	0.4631	0.0744	0.217	0.035
+5° Cant	38K	72.56	13.81	6.3652	8.44	0.5007	0.0787	0.233	0.037
-5° Cant	38K	72.56	13.81	6.7311	8.42	0.4335	0.0644	0.213	0.032
Endplate	38K	58.33	11.50	6.3733	6.38	0.4194	0.0658	0.153	0.024
No Flow Guide	38K	58.02	11.38	6.9259	6.29	0.4085	0.0590	0.146	0.021

Model Configuration	Re (-)	S (in ²)	b (in)	Maximum Endurance					
				C _L ^(3/2) /C _{Dmax} (-)	α (°)	C _L (-)	C _D (-)	L (lb)	D (lb)
Original	38K	72.58	13.81	4.2385	10.55	0.5625	0.0995	0.248	0.044
+5° Cant	38K	72.56	13.81	4.5040	8.44	0.5007	0.0787	0.233	0.037
-5° Cant	38K	72.56	13.81	4.5486	10.46	0.5422	0.0878	0.249	0.040
Endplate	38K	58.33	11.50	4.6633	10.53	0.6246	0.1059	0.225	0.038
No Flow Guide	38K	58.02	11.38	4.5238	10.52	0.5960	0.1017	0.213	0.036

4.3.1.2 Drag

Figure 98 plots the drag polar, C_D vs. C_L, for the five model configurations at a Reynolds number of 38K. The No Flow Guide Configuration has the lowest value of C_{D0} of all the five configurations. Table 17 compares the induced and parasite drag between all the model configurations. It is interesting to note at a Reynolds number of 38K the Endplate configuration had the least amount of induced drag percentage of the total drag. The – 5° Cant Configuration had the highest lift-to-induced drag of all the models whereas the +5° Cant Configuration had the lowest lift-to-induced drag. This phenomenon is probably due to the effective angle of attack of the flow guide which can be seen by the parameter induced drag to total drag, C_{Di}/C_D.

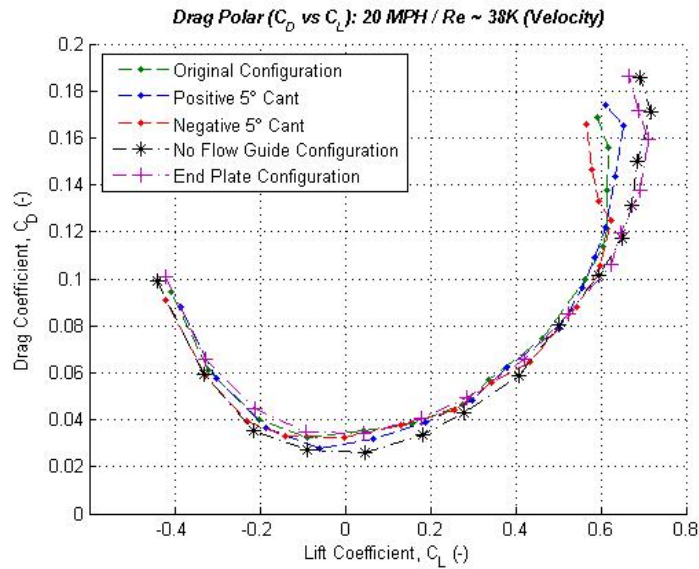


Figure 98: Drag Polar vs. Angle of Attack – Re ~ 38K / 20MPH

Table 17: Comparison of Induced and Parasite Drag of the Five Models – Re ~ 38K

Model Configuration	Re (-)	L/D _{max} (-)	C _D (-)	C _{D0} (-)	C _{Di} (-)	C _{Di} /C _D (-)	L (lb)	D (lb)	D _{min} (lb)	D _i (lb)	L/D _i (-)
Original	38K	6.2241	0.0744	0.0327	0.0417	56.0%	0.217	0.035	0.015	0.020	10.92
+5° Cant	38K	6.3652	0.0787	0.0278	0.0508	64.6%	0.233	0.037	0.014	0.023	10.31
-5° Cant	38K	6.7311	0.0644	0.0324	0.0320	49.7%	0.213	0.032	0.016	0.016	13.64
Endplate	38K	6.3733	0.0658	0.0344	0.0314	47.7%	0.153	0.024	0.012	0.012	13.26
No Flow Guide	38K	6.9259	0.0590	0.0260	0.0330	56.0%	0.146	0.021	0.009	0.012	12.11

4.3.1.3 Maximum Range and Endurance

A plot of lift-to-drag versus angle of attack for the five model configurations can be seen in Figure 98. A summary of the results is located in Table 16 and the percent change between models can be seen in Table 18. The No Flow Guide Configuration was the reference point for the other configurations. These results will help determine the best configuration for endurance. For a $Re \approx 38K$, the models with flow guides had a lower L/D_{max} than the reference No Flow Guide Configuration due to increased parasite drag.

The +5° Cant Configuration and the -5° Cant Configuration are shifted to either side of the Original Configuration due to the effective angle of attack of the canted flow guides.

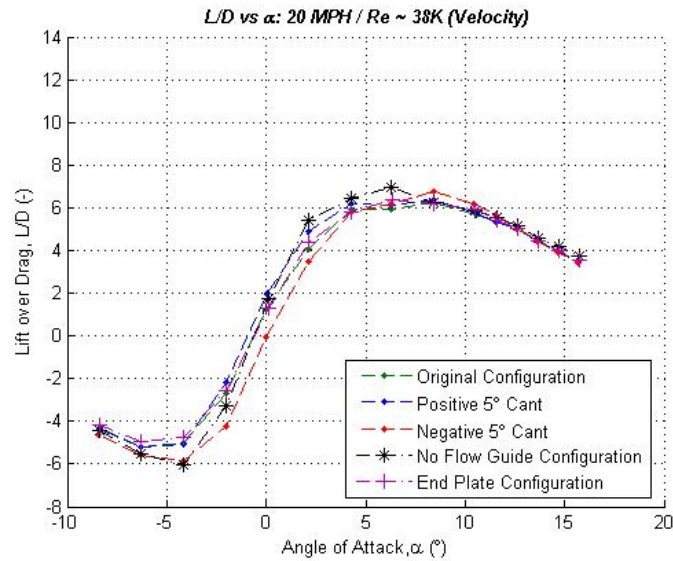


Figure 99: Lift-to-Drag vs. Angle of Attack – Re ~ 38K / 20MPH

Table 18: Comparison of L/D_{max} and $C_L^{3/2}/C_{Dmax}$ of the Five Models – Re ~ 38K

Model Configuration	Re (-)	% Change from No Flow Guide	
		L/D_{max}	$C_L^{3/2}/C_{Dmax}$
Original	38K	-10.1%	-6.3%
+5° Cant	38K	-8.1%	-0.4%
-5° Cant	38K	-2.8%	0.5%
Endplate	38K	-8.0%	3.1%
No Flow Guide	38K	-	-

A plot of $C_L^{3/2}/C_D$ versus angle of attack for the five model configurations can be seen in Figure 100. A summary of the results is located in Table 16 and the percent change between models can be seen in Table 18. The No Flow Guide Configuration was the reference point for the other configurations. These results will help determine the best configuration for endurance. For a $Re \approx 38K$, the model with the highest endurance

relative to the No Flow Guide Configuration was the Endplate Configuration due to its reduced induced drag.

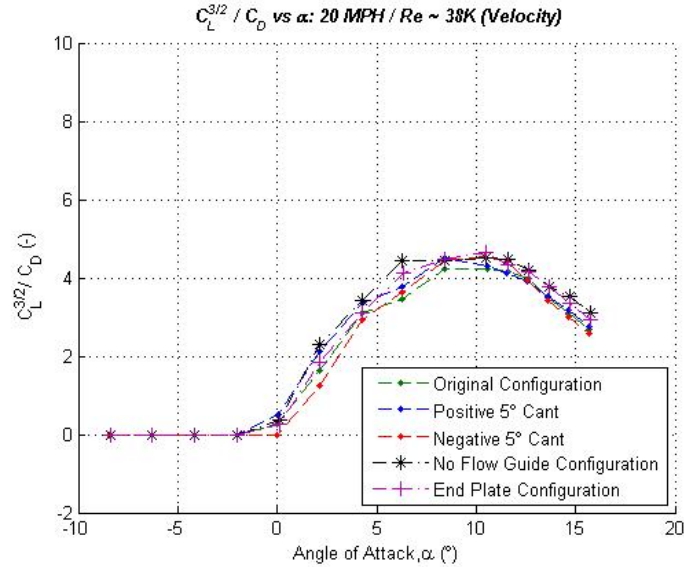


Figure 100: $C_L^{3/2}/C_D$ – Max Endurance vs. Angle of Attack – $Re \sim 38K$ / 20MPH

4.3.1.4 Effective Aspect Ratio

The effective aspect ratio, eAR , has been calculated for all five models at a $Re \approx 38K$. This data can be seen in Table 19. The induced drag coefficient and lift coefficient values were taken at L/D_{max} for all five configurations. The effective aspect ratio is highest for the -5° Cant Configuration at a $Re \approx 38K$.

Table 19: Comparison of Aspect Ratio for the Five Models – $Re \sim 38K$

Model Configuration	Re (-)	eAR
Original	38K	1.64
+5° Cant	38K	1.57
-5° Cant	38K	1.87
Endplate	38K	1.78
No Flow Guide	38K	1.61

4.3.2 $Re \approx 57K / 30 \text{ MPH}$

4.3.2.1 Summary

The data results of the five model configurations, which were presented in Section 4.2 at a Reynolds number of 57K (30 mph or 13.41 m/s), are compared to gauge the differences in aerodynamic performance of the models. The models that were included in the test were: the Original Configuration Model, the + 5° Cant Configuration Model, the – 5° Cant Configuration Model, the Endplate Configuration Model, and the No Flow Guide Configuration Model. The No Flow Guide Configuration Model served as the reference to base all the performance parameters.

A summary of aerodynamic performance comparisons between the five model configurations can be seen in Table 19. A discussion of the performance factors: drag, maximum range, maximum endurance, and effective aspect ratio will be discussed in this section with corresponding figures.

Table 20: Summary of the Aerodynamic Performance Comparison of the Five Models – Re ~ 57K

Model Configuration	Re (-)	S (in ²)	b (in)	Minimum Drag			Zero Lift	Slopes	
				C _{D0} (-)	α (°)	D (lb)	α _{0 Lift} (°)	C _{Lα} (1/°)	C _{mα} (1/°)
Original	57K	72.58	13.81	0.0275	-2.02	0.032	-1.33	0.056	0.010
+5° Cant	57K	72.56	13.81	0.0277	-2.01	0.033	-0.99	0.054	0.011
-5° Cant	57K	72.56	13.81	0.0273	0.01	0.032	-0.57	0.057	0.010
Endplate	57K	58.33	11.50	0.0296	0.11	0.028	-1.25	0.058	0.011
No Flow Guide	57K	58.02	11.38	0.0268	0.11	0.024	-1.09	0.057	0.010

Model Configuration	Re (-)	S (in ²)	b (in)	Maximum Range					
				L/D _{max} (-)	α (°)	C _L (-)	C _D (-)	L (lb)	D (lb)
Original	57K	72.58	13.81	9.4369	6.33	0.4252	0.0451	0.502	0.053
+5° Cant	57K	72.56	13.81	9.3534	6.34	0.4503	0.0481	0.520	0.056
-5° Cant	57K	72.56	13.81	9.3586	8.44	0.5054	0.0540	0.551	0.059
Endplate	57K	58.33	11.50	8.6825	6.39	0.4453	0.0513	0.419	0.048
No Flow Guide	57K	58.02	11.38	9.0696	6.30	0.4248	0.0468	0.389	0.043

Model Configuration	Re (-)	S (in ²)	b (in)	Maximum Endurance					
				C _L ^(3/2) /C _{Dmax} (-)	α (°)	C _L (-)	C _D (-)	L (lb)	D (lb)
Original	57K	72.58	13.81	7.0672	10.57	0.6110	0.0676	0.701	0.078
+5° Cant	57K	72.56	13.81	6.9491	10.58	0.6395	0.0736	0.715	0.082
-5° Cant	57K	72.56	13.81	6.6534	8.44	0.5054	0.0540	0.551	0.059
Endplate	57K	58.33	11.50	6.4561	10.52	0.6051	0.0729	0.587	0.071
No Flow Guide	57K	58.02	11.38	6.3719	10.52	0.5981	0.0726	0.549	0.067

4.3.2.2 Drag

Figure 101 plots the drag polar, C_D vs. C_L, for the five model configurations at a Reynolds number of 57K. The No Flow Guide Configuration has the lowest value of C_{D0} of all the five configurations. Table 21 compares the induced and parasite drag between all the model configurations. It is interesting to note at a Reynolds number of 57K the Endplate configuration had the least amount of induced drag percentage of the total drag. The + 5° Cant Configuration had the highest lift-to-induced drag of all the models.

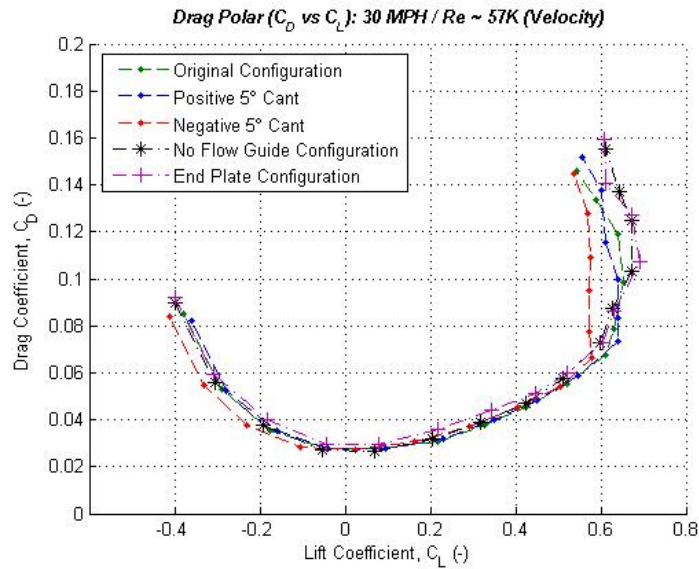


Figure 101: Drag Polar vs. Angle of Attack – Re ~ 57K / 30MPH

Table 21: Comparison of Induced and Parasite Drag of the Five Models – Re ~ 57K

Model Configuration	Re (-)	L/D _{max} (-)	C _D (-)	C _{Do} (-)	C _{Di} (-)	C _{Di} / C _D (-)	L (lb)	D (lb)	D _{min} (lb)	D _i (lb)	L/D _i (-)
Original	57K	9.4369	0.0451	0.0275	0.0175	38.9%	0.502	0.053	0.032	0.021	23.65
+5° Cant	57K	9.3534	0.0481	0.0277	0.0205	42.5%	0.520	0.056	0.033	0.023	22.85
-5° Cant	57K	9.3586	0.0540	0.0273	0.0267	49.5%	0.551	0.059	0.032	0.027	20.60
Endplate	57K	8.6825	0.0513	0.0296	0.0217	42.3%	0.419	0.048	0.028	0.020	20.85
No Flow Guide	57K	9.0696	0.0468	0.0268	0.0200	42.7%	0.389	0.043	0.024	0.019	20.57

4.3.2.3 Maximum Range and Endurance

A plot of lift-to-drag versus angle of attack for the five model configurations can be seen in Figure 102. A summary of the results is located in Table 20 and the percent change between models can be seen in Table 22. The No Flow Guide Configuration was the reference point for the other configurations. These results will help determine the best configuration for endurance. For a $Re \approx 57K$, the Original Configuration and + 5° Cant Configuration have the highest L/D_{max} values due to decreased induced drag. The +5°

Cant Configuration and the -5° Cant Configuration are shifted to either side of the Original Configuration due to the effective angle of attack of the canted flow guides.

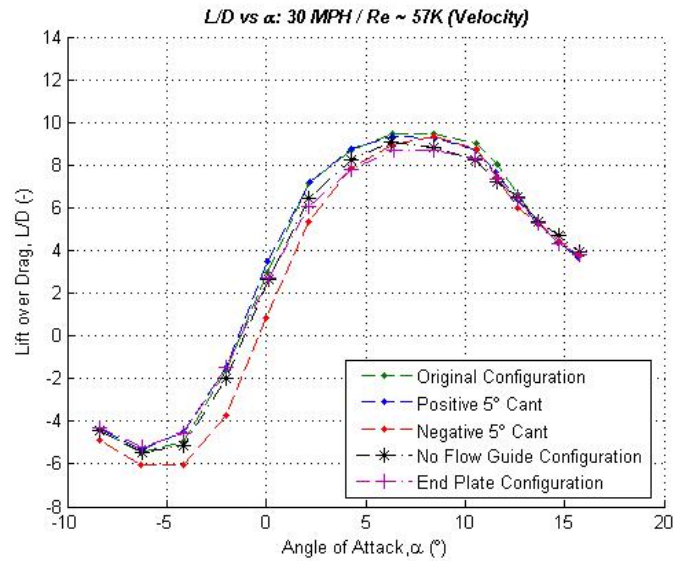


Figure 102: Lift-to-Drag vs. Angle of Attack – Re ~ 57K / 30MPH

Table 22: Comparison of L/D_{max} and $C_L^{3/2}/C_{Dmax}$ of the Five Models – Re ~ 57K

Model Configuration	Re (-)	% Change from No Flow Guide	
		L/D_{max}	$C_L^{(3/2)}/C_{Dmax}$
Original	57K	4.1%	10.9%
+5° Cant	57K	3.1%	9.1%
-5° Cant	57K	3.2%	4.4%
Endplate	57K	-4.3%	1.3%
No Flow Guide	57K	-	-

A plot of $C_L^{3/2}/C_D$ versus angle of attack for the five model configurations can be seen in Figure 103. A summary of the results is located in Table 20 and the percent change between models can be seen in Table 22. The No Flow Guide Configuration was the reference point for the other configurations. These results will help determine the best configuration for endurance. For a $Re \approx 57K$, the model with the highest endurance

relative to the No Flow Guide Configuration was the Original Configuration due to its relatively low value for induced drag.

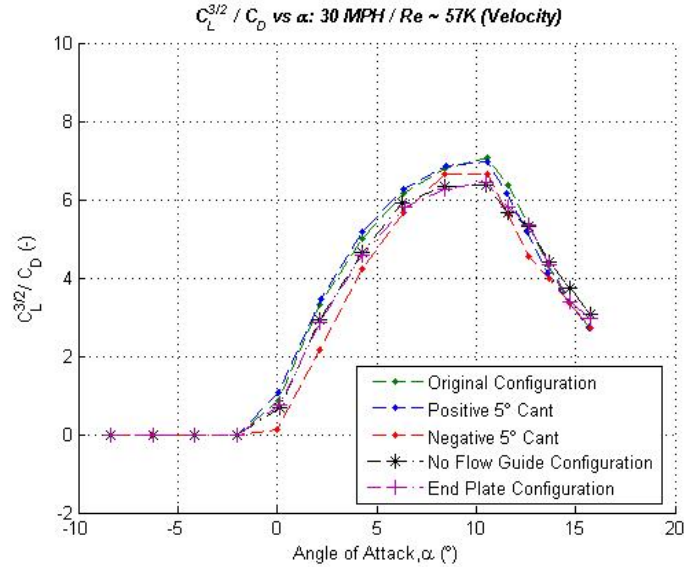


Figure 103: $C_L^{3/2}/C_D$ – Max Endurance vs. Angle of Attack – $Re \sim 57K$ / 30MPH

4.3.2.4 Effective Aspect Ratio

The effective aspect ratio, eAR , has been calculated for all five models at a $Re \approx 57K$. This data can be seen in Table 23. The induced drag coefficient and lift coefficient values were taken at L/D_{max} for all five configurations. The effective aspect ratio is highest for the Original Configuration at a $Re \approx 38K$.

Table 23: Comparison of Aspect Ratio for the Five Models – $Re \sim 57K$

Model Configuration	Re (-)	eAR
Original	57K	3.28
+5° Cant	57K	3.15
-5° Cant	57K	3.04
Endplate	57K	2.91
No Flow Guide	57K	2.87

4.3.3 $Re \approx 78K$ / 40 MPH

4.3.3.1 Summary

The data results of the five model configurations, which were presented in Section 4.2 at a Reynolds number of 78K (40 mph or 17.88 m/s), are compared to gauge the differences in aerodynamic performance of the models. The models that were included in the test were: the Original Configuration Model, the + 5° Cant Configuration Model, the – 5° Cant Configuration Model, the Endplate Configuration Model, and the No Flow Guide Configuration Model. The No Flow Guide Configuration Model served as the reference to base all the performance parameters.

A summary of aerodynamic performance comparisons between the five model configurations can be seen in Table 23. A discussion of the performance factors: drag, maximum range, maximum endurance, and effective aspect ratio will be discussed in this section with corresponding figures.

Table 24: Summary of the Aerodynamic Performance Comparison of the Five Models – Re ~ 78K

Model Configuration	Re (-)	S (in ²)	b (in)	Minimum Drag			Zero Lift	Slopes	
				C _{D0} (-)	α (°)	D (lb)	α _{0 Lift} (°)	C _{Lα} (l°)	C _{mα} (l°)
Original	78K	72.58	13.81	0.0251	0.03	0.053	-1.50	0.054	0.011
+5° Cant	78K	72.56	13.81	0.0250	-2.00	0.053	-1.78	0.054	0.010
-5° Cant	78K	72.56	13.81	0.0241	0.10	0.050	-0.65	0.054	0.011
Endplate	78K	58.33	11.50	0.0278	0.11	0.049	-1.37	0.056	0.011
No Flow Guide	78K	58.02	11.38	0.0233	0.11	0.039	-1.31	0.054	0.010

Model Configuration	Re (-)	S (in ²)	b (in)	Maximum Range					
				L/D _{max} (-)	α (°)	C _L (-)	C _D (-)	L (lb)	D (lb)
Original	78K	72.58	13.81	10.5512	6.32	0.4154	0.0394	0.896	0.085
+5° Cant	78K	72.56	13.81	10.3334	6.33	0.4284	0.0415	0.927	0.090
-5° Cant	78K	72.56	13.81	10.4259	8.43	0.4643	0.0445	1.000	0.096
Endplate	78K	58.33	11.50	9.2024	8.41	0.5198	0.0565	0.901	0.098
No Flow Guide	78K	58.02	11.38	9.9634	6.29	0.4052	0.0407	0.688	0.069

Model Configuration	Re (-)	S (in ²)	b (in)	Maximum Endurance					
				C _L ^(3/2) /C _{Dmax} (-)	α (°)	C _L (-)	C _D (-)	L (lb)	D (lb)
Original	78K	72.58	13.81	7.7068	10.56	0.5969	0.0598	1.267	0.127
+5° Cant	78K	72.56	13.81	7.3994	10.56	0.5971	0.0624	1.287	0.134
-5° Cant	78K	72.56	13.81	7.2532	10.55	0.5486	0.0560	1.167	0.119
Endplate	78K	58.33	11.50	6.9288	10.52	0.6064	0.0682	1.062	0.119
No Flow Guide	78K	58.02	11.38	7.1055	10.52	0.5962	0.0648	1.009	0.110

4.3.3.2 Drag

Figure 104 plots the drag polar, C_D vs. C_L, for the five model configurations at a Reynolds number of 78K. The No Flow Guide Configuration has the lowest value of C_{D0} of all the five configurations. Table 25 compares the induced and parasite drag between all the model configurations. It is interesting to note at a Reynolds number of 78K the Endplate configuration had the most amount of induced drag percentage of the total drag. The Original Configuration had the highest lift-to-induced drag of all the models.

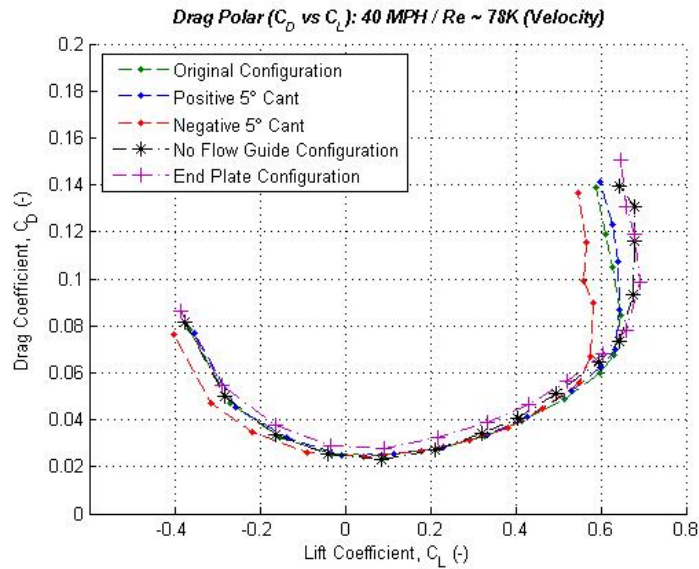


Figure 104: Drag Polar vs. Angle of Attack – Re ~ 78K / 40MPH

Table 25: Comparison of Induced and Parasite Drag of the Five Models – Re ~ 78K

Model Configuration	Re (-)	L/D _{max} (-)	C _D (-)	C _{Do} (-)	C _{Di} (-)	C _D /C _D (-)	L (lb)	D (lb)	D _{min} (lb)	D _i (lb)	L/D _i (-)
Original	78K	10.5512	0.0394	0.0251	0.0143	36.2%	0.896	0.085	0.053	0.032	27.971
+5° Cant	78K	10.3334	0.0415	0.0250	0.0164	39.6%	0.927	0.090	0.053	0.037	25.351
-5° Cant	78K	10.4259	0.0445	0.0241	0.0205	45.9%	1.000	0.096	0.050	0.046	21.594
Endplate	78K	9.2024	0.0565	0.0278	0.0286	50.7%	0.901	0.098	0.049	0.049	18.306
No Flow Guide	78K	9.9634	0.0407	0.0233	0.0174	42.8%	0.688	0.069	0.039	0.030	23.146

4.3.3.3 Maximum Range and Endurance

A plot of lift-to-drag versus angle of attack for the five model configurations can be seen in Figure 105. A summary of the results is located in Table 24 and the percent change between models can be seen in Table 26. The No Flow Guide Configuration was the reference point for the other configurations. These results will help determine the best configuration for endurance. For a $Re \approx 78K$, the Original Configuration has the highest L/D_{max} value due to decreased induced drag. The +5° Cant Configuration and the -5°

Cant Configuration are shifted to either side of the Original Configuration due to the effective angle of attack of the canted flow guides.

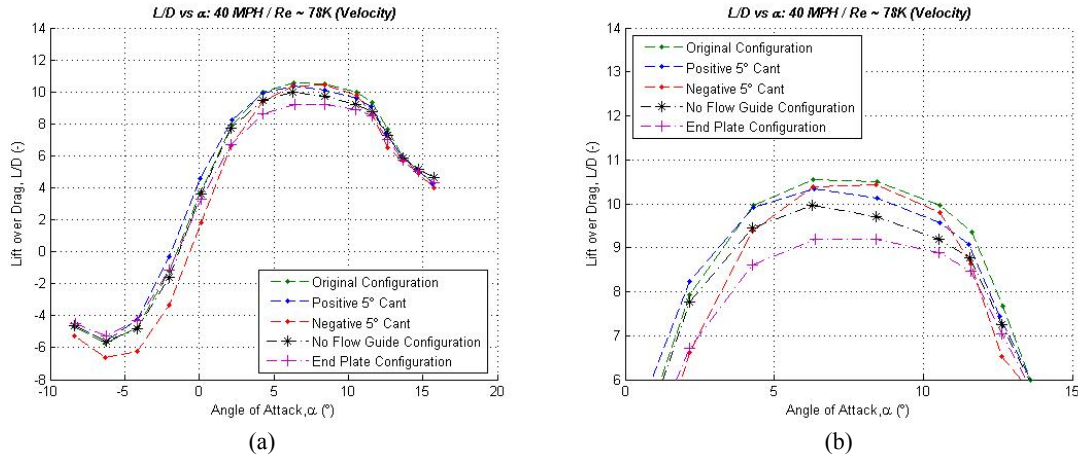


Figure 105: Lift-to-Drag vs. Angle of Attack – $Re \sim 78K / 40MPH$
 (a) Lift-to-Drag vs. Alpha, (b) Lift-to-Drag vs. Alpha – Magnified Section

Table 26: Comparison of L/D_{max} and $C_L^{3/2}/C_{Dmax}$ of the Five Models – $Re \sim 78K$

Model Configuration	Re (-)	% Change from No Flow Guide	
		L/D_{max}	$C_L^{(3/2)}/C_{Dmax}$
Original	78K	5.9%	8.5%
+5° Cant	78K	3.7%	4.1%
-5° Cant	78K	4.6%	2.1%
Endplate	78K	-7.6%	-2.5%
No Flow Guide	78K	-	-

A plot of $C_L^{3/2}/C_D$ versus angle of attack for the five model configurations can be seen in Figure 106. A summary of the results is located in Table 24 and the percent change between models can be seen in Table 26. The No Flow Guide Configuration was the reference point for the other configurations. These results will help determine the best configuration for endurance. For a $Re \approx 78K$, the model with the highest endurance relative to the No Flow Guide Configuration was the Original Configuration due to its relatively low value for induced drag.

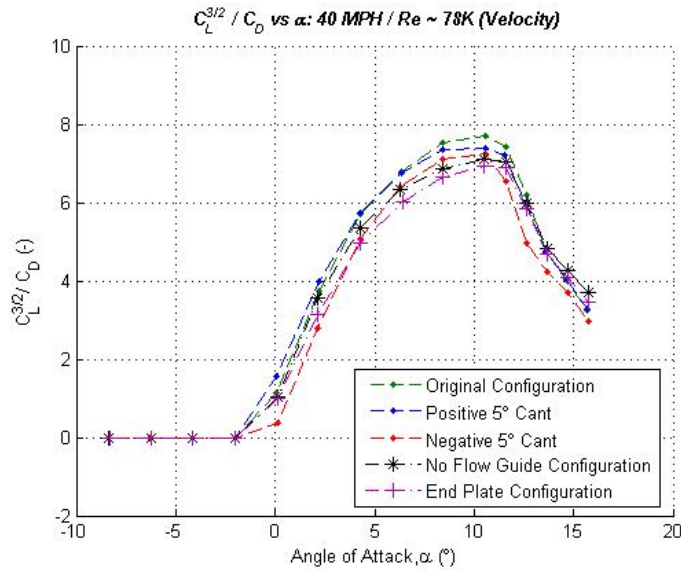


Figure 106: $C_L^{3/2}/C_D$ – Max Endurance vs. Angle of Attack – $Re \sim 78K$ / 40MPH

4.3.3.4 Effective Aspect Ratio

The effective aspect ratio, eAR , has been calculated for all five models at a $Re \approx 78K$. This data can be seen in Table 27. The induced drag coefficient and lift coefficient values were taken at L/D_{max} for all five configurations. The effective aspect ratio is highest for the Original Configuration at a $Re \approx 78K$.

Table 27: Comparison of Aspect Ratio for the Five Models – $Re \sim 78K$

Model Configuration	Re (-)	eAR
Original	78K	3.85
+5° Cant	78K	3.55
-5° Cant	78K	3.36
Endplate	78K	3.00
No Flow Guide	78K	3.01

4.3.4 $Re \approx 120K$ / 60 MPH

4.3.4.1 Summary

The data results of the five model configurations, which were presented in Section 4.2 at a Reynolds number of 120K (60 mph or 26.82 m/s), are compared to gauge the differences in aerodynamic performance of the models. The models that were included in the test were: the Original Configuration Model, the + 5° Cant Configuration Model, the – 5° Cant Configuration Model, the Endplate Configuration Model, and the No Flow Guide Configuration Model. The No Flow Guide Configuration Model served as the reference to base all the performance parameters.

A summary of aerodynamic performance comparisons between the five model configurations can be seen in Table 27. A discussion of the performance factors: drag, maximum range, maximum endurance, and effective aspect ratio will be discussed in this section with corresponding figures.

Table 28: Summary of the Aerodynamic Performance Comparison of the Five Models – Re ~ 120K

Model Configuration	Re (-)	S (in ²)	b (in)	Minimum Drag			Zero Lift	Slopes	
				C _{D0} (-)	α (°)	D (lb)	α _{0 Lift} (°)	C _{Lα} (l°)	C _{mα} (l°)
Original	120K	72.58	13.81	0.0204	0.12	0.098	-1.54	0.053	0.011
+5° Cant	120K	72.56	13.81	0.0218	0.13	0.102	-1.92	0.053	0.011
-5° Cant	120K	72.56	13.81	0.0201	0.11	0.095	-0.88	0.054	0.011
Endplate	120K	58.33	11.50	0.0251	0.11	0.099	-1.40	0.055	0.013
No Flow Guide	120K	58.02	11.38	0.0195	0.11	0.077	-1.58	0.052	0.012

Model Configuration	Re (-)	S (in ²)	b (in)	Maximum Range					
				L/D _{max} (-)	α (°)	C _L (-)	C _D (-)	L (lb)	D (lb)
Original	120K	72.58	13.81	11.8368	6.41	0.4240	0.0358	2.022	0.171
+5° Cant	120K	72.56	13.81	11.7204	6.33	0.4387	0.0374	2.099	0.179
-5° Cant	120K	72.56	13.81	11.9833	6.40	0.3945	0.0329	1.883	0.157
Endplate	120K	58.33	11.50	10.3918	8.41	0.5281	0.0508	2.075	0.200
No Flow Guide	120K	58.02	11.38	11.6871	6.29	0.4145	0.0355	1.648	0.141

Model Configuration	Re (-)	S (in ²)	b (in)	Maximum Endurance					
				C _L ^(3/2) /C _{Dmax} (-)	α (°)	C _L (-)	C _D (-)	L (lb)	D (lb)
Original	120K	72.58	13.81	8.5435	10.56	0.6003	0.0544	2.884	0.262
+5° Cant	120K	72.56	13.81	8.3031	8.45	0.5277	0.0462	2.552	0.223
-5° Cant	120K	72.56	13.81	8.3134	8.43	0.4842	0.0405	2.320	0.194
Endplate	120K	58.33	11.50	7.6841	10.53	0.6157	0.0629	2.424	0.247
No Flow Guide	120K	58.02	11.38	8.1126	10.52	0.6086	0.0585	2.392	0.230

4.3.4.2 Drag

Figure 107 plots the drag polar, C_D vs. C_L, for the five model configurations at a Reynolds number of 120K. The No Flow Guide Configuration has the lowest value of C_{D0} of all the five configurations. Table 29 compares the induced and parasite drag between all the model configurations. It is interesting to note at a Reynolds number of 120K the Endplate configuration had the most amount of induced drag percentage of the total drag. The – 5°Cant Configuration had the highest lift-to-induced drag of all the models.

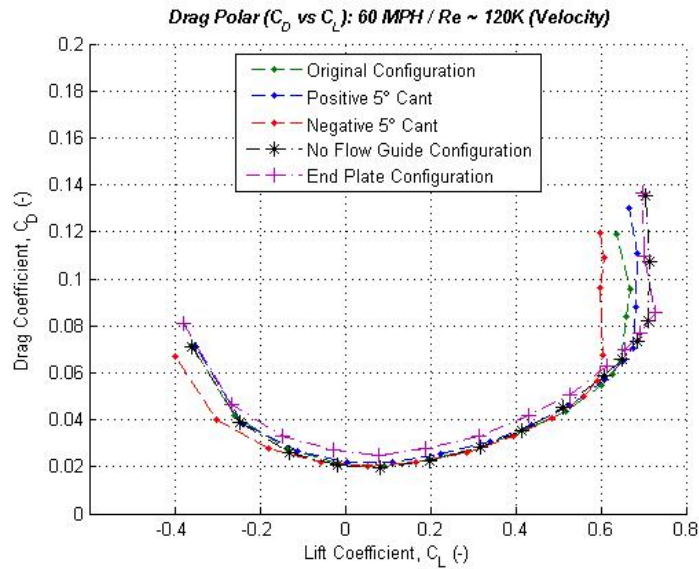


Figure 107: Drag Polar vs. Angle of Attack – Re ~ 120K / 60MPH

Table 29: Comparison of Induced and Parasite Drag of the Five Models – Re ~ 120K

Model Configuration	Re (-)	L/D _{max} (-)	C _D (-)	C _{Do} (-)	C _{Di} (-)	C _{Di} /C _D (-)	L (lb)	D (lb)	D _{min} (lb)	D _i (lb)	L/D _i (-)
Original	120K	11.8368	0.0358	0.0204	0.0154	43.0%	2.022	0.171	0.098	0.073	27.80
+5° Cant	120K	11.7204	0.0374	0.0218	0.0156	41.7%	2.099	0.179	0.102	0.077	27.36
-5° Cant	120K	11.9833	0.0329	0.0201	0.0128	38.9%	1.883	0.157	0.095	0.062	30.38
Endplate	120K	10.3918	0.0508	0.0251	0.0257	50.6%	2.075	0.200	0.099	0.100	20.65
No Flow Guide	120K	11.6871	0.0355	0.0195	0.0159	44.9%	1.648	0.141	0.077	0.064	25.64

4.3.4.3 Maximum Range and Endurance

A plot of lift-to-drag versus angle of attack for the five model configurations can be seen in Figure 108. A summary of the results is located in Table 28 and the percent change between models can be seen in Table 30. The No Flow Guide Configuration was the reference point for the other configurations. These results will help determine the best configuration for endurance. For a $Re \approx 120K$, the - 5° Cant Configuration has the highest L/D_{max} value due to decreased induced drag. The +5° Cant Configuration and the

-5° Cant Configuration are shifted to either side of the Original Configuration due to the effective angle of attack of the canted flow guides.

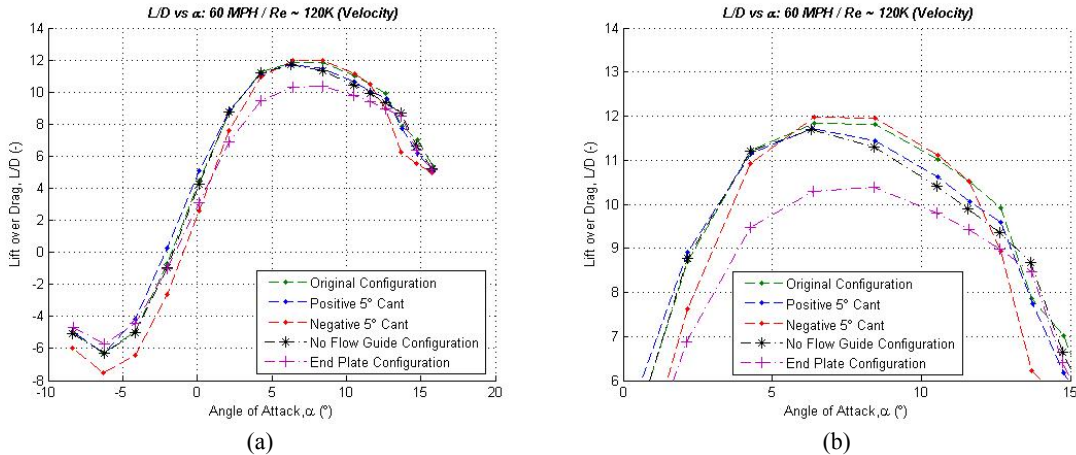


Figure 108: Lift-to-Drag vs. Angle of Attack – Re ~ 120K / 60MPH
 (a) Lift-to-Drag vs. Alpha, (b) Lift-to-Drag vs. Alpha – Magnified Section

Table 30: Comparison of L/D_{max} and $C_L^{3/2}/C_{Dmax}$ of the Five Models – Re ~ 120K

Model Configuration	Re (-)	% Change from No Flow Guide	
		L/D_{max}	$C_L^{(3/2)}/C_{Dmax}$
Original	120K	1.3%	5.3%
+5° Cant	120K	0.3%	2.3%
-5° Cant	120K	2.5%	2.5%
Endplate	120K	-11.1%	-5.3%
No Flow Guide	120K	-	-

A plot of $C_L^{3/2}/C_D$ versus angle of attack for the five model configurations can be seen in Figure 109. A summary of the results is located in Table 28 and the percent change between models can be seen in Table 30. The No Flow Guide Configuration was the reference point for the other configurations. These results will help determine the best configuration for endurance. For a $Re \approx 120K$, the model with the highest endurance relative to the No Flow Guide Configuration was the Original Configuration due to its relatively low value for induced drag.

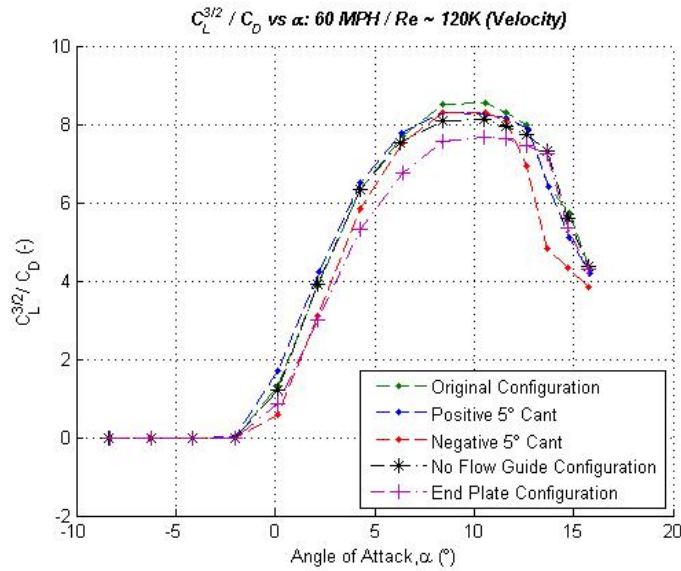


Figure 109: $C_L^{3/2}/C_D$ – Max Endurance vs. Angle of Attack – Re ~ 120K / 60MPH

4.3.4.4 Effective Aspect Ratio

The effective aspect ratio, eAR , has been calculated for all five models at a $Re \approx 120K$. This data can be seen in Table 31. The induced drag coefficient and lift coefficient values were taken at L/D_{max} for all five configurations. The effective aspect ratio is highest for the + 5° Cant Configuration at a $Re \approx 120K$.

Table 31: Comparison of Aspect Ratio for the Five Models – Re ~ 120K

Model Configuration	Re (-)	eAR
Original	120K	3.71
+5° Cant	120K	3.92
-5° Cant	120K	3.87
Endplate	120K	3.45
No Flow Guide	120K	3.43

4.3.5 Trends

The overall trend of results of the five model configurations, which were presented in this section at Reynolds numbers of 38K, 57K, 78K, and 120K, are presented in Table 32. The models that were included in the test were: the Original Configuration Model, the + 5° Cant Configuration Model, the – 5° Cant Configuration Model, the Endplate Configuration Model, and the No Flow Guide Configuration Model. The No Flow Guide Configuration Model served as the reference to base all the performance parameters. The 24” Houck Configuration Model with and without flow guides was also included for comparison.

Table 32: Aerodynamic Performance Comparison for the Models – Re ~ 38K, 57K, 78K, & 120K

Model Configuration	Re (-)	% Change from No Flow Guide (per Re #)		At L/D _{max}		
		L/D _{max} (-)	C _L ^(3/2) /C _{Dmax} (-)	C _{Di} / C _D (-)	L/D _i (-)	eAR
Original	38,000	-10.1%	-6.3%	56.0%	10.92	1.64
Original	57,000	3.1%	9.1%	38.9%	23.65	3.28
Original	78,000	5.9%	8.5%	36.2%	27.97	3.85
Original	120,000	1.3%	5.3%	43.0%	27.80	3.71
+5° Cant	38,000	-8.1%	-0.4%	64.6%	10.31	1.57
+5° Cant	57,000	3.1%	9.1%	42.5%	22.85	3.15
+5° Cant	78,000	3.7%	4.1%	39.6%	25.35	3.55
+5° Cant	120,000	0.3%	2.3%	41.7%	27.36	3.92
-5° Cant	38,000	-2.8%	0.5%	49.7%	13.64	1.87
-5° Cant	57,000	3.2%	4.4%	49.5%	20.60	3.04
-5° Cant	78,000	4.6%	2.1%	45.9%	21.59	3.36
-5° Cant	120,000	2.5%	2.5%	38.9%	30.38	3.87
Endplate	38,000	-8.0%	3.1%	47.7%	13.26	1.78
Endplate	57,000	-4.3%	1.3%	42.3%	20.85	2.91
Endplate	78,000	-7.6%	-2.5%	50.7%	18.31	3.00
Endplate	120,000	-11.1%	-5.3%	50.6%	20.65	3.45
No Flow Guide	38,000	-	-	56.0%	12.11	1.61
No Flow Guide	57,000	-	-	42.7%	20.57	2.87
No Flow Guide	78,000	-	-	42.8%	23.15	3.01
No Flow Guide	120,000	-	-	44.9%	25.64	3.43
Original 24" Houck	80,000	-2.50%	-12.80%	36.10%	17.93	1.64
Original 24" Houck	125,000	-0.30%	-3.40%	41.90%	17.63	1.65
NOFG Houck	80,000	-	-	48.90%	13.63	1.68
NOFG Houck	125,000	-	-	41.20%	17.96	1.74

The first aerodynamic performance parameter to be discussed is maximum lift-to-drag, L/D_{max} . This parameter is one of the aerodynamic performance parameters that is used to measure aircraft efficiency (maximum range). The percent change of L/D_{max} (percent change L/D_{max}) of all five models for all the tested Reynolds numbers is located in Figure 110.

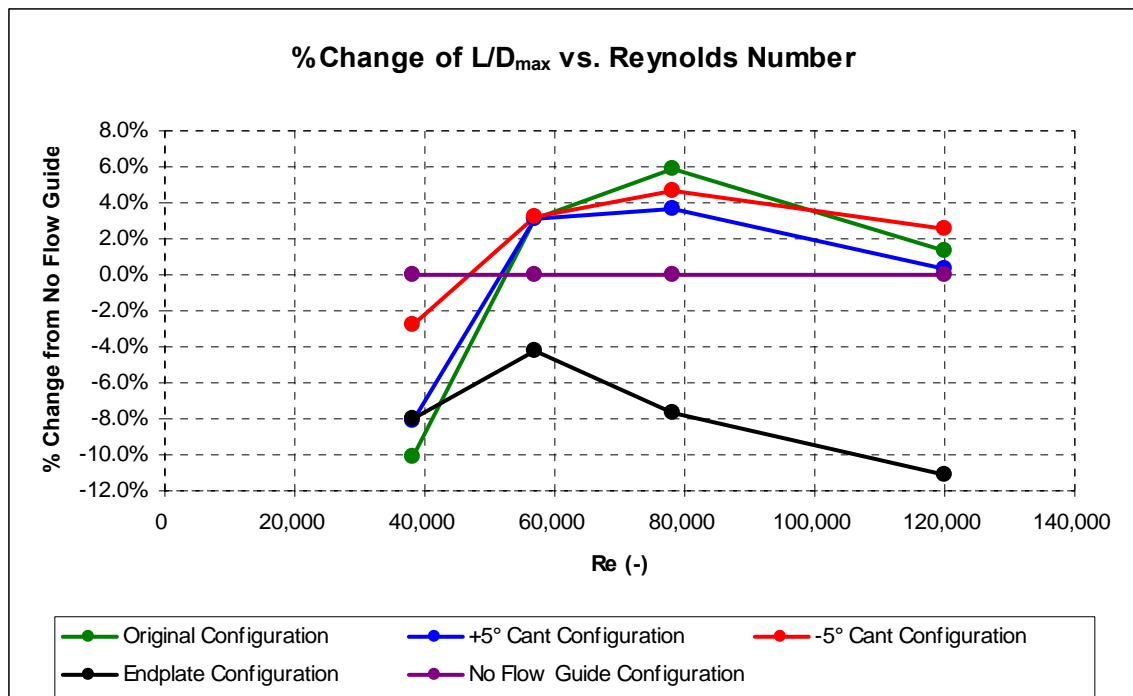


Figure 110: % Change of L/D_{max} vs. Reynolds Number – Re ~ 38K, 57K, 78K, & 120K

For all Reynolds $\geq 57K$, the Flow Guide Configurations exceed the percent change of L/D_{max} as compared to the No Flow Guide Configuration. The trend of the percent change L/D_{max} values of the flow guide configurations compared to the No Flow Guide Configuration is to increase the maximum range over the range of Re $\approx 57K$ to 120K. This performance trend is consistent with the results associated with the 24" Houck Configuration (Table 32). The 24" Houck Configuration had percent change

L/D_{\max} performance trend was increasing over its associated range of $Re \approx 80K$ to $125K$. However, the values of percent change L/D_{\max} were less than the associated No Flow Guide Configuration. The reasons for the increased percent change L/D_{\max} values for the five models, compared to the 24" Houck Configuration, are due to: the model body being less prominent, the trailing edges of the wings were cleaned up, and the balance holder on the model was more streamlined.

The second aerodynamic performance parameter to be discussed is maximum $C_L^{3/2}/C_D$. This parameter is one of the aerodynamic performance parameters that is used to measure aircraft efficiency (maximum endurance). The percent change of $C_L^{3/2}/C_{D_{\max}}$ (percent change $C_L^{3/2}/C_{D_{\max}}$) of all five models for all the tested Reynolds numbers is located in Figure 111. The percent change $C_L^{3/2}/C_{D_{\max}}$ values are located in Table 32.

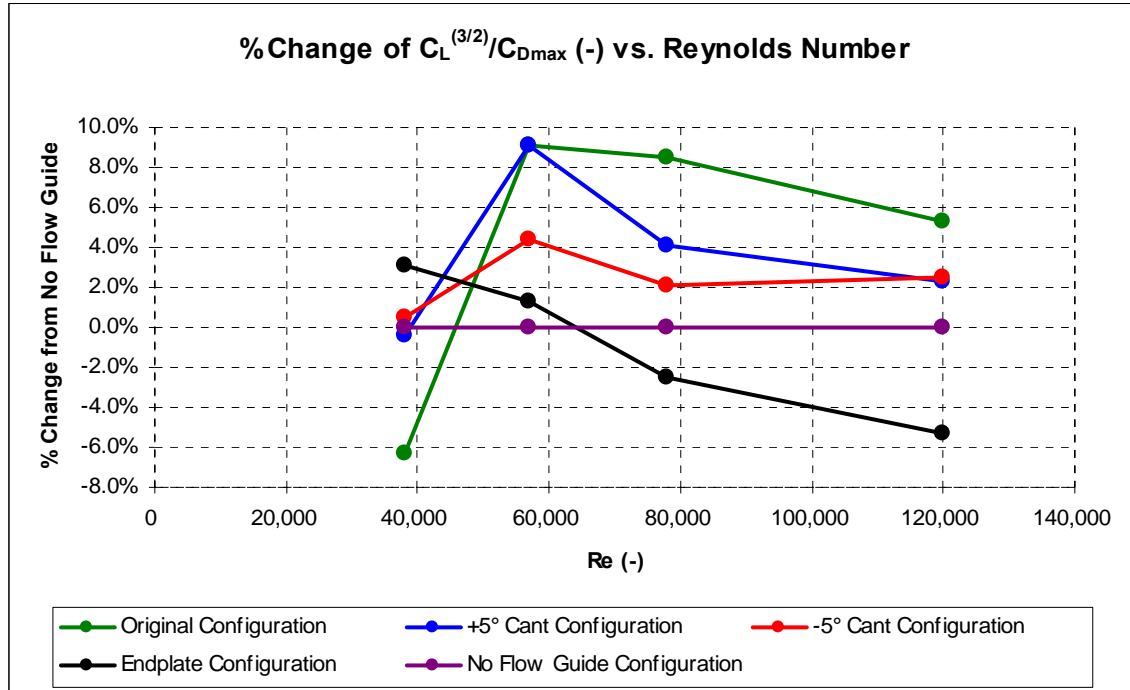


Figure 111: % Change of $C_L^{3/2}/C_{D_{\max}}$ vs. Reynolds Number – $Re \sim 38K, 57K, 78K, \& 120K$

For all Reynolds $\geq 57K$, the Flow Guide Configurations exceed the percent change of $C_L^{3/2}/C_{Dmax}$ as compared to the No Flow Guide Configuration. The trend of the percent change $C_L^{3/2}/C_{Dmax}$ values of the flow guide configurations compared to the No Flow Guide Configuration is to increase the maximum range over the range of $Re \approx 57K$ to $120K$. It is especially noteworthy that the Original Configuration had the best values for the percent change $C_L^{3/2}/C_{Dmax}$ over the range. This performance trend is consistent with the results associated with the 24" Houck Configuration (Table 32). The 24" Houck Configuration had percent change $C_L^{3/2}/C_{Dmax}$ performance trend was increasing over its associated range of $Re \approx 80K$ to $125K$. However, the values of percent change $C_L^{3/2}/C_{Dmax}$ were less than the associated No Flow Guide Configuration. Again, the reasons for the increased percent change $C_L^{3/2}/C_{Dmax}$ values for the five models, compared to the 24" Houck Configuration, are due to: the model body being less prominent, the trailing edges of the wings were cleaned up, and the balance holder on the model was more streamlined.

The average induced drag to total drag (C_{Di}/C_D) at L/D_{max} for the five models tested over the entire range of Reynolds numbers is 45.5%. For each individual model the C_{Di}/C_D is: 43.5% (Original Configuration), 47.1% (+5° Cant Configuration), 46.0% (-5° Cant Configuration), 47.8% (Endplate Configuration), and 46.6% (No Flow Guide Configuration). The percent of C_{Di}/C_D (% C_{Di}/C_D) of all five models for all the tested Reynolds numbers is located in Figure 112. The % C_{Di}/C_D values are located in Table 32.

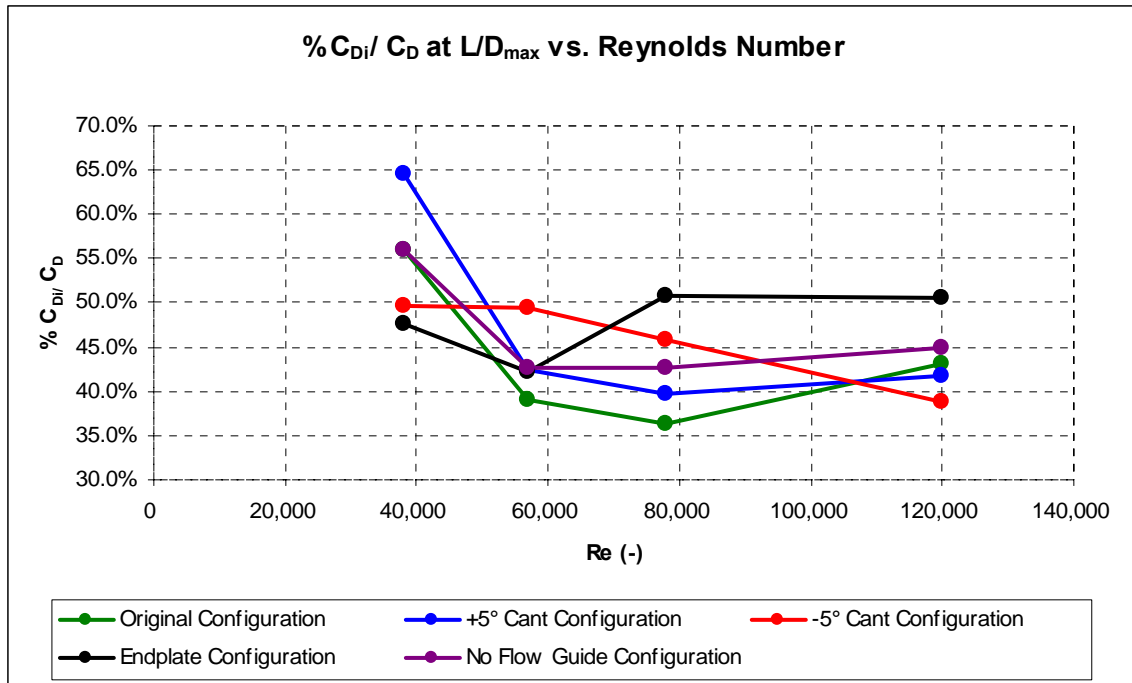


Figure 112: % C_{Di}/C_D vs. Reynolds Number – $Re \sim 38K, 57K, 78K, \& 120K$

Over the range of $Re \approx 38K$ to $120K$, the overall trend of the $\% C_{Di}/C_D$ values is for the Original Configuration, the +5° Cant Configurations, and eventually the -5° Cant Configuration to reduce the effect of induced drag. This trend is inconsistent with the 24" Houck results. As seen in Table 32, the 24" Houck Configuration increased its induced drag over the range of $Re \approx 80K$ to $125K$. The reasons for the decreased $\% C_{Di}/C_D$ values for the five models, compared to the 24" Houck Configuration, are due to: the model body being less prominent, the trailing edges of the wings were cleaned up, and the balance holder on the model was more streamlined.

The last aerodynamic performance parameter to be discussed is the span efficiency factor, e . The span efficiency factor is calculated from the effective aspect

ratio, eAR , divided by the aspect ratio, AR (Equation 20). The AR for a monoplane is given in equation 21 and the AR for a biplane is given in equation 22.

$$e = \frac{eAR}{AR} \quad (20)$$

$$AR = \frac{b^2}{S} \quad (21)$$

$$AR = \frac{2 \cdot b^2}{S} \quad (22)$$

where b is the span (in) and S is the planform area of the wing (in^2).

Table 33 lists the span efficiency factor for the five models and the 24” Houck configurations at each Reynolds number.

Table 33: Span Efficiency Comparison for the Models – $Re \sim 38K, 57K, 78K, \& 120K$

Model Configuration	Re (-)	S (in^2)	b (in)	eAR	Monoplane AR	Monoplane e	Biplane AR	Biplane e
Original	38,000	72.58	13.81	1.64	2.63	0.62	5.25	0.31
Original	57,000	72.58	13.81	3.28	2.63	1.25	5.25	0.62
Original	78,000	72.58	13.81	3.85	2.63	1.47	5.25	0.73
Original	120,000	72.58	13.81	3.71	2.63	1.41	5.25	0.71
+5° Cant	38,000	72.56	13.81	1.57	2.63	0.60	5.25	0.30
+5° Cant	57,000	72.56	13.81	3.15	2.63	1.20	5.25	0.60
+5° Cant	78,000	72.56	13.81	3.55	2.63	1.35	5.25	0.68
+5° Cant	120,000	72.56	13.81	3.92	2.63	1.49	5.25	0.75
-5° Cant	38,000	72.56	13.81	1.87	2.63	0.71	5.25	0.36
-5° Cant	57,000	72.56	13.81	3.04	2.63	1.16	5.25	0.58
-5° Cant	78,000	72.56	13.81	3.36	2.63	1.28	5.25	0.64
-5° Cant	120,000	72.56	13.81	3.87	2.63	1.47	5.25	0.74
Endplate	38,000	58.33	11.50	1.78	2.27	0.79	4.53	0.39
Endplate	57,000	58.33	11.50	2.91	2.27	1.28	4.53	0.64
Endplate	78,000	58.33	11.50	3.00	2.27	1.32	4.53	0.66
Endplate	120,000	58.33	11.50	3.45	2.27	1.52	4.53	0.76
No Flow Guide	38,000	58.02	11.38	1.61	2.23	0.72	4.46	0.36
No Flow Guide	57,000	58.02	11.38	2.87	2.23	1.29	4.46	0.64
No Flow Guide	78,000	58.02	11.38	3.01	2.23	1.35	4.46	0.67
No Flow Guide	120,000	58.02	11.38	3.43	2.23	1.54	4.46	0.77
Original 24" Houck	80,000	307.00	23.58	1.64	1.81	0.90	3.62	0.45
Original 24" Houck	125,000	307.00	23.58	1.65	1.81	0.91	3.62	0.46
NOFG Houck	80,000	254.00	20.33	1.68	1.63	1.03	3.25	0.52
NOFG Houck	125,000	254.00	20.33	1.74	1.63	1.07	3.25	0.54

For a $Re = 38K$, the span efficiency factor is less than one for the monoplane span efficiency factor (all models except for No Flow Guide Houck). However, for all the biplane models, span efficiency factors all the values are less than one. Since the elliptical lift distribution has the least amount of induced drag and therefore an $e = 1$, there cannot be a value that is greater than one. It is interesting to note that e is increasing for all five models as the Reynolds number increases. The e is best, as compared to the five models, at all Reynolds for the No Flow Guide Configuration.

4.4 Neutral Longitudinally Stable $C_{m\alpha}$

4.5.1 Calculation

In order to calculate the neutral longitudinally stable $C_{m\alpha}$, the reference location for the aircraft's center of gravity (x-axis) was varied from the reference measured $X_{cg} = 2.1625''$ ($X_{cmb} = 1.0025''$) to a new measured $X_{cg} = 1.4''$ ($X_{cmb} = 1.765''$). Using the *MATLAB* code and method outlined in Section 3.5.1, the pitching moment coefficient, C_m , was determined.

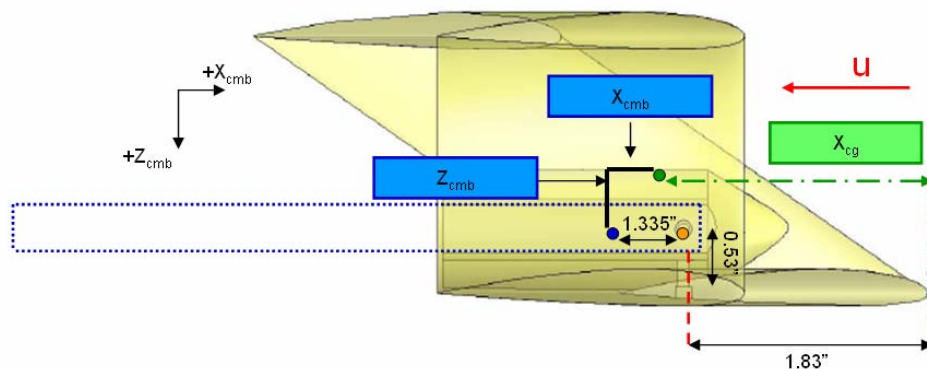


Figure 113: Variation of Aircraft Center of Gravity and Balance Moment Center

The final step to determine $C_{m\alpha}$, was to calculate the slope of the C_m vs. α data over the linear region ($\alpha = -8^\circ$ to 8°).

4.5.2 Results

The results of the $C_{m\alpha}$ calculation described in Section 4.5.1 for the five models at a $Re \approx 120K$ are located in Table 34. The neutral longitudinally stable $C_{m\alpha}$ is located where $C_{m\alpha} = 0$. For the five models it is approximately located at an $X_{cmb} = 1.5750''$ ($X_{cg} = 1.59''$). The range for X_{cg} was chosen so that the region would encompass $C_{m\alpha}$ slopes that are both positive and negative to bound the neutral longitudinal stability $C_{m\alpha}$. Figure 114 shows the graphed C_m curves with their respective linear fits to determine $C_{m\alpha}$ for the Original Configuration Model at a $Re \approx 120K$. The result of $X_{cg} = 1.59''$ suggests that the lower wing produces more lift than the upper wing. Therefore the location of the aircraft's aerodynamic center at the average of the quarter chord of the upper and lower wing produces an aircraft that is longitudinally unstable. Any reference X_{cg} that is less than $1.59''$ (from model nose) will produce a longitudinally stable aircraft.

Table 34: Varying $C_{m\alpha}$ for the Models – $Re \sim 120K$

Re \approx 120K	$C_{m\alpha} (-)$				
X_{cmb} (in)	Original Config	+ 5° Cant Config	- 5° Cant Config	Endplate Config	NOFG Config
1.0025	0.0114	0.0113	0.0112	0.0125	0.0115
1.5750	0.0000	-0.0001	-0.0003	0.0008	0.0003
1.7650	-0.0038	-0.0039	-0.0042	-0.0031	-0.0035

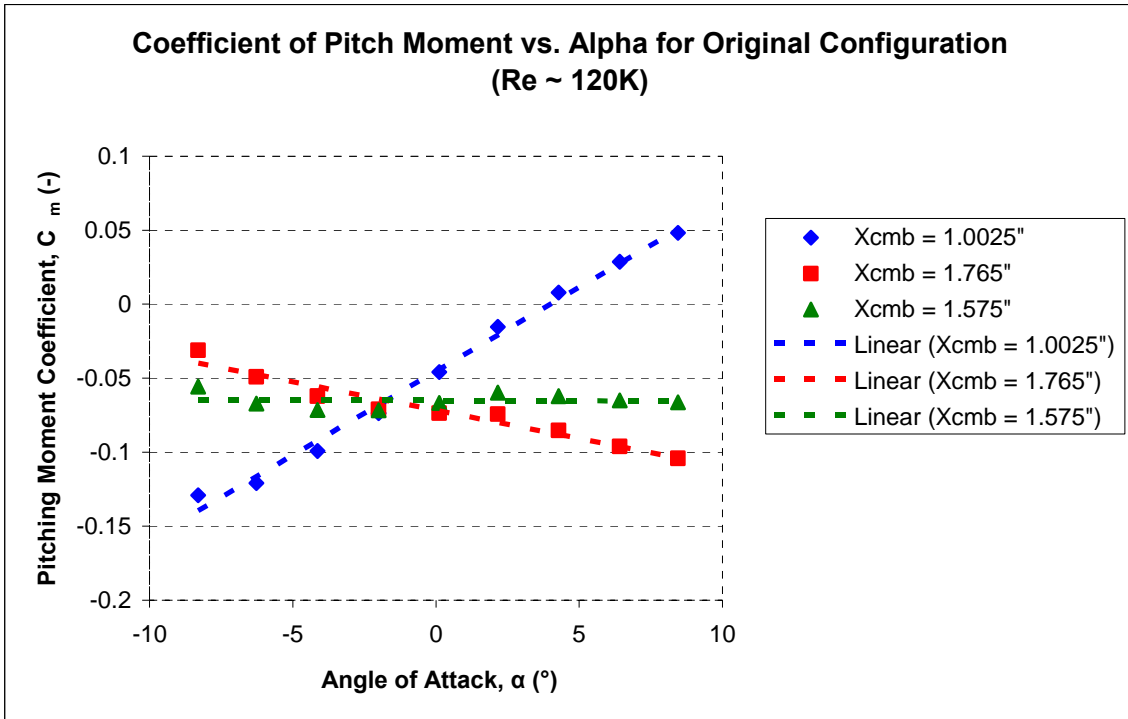


Figure 114: Coefficient of Pitch Moment vs. Alpha to determine the Neutral Longitudinally Stable $C_{m\alpha}$

4.5 Vortex Centroid and Moment Calculations and Results

The vortex moment (rad-mm/s) in the y-direction and the y-coordinate of the vortex centroid were calculated from the Hot-Wire analysis data of the 24" Houck Configuration documented in Walker's thesis (30). The vortex moment was calculated for the 24" Houck Configuration (with and without flow guides) at an $\alpha \approx 4.13^\circ$ and a $Re \approx 125K$. The vorticity data was extracted from *Tecplot*, which was used to plot the vorticity in Figure 115.

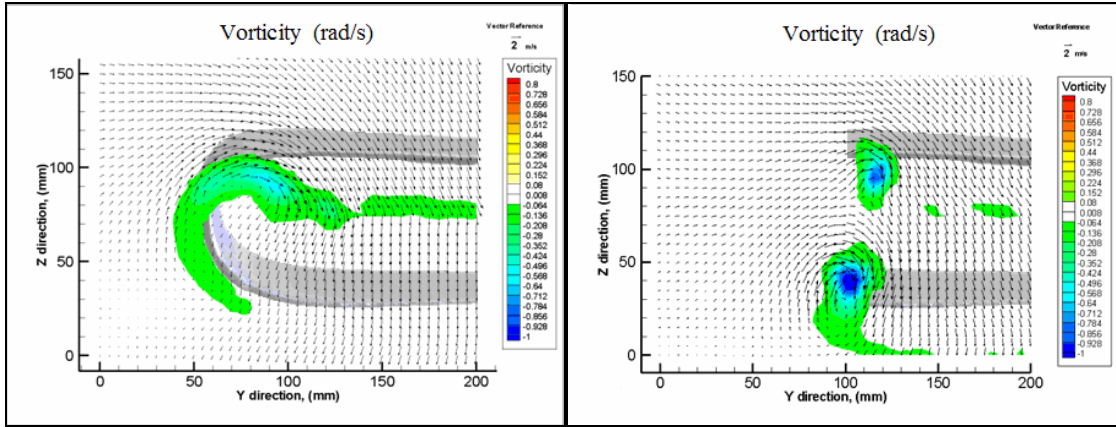


Figure 115: Hot-Wire Vorticity Analysis – $Re \sim 125K$ & $\alpha = 4.13^\circ$ (reproduced from Reference 30)
 (a) Houck 24” Vorticity with v & w vectors shown, (b) Houck 24” No Flow Guides Vorticity with v & w vectors shown

Once this data was extracted through a manual method involving multiple file conversions, a *MATLAB* code was used to reduce the data (App D). The first step in the reduction of the data was to filter out the positive vorticity noise. The next step was to sum the vorticity values at each y -direction coordinate. Once that was accomplished, the vortex moment could be found by multiplying the sum of the vortices at that y -coordinate (mm) by the y -coordinate value (Equation 23). The total vortex moment is the sum each vortex moment (Equation 24).

$$\Omega_{x\text{-}y\text{-moment}} = \left(\sum \omega_{x\text{-}y_i} \right) \cdot y_i \quad (23)$$

$$\Omega_{\text{total-x}\text{-}y\text{-moment}} = \sum \Omega_{x\text{-}y\text{-moment}_i} \quad (24)$$

where $\Omega_{x\text{-}y\text{-moment}}$ is the vortex moment in the y -direction (rad-mm/s), $\omega_{x\text{-}y_i}$ is the vorticity value at the y -coordinate, y_i is the y -coordinate, $\Omega_{\text{total-x}\text{-}y\text{-moment}}$ (rad-mm/s) is the total vortex moment for the entire grid. Finite wing theory suggests that, for a given lift per unit span, the circulation of the trailing vortex system should be equal for the two cases.

An outward displacement of the streamwise vortex system is consistent with a reduction of induced drag.

Once the total vortex moment was calculated, the next step was to divide the total vortex moment by the total vorticity of the entire grid to get the y-coordinate centroid location (Equation 25).

$$y_{\text{vortex centroid}} = \frac{\Omega_{\text{total-x y-moment}}}{\omega_{\text{total}}} \quad (25)$$

where $y_{\text{vortex centroid}}$ is the y-coordinate of the vortex centroid from the mid-span (mm), $\Omega_{\text{total-x,y-moment}}$ (rad-mm/s) is the total vortex moment for the entire grid, and ω_{total} is the total vorticity of the grid (rad/s).

The results for $y_{\text{vortex centroid ND}}$ and $y_{\text{vortex centroid}}$ calculations are located in Table 35 and they are plotted on Figure 116.

Table 35: Vortex Centroid Calculations – Re ~ 120K

Model Configuration	Lift (lbs)	Drag (lbs)	$y_{\text{vortex centroid}}$ (mm)
24" Houck	0.609	0.094	250.8449
24" Houck NOFG	0.586	0.088	238.2817

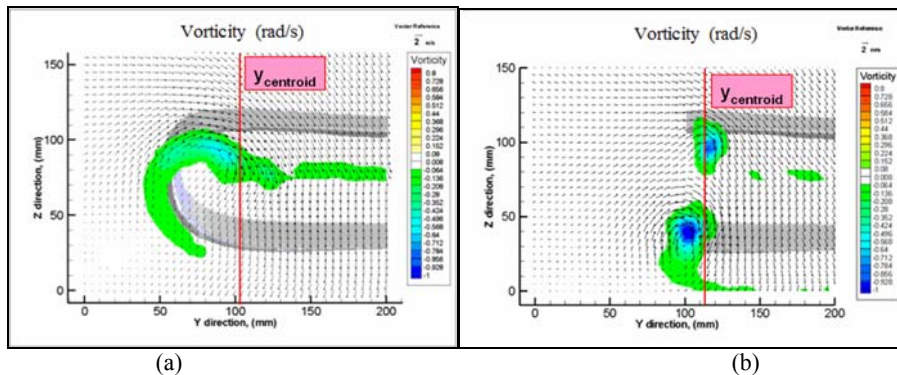


Figure 116: Y-coordinate Centroid on Hot-Wire Vorticity Analysis – Re ~ 125K & $\alpha = 4.13^\circ$ (reproduced from Reference 31)

(a) Houck 24" Vorticity with v & w vectors shown, (b) Houck 24" No Flow Guides Vorticity with v & w vectors shown

From these results, the y-coordinate of the vortex centroid of the No Flow Guide 24" Houck has a greater value than the flow guide case. This result suggests the Flow Guide 24" model is able to displace the vortex centroid farther out than the No Flow Guide model. Lift-to-drag for the two cases are $L/D = 6.5$ for the Flow Guide model and $L/D = 6.67$ for the No Flow Guide model (30).

V. Conclusions and Recommendations

5.1 Conclusions of Research

The purpose of this study was to investigate the aerodynamic performance of Claim 14 and 17 in the Houck Lifting Foil Patent (16) that relates to the design of the flow guides. It has been shown that three of the five models (Original Configuration, +5° Cant, and -5° Cant) that were constructed for use in this study followed the description outlined in the claim (curved, variable camber, etc.). The other two models (Endplate and No Flow Guide Configurations) were built as references for comparison.

When compared to the No Flow Guide Configuration Model, the Original Configuration Model was shown to have a 10.1% decrease in L/D_{\max} at $Re \approx 38K$, a 3.1% increase at $Re \approx 57K$, a 5.9% increase at $Re \approx 78K$, and a 1.3% increase at $Re \approx 120K$. It has also been shown to have a 6.3% decrease in $C_L^{(3/2)}/C_D$ at $Re = 38K$, a 9.1% increase at $Re = 57K$, a 8.5% increase at $Re = 78K$, and a 5.3% increase at $Re = 120K$. For both cases, maximizing range and endurance, the performance of the Original Configuration Model increased to become a positive parameter; but towards the higher Reynolds number, the trend of performance increase diminished. Further testing is needed to determine if the trend would cause a performance gap in these parameters.

When compared to the No Flow Guide Configuration Model, the +5° Cant Model was shown to have an 8.1% decrease in L/D_{\max} at $Re \approx 38K$, a 3.1% increase at $Re \approx 57K$, a 3.7% increase at $Re \approx 78K$, and a 0.3% increase at $Re \approx 120K$. It has also been shown to have a 0.4% decrease in $C_L^{(3/2)}/C_D$ at $Re = 38K$, a 9.1% increase at $Re = 57K$, a 4.1% increase at $Re = 78K$, and a 2.3% increase at $Re = 120K$. For both cases,

maximizing range and endurance, the performance of the +5° Cant Configuration Model increased to become a positive parameter; but towards the higher Reynolds number, the trend of performance increase diminished. Further testing is needed to determine if the trend would cause a performance gap in these parameters. As compared to the Original Flow Guide Configuration Model, the +5° Cant Configuration Model was less efficient at the higher Reynolds numbers proving the variation in flow guide geometry was a performance factor. Further testing of the geometrical variation of the flow guides is needed to determine its effects.

When compared to the No Flow Guide Configuration Model, the -5° Cant Model was shown to have a 2.8% decrease in L/D_{\max} at $Re \approx 38K$, a 3.2% increase at $Re \approx 57K$, a 4.6% increase at $Re \approx 78K$, and a 2.5% increase at $Re \approx 120K$. It has also been shown to have a 0.5% increase in $C_L^{(3/2)}/C_D$ at $Re = 38K$, a 4.4% increase at $Re = 57K$, a 2.1% increase at $Re = 78K$, and a 2.5% increase at $Re = 120K$. For both cases, maximizing range and endurance, the positive performance of the -5° Cant Configuration Model increased; but towards the higher Reynolds number, the trend of performance increase diminished. As compared to the Original Flow Guide Configuration Model, the -5° Cant Configuration Model was more efficient at the lower Reynolds number proving the variation in flow guide geometry was a performance factor. Further testing of the geometrical variation of the flow guides is needed to determine its effects.

The aerodynamic efficiency, measured by L/D_{\max} , of the flow guide configurations over the range of $Re \approx 57K$ to $120K$ were about 2-5% better than the No Flow Guide Configuration. At a Reynolds number of $38K$, the increase in skin friction

drag outweighed any possible reduction of induced drag for the flow guide configurations. The baseline value for the aerodynamic efficiency for the addition of winglets on a low-aspect-ratio delta wing is about 6.96% for a Reynolds number of 1,900K (27:38). The addition of flow guides does provide a comparable efficiency increase as compared to the addition of winglets on a low-aspect-ratio delta wing configuration.

When compared to the No Flow Guide Configuration Model, the Endplate Configuration Model was shown to have an 8.0% decrease in L/D_{\max} at $Re \approx 38K$, a 4.3% decrease at $Re \approx 57K$, a 7.6% decrease at $Re \approx 78K$, and a 11.1% decrease at $Re \approx 120K$. It has also been shown to have a 3.1% increase in $C_L^{(3/2)}/C_D$ at $Re = 38K$, a 1.3% increase at $Re = 57K$, a 2.5% decrease at $Re = 78K$, and a 5.3% decrease at $Re = 120K$. For both cases, maximizing range and endurance, the Endplate Configuration Model had a trend of decreasing performance to an over performance gap at the higher Reynolds numbers. Further testing of endplate geometry, possibly adding an airfoil shape to the endplate cross-section, is needed to determine its effects.

The tested error analysis was conducted on the Original Configuration Model at all Reynolds numbers. The percent error of lift-to-drag for the Original Configuration Model is nominally the same for all the models. This error analysis provided a confidence interval of approximately 99.9% due to a sample size of 22 points. At each model's given L/D_{\max} there is an approximate worst error of 4.23% and realistic error of 3.36% for $Re \approx 38K$, an approximate worst error of 1.96% and realistic error of 1.96% for $Re \approx 57K$, an approximate worst error of 1.30% and realistic error of 1.24% for $Re \approx 78K$, and an

approximate worst error of 0.64% and realistic error of 0.58% for $Re \approx 120K$. For the L/D_{max} comparison to the No Flow Guide Configuration the comparison errors are as follows: approximate worst error of 8.46% and realistic error of 6.72% for $Re \approx 38K$, an approximate worst error of 3.92% and realistic error of 3.92% for $Re \approx 57K$, an approximate worst error of 2.60% and realistic error of 2.28% for $Re \approx 78K$, and an approximate worst error of 1.28% and realistic error of 1.16% for $Re \approx 120K$.

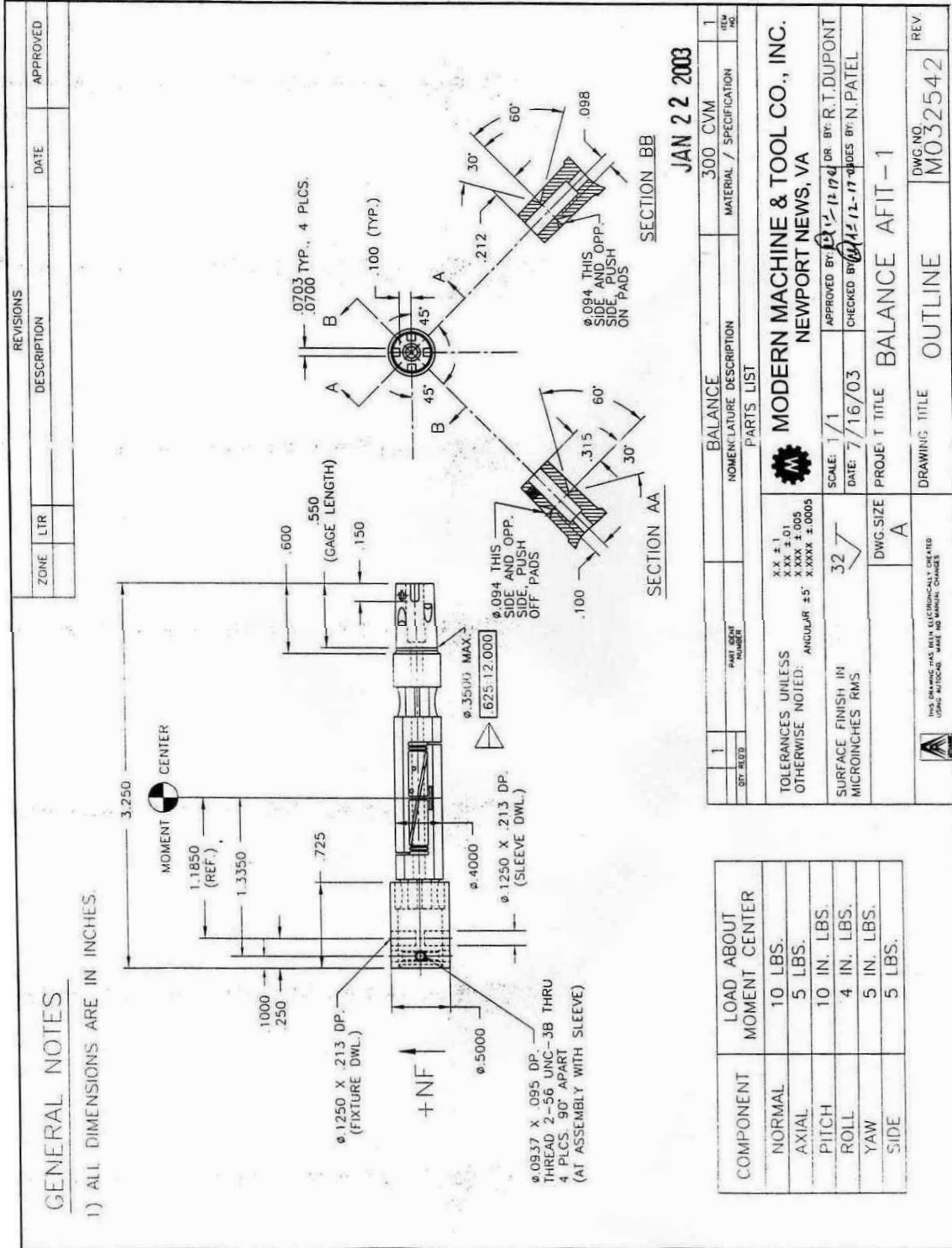
It has been shown in Section 4.3 that the effective aspect ratios, eAR, of the three flow guide configuration models (Original Configuration, +5° Cant, and -5° Cant) were greater than the No Flow Guide Configuration Model's effective aspect ratio at Reynolds numbers higher than 38K. From previous thesis research, it has been proven that the flow guides are successful in combining the upper and lower wing-tip vortices into one single vortex (31: 101). The effect of the combination of the vortices with the use of flow guides on an aerodynamic model as compared to an identical aerodynamic model without flow guides is an improvement in aerodynamic efficiency over a certain range of velocities. However, further investigation of the flow guide configuration will need to be conducted to determine the successful implementation of this configuration on other aircraft designs.

5.2 Recommendations for Future Research

It is recommended that there be continued testing of the flow guide configuration that is part of Houck Lifting Foil concept in order to better understand the design and its aerodynamic influence. CFD and experimental wind tunnel testing is suggested. CFD analysis should be utilized to explore geometric flow guide designs, in order to optimize design before experimental testing, and to compare data with experimental results.

Experimentally, more variable geometric flow guides with varying camber need to be utilized in order to validate patent claims and to further optimize the design. Also, a more aerodynamic baseline model should be designed to decrease the influence of aerodynamic parameters that conflict with the flow guide design. This baseline model should utilize the same wingspan and planform area as the models with flow guides.

Appendix A: 10 lb Balance Dimensions



Appendix B: *MATLAB* 10 lb Balance Code

```

%*****
%*****
%*****      Lt. Gebbie & Capt Anthony DeLuca      *****
%*****  Adapted for the Balance AFIT 1 by Lt. Rivera Parga *****
%*****  re-adapted by Troy Leveron, ENS, USNR      *****
%*****  Calculation of Lift, Drag, Moments           *****
%*****  FLEX WING, Prop OFF, ALPHA SWEEPS         *****
%*****
%*****  re-adapted by 1Lt Michael Walker, ENY, USAF *****
%*****  re-adapted by ENS Dermot Killian, ENY, USN *****
%*****
%This Code will transfer measured Forces and Moments on the AFIT 1 balance to Wind
%(earth) centered frame of reference by correcting for tare effects, balance
%interactions, and wind tunnel irregularities, then gives a file with all the
%corrected data

clear; clc; close all;
format long
%#####
%                               INPUT DECK
%FIRST FILL THE FOLLOWING INFORMATION (modified by D. Killian on 17 Apr, 2007)

Masskg=0.346;      %kgs - Mass of Original Configuration Model (0.7628lbs)

T_room = mean([74.2]) + 459.67;      %deg R  ****Room Temperature on 23 Apr 2007****
P_barro = mean(28.9723) * 0.4911541;  %Psi  ****Pressure on 23 Apr 2007****

load killian_origcfg2_tare_a_n8to15.txt;      %tarefile tare.txt - CHANGE FOR EACH TEST RUN
TareFile = killian_origcfg2_tare_a_n8to15(:,1:9);

load killian_60m_origcfg2_a_n8to15.txt;      %datafile .txt - CHANGE FOR EACH TEST RUN
DataFile = killian_60m_origcfg2_a_n8to15(:,1:9);

%Offset distances from the Mounting Block to the Model C.G.,%(inches)
Y_cmb = 0;
X_cmb = 1.0025;      %inches (from origin @ balance center w/ + forward)
Z_cmb = -0.53;      %inches (from origin @ balance center w/ + down)

% Required for the Solid body blockage corrections due to wing and fuselage

Body_Volume = 17.78/(12^3);      %(ft^3): SOLIDWORKS Original Model
Wing_Area = 72.58/(12^2);      %(ft^2): SOLIDWORKS Original Model
c_bar = 2.55/12;      % (ft): SOLIDWORKS Original Model
span = 13.808/12;      % (ft): SOLIDWORKS Original Model
root_chord = 2.55/12;      % (ft): SOLIDWORKS Original Model
%*****
% Required for the Pitching Moment Correction (NOT USED FOR HOUCK MODEL)

% l_t = 9/12;      % ft = length from tail MAC to aircraft CG
% Span_t =(4+(6/16)) / 12;      % ft = horizontal span
% Tail_Area = (9.42962435) / 144;      % ft^2 = horizontal tail area
%*****

```

```

#####
%II.- Room Conditions and Model Specifics :
%   UNITS are in Ft, Sec, lbm, Psf, Rankine, fps
#####

Mass = (Masskg * 1000) * 0.0022046;           %lbm (24 in Houck Model)
Gas_Const = 1716;                             %ft-lbf/Slug-R
Density = (P_barro * 144)/(1716 * T_room);     %lbm/ft^3 or lbf-s^2/ft^4
Root_Chord = root_chord;                       %ft
Span = span;                                   %ft
Aspect_Ratio = Span^2 / Wing_Area;
Kinematic_Viscosity = .372e-6;                %slug/ft-s
Speed_of_Sound = sqrt(1.4 * T_room * Gas_Const); %fps

#####
%III.- Solid body blockage corrections due to wing and fuselage
#####

K_1 = 0.9;
K_3 = 0.93;
delta = 0.1177;
Tau_1 = 0.83125;                               % from page XXX in text - Figure XX
X_Section = (31/12)*(44/12);                   %ft^2
Wing_Volume = Body_Volume;                     %ft^3

Epsilon_sb_w = (K_1*Tau_1*Wing_Volume) / X_Section^(3/2);
Epsilon_sb_b = (K_3*Tau_1*Body_Volume) / X_Section^(3/2);
Epsilon_tot = Epsilon_sb_w + Epsilon_sb_b;
%Epsilon_tot = Epsilon_sb_w ;

#####
% III.- Load the static tare data for the alpha sweep w/o the wind ,
%   separate each force from the file, and fit a 4th order poly
%   as an x-y plot (AoA vs.Force) for each of the 6 force sensors.
#####

FILE=TareFile(,:);                             % Pulls in tare data file

j=1;
k=1;
L=length(FILE);

for i=1:L                                       %Run for all data points # of rows
    if i~=L                                    %if current row is not last row, go to next
        NEXT=i+1;                             %set next equal to the value of the next row
        VALUE2=FILE(NEXT,1);                 %set value2 as next row column 1
    else if i==L                               %unless the it is the last value
        VALUE2=50;                           %value2 set to 50 to end the sequence
    end
    end
    A(j,:)=FILE(i,:);                         %set row j of A equal to row i of FILE
    VALUE1=FILE(i,1);                         %set value1 equal to row i column 1 of FILE
    if VALUE1==VALUE2                         %if value1 equals value2, go to next row
        j=j+1;
    end
end

```

```

else if VALUE1~=VALUE2           %if value1 and value2 are different check
    if length(A(:,1))<5          %if less than 5 values, ignored due to angle change
        j=1;
        clear A;
    else if length(A(:,1))>5      %if more than 5 values
        C=length(A(:,1));        %find length of A
        for m=1:9                 %Average all rows of the like values in A
            B(k,m)=mean(A(4:C,m)); %disregarding first 3 for vibrations
        end
        j=1;
        k=k+1;
        clear A
    end
end

end
end
end

if B(k-1,1)<B((k-2),1)
    B=B(1:(k-2),:)
end

tare=[B];

%_____End of inserted code
[row,col] = size(tare);

for k = 1:row;

theta_tare(k,:) = tare(k,1).*(pi/180);
NF_tare(k,:) = tare(k,4);
PM_tare(k,:) = tare(k,5);
AF_tare(k,:) = tare(k,6);
SF_tare(k,:) = tare(k,7);
YM_tare(k,:) = tare(k,8);
RM_tare(k,:) = tare(k,9);

end

NF_poly = polyfit(theta_tare,NF_tare,4);
PM_poly = polyfit(theta_tare,PM_tare,4);
AF_poly = polyfit(theta_tare,AF_tare,4);
SF_poly = polyfit(theta_tare,SF_tare,4);
YM_poly = polyfit(theta_tare,YM_tare,4);
RM_poly = polyfit(theta_tare,RM_tare,4);

```

```

#####
%IV.- Load the specific test run files,
#####

clear('AA','B','C','L')
%_____

FILE=DataFile(:,:);          % Pulls in test data file

j=1;
k=1;
L=length(FILE);

for i=1:L                    %Run for all data points # of rows
    if i~=L                  %if current row is not last row, go to next
        NEXT=i+1;           %set next equal to the value of the next row
        VALUE2=FILE(NEXT,1); %set value2 as next row column 1
    else if i==L             %unless the it is the last value
        VALUE2=50;          %value2 set to 50 to end the sequence
    end
    end
    A(j,:)=FILE(i,:);        %set row j of A equal to row i of FILE
    VALUE1=FILE(i,1);        %set value1 equal to row i column 1 of FILE
    if VALUE1==VALUE2        %if value1 equals value2, go to next row
        j=j+1;
    else if VALUE1~=VALUE2   %if value1 and value2 are different check
        if length(A(:,1))<5 %if less than 5 values, ignored due to angle change
            j=1;
            clear A;
        else if length(A(:,1))>5 %if more than 5 values
            C=length(A(:,1)); %find length of A
            for m=1:9          %Average all rows of the like values in A
                B(k,m)=mean(A(4:C,m)); %disregarding first 3 for vibrations
            end
            j=1;
            k=k+1;
            clear A;
        end
    end
end
end
end
end

% if B(k-1,1)<B((k-2),1)
% B=B(1:(k-2),:)
% end

sample_data=[B];

%_____End of inserted code

[row2,col2] = size(sample_data);
for i = 1:row2;

```

%Angles of the model during test runs (Roll, Pitch {AoA}, Yaw {Beta}):

```
phi = 0;
theta(i,:) = sample_data(i,1) .* (pi/180)-(0*pi/180); %radians
si(i,:) = sample_data(i,2) .* (pi/180); %radians
Wind_Speed(i,:) = sample_data(i,3) .* (5280/3600); %fps
```

%Flight Parameters (Re#, Ma#, Dynamic Pressure):

```
q = (.5 * Density) .* Wind_Speed.^2; %lbf/ft^2
q_Corrected = q .* (1 + Epsilon_tot)^2; %lbf/ft^2
Wind_Speed_Corrected = Wind_Speed .* (1 + Epsilon_tot); %fps
Mach_Number = Wind_Speed_Corrected ./ Speed_of_Sound; %NonDimensional
Reynolds_Number = ((Density * Root_Chord) .* Wind_Speed_Corrected) ./ Kinematic_Viscosity; %NonDimensional
Flight_Parameters = [Mach_Number Reynolds_Number q_Corrected]
```

%individual forces and moments for each sensor:

%NEW NOTATION

```
NF_test(i,:,:) = sample_data(i,4);
PM_test(i,:,:) = sample_data(i,5);
AF_test(i,:,:) = sample_data(i,6);
SF_test(i,:,:) = sample_data(i,7);
YM_test(i,:,:) = sample_data(i,8);
RM_test(i,:,:) = sample_data(i,9);
```

```
%#####
%V.- Subtract the effect of the static
% weight with the tare polynomials above
%#####
```

**%Evaluating the actual test theta angle (AoA) in the tare polynomial to
%determine the tare values for the angles tested in each run.**

```
NF_eval = polyval(NF_poly,theta);
PM_eval = polyval(PM_poly,theta);
AF_eval = polyval(AF_poly,theta);
SF_eval = polyval(SF_poly,theta);
YM_eval = polyval(YM_poly,theta);
RM_eval = polyval(RM_poly,theta);
```

**%The Time-Averaged (raw) forces and momentums NF,AF,SF,PM,YM AND RM measurd in the wind
%tunnel (body axis) with the tare effect of the weight subtracted off.**

```
NF_resolved = NF_test - (NF_eval);
PM_resolved = PM_test - (PM_eval);
AF_resolved = AF_test - (AF_eval); % check this 8-17-04
SF_resolved = SF_test - (SF_eval);
YM_resolved = YM_test - (YM_eval);
RM_resolved = RM_test - (RM_eval);
```

```
Forces_minus_tare = [NF_resolved, AF_resolved, PM_resolved, RM_resolved, YM_resolved, SF_resolved];
```

```

%#####
%VI.- CORRECT FORCES AND MOMENTS FOR BALANCE INTERATIONS (body axis)
%#####

%USING THE REDUCTION EQUATIONS
%LET US SET A MAXIMUN NUMBER OF INTERATIONS (FOR AVOIDING AN INFINIT LOOP)
MAXIT=100;
%SET THE LIMIT FOR THE DIFFERENCE BETWEEN INTERATIONS(CRITERIA FOR FINISH
THE INTERATIONS)
LIMIT= 10E-14;

%MATCHING EACH NAME WITH THE DATA
% Prof. Reeder added :i
MNF=NF_resolved(i);
MAF=AF_resolved(i);
MPM=PM_resolved(i);
MRM=RM_resolved(i);
MYM=YM_resolved(i);
MSF=SF_resolved(i);

%INPUT OF THE CONSTANTS VALUES FROM THE MATRIX FOR SENSITIVITIES AND
INTERATIONS
K=[0 -1.3567E-03 -3.8021E-03 -4.2814E-03 -1.6966E-03 1.7567E-03 ...
5.3167E-05 -1.3867E-04 -5.5629E-05 3.5181E-05 1.0601E-05 -2.5271E-04...
5.6693E-05 -1.9537E-04 1.7908E-05 -3.6606E-05 -4.9934E-05 4.1205E-05...
2.5648E-05 -1.9289E-05 8.9661E-05 -1.9594E-05 -4.9859E-04 -1.1599E-03...
5.7163E-05 8.9798E-05 -7.8591E-05 9.3187E-03 0 -3.8421E-03 3.5740E-03...
9.7714E-05 -2.7776E-03 -1.3552E-04 5.1538E-04 2.2082E-04 -1.2706E-05...
-2.3637E-05 1.3686E-05 1.1085E-04 -3.6557E-06 4.9876E-06 8.1085E-06...
3.7381E-05 1.2791E-04 -9.4527E-06 -2.3083E-06 -1.2046E-06 7.8161E-04...
-1.1997E-03 -3.0560E-05 -6.6202E-05 3.7227E-04 -2.1469E-04 4.8386E-03...
-3.7387E-03 0 -1.8479E-02 3.9077E-03 9.9165E-04 -1.4825E-05 -1.4830E-06...
6.0845E-05 8.0667E-05 1.8547E-05 -5.0212E-05 1.0539E-04 -2.2676E-04...
4.3793E-05 -1.0456E-05 -8.1186E-06 -2.1653E-05 -3.3070E-05 1.7280E-05...
-7.4509E-05 -3.4399E-05 -8.2999E-04 -6.7962E-04 4.0521E-05 -5.1604E-05...
9.1132E-06 -5.7360E-03 -2.2213E-04 9.9131E-04 0 -9.5790E-03 6.7114E-03...
3.6824E-05 1.0056E-04 -3.7105E-05 -9.0295E-05 -7.4580E-05 1.4814E-04...
7.2634E-05 -8.4778E-06 6.3486E-05 5.6328E-05 -1.3617E-04 2.2196E-05...
1.3606E-05 -3.6689E-05 8.3283E-05 1.1865E-04 1.8544E-05 -1.9831E-05...
1.7894E-05 -6.8164E-05 -7.0892E-05 1.2378E-03 1.6961E-03 -6.5102E-03...
-9.3202E-03 0 5.1349E-03 1.3612E-05 -1.3175E-04 7.2442E-06 5.6705E-04...
-1.4723E-05 -4.8656E-05 -1.4282E-04 5.9711E-05 5.9046E-05 -3.6490E-04...
7.4881E-05 5.4601E-06 1.0129E-03 -1.3867E-04 8.1617E-05 6.6053E-05...
-1.3417E-05 9.0025E-05 -4.5362E-05 -4.4672E-06 9.5087E-05 -3.4077E-02...
7.9142E-04 1.6667E-03 -6.6512E-03 8.1538E-03 0 -1.4185E-05 7.3209E-05...
-2.5849E-05 1.2325E-03 -4.1696E-05 4.6266E-05 8.6146E-05 2.1436E-05...
5.0874E-05 -3.2738E-04 2.2218E-04 8.6478E-06 7.3395E-04 -4.1453E-05...
3.5719E-05 2.5313E-05 1.5182E-04 3.6007E-05 -2.8844E-05 8.9741E-05...
-7.3257E-05];

```

%COMPUTE THE UNCORRECTED FORCES AND MOMENTS BY
 %CONSIDERING THAT THE PRIME SENSITIVITY CONSTANTS ARE ALREADY APLIED:

NF1=MNF;
 AF1=MAF;
 PM1=MPM;
 RM1=MRM;
 YM1=MYM;
 SF1=MSF;

%FOR THE FIRST INTERACTION LET US INITIALIZE THE VALUES OF FORCES AND
 %MOMENTS WITH THE VALUES OF THE UNCORRECTED FORCES AND MOMENTS

NF(1)=NF1;
 AF(1)=AF1;
 PM(1)=PM1;
 RM(1)=RM1;
 YM(1)=YM1;
 SF(1)=SF1;

%DOING THE INTERACTION EQUATIONS:

for n=2:MAXIT;

NF(n)=NF1-((K(2)*AF(n-1))+K(3)*PM(n-1))+K(4)*RM(n-1))+K(5)*YM(n-1))+K(6)*SF(n-1))+K(7)*NF(n-1)^2)+...
 (K(8)*(NF(n-1)*AF(n-1)))+(K(9)*(NF(n-1)*PM(n-1)))+(K(10)*(NF(n-1)*RM(n-1)))+(K(11)*(NF(n-1)*YM(n-1)))+...
 (K(12)*(NF(n-1)*SF(n-1)))+(K(13)*(AF(n-1)^2))+K(14)*(AF(n-1)*PM(n-1))+K(15)*(AF(n-1)*RM(n-1))+...
 (K(16)*(AF(n-1)*YM(n-1)))+(K(17)*(AF(n-1)*SF(n-1)))+(K(18)*(PM(n-1)^2))+K(19)*(PM(n-1)*RM(n-1))+...
 (K(20)*(PM(n-1)*YM(n-1)))+(K(21)*(PM(n-1)*SF(n-1)))+(K(22)*(RM(n-1)^2))+K(23)*(RM(n-1)*YM(n-1))+...
 (K(24)*(RM(n-1)*SF(n-1)))+(K(25)*(YM(n-1)^2))+K(26)*(YM(n-1)*SF(n-1))+K(27)*(SF(n-1)^2));

AF(n)=AF1-((K(28)*NF(n-1))+K(30)*PM(n-1))+K(31)*RM(n-1))+K(32)*YM(n-1))+K(33)*SF(n-1))+K(34)*NF(n-1)^2)+...
 (K(35)*(NF(n-1)*AF(n-1)))+(K(36)*(NF(n-1)*PM(n-1)))+(K(37)*(NF(n-1)*RM(n-1)))+(K(38)*(NF(n-1)*YM(n-1)))+...
 (K(39)*(NF(n-1)*SF(n-1)))+(K(40)*(AF(n-1)^2))+K(41)*(AF(n-1)*PM(n-1))+K(42)*(AF(n-1)*RM(n-1))+...
 (K(43)*(AF(n-1)*YM(n-1)))+(K(44)*(AF(n-1)*SF(n-1)))+(K(45)*(PM(n-1)^2))+K(46)*(PM(n-1)*RM(n-1))+...
 (K(47)*(PM(n-1)*YM(n-1)))+(K(48)*(PM(n-1)*SF(n-1)))+(K(49)*(RM(n-1)^2))+K(50)*(RM(n-1)*YM(n-1))+...
 (K(51)*(RM(n-1)*SF(n-1)))+(K(52)*(YM(n-1)^2))+K(53)*(YM(n-1)*SF(n-1))+K(54)*(SF(n-1)^2));

PM(n)=PM1-((K(55)*NF(n-1))+K(56)*AF(n-1))+K(58)*RM(n-1))+K(59)*YM(n-1))+K(60)*SF(n-1))+K(61)*NF(n-1)^2)+...
 (K(62)*(NF(n-1)*AF(n-1)))+(K(63)*(NF(n-1)*PM(n-1)))+(K(64)*(NF(n-1)*RM(n-1)))+(K(65)*(NF(n-1)*YM(n-1)))+...

$$\begin{aligned}
& (K(66)*(NF(n-1)*SF(n-1)))+(K(67)*(AF(n-1)^2))+(K(68)*(AF(n-1)*PM(n-1)))+(K(69)*(AF(n-1)*RM(n-1)))+... \\
& (K(70)*(AF(n-1)*YM(n-1)))+(K(71)*(AF(n-1)*SF(n-1)))+(K(72)*(PM(n-1)^2))+(K(73)*(PM(n-1)*RM(n-1)))+... \\
& (K(74)*(PM(n-1)*YM(n-1)))+(K(75)*(PM(n-1)*SF(n-1)))+(K(76)*(RM(n-1)^2))+(K(77)*(RM(n-1)*YM(n-1)))+... \\
& (K(78)*(RM(n-1)*SF(n-1)))+(K(79)*(YM(n-1)^2))+(K(80)*(YM(n-1)*SF(n-1)))+(K(81)*(SF(n-1)^2));
\end{aligned}$$

$$\begin{aligned}
RM(n)=RM1- & ((K(82)*NF(n-1))+(K(83)*AF(n-1))+(K(84)*PM(n-1))+(K(86)*YM(n-1))+(K(87)*SF(n-1)))+(K(88)*NF(n-1)^2)+... \\
& (K(89)*(NF(n-1)*AF(n-1)))+(K(90)*(NF(n-1)*PM(n-1)))+(K(91)*(NF(n-1)*RM(n-1)))+(K(92)*(NF(n-1)*YM(n-1)))+... \\
& (K(93)*(NF(n-1)*SF(n-1)))+(K(94)*(AF(n-1)^2))+(K(95)*(AF(n-1)*PM(n-1)))+(K(96)*(AF(n-1)*RM(n-1)))+... \\
& (K(97)*(AF(n-1)*YM(n-1)))+(K(98)*(AF(n-1)*SF(n-1)))+(K(99)*(PM(n-1)^2))+(K(100)*(PM(n-1)*RM(n-1)))+... \\
& (K(101)*(PM(n-1)*YM(n-1)))+(K(102)*(PM(n-1)*SF(n-1)))+(K(103)*(RM(n-1)^2))+(K(104)*(RM(n-1)*YM(n-1)))+... \\
& (K(105)*(RM(n-1)*SF(n-1)))+(K(106)*(YM(n-1)^2))+(K(107)*(YM(n-1)*SF(n-1)))+(K(108)*(SF(n-1)^2));
\end{aligned}$$

$$\begin{aligned}
YM(n)=YM1- & ((K(109)*NF(n-1))+(K(110)*AF(n-1))+(K(111)*PM(n-1))+(K(112)*RM(n-1)))+(K(114)*SF(n-1))+(K(115)*NF(n-1)^2)+... \\
& (K(116)*(NF(n-1)*AF(n-1)))+(K(117)*(NF(n-1)*PM(n-1)))+(K(118)*(NF(n-1)*RM(n-1)))+(K(119)*(NF(n-1)*YM(n-1)))+... \\
& (K(120)*(NF(n-1)*SF(n-1)))+(K(121)*(AF(n-1)^2))+(K(122)*(AF(n-1)*PM(n-1)))+(K(123)*(AF(n-1)*RM(n-1)))+... \\
& (K(124)*(AF(n-1)*YM(n-1)))+(K(125)*(AF(n-1)*SF(n-1)))+(K(126)*(PM(n-1)^2))+(K(127)*(PM(n-1)*RM(n-1)))+... \\
& (K(128)*(PM(n-1)*YM(n-1)))+(K(129)*(PM(n-1)*SF(n-1)))+(K(130)*(RM(n-1)^2))+(K(131)*(RM(n-1)*YM(n-1)))+... \\
& (K(132)*(RM(n-1)*SF(n-1)))+(K(133)*(YM(n-1)^2))+(K(134)*(YM(n-1)*SF(n-1)))+(K(135)*(SF(n-1)^2));
\end{aligned}$$

$$\begin{aligned}
SF(n)=SF1- & ((K(136)*NF(n-1))+(K(137)*AF(n-1))+(K(138)*PM(n-1))+(K(139)*RM(n-1)))+(K(140)*YM(n-1))+(K(142)*NF(n-1)^2)+... \\
& (K(143)*(NF(n-1)*AF(n-1)))+(K(144)*(NF(n-1)*PM(n-1)))+(K(145)*(NF(n-1)*RM(n-1)))+(K(146)*(NF(n-1)*YM(n-1)))+... \\
& (K(147)*(NF(n-1)*SF(n-1)))+(K(148)*(AF(n-1)^2))+(K(149)*(AF(n-1)*PM(n-1)))+(K(150)*(AF(n-1)*RM(n-1)))+... \\
& (K(151)*(AF(n-1)*YM(n-1)))+(K(152)*(AF(n-1)*SF(n-1)))+(K(153)*(PM(n-1)^2))+(K(154)*(PM(n-1)*RM(n-1)))+... \\
& (K(155)*(PM(n-1)*YM(n-1)))+(K(156)*(PM(n-1)*SF(n-1)))+(K(157)*(RM(n-1)^2))+(K(158)*(RM(n-1)*YM(n-1)))+... \\
& (K(159)*(RM(n-1)*SF(n-1)))+(K(160)*(YM(n-1)^2))+(K(161)*(YM(n-1)*SF(n-1)))+(K(162)*(SF(n-1)^2));
\end{aligned}$$

```
% SET THE LIMIT FOR THE DIFFERENCE BETWEEN ITERATIONS(CRITERIA FOR FINISH
THE ITERATIONS)
```

```
DIFFNF(n)=abs(NF(n)-NF(n-1));
DIFFAF(n)=abs(AF(n)-AF(n-1));
DIFFPM(n)=abs(PM(n)-PM(n-1));
DIFFRM(n)=abs(RM(n)-RM(n-1));
DIFFYM(n)=abs(YM(n)-YM(n-1));
DIFFSF(n)=abs(SF(n)-SF(n-1));
```

```
if DIFFNF(n)&DIFFAF(n)&DIFFPM(n)&DIFFRM(n)&DIFFYM(n)&DIFFSF(n) < LIMIT
break
```

```
end
```

```
end
```

```
%disp('THE FINAL VALUES ARE (NF,AF,PM,RM,YM,SF):')
Corrected_Data(:,i)=[NF(n);AF(n);PM(n);RM(n);YM(n);SF(n)];
```

```
%disp('THE FINAL DIFFERENCE BETWEEN ITERATIONS ARE(FOR NF,AF,PM,RM,YM,SF) :')
%FINAL_DIFFERENCE=[DIFFNF(n),DIFFAF(n),DIFFPM(n),DIFFRM(n),DIFFYM(n),DIFFSF(n)]
```

```
%disp('THE NUMBER OF ITERATIONS USED WAS:')
%n
```

```
%#####
%VII.- Calculation of the Axial, Side, & Normal Forces from the corrected balance
% forces in the Body Axis reference frame
%#####
```

```
Forces_b(:,i)=[Corrected_Data(2,i); Corrected_Data(6,i); Corrected_Data(1,i)];
```

```
%Calculation of the Drag, Side, & Lift Forces in the Wind Axis reference
%frame
```

```
Forces_w=[Forces_b(1,:).*cos(theta').*cos(si')+Forces_b(2,:).*sin(si')+Forces_b(3,:).*sin(theta').*cos(si');
%in radians
-Forces_b(1,:).*sin(si').*cos(theta')+Forces_b(2,:).*cos(si')-Forces_b(3,:).*sin(theta').*sin(si');
-Forces_b(1,:).*sin(theta')+Forces_b(3,:).*cos(theta)];
```

```
%First entry is the moments calculated by the balance or direct calculation
%in the Body Reference Frame. Balance measures Roll (l), Yaw is about the
%z-axis (n), and Pitch is about the y-axis (m). Distances from strain
%gages to C.G. are in INCHES. Moments are in-lbf. See pp. 236-238 of
%Barlow et. al., 3rd ed.
```

```
m = Corrected_Data(3,i);
n = Corrected_Data(5,i);
l = Corrected_Data(4,i);
```

```
Moments_b(:,i)=[l; m; n];
```

```

%Second entry is the conversion from the "Balance Centeric" moments to the
%Wind Reference moments with respect to the Balance Center (bc)

Moments_w_bc = [Moments_b(1,:).*cos(theta').*cos(si')-
Moments_b(2,:).*sin(si')+Moments_b(3,:).*sin(theta').*cos(si');

Moments_b(1,:).*sin(si').*cos(theta')+Moments_b(2,:).*cos(si')+Moments_b(3,:).*sin(theta').*sin(si');
-Moments_b(1,:).*sin(theta')+Moments_b(3,:).*cos(theta)'];

%Finally, the balance centered moments are converted to moments about the
%Model's Center of Mass (cm) or Center of Gravity (CG)

cgdist=sqrt((X_cmb)^2+(Z_cmb)^2); %Obtaining the direct distance between the
%center of the balance and the center of mass
w=atan(-Z_cmb/X_cmb); %Obtaining the angle between cgdist and the x axes at zero angle of attack

X_cm(i,:)= cos(theta(i,:)+w)*cos(si(i,:))*(cgdist);
Y_cm(i,:)= Y_cmb + X_cm(i,:)*tan(si(i,:)); % appropriate for very small y_cmb and reasonable si
Z_cm(i,:)= -sin(theta(i,:)+w)*(cgdist);

Moments_w_cg_u = [Moments_w_bc(1,:) + Z_cm(i,:)*Forces_w(2,:) + Forces_w(3,)* Y_cm(i,:);
Moments_w_bc(2,:) - Forces_w(3,)* X_cm(i,:) + Forces_w(1,)* Z_cm(i,:);
Moments_w_bc(3,:) - Forces_w(1,)* Y_cm(i,:) - Forces_w(2,)* X_cm(i,:)];

%#####

%VIII.- Calculation of the actual Lift and Drag nondimensional Coefficients, uncorrected for tunnel
effects, (Cl
% and Cd)
%#####

C_D_u = Forces_w(1,:) ./ (q_Corrected' .* Wing_Area);
C_Y_u = Forces_w(2,:) ./ (q_Corrected' .* Wing_Area);
C_L_u = Forces_w(3,:) ./ (q_Corrected' .* Wing_Area); %Keuthe & Chow pg 178
Coefficients = [C_L_u; C_D_u; C_Y_u]';
Ave_Cl = mean(Coefficients(:,1));
Ave_Cd = mean(Coefficients(:,2));

end

%#####
%IX Drag Coefficient Correction
%#####

C_D_o = min(Coefficients(:,2));
C_L_u_sqrd = Coefficients(:,1).^2;
Delta_C_D_w = ((delta * Wing_Area) / X_Section) .* C_L_u_sqrd;
C_D_Corrected = C_D_u' + Delta_C_D_w;

```

```

#####
%X.- Angle of Attack due to upwash Correction
#####

alpha_before = sample_data(:,1);
alpha =[alpha_before]-[0]; %18APR05 change to 5 for sting block angle, then back to 0 for Aero 517 SU
2005 *****
Delta_alpha_w = ((delta * Wing_Area) / X_Section) .* (57.3 * C_L_u);
alpha_Corrected = alpha + Delta_alpha_w';

#####
%XI.- Pitching Moment Correction
#####

% tau2 = 0.65;
c_bar = c_bar; % ft = Mean Chord of wing
% V_bar = 0 / (Wing_Area * c_bar); % Horizontal tail volume ratio
% eta_t = 1.0;
% epsilon_o = 0;
% i_t = pi/4; % radians
% i_w = 0;
% Aspect_Ratio_t = Span_t^2 / Tail_Area;
%
% D_epsilon_D_alpha = ((2 .* C_L_u) ./ (pi* Aspect_Ratio))';
% epsilon = epsilon_o + (D_epsilon_D_alpha .* alpha_Corrected);
% alpha_t = alpha_Corrected - i_w - epsilon + i_t;
% C_L_alpha_t = 0 %((0.1* Aspect_Ratio) / (Aspect_Ratio_t +2)) * 0.8;
% D_Cm_cg_t_D_alpha_t = -C_L_alpha_t * V_bar * eta_t;
% Delta_C_m_cg_t = ((D_Cm_cg_t_D_alpha_t) * (delta*tau2) * (Wing_Area / X_Section) .* (C_L_u *
57.3))';

Cl_w_cg = Moments_w_cg_u(1,:) ./ (q_Corrected' .* (Wing_Area * Span*12));
Cm_w_cg_u = Moments_w_cg_u(2,:) ./ (q_Corrected' .* (Wing_Area * c_bar*12));
Cn_w_cg = Moments_w_cg_u(3,:) ./ (q_Corrected' .* (Wing_Area * Span*12));

Cm_w_cg_corrected = Cm_w_cg_u %-Delta_C_m_cg_t'; %no tail
Corrected_Moment_Coefficients = [Cl_w_cg' Cm_w_cg_corrected' Cn_w_cg'];

%OBTAINING THE MOMENT COEFFICIENTS CORRECTED ABOUT THE CENTER OF THE
%BALANCE

Cl_w_bc = Moments_w_bc(1,:) ./ (q_Corrected' .* (Wing_Area * Span*12));
Cm_w_bc_u = Moments_w_bc(2,:) ./ (q_Corrected' .* (Wing_Area * c_bar*12));
Cn_w_bc = Moments_w_bc(3,:) ./ (q_Corrected' .* (Wing_Area * Span*12));

Cm_w_bc_corrected = Cm_w_bc_u; %no tail
Corrected_Moment_Coefficients_bc = [Cl_w_bc' Cm_w_bc_corrected' Cn_w_bc'];

```

```

#####
%XII.- OUTPUT VARIABLES FORMATING
#####

alpha = sample_data(:,1);

% fprintf(' Mach Number Reynolds Number Dynamic Pressure(Psf)\r')
% % Flight_Parameters
% fprintf('\r');
% fprintf(' Loads are in lbf and arranged [D S L] across the top and increments of alpha down the side \r')
% Forces_w'
% fprintf('\r')
% fprintf(' Moments are in in-lbf and arranged [L M N] down the side and increments of alpha along the
top \r')
% % Moments_w_cg_u
% fprintf('\r')
% fprintf(' Cl_u Cd_u CY_u \r');
% % Coefficients
% fprintf('\r')
% fprintf(' Del_CD_w CD_u CD_Corrected \r');
% Compare_CD = [Delta_C_D_w C_D_u' C_D_Corrected]
% fprintf('\r')
% fprintf(' Del_alpha_w alpha_g alpha_Corrected \r');
% Compare_alpha = [Delta_alpha_w' alpha alpha_Corrected ]
% fprintf('\r')
% fprintf(' Cl_cg_wind Cm_cg_corrected_w Cn_cg_wind \r');
% % Corrected_Moment_Coefficients
% fprintf('\r')
% fprintf(' M# Re# q_c Uoo alpha_c C_L C_D_c Cl_cg_w
Cm_cg_c_w Cn_cg_w C_Y \r');
YY=[Flight_Parameters (Wind_Speed_Corrected.*(3600/5280)) alpha_Corrected C_L_u' C_D_Corrected
Corrected_Moment_Coefficients C_Y_u' NF_resolved AF_resolved]
% XX=['M#', 'Re#', 'q_c', 'Uoo', 'alpha_c', 'C_L', 'C_D_c', 'Cl_cg_w', 'Cm_cg_c_w', 'Cn_cg_w', 'C_Y_u'];

% ZZ=[XX; YY];
% wk1write('output.xls',YY,2,1)

% Max_Cl = max(Coefficients(:,1))

% LET US SAVE TOTAL DATA IN A EXTERNAL FILE

dlmwrite('output_killian_origcfg_23APR07_60m_a_n8to15',YY,'t')

```

Appendix C: Aerodynamic Data of the Five Model Configurations

The following data was taken in the AFIT low-speed wind tunnel using the 10lb balance and resolved using the *MATLAB* code found in Appendix B.

Table 36: Original Configuration at 20 mph: Alpha Sweep

Original Configuration at 20 mph: Alpha Sweep - 17th April 2007, $T_{room} = 71.0^\circ F$, $P_{baro} = 14.15$ psi, $S = 72.58$ in ² , $b = 13.808$ in										
Mach (-)	Re (-)	q (lb _f /ft ²)	V (mph)	α (°)	L (lbs)	D (lbs)	C_L (-)	C_D (-)	C_m (-)	L/D (-)
0.0253	36499	0.9123	19.47	-8.41	-0.190	0.015	-0.4074	0.0946	-0.1412	-4.44
0.0253	36570	0.9158	19.51	-6.29	-0.149	0.012	-0.3197	0.0614	-0.1261	-5.54
0.0257	37114	0.9433	19.80	-4.16	-0.096	0.012	-0.2012	0.0400	-0.0952	-6.06
0.0253	36512	0.9129	19.48	-2.03	-0.040	0.014	-0.0876	0.0327	-0.0714	-3.24
0.0250	36018	0.8884	19.21	0.02	0.020	0.016	0.0442	0.0356	-0.0576	1.76
0.0253	36539	0.9143	19.49	2.14	0.073	0.016	0.1569	0.0384	-0.0354	5.40
0.0254	36707	0.9227	19.58	4.27	0.129	0.013	0.2748	0.0464	-0.0139	6.47
0.0261	37686	0.9726	20.10	6.30	0.167	0.011	0.3385	0.0571	0.0125	6.92
0.0255	36849	0.9298	19.66	8.43	0.219	0.004	0.4631	0.0744	0.0388	6.25
0.0248	35775	0.8765	19.08	10.55	0.251	-0.001	0.5625	0.0995	0.0500	5.86
0.0247	35644	0.8700	19.01	11.61	0.268	-0.003	0.6044	0.1135	0.0647	5.55
0.0253	36479	0.9113	19.46	12.66	0.287	-0.006	0.6158	0.1213	0.0719	5.13
0.0255	36810	0.9279	19.64	13.61	0.293	-0.004	0.6137	0.1375	0.0485	4.56
0.0250	36054	0.8902	19.23	14.66	0.285	-0.001	0.6186	0.1559	0.0556	4.19
0.0251	36178	0.8963	19.30	15.69	0.276	0.003	0.5910	0.1688	0.0617	3.73

Table 37: Original Configuration at 30 mph: Alpha Sweep

Original Configuration at 30 mph: Alpha Sweep - 17th April 2007, $T_{room} = 71.0^\circ F$, $P_{baro} = 14.15$ psi, $S = 72.58$ in ² , $b = 13.808$ in										
Mach (-)	Re (-)	q (lb _f /ft ²)	V (mph)	α (°)	L (lbs)	D (lbs)	C_L (-)	C_D (-)	C_m (-)	L/D (-)
0.0395	56773	2.2175	30.43	-8.38	-0.441	0.032	-0.3984	0.0896	-0.1430	-4.45
0.0398	57241	2.2542	30.68	-6.26	-0.342	0.024	-0.3063	0.0559	-0.1257	-5.48
0.0396	56928	2.2296	30.51	-4.14	-0.208	0.027	-0.1920	0.0375	-0.1025	-5.12
0.0397	56976	2.2333	30.53	-2.02	-0.052	0.031	-0.0533	0.0270	-0.0870	-1.97
0.0395	56777	2.2178	30.43	0.11	0.096	0.034	0.0705	0.0268	-0.0677	2.63
0.0397	57034	2.2379	30.57	2.15	0.261	0.029	0.2054	0.0317	-0.0493	6.48
0.0401	57621	2.2842	30.88	4.27	0.388	0.018	0.3188	0.0387	-0.0252	8.24
0.0400	57478	2.2728	30.80	6.30	0.503	0.000	0.4248	0.0468	0.0034	9.08
0.0401	57640	2.2857	30.89	8.41	0.607	-0.022	0.5103	0.0576	0.0268	8.86
0.0401	57563	2.2796	30.85	10.52	0.700	-0.049	0.5981	0.0726	0.0437	8.24
0.0402	57797	2.2982	30.97	11.57	0.732	-0.054	0.6260	0.0872	0.0355	7.18
0.0400	57530	2.2770	30.83	12.63	0.762	-0.051	0.6718	0.1034	0.0357	6.50
0.0398	57245	2.2545	30.68	13.67	0.731	-0.036	0.6714	0.1251	0.0158	5.37
0.0401	57583	2.2812	30.86	14.71	0.700	-0.019	0.6421	0.1374	0.0026	4.67
0.0402	57729	2.2928	30.94	15.74	0.664	-0.004	0.6113	0.1552	-0.0005	3.94

Table 38: Original Configuration at 40 mph: Alpha Sweep

Original Configuration at 40 mph: Alpha Sweep - 17th April 2007, $T_{room} = 71.0^\circ F$, $P_{baro} = 14.15$ psi, $S = 72.58$ in ² , $b = 13.808$ in										
Mach (-)	Re (-)	q (lb _f /ft ²)	V (mph)	α (°)	L (lbs)	D (lbs)	C_L (-)	C_D (-)	C_m (-)	L/D (-)
0.0549	78867	4.2791	42.27	-8.37	-0.791	0.049	-0.3754	0.0815	-0.1339	-4.61
0.0544	78128	4.1994	41.87	-6.25	-0.586	0.037	-0.2815	0.0503	-0.1252	-5.60
0.0535	76895	4.0679	41.21	-4.13	-0.331	0.045	-0.1619	0.0338	-0.1111	-4.79
0.0532	76509	4.0271	41.00	-2.01	-0.064	0.053	-0.0410	0.0256	-0.0894	-1.60
0.0543	78089	4.1951	41.85	0.11	0.196	0.055	0.0842	0.0233	-0.0618	3.61
0.0545	78324	4.2205	41.97	2.15	0.469	0.045	0.2121	0.0273	-0.0382	7.77
0.0539	77401	4.1216	41.48	4.27	0.694	0.022	0.3212	0.0339	-0.0147	9.47
0.0545	78284	4.2162	41.95	6.29	0.897	-0.009	0.4052	0.0407	0.0105	9.96
0.0547	78637	4.2543	42.14	8.40	1.089	-0.052	0.4966	0.0511	0.0306	9.72
0.0544	78151	4.2018	41.88	10.52	1.263	-0.101	0.5962	0.0648	0.0480	9.20
0.0544	78108	4.1972	41.86	11.58	1.342	-0.123	0.6420	0.0731	0.0536	8.78
0.0542	77825	4.1668	41.71	12.63	1.394	-0.121	0.6771	0.0934	0.0425	7.25
0.0543	78069	4.1931	41.84	13.67	1.358	-0.090	0.6796	0.1163	0.0173	5.84
0.0539	77437	4.1254	41.50	14.72	1.325	-0.076	0.6779	0.1309	-0.0001	5.18
0.0537	77179	4.0979	41.36	15.75	1.290	-0.047	0.6434	0.1394	-0.0128	4.62

Table 39: Original Configuration at 60 mph: Alpha Sweep

Original Configuration at 60 mph: Alpha Sweep - 23rd April 2007, $T_{room} = 74.2^\circ F$, $P_{baro} = 28.9723$ inHg, $S = 72.58$ in ² , $b = 13.808$ in										
Mach (-)	Re (-)	q (lb _f /ft ²)	V (mph)	α (°)	L (lbs)	D (lbs)	C_L (-)	C_D (-)	C_m (-)	L/D (-)
0.0825	120370	9.8340	63.64	-8.36	-1.762	0.088	-0.3585	0.0711	-0.1470	-5.04
0.0824	120190	9.8043	63.54	-6.24	-1.238	0.060	-0.2453	0.0388	-0.1330	-6.32
0.0823	120000	9.7731	63.44	-4.12	-0.649	0.085	-0.1313	0.0261	-0.1105	-5.03
0.0820	119590	9.7068	63.23	-2.01	-0.073	0.103	-0.0193	0.0208	-0.0850	-0.93
0.0822	119850	9.7493	63.36	0.11	0.434	0.102	0.0827	0.0195	-0.0543	4.24
0.0822	119850	9.7488	63.36	2.14	0.970	0.082	0.1982	0.0226	-0.0259	8.77
0.0818	119270	9.6548	63.06	4.27	1.527	0.031	0.3193	0.0285	-0.0040	11.20
0.0827	120570	9.8663	63.74	6.29	2.020	-0.044	0.4145	0.0355	0.0163	11.68
0.0829	120900	9.9207	63.92	8.41	2.481	-0.143	0.5100	0.0451	0.0349	11.31
0.0822	119880	9.7538	63.38	10.52	2.870	-0.255	0.6086	0.0585	0.0483	10.40
0.0824	120140	9.7952	63.51	11.58	3.041	-0.313	0.6487	0.0656	0.0526	9.89
0.0826	120450	9.8468	63.68	12.63	3.186	-0.370	0.6841	0.0731	0.0550	9.36
0.0828	120700	9.8880	63.81	13.68	3.233	-0.349	0.7119	0.0820	0.0544	8.68
0.0822	119820	9.7442	63.35	14.73	3.234	-0.357	0.7131	0.1074	0.0306	6.64
0.0820	119570	9.7031	63.21	15.77	3.115	-0.267	0.7049	0.1354	0.0067	5.21

Table 40: +5° Cant Configuration at 20 mph: Alpha Sweep

+5° Cant Configuration at 20 mph: Alpha Sweep - 17th April 2007, $T_{room} = 71.0^\circ F$, $P_{baro} = 14.15$ psi, $S = 72.56$ in ² , $b = 13.806$ in										
Mach (-)	Re (-)	q (lb _f /ft ²)	V (mph)	α (°)	L (lbs)	D (lbs)	C_L (-)	C_D (-)	C_m (-)	L/D (-)
0.0252	36329	0.9038	19.38	-8.40	-0.175	0.040	-0.3846	0.0878	-0.1391	-4.38
0.0250	36011	0.8881	19.21	-6.28	-0.135	0.026	-0.3012	0.0576	-0.1278	-5.22
0.0254	36706	0.9226	19.58	-4.15	-0.086	0.017	-0.1851	0.0363	-0.0934	-5.10
0.0260	37570	0.9666	20.04	-2.02	-0.029	0.014	-0.0599	0.0278	-0.0633	-2.15
0.0253	36510	0.9128	19.48	0.02	0.030	0.015	0.0653	0.0321	-0.0534	2.03
0.0250	36107	0.8928	19.26	2.16	0.085	0.017	0.1895	0.0389	-0.0371	4.88
0.0254	36634	0.9190	19.54	4.28	0.137	0.022	0.2968	0.0480	-0.0126	6.18
0.0257	37125	0.9439	19.80	6.31	0.181	0.029	0.3801	0.0620	0.0147	6.13
0.0255	36729	0.9238	19.59	8.44	0.233	0.037	0.5007	0.0787	0.0444	6.37
0.0256	36909	0.9329	19.69	10.55	0.261	0.045	0.5562	0.0965	0.0547	5.77
0.0258	37189	0.9471	19.84	11.51	0.280	0.052	0.5866	0.1093	0.0622	5.37
0.0259	37385	0.9571	19.94	12.57	0.294	0.059	0.6106	0.1217	0.0651	5.02
0.0253	36533	0.9140	19.49	13.62	0.292	0.066	0.6347	0.1435	0.0495	4.42
0.0246	35515	0.8637	18.95	14.67	0.284	0.072	0.6524	0.1653	0.0551	3.95
0.0251	36255	0.9001	19.34	15.70	0.277	0.079	0.6110	0.1739	0.0610	3.51

Table 41: +5° Cant Configuration at 30 mph: Alpha Sweep

+5° Cant Configuration at 30 mph: Alpha Sweep - 17th April 2007, T _{room} = 71.0° F, P _{baro} = 14.15 psi, S = 72.56 in ² , b = 13.806 in										
Mach (-)	Re (-)	q (lb/ft ²)	V (mph)	α (°)	L (lbs)	D (lbs)	C _L (-)	C _D (-)	C _m (-)	L/D (-)
0.0402	57980	2.3021	30.93	-8.39	-0.417	0.095	-0.3593	0.0823	-0.1261	-4.37
0.0398	57410	2.2570	30.62	-6.27	-0.317	0.059	-0.2787	0.0522	-0.1147	-5.34
0.0400	57711	2.2807	30.78	-4.14	-0.182	0.041	-0.1586	0.0355	-0.0920	-4.47
0.0406	58649	2.3555	31.29	-2.01	-0.047	0.033	-0.0400	0.0277	-0.0700	-1.45
0.0410	59109	2.3926	31.53	0.03	0.116	0.033	0.0961	0.0278	-0.0563	3.46
0.0408	58889	2.3748	31.41	2.17	0.276	0.038	0.2303	0.0320	-0.0379	7.20
0.0404	58267	2.3249	31.08	4.30	0.409	0.047	0.3489	0.0398	-0.0135	8.77
0.0401	57867	2.2931	30.87	6.34	0.520	0.056	0.4503	0.0481	0.0140	9.35
0.0398	57422	2.2579	30.63	8.46	0.622	0.067	0.5468	0.0588	0.0395	9.30
0.0394	56916	2.2183	30.36	10.58	0.715	0.082	0.6395	0.0736	0.0612	8.69
0.0401	57851	2.2919	30.86	11.53	0.740	0.096	0.6407	0.0834	0.0548	7.69
0.0409	59009	2.3845	31.48	12.58	0.770	0.120	0.6411	0.0995	0.0415	6.44
0.0411	59373	2.4140	31.67	13.61	0.742	0.140	0.6101	0.1155	0.0213	5.28
0.0403	58109	2.3123	31.00	14.65	0.699	0.161	0.6002	0.1379	0.0271	4.35
0.0404	58299	2.3274	31.10	15.68	0.651	0.178	0.5552	0.1516	0.0417	3.66

Table 42: +5° Cant Configuration at 40 mph: Alpha Sweep

+5° Cant Configuration at 40 mph: Alpha Sweep - 17th April 2007, T _{room} = 71.0° F, P _{baro} = 14.15 psi, S = 72.56 in ² , b = 13.806 in										
Mach (-)	Re (-)	q (lb/ft ²)	V (mph)	α (°)	L (lbs)	D (lbs)	C _L (-)	C _D (-)	C _m (-)	L/D (-)
0.0542	78227	4.1906	41.73	-8.39	-0.745	0.162	-0.3530	0.0768	-0.1266	-4.59
0.0543	78384	4.2075	41.81	-6.27	-0.541	0.097	-0.2552	0.0456	-0.1114	-5.60
0.0542	78178	4.1853	41.70	-4.14	-0.288	0.068	-0.1365	0.0324	-0.0929	-4.22
0.0544	78456	4.2151	41.85	-2.00	-0.017	0.053	-0.0078	0.0250	-0.0734	-0.31
0.0546	78746	4.2464	42.01	0.04	0.247	0.054	0.1153	0.0253	-0.0474	4.55
0.0546	78851	4.2577	42.06	2.17	0.498	0.060	0.2320	0.0282	-0.0202	8.24
0.0553	79758	4.3563	42.55	4.29	0.734	0.074	0.3343	0.0337	-0.0028	9.91
0.0549	79189	4.2943	42.24	6.33	0.927	0.090	0.4284	0.0415	0.0209	10.33
0.0543	78294	4.1978	41.76	8.45	1.120	0.111	0.5294	0.0523	0.0424	10.12
0.0548	79044	4.2785	42.16	10.56	1.287	0.134	0.5971	0.0624	0.0577	9.58
0.0548	79026	4.2767	42.16	11.53	1.363	0.150	0.6323	0.0697	0.0627	9.07
0.0552	79620	4.3411	42.47	12.58	1.409	0.189	0.6441	0.0866	0.0484	7.44
0.0550	79337	4.3103	42.32	13.62	1.392	0.234	0.6408	0.1076	0.0217	5.96
0.0547	78989	4.2726	42.14	14.66	1.351	0.265	0.6274	0.1231	0.0157	5.10
0.0549	79289	4.3052	42.30	15.69	1.297	0.306	0.5978	0.1410	0.0146	4.24

Table 43: +5° Cant Configuration at 60 mph: Alpha Sweep

+5° Cant Configuration at 60 mph: Alpha Sweep - 23rd April 2007, $T_{room} = 74.8^\circ F$, $P_{baro} = 28.9373 \text{ inHg}$, $S = 72.58 \text{ in}^2$, $b = 13.808 \text{ in}$										
Mach (-)	Re (-)	q (lb _f /ft ²)	V (mph)	α (°)	L (lbs)	D (lbs)	C_L (-)	C_D (-)	C_m (-)	L/D (-)
0.0811	117080	9.4124	62.62	-8.39	-1.666	0.337	-0.3513	0.0712	-0.1326	-4.94
0.0809	116790	9.3667	62.47	-6.26	-1.139	0.181	-0.2413	0.0384	-0.1184	-6.28
0.0807	116570	9.3302	62.35	-4.13	-0.525	0.125	-0.1117	0.0266	-0.0992	-4.20
0.0807	116640	9.3413	62.39	-2.00	0.028	0.103	0.0059	0.0219	-0.0735	0.27
0.0806	116490	9.3178	62.31	0.13	0.525	0.102	0.1117	0.0218	-0.0448	5.12
0.0807	116500	9.3194	62.31	2.17	1.053	0.118	0.2243	0.0252	-0.0148	8.92
0.0812	117280	9.4444	62.73	4.30	1.623	0.145	0.3410	0.0306	0.0069	11.16
0.0814	117610	9.4984	62.91	6.33	2.099	0.179	0.4387	0.0374	0.0283	11.72
0.0819	118230	9.5985	63.24	8.45	2.552	0.223	0.5277	0.0462	0.0468	11.43
0.0819	118240	9.5993	63.24	10.57	2.937	0.277	0.6072	0.0572	0.0597	10.61
0.0811	117090	9.4138	62.63	11.63	3.105	0.309	0.6546	0.0650	0.0642	10.06
0.0817	118050	9.5686	63.14	12.68	3.251	0.339	0.6743	0.0703	0.0653	9.60
0.0821	118550	9.6503	63.41	13.72	3.313	0.428	0.6814	0.0880	0.0502	7.75
0.0812	117270	9.4429	62.72	14.77	3.263	0.528	0.6858	0.1110	0.0311	6.18
0.0810	117040	9.4066	62.60	15.80	3.159	0.617	0.6664	0.1301	0.0187	5.12

Table 44: -5° Cant Configuration at 20 mph: Alpha Sweep

-5° Cant Configuration at 20 mph: Alpha Sweep - 18th April 2007, $T_{room} = 69.9^\circ F$, $P_{baro} = 14.10 \text{ psi}$, $S = 72.56 \text{ in}^2$, $b = 13.806 \text{ in}$										
Mach (-)	Re (-)	q (lb _f /ft ²)	V (mph)	α (°)	L (lbs)	D (lbs)	C_L (-)	C_D (-)	C_m (-)	L/D (-)
0.0254	36561	0.9167	19.53	-8.41	-0.194	0.042	-0.4204	0.0910	-0.1418	-4.62
0.0259	37305	0.9544	19.93	-6.29	-0.157	0.028	-0.3271	0.0587	-0.1154	-5.57
0.0255	36702	0.9238	19.61	-4.17	-0.108	0.018	-0.2313	0.0397	-0.0955	-5.82
0.0245	35271	0.8532	18.84	-2.05	-0.060	0.014	-0.1393	0.0330	-0.0734	-4.22
0.0246	35446	0.8617	18.94	0.00	-0.001	0.014	-0.0027	0.0324	-0.0525	-0.08
0.0245	35204	0.8499	18.81	2.13	0.056	0.016	0.1298	0.0374	-0.0387	3.47
0.0246	35349	0.8569	18.88	4.27	0.111	0.019	0.2562	0.0442	-0.0180	5.80
0.0254	36546	0.9160	19.52	6.30	0.159	0.026	0.3437	0.0556	0.0087	6.18
0.0262	37711	0.9753	20.15	8.42	0.213	0.032	0.4335	0.0644	0.0392	6.73
0.0253	36456	0.9114	19.48	10.46	0.249	0.040	0.5422	0.0878	0.0537	6.18
0.0249	35828	0.8803	19.14	11.52	0.266	0.047	0.5987	0.1053	0.0577	5.68
0.0247	35506	0.8646	18.97	12.57	0.273	0.054	0.6256	0.1248	0.0494	5.01
0.0252	36322	0.9048	19.40	13.60	0.271	0.061	0.5937	0.1331	0.0333	4.46
0.0253	36406	0.9090	19.45	14.64	0.265	0.067	0.5796	0.1466	0.0368	3.95
0.0249	35776	0.8778	19.11	15.68	0.250	0.073	0.5653	0.1657	0.0516	3.41

Table 45: -5° Cant Configuration at 30 mph: Alpha Sweep

-5° Cant Configuration at 30 mph: Alpha Sweep - 18th April 2007, $T_{room} = 69.9^\circ F$, $P_{baro} = 14.10 \text{ psi}$, $S = 72.56 \text{ in}^2$, $b = 13.806 \text{ in}$										
Mach (-)	Re (-)	q (lb _f /ft ²)	V (mph)	α (°)	L (lbs)	D (lbs)	C_L (-)	C_D (-)	C_m (-)	L/D (-)
0.0396	57000	2.2282	30.45	-8.41	-0.462	0.094	-0.4115	0.0840	-0.1367	-4.90
0.0398	57259	2.2485	30.59	-6.29	-0.374	0.062	-0.3302	0.0545	-0.1162	-6.06
0.0401	57786	2.2900	30.87	-4.17	-0.265	0.044	-0.2297	0.0380	-0.0863	-6.05
0.0406	58408	2.3396	31.20	-2.04	-0.125	0.034	-0.1060	0.0286	-0.0677	-3.71
0.0406	58378	2.3372	31.19	0.01	0.027	0.032	0.0231	0.0273	-0.0532	0.85
0.0399	57460	2.2643	30.70	2.15	0.186	0.035	0.1627	0.0306	-0.0392	5.32
0.0397	57095	2.2356	30.50	4.28	0.330	0.042	0.2929	0.0374	-0.0149	7.83
0.0394	56668	2.2023	30.27	6.32	0.448	0.050	0.4037	0.0452	0.0129	8.93
0.0390	56171	2.1639	30.01	8.44	0.551	0.059	0.5054	0.0540	0.0415	9.36
0.0393	56513	2.1903	30.19	10.56	0.640	0.073	0.5801	0.0664	0.0592	8.73
0.0404	58088	2.3141	31.03	11.60	0.669	0.090	0.5738	0.0773	0.0485	7.42
0.0407	58534	2.3497	31.27	12.64	0.677	0.112	0.5720	0.0950	0.0261	6.02
0.0402	57876	2.2971	30.92	13.68	0.666	0.127	0.5751	0.1093	0.0191	5.26
0.0400	57563	2.2724	30.75	14.73	0.650	0.146	0.5679	0.1277	0.0150	4.45
0.0400	57531	2.2698	30.73	15.76	0.614	0.166	0.5370	0.1448	0.0215	3.71

Table 46: -5° Cant Configuration at 40 mph: Alpha Sweep

-5° Cant Configuration at 40 mph: Alpha Sweep - 18th April 2007, T_{room} = 69.9° F, P_{baro} = 14.10 psi, S = 72.56 in², b = 13.806 in										
Mach (-)	Re (-)	q (lb _f /ft ²)	V (mph)	α (°)	L (lbs)	D (lbs)	C _L (-)	C _D (-)	C _m (-)	L/D(-)
0.0540	77783	4.1492	41.55	-8.40	-0.839	0.159	-0.4011	0.0762	-0.1343	-5.27
0.0542	78093	4.1824	41.72	-6.29	-0.662	0.100	-0.3141	0.0474	-0.1116	-6.63
0.0537	77340	4.1021	41.32	-4.17	-0.450	0.072	-0.2179	0.0349	-0.0890	-6.25
0.0535	77020	4.0682	41.15	-2.03	-0.180	0.054	-0.0878	0.0263	-0.0729	-3.34
0.0536	77216	4.0889	41.25	0.10	0.089	0.050	0.0431	0.0241	-0.0499	1.79
0.0538	77455	4.1143	41.38	2.15	0.369	0.056	0.1779	0.0268	-0.0235	6.63
0.0541	77861	4.1575	41.59	4.28	0.610	0.065	0.2912	0.0310	-0.0029	9.39
0.0544	78326	4.2074	41.84	6.31	0.808	0.078	0.3811	0.0367	0.0217	10.40
0.0548	78961	4.2758	42.18	8.43	1.000	0.096	0.4643	0.0445	0.0423	10.43
0.0545	78470	4.2228	41.92	10.55	1.167	0.119	0.5486	0.0560	0.0583	9.79
0.0545	78528	4.2291	41.95	11.60	1.230	0.142	0.5772	0.0668	0.0578	8.64
0.0548	78827	4.2614	42.11	12.64	1.253	0.192	0.5837	0.0895	0.0324	6.52
0.0554	79717	4.3581	42.59	13.68	1.229	0.217	0.5597	0.0990	0.0188	5.66
0.0546	78550	4.2314	41.96	14.73	1.208	0.246	0.5665	0.1154	0.0162	4.91
0.0543	78124	4.1857	41.74	15.76	1.155	0.288	0.5478	0.1364	0.0096	4.02

Table 47: -5° Cant Configuration at 60 mph: Alpha Sweep

-5° Cant Configuration at 60 mph: Alpha Sweep - 23rd April 2007, T_{room} = 74.8° F, P_{baro} = 28.9373 inHg, S = 72.58 in², b = 13.808 in										
Mach (-)	Re (-)	q (lb _f /ft ²)	V (mph)	α (°)	L (lbs)	D (lbs)	C _L (-)	C _D (-)	C _m (-)	L/D(-)
0.0813	117480	9.4773	62.84	-8.40	-1.907	0.320	-0.3994	0.0670	-0.1361	-5.97
0.0816	117900	9.5446	63.06	-6.28	-1.447	0.192	-0.3008	0.0400	-0.1123	-7.53
0.0816	117860	9.5383	63.04	-4.15	-0.855	0.134	-0.1780	0.0278	-0.0932	-6.40
0.0812	117240	9.4386	62.71	-2.02	-0.271	0.104	-0.0570	0.0218	-0.0710	-2.62
0.0809	116920	9.3871	62.54	0.11	0.248	0.095	0.0524	0.0201	-0.0439	2.61
0.0818	118110	9.5787	63.17	2.15	0.805	0.106	0.1667	0.0219	-0.0135	7.62
0.0818	118200	9.5927	63.22	4.28	1.384	0.127	0.2863	0.0262	0.0090	10.93
0.0813	117460	9.4732	62.83	6.40	1.883	0.157	0.3945	0.0329	0.0286	11.98
0.0815	117680	9.5093	62.95	8.43	2.320	0.194	0.4842	0.0405	0.0466	11.95
0.0816	117860	9.5384	63.04	10.55	2.684	0.242	0.5585	0.0503	0.0610	11.11
0.0817	117980	9.5580	63.11	11.60	2.851	0.271	0.5920	0.0563	0.0658	10.52
0.0826	119370	9.7840	63.85	12.65	2.975	0.333	0.6034	0.0676	0.0614	8.93
0.0821	118580	9.6547	63.42	13.69	2.911	0.468	0.5983	0.0962	0.0294	6.22
0.0813	117460	9.4735	62.83	14.74	2.896	0.521	0.6066	0.1092	0.0228	5.56
0.0814	117610	9.4977	62.91	15.78	2.859	0.573	0.5973	0.1198	0.0219	4.99

Table 48: Endplate Configuration at 20 mph: Alpha Sweep

Endplate Configuration at 20 mph: Alpha Sweep - 20th April 2007, T_{room} = 72.6° F, P_{baro} = 29.1564 inHg, S = 58.33 in², b = 11.5 in										
Mach (-)	Re (-)	q (lb _f /ft ²)	V (mph)	α (°)	L (lbs)	D (lbs)	C _L (-)	C _D (-)	C _m (-)	L/D(-)
0.0253	36869	0.9226	19.49	-8.38	-0.157	0.038	-0.4210	0.1007	-0.1516	-4.18
0.0253	36879	0.9231	19.50	-6.27	-0.122	0.025	-0.3265	0.0660	-0.1347	-4.95
0.0251	36602	0.9093	19.35	-4.15	-0.078	0.016	-0.2123	0.0446	-0.1073	-4.76
0.0248	36158	0.8873	19.12	-2.03	-0.033	0.013	-0.0905	0.0350	-0.0763	-2.59
0.0249	36320	0.8953	19.20	0.10	0.016	0.012	0.0449	0.0344	-0.0560	1.31
0.0254	37073	0.9328	19.60	2.14	0.067	0.015	0.1781	0.0405	-0.0362	4.40
0.0255	37246	0.9415	19.69	4.26	0.109	0.019	0.2861	0.0492	-0.0133	5.82
0.0250	36451	0.9018	19.27	6.38	0.153	0.024	0.4194	0.0658	0.0100	6.37
0.0250	36488	0.9036	19.29	8.41	0.192	0.031	0.5258	0.0852	0.0423	6.17
0.0248	36164	0.8876	19.12	10.53	0.225	0.038	0.6246	0.1058	0.0616	5.90
0.0251	36641	0.9112	19.37	11.58	0.238	0.044	0.6454	0.1197	0.0592	5.39
0.0250	36434	0.9009	19.26	12.63	0.252	0.050	0.6908	0.1376	0.0660	5.02
0.0247	36088	0.8839	19.08	13.68	0.254	0.057	0.7107	0.1593	0.0527	4.46
0.0250	36471	0.9027	19.28	14.72	0.252	0.063	0.6896	0.1718	0.0378	4.01
0.0251	36585	0.9084	19.34	15.76	0.245	0.069	0.6654	0.1862	0.0412	3.57

Table 49: Endplate Configuration at 30 mph: Alpha Sweep

Endplate Configuration at 30 mph: Alpha Sweep - 20th April 2007, $T_{room} = 72.6^\circ F$, $P_{baro} = 29.1564$ inHg, $S = 58.33$ in ² , $b = 11.5$ in										
Mach (-)	Re (-)	q (lb/ft ²)	V (mph)	α (°)	L (lbs)	D (lbs)	C_L (-)	C_D (-)	C_m (-)	L/D (-)
0.0400	58326	2.3088	30.84	-8.38	-0.371	0.086	-0.3970	0.0924	-0.1397	-4.30
0.0401	58493	2.3221	30.92	-6.26	-0.290	0.056	-0.3082	0.0591	-0.1242	-5.21
0.0405	59020	2.3641	31.20	-4.14	-0.174	0.038	-0.1813	0.0398	-0.0992	-4.56
0.0405	59011	2.3634	31.20	-2.01	-0.041	0.028	-0.0433	0.0297	-0.0847	-1.46
0.0403	58813	2.3475	31.09	0.11	0.076	0.028	0.0799	0.0296	-0.0631	2.70
0.0401	58508	2.3233	30.93	2.15	0.205	0.034	0.2184	0.0359	-0.0430	6.08
0.0399	58140	2.2942	30.74	4.27	0.320	0.041	0.3446	0.0441	-0.0171	7.81
0.0401	58473	2.3205	30.91	6.39	0.419	0.048	0.4453	0.0513	0.0131	8.68
0.0406	59247	2.3823	31.32	8.41	0.503	0.058	0.5218	0.0601	0.0399	8.68
0.0407	59428	2.3969	31.42	10.52	0.587	0.071	0.6051	0.0729	0.0602	8.30
0.0409	59599	2.4108	31.51	11.57	0.617	0.084	0.6321	0.0863	0.0544	7.32
0.0401	58525	2.3246	30.94	12.63	0.650	0.101	0.6909	0.1076	0.0487	6.42
0.0401	58549	2.3266	30.95	13.67	0.633	0.120	0.6720	0.1270	0.0210	5.29
0.0407	59368	2.3921	31.39	14.70	0.593	0.136	0.6121	0.1408	0.0144	4.35
0.0406	59181	2.3770	31.29	15.74	0.584	0.153	0.6065	0.1592	0.0069	3.81

Table 50: Endplate Configuration at 40 mph: Alpha Sweep

Endplate Configuration at 40 mph: Alpha Sweep - 20th April 2007, $T_{room} = 72.6^\circ F$, $P_{baro} = 29.1564$ inHg, $S = 58.33$ in ² , $b = 11.5$ in										
Mach (-)	Re (-)	q (lb/ft ²)	V (mph)	α (°)	L (lbs)	D (lbs)	C_L (-)	C_D (-)	C_m (-)	L/D (-)
0.0548	79936	4.3367	42.26	-8.29	-0.676	0.151	-0.3850	0.0861	-0.1333	-4.47
0.0543	79240	4.2615	41.89	-6.26	-0.500	0.095	-0.2897	0.0549	-0.1259	-5.28
0.0542	79064	4.2426	41.80	-4.13	-0.278	0.065	-0.1620	0.0376	-0.1069	-4.31
0.0545	79517	4.2913	42.04	-2.01	-0.056	0.050	-0.0323	0.0289	-0.0852	-1.12
0.0547	79748	4.3163	42.16	0.11	0.159	0.049	0.0909	0.0278	-0.0578	3.27
0.0542	79018	4.2376	41.78	2.15	0.375	0.056	0.2183	0.0325	-0.0288	6.72
0.0542	79040	4.2400	41.79	4.27	0.573	0.067	0.3339	0.0388	-0.0076	8.61
0.0541	78871	4.2219	41.70	6.38	0.734	0.080	0.4294	0.0467	0.0199	9.19
0.0544	79404	4.2791	41.98	8.41	0.901	0.098	0.5198	0.0565	0.0444	9.20
0.0547	79802	4.3222	42.19	10.52	1.062	0.119	0.6064	0.0682	0.0638	8.89
0.0542	79059	4.2421	41.80	11.58	1.135	0.134	0.6607	0.0780	0.0705	8.47
0.0541	78910	4.2261	41.72	12.64	1.186	0.169	0.6928	0.0985	0.0564	7.03
0.0547	79717	4.3129	42.14	13.67	1.184	0.208	0.6780	0.1188	0.0240	5.71
0.0545	79457	4.2849	42.01	14.71	1.143	0.227	0.6583	0.1307	0.0059	5.04
0.0539	78673	4.2008	41.59	15.75	1.100	0.256	0.6463	0.1506	-0.0011	4.29

Table 51: Endplate Configuration at 60 mph: Alpha Sweep

Endplate Configuration at 60 mph: Alpha Sweep - 20th April 2007, $T_{room} = 72.6^\circ F$, $P_{baro} = 29.1564$ inHg, $S = 58.33$ in ² , $b = 11.5$ in										
Mach (-)	Re (-)	q (lb _f /ft ²)	V (mph)	α (°)	L (lbs)	D (lbs)	$C_{l(-)}$	$C_{D(-)}$	$C_{m(-)}$	L/D (-)
0.0823	120030	9.7777	63.46	-8.28	-1.506	0.320	-0.3802	0.0809	-0.1465	-4.70
0.0820	119580	9.7044	63.22	-6.25	-1.041	0.183	-0.2649	0.0466	-0.1364	-5.68
0.0815	118820	9.5824	62.82	-4.13	-0.566	0.128	-0.1459	0.0330	-0.1138	-4.42
0.0817	119120	9.6297	62.97	-2.01	-0.109	0.105	-0.0280	0.0269	-0.0850	-1.04
0.0822	119860	9.7505	63.37	0.11	0.308	0.099	0.0780	0.0251	-0.0514	3.11
0.0824	120210	9.8075	63.55	2.14	0.753	0.110	0.1896	0.0276	-0.0185	6.87
0.0824	120150	9.7969	63.52	4.26	1.250	0.132	0.3149	0.0333	0.0049	9.46
0.0817	119180	9.6401	63.01	6.39	1.688	0.164	0.4322	0.0420	0.0260	10.29
0.0820	119560	9.7013	63.21	8.41	2.075	0.200	0.5281	0.0508	0.0491	10.40
0.0821	119660	9.7181	63.26	10.53	2.424	0.247	0.6157	0.0629	0.0644	9.79
0.0820	119660	9.7175	63.26	11.58	2.589	0.275	0.6578	0.0698	0.0698	9.42
0.0823	119960	9.7670	63.42	12.64	2.739	0.305	0.6924	0.0772	0.0724	8.97
0.0821	119690	9.7234	63.28	13.69	2.868	0.338	0.7281	0.0859	0.0727	8.48
0.0827	120560	9.8640	63.74	14.72	2.800	0.438	0.7009	0.1096	0.0378	6.40
0.0820	119550	9.7005	63.21	15.77	2.746	0.535	0.6989	0.1363	0.0130	5.13

Table 52: No Flow Guide Configuration at 20 mph: Alpha Sweep

No Flow Guide Configuration at 20 mph: Alpha Sweep - 18th April 2007, $T_{room} = 71.2^\circ F$, $P_{baro} = 14.09$ psi, $S = 58.02$ in ² , $b = 11.38$ in										
Mach (-)	Re (-)	q (lb _f /ft ²)	V (mph)	α (°)	L (lbs)	D (lbs)	$C_{l(-)}$	$C_{D(-)}$	$C_{m(-)}$	L/D (-)
0.0244	35066	0.8460	18.79	-8.39	-0.150	0.034	-0.4396	0.0989	-0.1624	-4.44
0.0248	35700	0.8768	19.13	-6.27	-0.117	0.021	-0.3300	0.0596	-0.1385	-5.54
0.0250	35934	0.8883	19.26	-4.15	-0.077	0.013	-0.2144	0.0354	-0.1037	-6.05
0.0245	35262	0.8554	18.90	-2.03	-0.031	0.009	-0.0889	0.0274	-0.0759	-3.25
0.0246	35349	0.8597	18.94	0.10	0.016	0.009	0.0458	0.0260	-0.0566	1.76
0.0248	35673	0.8755	19.12	2.14	0.065	0.012	0.1832	0.0339	-0.0405	5.40
0.0251	36012	0.8922	19.30	4.25	0.100	0.016	0.2795	0.0432	-0.0142	6.47
0.0250	35856	0.8845	19.22	6.29	0.146	0.021	0.4085	0.0590	0.0044	6.93
0.0249	35755	0.8795	19.16	8.41	0.178	0.028	0.5026	0.0804	0.0250	6.25
0.0250	35881	0.8857	19.23	10.52	0.213	0.036	0.5960	0.1017	0.0377	5.86
0.0248	35638	0.8738	19.10	11.58	0.229	0.041	0.6516	0.1173	0.0486	5.55
0.0252	36174	0.9002	19.39	12.63	0.244	0.048	0.6719	0.1311	0.0523	5.13
0.0250	35963	0.8898	19.27	13.67	0.245	0.054	0.6845	0.1502	0.0389	4.56
0.0246	35414	0.8628	18.98	14.73	0.249	0.059	0.7162	0.1711	0.0304	4.19
0.0246	35418	0.8630	18.98	15.76	0.241	0.065	0.6930	0.1856	0.0331	3.74

Table 53: No Flow Guide Configuration at 30 mph: Alpha Sweep

No Flow Guide Configuration at 30 mph: Alpha Sweep - 18th April 2007, $T_{room} = 71.2^\circ F$, $P_{baro} = 14.09$ psi, $S = 58.02$ in ² , $b = 11.38$ in										
Mach (-)	Re (-)	q (lb _f /ft ²)	V (mph)	α (°)	L (lbs)	D (lbs)	$C_{l(-)}$	$C_{D(-)}$	$C_{m(-)}$	L/D (-)
0.0395	56773	2.2175	30.43	-8.38	-0.356	0.080	-0.3984	0.0896	-0.1430	-4.45
0.0398	57241	2.2542	30.68	-6.26	-0.278	0.051	-0.3063	0.0559	-0.1257	-5.48
0.0396	56928	2.2296	30.51	-4.14	-0.172	0.034	-0.1920	0.0375	-0.1025	-5.12
0.0397	56976	2.2333	30.53	-2.02	-0.048	0.024	-0.0533	0.0270	-0.0870	-1.97
0.0395	56777	2.2178	30.43	0.11	0.063	0.024	0.0705	0.0268	-0.0677	2.63
0.0397	57034	2.2379	30.57	2.15	0.185	0.029	0.2054	0.0317	-0.0493	6.47
0.0401	57621	2.2842	30.88	4.27	0.293	0.036	0.3188	0.0387	-0.0252	8.24
0.0400	57478	2.2728	30.80	6.30	0.389	0.043	0.4248	0.0468	0.0034	9.07
0.0401	57640	2.2857	30.89	8.41	0.470	0.053	0.5103	0.0576	0.0268	8.85
0.0401	57563	2.2796	30.85	10.52	0.549	0.067	0.5981	0.0726	0.0437	8.24
0.0402	57797	2.2982	30.97	11.57	0.580	0.081	0.6260	0.0872	0.0355	7.18
0.0400	57530	2.2770	30.83	12.63	0.616	0.095	0.6718	0.1034	0.0357	6.50
0.0398	57245	2.2545	30.68	13.67	0.610	0.114	0.6714	0.1251	0.0158	5.37
0.0401	57583	2.2812	30.86	14.71	0.590	0.126	0.6421	0.1374	0.0026	4.67
0.0402	57729	2.2928	30.94	15.74	0.565	0.143	0.6113	0.1552	-0.0005	3.94

Table 54: No Flow Guide Configuration at 40 mph: Alpha Sweep

No Flow Guide Configuration at 40 mph: Alpha Sweep - 18th April 2007, $T_{room} = 71.2^\circ F$, $P_{baro} = 14.09$ psi, $S = 58.02$ in ² , $b = 11.38$ in										
Mach (-)	Re (-)	q (lb _f /ft ²)	V (mph)	α (°)	L (lbs)	D (lbs)	C_L (-)	C_D (-)	C_m (-)	L/D (-)
0.0549	78867	4.2791	42.27	-8.37	-0.647	0.141	-0.3754	0.0815	-0.1339	-4.61
0.0544	78128	4.1994	41.87	-6.25	-0.476	0.085	-0.2815	0.0503	-0.1252	-5.60
0.0535	76895	4.0679	41.21	-4.13	-0.265	0.055	-0.1619	0.0338	-0.1111	-4.79
0.0532	76509	4.0271	41.00	-2.01	-0.066	0.042	-0.0410	0.0256	-0.0894	-1.60
0.0543	78089	4.1951	41.85	0.11	0.142	0.039	0.0842	0.0233	-0.0618	3.62
0.0545	78324	4.2205	41.97	2.15	0.361	0.047	0.2121	0.0273	-0.0382	7.76
0.0539	77401	4.1216	41.48	4.27	0.533	0.056	0.3212	0.0339	-0.0147	9.46
0.0545	78284	4.2162	41.95	6.29	0.688	0.069	0.4052	0.0407	0.0105	9.96
0.0547	78637	4.2543	42.14	8.40	0.851	0.088	0.4966	0.0511	0.0306	9.71
0.0544	78151	4.2018	41.88	10.52	1.009	0.110	0.5962	0.0648	0.0480	9.20
0.0544	78108	4.1972	41.86	11.58	1.086	0.124	0.6420	0.0731	0.0536	8.78
0.0542	77825	4.1668	41.71	12.63	1.137	0.157	0.6771	0.0934	0.0425	7.25
0.0543	78069	4.1931	41.84	13.67	1.148	0.196	0.6796	0.1163	0.0173	5.84
0.0539	77437	4.1254	41.50	14.72	1.127	0.218	0.6779	0.1309	-0.0001	5.18
0.0537	77179	4.0979	41.36	15.75	1.062	0.230	0.6434	0.1394	-0.0128	4.62

Table 55: No Flow Guide Configuration at 60 mph: Alpha Sweep

No Flow Guide Configuration at 60 mph: Alpha Sweep - 20th April 2007, $T_{room} = 71.9^\circ F$, $P_{baro} = 29.1699$ inHg, $S = 58.02$ in ² , $b = 11.38$ in										
Mach (-)	Re (-)	q (lb _f /ft ²)	V (mph)	α (°)	L (lbs)	D (lbs)	C_L (-)	C_D (-)	C_m (-)	L/D (-)
0.0825	120370	9.8340	63.64	-8.36	-1.421	0.282	-0.3585	0.0711	-0.1470	-5.04
0.0824	120190	9.8043	63.54	-6.24	-0.969	0.153	-0.2453	0.0388	-0.1330	-6.32
0.0823	120000	9.7731	63.44	-4.12	-0.517	0.103	-0.1313	0.0261	-0.1105	-5.02
0.0820	119590	9.7068	63.23	-2.01	-0.076	0.082	-0.0193	0.0208	-0.0850	-0.93
0.0822	119850	9.7493	63.36	0.11	0.325	0.077	0.0827	0.0195	-0.0543	4.23
0.0822	119850	9.7488	63.36	2.14	0.779	0.089	0.1982	0.0226	-0.0259	8.77
0.0818	119270	9.6548	63.06	4.27	1.242	0.111	0.3193	0.0285	-0.0040	11.21
0.0827	120570	9.8663	63.74	6.29	1.648	0.141	0.4145	0.0355	0.0163	11.69
0.0829	120900	9.9207	63.92	8.41	2.039	0.180	0.5100	0.0451	0.0349	11.30
0.0822	119880	9.7538	63.38	10.52	2.392	0.230	0.6086	0.0585	0.0483	10.40
0.0824	120140	9.7952	63.51	11.58	2.560	0.259	0.6487	0.0656	0.0526	9.89
0.0826	120450	9.8468	63.68	12.63	2.714	0.290	0.6841	0.0731	0.0550	9.36
0.0828	120700	9.8880	63.81	13.68	2.836	0.327	0.7119	0.0820	0.0544	8.68
0.0822	119820	9.7442	63.35	14.73	2.800	0.422	0.7131	0.1074	0.0306	6.64
0.0820	119570	9.7031	63.21	15.77	2.756	0.529	0.7049	0.1354	0.0067	5.21

Appendix D: MATLAB Code for Vortex Centroid Calculations

```
clear all
%clc

%6 inch offset converted to mm%
offset = 25.4*6;

%offset = 0;

%Wingspan converted to mm
b = 23.58*25.4;

%Reading the Excel Sheet from the 4deg aoa tecplot%
A = xlsread('vorticity_new good Houck 4aoa.xls');

%Calibrating the y so it can be used for moment calculation
y_excel = A(:,1);
y_calibrated = abs(y_excel-200);
y = offset+y_calibrated;
z = A(:,2);
w_x_unf = A(:,10);

%Loop to filter out positive vorticity
for(i = 1:max(size(w_x_unf)))
    if(w_x_unf(i) > 0)
        w_x(i,1) = 0;
    else
        w_x(i,1) = w_x_unf(i);
    end
end

%w_x = w_x_unf;
TABLE(:,1) = y;
TABLE(:,2) = w_x;

%Loop to sum vorticity for each y coordinate%
i = 1;
j = 1;
w_x_new(i,1) = w_x(i);

for(i = 2:max(size(w_x)))
    if(y(i) == y(i-1))
        w_x_new(i,1) = w_x(i) + w_x_new(i-1,1);
        if(i < max(size(w_x)))
            if(y(i) ~= y(i+1))
                omega(j,1) = y(i);
                omega(j,2) = w_x_new(i);
                w_x_new(i,1) = 0;
                j=j+1;
            end
        elseif(i == max(size(w_x)))
            omega(j,1) = y(i);
        end
    end
end
```

```

                                omega(j,2) = w_x_new(i);
                                end
                                else
                                w_x_new(i,1) = 0;
                                end
                                end

%Loop to calculate total moment%
for(k = 1:max(size(omega)))
    y_moment(k,1) = omega(k,1)*omega(k,2);
end

y_moment_tot = sum(y_moment);
y_tot = 200;
w_x_tot = sum(w_x)
y_bar_FG = y_moment_tot/(w_x_tot)
half_span = b/2;
y_non_dim_FG = y_bar_FG/half_span

%y_bar_FG =
    %250.7439

%y_non_dim_FG =
    %0.8373

```

Bibliography

1. Ahmed, N. A. & Archer, R. D. "Performance Improvements of a Biplane with Endplates." *Journal of Aircraft*, Vol. 38, No. 2, 2001. pp. 398-400.
2. Anderson, J. D. *Fundamentals of Aerodynamics*. New York: McGraw-Hill, 1991. pp. 1-772.
3. Barlow, J. B., Rae, W. H. & Pope, A. *Low-Speed Wind Tunnel Testing* New York: John Wiley & Sons, 1999. pp. 1-713.
4. "Boeing: Commercial airplanes - 737 – winglets." The Boeing Company. n. pag. <http://www.boeing.com/commercial/737family/winglets/wing2.html>. May 2007
5. Brandt, S. A. *Introduction to Aeronautics: A Design Perspective, 2nd ed.* Reston, VA: American Institute of Aeronautics and Astronautics, 2004. pp. 1-391.
6. Bryant, M. E. "Unique stealth UAV Houck Aircraft Design Program." Collaborative Project Order FA8650-05-3-9017. 6th November, 2006.
7. Chattot, J. J. "Low Speed Design and Analysis of Wing/Winglet Combinations Including Viscous Effects." *Journal of Aircraft*, Vol. 43, No. 2, 2006. pp. 386-389.
8. Corneille, J. & Franke, M. E. "Wind Tunnel Tests of a Joined-Wing Missile Model." AIAA 38th Aerospace Sciences Meeting, 10-13 January 2000. pp. 1-8.
9. Craig, G. M. *Introduction to Aerodynamics: Basic Aerodynamics in Newtonian Terms, 1st ed.* Anderson, IN: Regenerative Press, 2000. pp. 1-214.
10. DeLuca, A. M. *Experimental Investigation into the Aerodynamic Performance of both Rigid and Flexible Wing Structured Micro-Air-Vehicles*. Thesis, Air Force Institute of Technology, WPAFB OH, March 2004.
11. Dole, C. E. & Lewis, J. E. *Flight Theory and Aerodynamics : A Practical Guide for Operational Safety, 2nd ed.* New York: John Wiley & Sons, 2000. pp. 1-314.
12. Filippone, A. *Advanced Topics in Aerodynamics, Computational Fluid Dynamics, Aeronautics, Propulsion Systems*. n. pag. <http://www.aerodyn.org>. April 2007.
13. Gall, P. D. & Smith, H. C. "Study of Winglets Applied to Biplanes" NASA-TM-86350 ed., Washington, DC: National Aeronautics and Space Administration, 1985. pp. 1-19.
14. Gallman, J. W., Smith, S. C. & Kroo, I. M. "Optimization of Joined-Wing Aircraft." *Journal of Aircraft*, Vol. 30, No. 6, 1993. pp. 897-905.

15. Gallman, J. W. & Kroo, I. M. "Structural Optimization for Joined-Wing Synthesis." *Journal of Aircraft*, Vol. 33, No. 1, 1996. pp. 214-223.
16. Houck II, R. G. *Lifting Foil*. Patent 7,100,867. September 2006.
17. Kuethe, A. M. & Chow, C. Y. *Foundations of Aerodynamics : Bases of Aerodynamic Design, 5th ed.* New York: John Wiley & Sons, 1998. pp. 1-572.
18. Lin, C. S., Ng, T. T. & Skaff, A. "An Experimental Study of Wing Tips for Wing Performance Improvement." AIAA Paper 1996-2413, 1996. pp. 304-314.
19. Loftin, L. K. *The Quest for Performance: The Evolution of Modern Aircraft*. n. pag. <http://www.hq.nasa.gov/pao/History/SP-468/cover.htm>. April 2007.
20. Masak, P. "Winglet Design Considerations." *Schreder Sailplane Design*. n. pag. Retrieved 4/8/2007, 2007, <http://www.soaridaho.com/Schreder/Technical/Winglets/Masak.htm>. April 2007.
21. Maughmer, M.D., Swan, T.S. & Willits, S.M. "Design and Testing of a Winglet Airfoil for Low-Speed Aircraft." *Journal of Aircraft*, Vol. 39, No. 4, 2002. pp. 654-661.
22. Maughmer, M. D. "The Design of Winglets for High-Performance Sailplanes." AIAA Paper 2001-2406, 2001.
23. Mock, R. M. "The Distribution of Loads Between the Wings of a Biplane Having Decalage." NASA, NACA-TN-269, 1927. pp. 1-47.
24. Oligney, B., Frash, M. & Yechout, T. R. *Aerodynamic and Stability Evaluation of the Houck Joined Wing Aircraft*. Senior Project, US Air Force Academy, USAFA CO, January 2007. pp 1-29.
25. Rivera Parga, J. R. *Wind Tunnel Investigation of the Static Stability and Control Effectiveness of a Rotary Tail in a Portable UAV*. Thesis, Air Force Institute of Technology, WPAFB OH, December 2004.
26. "SolidWorks for Students." SolidWorks Corporation. n. pag. <http://www.solidworks.com/pages/products/edu/solidworksforstudents.html>. May 2007.
27. Smith, A.S. & Campbell, R.L. "Effects of Winglets on the Drag of a Low-Aspect-Ratio Configuration" NASA, NACA-TP-3563, 1996. pp. 1-66.
28. Talay, T. A. "Subsonic flow effects." *Introduction to the Aerodynamics of Flight*. n. pag. <http://history.nasa.gov/SP-367/chapt4.htm#4.1>. April 2007.

29. Traub, L. W. "Theoretical and Experimental Investigation of Biplane Delta Wings." *Journal of Aircraft*, Vol. 38, No. 3, 2001. pp. 536-546.
30. "UIUC airfoil coordinates database." University of Illinois at UrbanaChampaign. n. pag.
http://www.ae.uiuc.edu/mseelig/ads/coord_database.html. December 2006.
31. Walker, M. M. *The Aerodynamic Performance of the 24 inch Houck Configuration*. Thesis, Air Force Institute of Technology, WPAFB OH, March 2006.
32. Wolkovitch, J. *Joined Wing Aircraft*. Patent 4,365,773. September 1980.
33. Wolkovitch, J. "The Joined Wing: An Overview." *Journal of Aircraft*, Vol. 23, 1986. pp. 161-178.
34. Yechout, T. R. & Morris, S. L. *Introduction to Aircraft Flight Mechanics: Performance, Static Stability, Dynamic Stability, and Classical Feedback Control*. Reston, VA: American Institute of Aeronautics and Astronautics, 2003. pp. 1-634.

Vita.

Dermot Killian was born in Portland, Maine. He graduated from Cheverus High School, in Portland, Maine in 2002. He went on to earn a Bachelors degree in Mechanical Engineering from the United States Naval Academy in Annapolis, Maryland from 2002 to 2006. Following graduation, he was commissioned as an Officer in the United States Navy. In the Summer of 2006 he began attending the Air Force Institute of Technology at Wright Patterson Air Force Base, Ohio for completion of his Masters Degree in Aeronautical Engineering. After graduation in Summer 2007, he will be stationed in NAS Pensacola to start student naval aviator training and work towards his wings of gold.

REPORT DOCUMENTATION PAGE				<i>Form Approved</i> OMB No. 074-0188	
<p>The public reporting burden for this collection of information is estimated to average 1 hour per response, including the time for reviewing instructions, searching existing data sources, gathering and maintaining the data needed, and completing and reviewing the collection of information. Send comments regarding this burden estimate or any other aspect of the collection of information, including suggestions for reducing this burden to Department of Defense, Washington Headquarters Services, Directorate for Information Operations and Reports (0704-0188), 1215 Jefferson Davis Highway, Suite 1204, Arlington, VA 22202-4302. Respondents should be aware that notwithstanding any other provision of law, no person shall be subject to a penalty for failing to comply with a collection of information if it does not display a currently valid OMB control number.</p> <p>PLEASE DO NOT RETURN YOUR FORM TO THE ABOVE ADDRESS.</p>					
1. REPORT DATE (DD-MM-YYYY) 14-06-2007		2. REPORT TYPE Master's Thesis		3. DATES COVERED (From - To) October 2006 - June 2007	
4. TITLE AND SUBTITLE THE AERODYNAMIC PERFORMANCE OF THE HOUCK CONFIGURATION FLOW GUIDES				5a. CONTRACT NUMBER JON ENY 07-249	
				5b. GRANT NUMBER	
				5c. PROGRAM ELEMENT NUMBER	
6. AUTHOR(S) Killian II, Dermot N., Ensign, USN				5d. PROJECT NUMBER	
				5e. TASK NUMBER	
				5f. WORK UNIT NUMBER	
7. PERFORMING ORGANIZATION NAMES(S) AND ADDRESS(S) Air Force Institute of Technology Graduate School of Engineering and Management (AFIT/EN) 2950 Hobson Way, Building 640 WPAFB OH 45433-8865				8. PERFORMING ORGANIZATION REPORT NUMBER AFIT/GAE/ENY/07-J09	
9. SPONSORING/MONITORING AGENCY NAME(S) AND ADDRESS(ES) AFRL/VAAA Attn: Capt Elaine Bryant or Mr. Cale Zeune Building 45, 2130 8 th St WPAFB OH 45433				10. SPONSOR/MONITOR'S ACRONYM(S)	
				11. SPONSOR/MONITOR'S REPORT NUMBER(S)	
12. DISTRIBUTION/AVAILABILITY STATEMENT APPROVED FOR PUBLIC RELEASE; DISTRIBUTION UNLIMITED.					
13. SUPPLEMENTARY NOTES					
14. ABSTRACT In an effort to explore efficient wing designs for UAV's, the Air Force is investigating the patented Houck Aircraft Configuration, which is a joined-wing aircraft with curved flow guides of varying camber connecting the upper and lower wingtips. Models were drawn in three-dimensions using Solidworks® with upper and lower wings drawn as identical NACA 2412 airfoil sections for all models. A variety of airfoil sections between the upper and lower wingtips were drawn and rotated to achieve a combination of cant and angle of attack variation. Subsequently, a solid part was lofted through these sections and merged with the upper and lower wings. Each model was built by a rapid prototype machine. A six-component balance in the AFIT low-speed wind tunnel provided measurements yielding the aerodynamic data of each model. Comparisons are made to the same basic planform area without flow guides and to a case where the wingtips are joined with a flat plate. At a Reynolds number of 38K, the increase in skin friction drag outweighed any possible reduction of induced drag. However for Reynolds numbers in the 57K to 120K range, improvements in L/D_{max} of about 2-5% over the no flow guide case were measured.					
15. SUBJECT TERMS Joined wing, Biplane, Lift-to-drag, Low-speed wind tunnel, Hot-wire analysis, Flow visualization, Flow guides, Winglets, Wing-tip vortices, Aerodynamic efficiency, Effective aspect ratio, Span efficiency factor					
16. SECURITY CLASSIFICATION OF:			17. LIMITATION OF ABSTRACT UU	18. NUMBER OF PAGES 184	19a. NAME OF RESPONSIBLE PERSON Dr. Mark Reeder
a. REPORT U	b. ABSTRACT U	c. THIS PAGE U			19b. TELEPHONE NUMBER (Include area code) (937) 255-6565, ext 4530 (mark.reeder@afit.edu)